HYDROGEN BURNING OF THE RARE OXYGEN ISOTOPES

Matthew Quinn Buckner

A dissertation submitted to the faculty at the University of North Carolina at Chapel Hill in partial fulfillment of the requirements for the degree of Doctor of Philosophy in the Department of Physics.

Chapel Hill
2014

Approved by:

Christian Iliadis

Gerald Cecil

Arthur E. Champagne

Thomas B. Clegg

Fabian Heitsch

ABSTRACT

Matthew Quinn Buckner: HYDROGEN BURNING OF THE RARE OXYGEN ISOTOPES
(Under the direction of Christian Iliadis)

At the Laboratory for Experimental Nuclear Astrophysics (LENA), two rare oxygen isotope proton capture studies were performed at low energies—^{18}O(p,γ)^{19}F and ^{17}O(p,γ)^{18}F. The goal of each study was to improve thermonuclear reaction rates at stellar plasma temperatures relevant to ^{18}O and ^{17}O destruction, respectively. The stellar nucleosynthesis temperature regime corresponds to very low proton bombarding energies. At these low energies, the Coulomb barrier suppresses the reaction yield in the laboratory, and environmental backgrounds dominate the detected signal, making it difficult to differentiate the γ-cascade from background. At LENA, the electron cyclotron resonance (ECR) ion source produces intense, low-energy proton beam, and these high currents boost the reaction yield. LENA, a "sea-level" facility dedicated to nuclear astrophysics, also has a coincidence detector setup that reduces environmental background contributions and boosts signal-to-noise. The sensitivity afforded by $\gamma\gamma$-coincidence and high beam current allowed these rare oxygen isotope reactions to be probed at energies that correspond to stellar plasma temperatures.

For stars with masses between 0.8 $M_\odot \leq M \leq$ 8.0 $M_\odot$, nucleosynthesis enters its final phase during the asymptotic giant branch (AGB) stage. This is an evolutionary period characterized by grain condensation that occurs in the stellar atmosphere; the star also experiences significant mass loss during this period of instability. Presolar grain production can often be attributed to this unique stellar environment. A subset of presolar oxide grains features dramatic ^{18}O depletion that can not be explained by the standard asymptotic giant star burning stages and dredge-up models. An extra mixing process for low-mass asymptotic giant branch stars, known as *cool bottom processing* (CBP), was used in the literature to explain this and other anomalies. Cool bottom processing can also occur during the red giant branch (RGB) phase, but it is not thought to contribute to the *extreme* ^{18}O depletion observed within certain stellar environments and within presolar grain samples. However, intense depletion could result from the ^{18}O + p processes during cool bottom processing in low-mass AGB stars. A portion of this dissertation describes a study of the ^{18}O(p,γ)^{19}F reaction at low energies performed at LENA. Based on these new results, it was found that the resonance at E_R = 95 keV has a negligible effect on the reaction rate at the temperatures associated with cool bottom processing when compared to the (p,α) reaction. It was also observed that the direct capture S-factor is almost a factor of 2 lower than the previously recommended value at low energies. The product

of this research is a new thermonuclear reaction rate for $^{18}O(p,\gamma)^{19}F$. These results were published in Buckner *et al.* (2012) [1].

Classical novae are thought to be among the dominant sources of ^{17}O in the Galaxy. These energetic events produce ^{18}F that, as it decays to ^{18}O, emits positrons that annihilate with electrons producing 511 keV γ-rays. These emissions occur at timescales that correspond to a transparent nova expansion envelope making their observation possible and important for constraining nova stellar models. The importance of the non-resonant component of the $^{17}O(p,\gamma)^{18}F$ reaction is well established, and numerous studies have been performed to analyze this reaction. The experimental tools available at LENA, in addition to a novel spectral analysis method, allowed the $^{17}O(p,\gamma)^{18}F$ reaction to be studied within the classical nova Gamow window, and new total S-factors were measured. The lowest energy *in-beam* $^{17}O(p,\gamma)^{18}F$ measurement ever made was collected during this experiment. A new direct capture S-factor was determined, and it was confirmed that this S-factor is constant at low energies. The $E_R = 193$ and 518 keV resonances were also measured, and new resonance strengths were determined. New $^{17}O(p,\gamma)^{18}F$ thermonuclear reaction rates are reported within this thesis. The direct capture contribution, combined with updated partial widths and strengths from the literature, improved reaction rate uncertainties at low temperatures and may also impact ^{17}O overproduction in asymptotic giant branch stellar models. With the improved direct capture S-factor and new resonance strengths, rate uncertainties at classical nova temperatures decreased.

For Megan.

"Nevertheless I long—I pine, all my days—to travel home and see the dawn of my return. And if a god will wreck me yet again on the wine-dark sea, I can bear that too, with a spirit tempered to endure. Much have I suffered, labored long and hard by now in the waves and wars. Add this to the total—bring the trial on!" (*The Odyssey* 5:242-48 [2])

ACKNOWLEDGEMENTS

I do not think I can convey how truly grateful I am to Dr. Thomas Clegg for recognizing my potential, and during my first visit to the University of North Carolina at Chapel Hill, encouraging me to consider a generous offer from the Department of Physics and Astronomy. He also convinced me to work at the Laboratory for Experimental Nuclear Astrophysics (LENA) at Triangle Universities Nuclear Laboratory (TUNL). Tom and Dr. Christian Iliadis became my Master's research advisors, and I began working on several different projects for them as I took classes my first year and studied for the written qualifying examination. Tom pushed me to apply for several fellowships, and I credit Tom for my successful application to the DOE NNSA Stewardship Science Graduate Fellowship. Additionally, Tom's friendship with Dr. Jay Davis at Lawrence Livermore National Laboratory (LLNL) facilitated my placement at LLNL's Center for Accelerator Mass Spectrometry (CAMS) during the summer of 2010. This summer practicum fulfilled the internship requirement stipulated by my DOE fellowship. Tom guided me during my first project at LENA, pulsing the electron cyclotron resonance (ECR) ion source proton beam and several other instrumentation projects. I love building and developing new hardware, and being able to work on a few instrumentation projects early in my graduate career helped me transition from my scholarly pursuits as an undergraduate to working in a laboratory environment as a graduate student.

When I started working with Christian in addition to Tom, my longterm research goals began to really take shape. My thesis advisor, Dr. Christian Iliadis, is a titan within the nuclear astrophysics community, and it is an honor and a privilege to work with him. His input, advice, criticism, and support were incredibly valuable throughout my graduate experience, and I am eternally indebted to him for his patience and his willingness to provide guidance. His expertise in detector setup, data acquisition electronics, and spectral analysis were invaluable, and I gained a significant amount of experience and understanding working alongside him as I developed my detector and DAQ configuration. He shared his indomitable wealth of knowledge and experience with regard to all aspects of my graduate endeavors, from theoretical calculations to experiment design to drafting peer reviewed papers. Christian was also extremely approachable and always eager to meet and discuss progress, setbacks, and anomalies over a cup of coffee; he was the quintessential thesis advisor and I can not thank him enough.

Dr. Arthur Champagne always proved to be a valuable asset and a monumental motivational force at LENA. I am indebted to him for his efforts to develop and maintain LENA and for ensuring that the

resources necessary for LENA to endure were always on hand. I recall numerous occasions where Art and I worked on conditioning the accelerators, and my familiarity with ion sorcery stems directly from these collaborations. Not only is Art a truly impressive experimentalist, he is also a gifted educator. Perhaps my fondest memory of graduate coursework at UNC was when Art took the reigns of a nuclear physics class and taught us material that would prove essential to my thesis work. I have also often relied on Art for his expert advice on technical and experimental issues, and I have him to thank for so many of the technical skills I have acquired.

Thank you to Dr. Fabian Heitsch and Dr. Gerald Cecil for their role as my dissertation committee members. I acknowledge the support of the US Department of Energy under Contract no. DE-FG02-97ER41041 and the DOE NNSA Stewardship Science Graduate Fellowship under Grant no. DE-FC52-08NA28752.

Aside from Professors Clegg, Iliadis, and Champagne, the one person who is most responsible for my evolution from undergraduate astrophysics scholar to a nuclear astrophysics doctoral candidate is Dr. John "Johnny" Cesaratto. When I first arrived at LENA, I found Johnny to be incredibly talented and intimidating. His focus, tenacity, and technical skills were both terrifying and awe-inspiring. However, I realized quickly that I could learn a lot from Johnny Cesaratto. I remember struggling to master conditioning the ECR ion source and tuning the accelerators under his tutelage. I am sure my persistent, naive questions were a constant frustration for him, but his calm, patient explanations of electronics, beam transport, signal processing, and ion sorcery were unequivocally critical to my progression, growth, and success as a graduate student. Johnny filled a void at LENA that became all the more apparent after his departure. I assert that if I even somewhat live up to his legacy and fill the vacuum he left behind at this laboratory, I do so because I learned from the best; I am the scientist I am today because of Johnny Cesaratto, and I can not think of a better role model and mentor.

At this point in my graduate career, I thank Dr. Chris Howard nearly every time I see him for the computational skills he helped me acquire. Chris inherited numerous, challenging projects when he became a post-doctoral fellow at UNC. He rose to those challenges, and unprompted, he also adopted the role of programming guru and teacher. As a graduate student with extremely deficient computational skills, I desperately needed to learn a programming language. As an undergraduate student, Mathematica and Excel were all I needed to satisfy Lehigh University's astrophysics curriculum, but actual research demands a significantly more sophisticated toolkit. Chris made himself available to provide feedback and advice as I learned to program in C and C++. He also taught me to use ROOT, GEANT4, and the command prompt. At the culmination of this computational education, I built my own linux analysis server and was performing calculations that had taken me months with Excel and Mathematica in under a week. Because

of this experience, I advise every new graduate student that joins the LENA group to learn a programming language and to start exploring ROOT.

Dr. Stephen Daigle was always an excellent sounding board for theories and thought experiments. Whether it was refining a computational goal, tweaking the progression of an experiment, or pouring over a textbook to extract a key piece of information, Stephen was helpful, jovial, and amiable. Stephen and I spent a lot of time working together during the laboratory phase of his ^{14}N(p,γ)^{15}O experiment, and that experience bolstered my technical skills, giving me the opportunity to refresh my accelerator operation technique. I appreciate everything Stephen did for me during my graduate career; he was always quick to offer advice or help when necessary.

The other post-doctoral fellow working at LENA, Dr. Anne Sallaska, also made a valuable contribution to my overall development as a doctoral student. During her career, Anne gained computational and experimental experience, and endured and succeeded despite periodic setbacks and unexpected challenges. Because of her experiences as a graduate student and post-doc, I consider Anne extremely competent and even battle-hardened, and I value her opinion and critiques. I hope that if I am ever in her position, I can provide the quality constructive criticism and insights that I came to expect from her.

I believe that we only truly learn something when we are given the opportunity to teach it to someone else. Keegan Kelly proved that he is not only a brilliant and eager student, he was also incredibly helpful with everything from detector setup to data collection. His role as copilot during Stephen's ^{14}N(p,γ)^{15}O experiment and my ^{17}O(p,γ)^{18}F experiment was critical for Stephen and I to each proceed to graduation; I am forever indebted to Keegan for his willingness to commit time and energy to these projects, and I am certain this process benefited his growth as an experimental physicist.

Dr. Richard Longland and Dr. Joseph Newton each contributed in small ways to my research by writing codes that I used or augmented, or by having important conceptual conversations with me.

TUNL technical staff members Jeff Addison, Bret Carlin, John Dunham, Patrick Mulkey, Richard O′Quinn, and Chris Westerfeldt were all extremely helpful, and I can not thank them enough for their contributions. I am particularly indebted to Bret for actively participating in brainstorming and troubleshooting sessions, and for making major contributions to my progression towards graduation.

During my experiment, Lori Downen was an excellent assistant and student. She was very helpful during the data acquisition phase of my ^{17}O(p,γ)^{18}F experiment.

Sean Hunt, Jack Dermigny, and Andrew Cooper devoted considerable time and energy to my experiment. The three of them shouldered a lot of responsibility and tackled several formidable obstacles. Sean and Jack exhaustively optimized the LENA evaporator. Andrew developed the ECRIS magnet control mechanisms and worked on the beam rastering system with Jason Surbrook. They were also incredibly helpful during

data acquisition.

Additionally, I would like to thank Grayson Rich for upgrading the ECRIS remote control system. This was truly a daunting project, but I had complete faith in Grayson's incredible attention to detail and ability to design and to engineer complex control systems. The system he gave us is superb and I can not thank him enough.

The Duke University and UNC machine shops were also contributors to the realization and fabrication of key items critical to the completion of this research. Both shops contributed to the production of a new target box, anodization chamber, ECR ion source aluminum liner, and plasma chamber heat sink.

I can not thank all of these scholars, educators, and technicians without thanking that one educator who over a decade ago taught me the fundamental laws of Nature and encouraged me to pursue higher education in the sciences. Thank you, Mr. Frank Romano for challenging me, motivating me, and inspiring me to excel. Thank you for helping me discover that I could harness both my intellect and my creativity, and simultaneously wield them to uncover the mysteries of the Universe and peer into the depths of cosmic cauldrons.

Also, a special thanks to visionary artist, and my good friend, Mr. John Cheer. John, you unwittingly provided me with my first "laboratory" experience and fodder for all of those graduate school essays. Thank you for your friendship and the steady income during college.

I would like to thank my friend Jennifer White for not only agreeing to proofread this dissertation, but for actually reading through the entire document (twice) and supplying me with grammatical corrections. I can not think of many people I know who would agree to review my thesis, put in the time and effort to actually follow through, and provide valuable feedback. Thank you, Jenn.

Mom and Dad, throughout my life you were my loudest supporters, and I know that I won your love and affection on day one. I know I did not need to get a doctoral degree to make you proud of me, but I went ahead and did it anyway. Thank you both for giving Ben and me everything you had. Thank you for answering all of my questions as a child, for telling me stories, for reading to me, for taking me on walks behind Rockledge looking for whales, for teaching me so much, and for nurturing both the profoundly creative and intensely quizzical sides of my personality. I love you both so much. Thank you.

Benjamin, thank you for always believing in me and encouraging me. You are an amazing brother and one of my best friends; the relationship we are able to have as adults seems to be rare among siblings. You never cease to amaze me and serve as a reminder to flex my own creativity and imagination.

And finally, my dear wife, Megan Francis Gallagher, thank you. Thank you for taking that risk and turning your life upside down to move to North Carolina to live with me. Thank you for sacrificing so many things for me to follow this improbable and often incomprehensible trajectory. Thank you for putting

yourself through excruciating torture and enduring it for us and for our future. Thank you for shouldering more stress and responsibility than humanly possible and not buckling. Thank you for being so incredibly strong, so incredibly brave, and a daily inspiration. Thank you for all of your love and for sharing this life with me. Thank you for preserving my sanity, maintaining my motivation, and imbuing me with your strength and relentless tenacity. I love you. This manuscript is as much for you as it is for me. That is why I hereby dedicate this doctoral dissertation to you.

TABLE OF CONTENTS

LIST OF TABLES

LIST OF FIGURES

CHAPTER 1: INTRODUCTION

Section 1.1: Astrophysical Motivation

Visualizing stellar evolution is facilitated by a *color-magnitude diagram* or Hertzsprung-Russell diagram. By plotting luminosity versus surface temperature (with decreasing temperature from right to left), the relationship between stellar mass, luminosity, surface temperature, age, and evolutionary stage can be understood. Figure 1.1 [3] is a common example of a Hertzsprung-Russell diagram because it features a lot of structure that can be attributed to the different stages of stellar evolution. In this figure, the B−V color index is used instead of surface temperature, and absolute magnitude is used instead of luminosity. Important features are labeled in Fig. 1.1; when a star is burning hydrogen to helium in its core, it lies along the main sequence (MS). The Sun, for example, is a main sequence star, and at a core temperature of 15 MK, four protons fuse to helium and release a substantial amount of energy (along with two positrons and two neutrinos):

$$4\mathrm{H} \rightarrow {}^{4}\mathrm{He} + 2e^{+} + 2\nu + 26.7 \text{ MeV}. \tag{1.1}$$

Based on the mass of a particular star, it may remain on the main sequence for millions to billions of years—more massive stars exhaust their supply of core hydrogen and evolve off the main sequence before lower mass stars. The main sequence turn-off point (TO) is a luminosity versus temperature feature that corresponds to the age of a cluster. If it can be assumed that the stars in a cluster all formed at the same time, and the mass is proportional to the time spent on the main sequence ($\approx 90\%$ of the star's lifespan), then the turn-off point corresponds to the mass/age threshold between core hydrogen burning and envelope expansion, core contraction, and ascension of the red giant branch (RGB). During the red giant branch phase, core hydrogen burning has ended, but hydrogen still burns in a shell that surrounds a helium core. Before helium can begin to fuse in the core, temperatures need to rise dramatically. The core contracts and heats; temperatures increase in the hydrogen shell, and the convective envelope expands. Hydrogen fuses to helium in the shell with the help of carbon, nitrogen, and oxygen catalyst isotopes in processes called CNO(F) fusion cycles. The products of this nucleosynthesis are *dredged-up* by the convective envelope and brought to the surface of the star. At a helium core temperature of 100 MK, helium burning to carbon commences, and the star occupies the horizontal branch (HB) of the color-magnitude diagram. A star ascends the giant branch a second time, the asymptotic giant branch (AGB) phase, when core helium is exhausted. Shells of helium

and then hydrogen encase a carbon-oxygen core (an oxygen-neon core in more massive stars). During the asymptotic giant branch phase, recurrent periods of instability gradually drive off a star's envelope creating a planetary nebula and exposing the electron-degenerate core, a stellar corpse called a white dwarf. Stars more massive than ≈11 $M_\odot$ (where $M_\odot$ is the mass of the Sun) end their lives violently as supernovae producing a compact remnant—either a black hole or neutron star (depending on the mass of the progenitor).

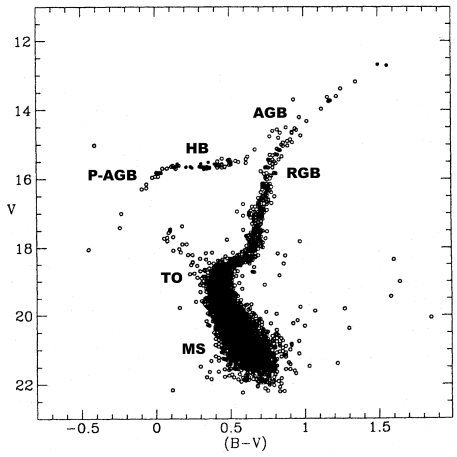

Figure 1.1: From Ref. [3], the globular cluster M3 is the population of stars shown in this color-magnitude diagram. The x-axis is the B−V color index. Along the y-axis, the absolute magnitude is shown. The main sequence branch (MS), the main sequence turn-off point (TO), the red giant branch (RGB), the asymptotic giant branch (AGB), the horizontal branch (HB), and the post-asymptotic giant brand (P-AGB) are shown on this plot. These features correspond to different burning stages during stellar evolution. See Ref. [4] for more information on stellar evolution.

1.1.1: Cool Bottom Processing in Low-Mass AGB Stars

Matter in our solar system has a unique $^{18}O/^{16}O$ isotopic signature—$(2.09^{+0.13}_{-0.12})\times10^{-3}$ [5]. However, a collection of presolar grain samples features peculiar oxygen isotopic ratios. Presolar grains are dust particles that condensed in the ejecta of evolved stars, supernovae, or, in some cases, classical novae [6] (see Fig. 1.2). These grains can be isolated from meteorites and then probed with secondary ion mass spectrometry (SIMS) or resonance ionization mass spectrometry (RIMS) [7]. Grains can provide insight into Galactic chemical evolution, stellar nucleosynthesis and evolution, and circumstellar and interstellar dust formation [8, 6]. Certain alumina (Al_2O_3) grains are considered outliers with respect to the trove of presolar grains gathered over the years from primitive meteorites and interplanetary dust particles. The ^{18}O study presented in this thesis is motivated by observations of presolar grains that nucleated in the atmospheres of distant, evolved stars before the formation of the Sun. These grains retain the isotopic ratios of the stellar surface they originated from. During the birth of the Sun, most presolar grains were annihilated as gas and

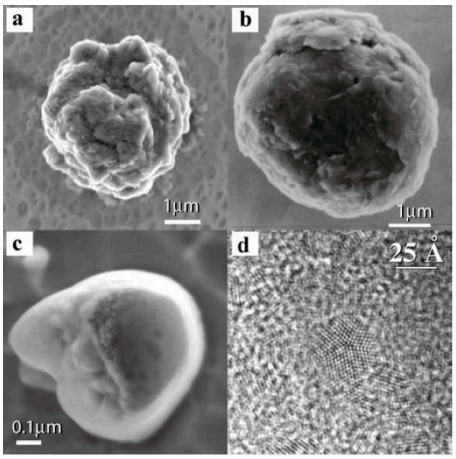

Figure 1.2: From Ref. [9], (a) a scanning electron (SE) micrograph image of a 3 μm presolar SiC grain, (b) a SE image of a 5 μm presolar graphite grain, (c) a SE image of a 0.5 μm presolar Al_2O_3 grain, and (d) a high-resolution transmission electron microscope image of presolar nanodiamonds.

dust collapsed to form the nascent star. As the solar system cooled and the Sun ascended the main sequence, the presolar grains that survived were incorporated into primitive meteorites. The study of their abnormal isotopic ratios provides crucial constraints for astrophysical models. The $^{18}O(p,\gamma)^{19}F$ portion of this thesis focuses on oxide grains referred to as *Group 2* grains, approximately 15% of all presolar oxides [6] (see Fig. 1.3a). They exhibit a characteristic $^{18}O/^{16}O$ abundance ratio $\leq 1.5\times10^{-3}$ [10], reflecting substantial ^{18}O depletion [7] with respect to the Solar value.

The depletion of ^{18}O may occur due to *cool bottom processing* (CBP) [6] in low-mass red giant branch (RGB) and asymptotic giant branch (AGB) stars [10]. This *extra mixing* process was proposed by Ref. [12] to account for isotopic anomalies, including ^{18}O depletion, in presolar grains. During cool bottom processing, material circulates between the convective envelope and the radiative zone that separates the envelope from the hydrogen burning shell (see Fig. 1.4). The base of the convective envelope remains cool, thus distinguishing this process from *hot bottom burning* (HBB) that occurs in 4−7 $M_\odot$ asymptotic giant branch stars [12, 6]. Hot bottom burning peak temperatures range from 30 MK to about 100 MK and may be as high as 125 MK [14] ($^{17}O + p$ may impact hot bottom burning at these temperatures [15] and will be discussed later in Chapter 6). During cool bottom processing, as the circulated matter approaches the hydrogen shell, it reaches temperatures high enough to destroy ^{18}O via hydrogen burning. The processed material is then recirculated into the convective envelope and transported to the stellar surface. The mechanism driving cool bottom processing is not understood, and several explanations have been proposed, including magnetic buoyancy [16, 17], gravity waves [18], shear instability [19, 20, 21, 22], meridional circulation [23, 24], molecular weight inversion [25], and thermohaline double-diffusion [26, 27].

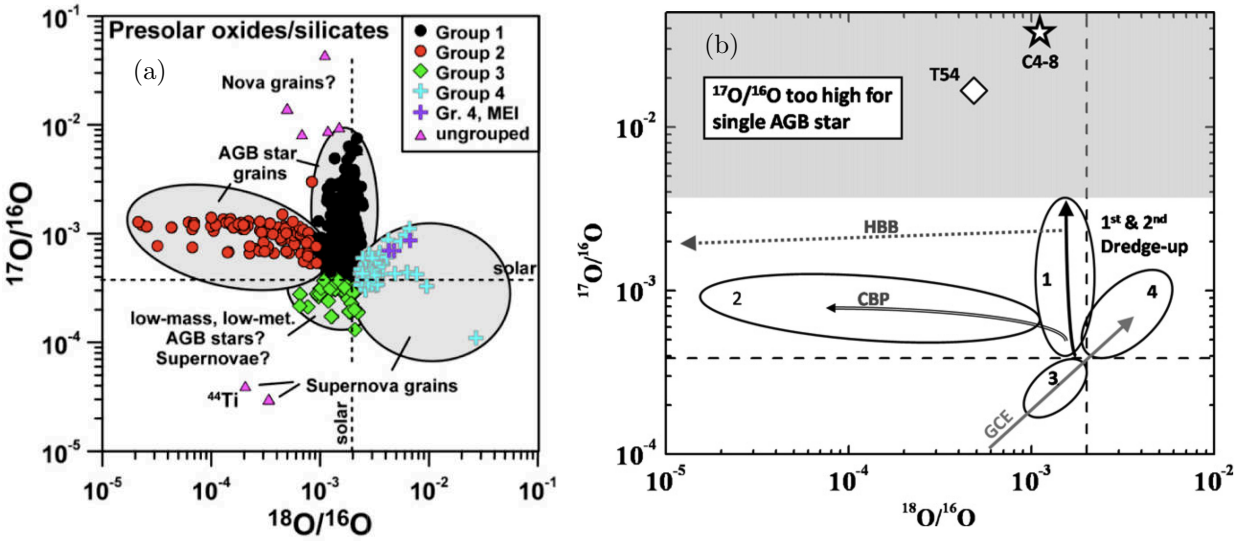

Figure 1.3: (a) From Ref. [7], a plot of the different presolar oxide grains with $^{17}O/^{16}O$ on the y-axis and $^{18}O/^{16}O$ on the x-axis. The dashed lines represent the Solar values. The solid red circles, Group 2, represent roughly 15% of all presolar oxides and exhibit extreme ^{18}O depletion [6]. (b) From Ref. [11], a simplified version where the T54 and C4-8 grains—thought to be produced by classical novae (see Sec. 1.1.2)—are emphasized. The abbreviations GCE, CBP, and HBB refer to Galactic chemical evolution, cool bottom processing, and hot bottom burning, respectively.

However, as pointed out by Refs. [28, 29], there is a finite amount of time during an evolutionary stage in which nucleosynthesis due to extra-mixing processes can occur and produce observed isotopic abundances. Mechanisms like magnetic buoyancy are fast and could satisfy this constraint [16, 30, 17], while diffusive and rotational processes are slow and less likely to drive cool bottom processing [31, 32].

For a 1.0 $M_\odot \leq M \leq$ 1.5−1.7 $M_\odot$ red giant branch star, moderate ^{18}O depletion might occur due to cool bottom processing, and this depletion is reflected in the *Group 1* grains [33] in Fig. 1.3a [10]. According to Palmerini *et al.* (2011a) [10], cool bottom processing in RGB stars is a viable, but moderate, ^{18}O destruction mechanism if the maximum temperature of the circulated material approaches $T_P \approx 24$ MK and the hydrogen-burning shell is (at most) $T_H \approx 38$ MK. Cool bottom processing in RGB stars can not account for the Group 2 presolar grains in Fig. 1.3a [10], and there must be another stellar environment where cool bottom processing occurs [34]. It is hypothesized that low-mass asymptotic giant branch stars are this ^{18}O depletion site [6, 10].

During the asymptotic giant branch stage—the final phase of nucleosynthesis during the evolution of a 0.8−8.0 $M_\odot$ star [35, 36]—a star undergoes substantial nucleosynthesis and mass loss. Peeling away the surface layers enveloping an asymptotic giant branch star reveals numerous burning sites and a complex interplay between these regions. A stellar core, composed of *partially* electron-degenerate carbon and oxygen, is surrounded by alternately burning helium and hydrogen shells. Degeneracy refers to the Pauli Exclusion

Principle, *no more than two spin 1/2 particles can occupy a given quantum state simultaneously.* Degenerate gas resists compression because all lower-lying states are occupied; pressure no longer depends on temperature [4]. During periods of helium-burning, referred to as thermal pulses, thermonuclear runaway (TNR) occurs and drives convection between the two burning sites. When the thermonuclear runaway subsides, the star compensates for this period of activity by expanding and cooling. The hydrogen burning shell is quenched during expansion, and the convective envelope dredges the products of nucleosynthesis to the surface of the star (third dredge-up). After this dredge-up event, the star contracts, and the hydrogen shell reignites. This interplay between the helium and hydrogen shells repeats episodically [35].

The ^{18}O depletion observed in Group 2 presolar oxide grains and AGB stellar atmospheres helped to motivate the introduction of cool bottom processing into AGB stellar models. These models provided some insight into the class of asymptotic giant branch stars that might experience cool bottom processing and the temperature of the stellar plasma at the site of this extra mixing. According to Ref. [10], ^{18}O depletion by cool bottom processing is possible in $M \leq 1.5\ M_{\odot}$ asymptotic giant branch stars; temperatures of the circulated material between $T_P \approx 38-48$ MK, where the maximum H-burning shell temperature is $T_H \approx$

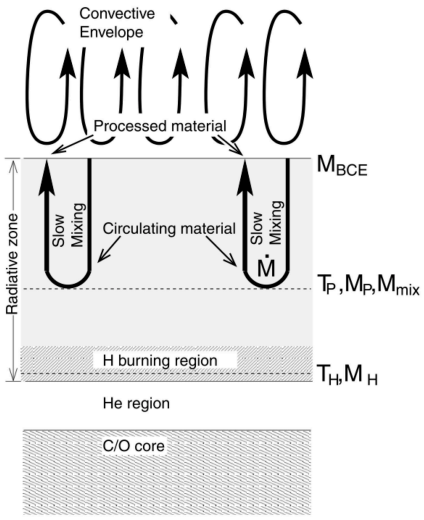

Figure 1.4: Drawing, from Ref. [13], of the interior of an evolved star where cool bottom processing (CBP) occurs by some unknown extra mixing mechanism (not drawn to scale). The main regions are the C/O core, the He region, the H-burning region, the radiative zone, and the convective envelope. Material from the envelope slowly circulates deep into the radiative zone, and undergoes nuclear processing near the hydrogen shell. The processed material, now depleted in ^{18}O, circulates back into the envelope. The labels, M_{BCE}, M_P, and M_H are the mass coordinates of the convective envelope boundary, the cool bottom processing region, and the hydrogen shell, respectively. The other labels, T_P, T_H, and $\dot{M}$ refer to the temperature of the circulated material, the plasma temperature of the hydrogen shell, and the cool bottom processing circulation rate, respectively.

60 MK, are necessary to reproduce observed $^{18}O/^{16}O$ abundances [10]. Group 2 presolar grains nucleate in the AGB stellar atmosphere depleted in ^{18}O due to processes that occurred deep within the star—the products of nucleosynthesis were dredged up to the surface of the star. Then, powerful stellar winds inject these grains into the interstellar medium.

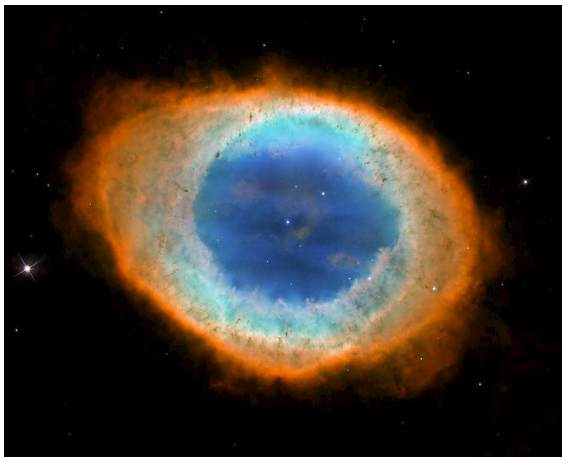

Figure 1.5: M57: the Ring Nebula [37], a planetary nebula with a central white dwarf that was produced after an asymptotic giant branch star shed its convective envelope [38].

The depletion of ^{18}O in a stellar plasma at low temperatures is driven by $^{18}O(p,\alpha)^{15}N$ and, to a lesser extent, $^{18}O(p,\gamma)^{19}F$. These two ^{18}O destruction mechanisms are a part of the CNO cycle (see Fig. 1.6b). The (p,α) reaction was recently studied indirectly by Ref. [39]. Within the cool bottom processing temperature regime, the $^{18}O(p,\gamma)^{19}F$ reaction rate may be influenced by an unobserved, low-energy resonance at E_R = 95 ± 3 keV [40, 41] (see Fig. 5.1). Note that all bombarding and resonance energies reported in this thesis are in the laboratory reference frame unless noted otherwise. In the present work, a direct, low-energy measurement of the $^{18}O(p,\gamma)^{19}F$ reaction is reported. The goal of this measurement was to improve our knowledge of levels in the ^{19}F compound nucleus relevant to nuclear astrophysics.

1.1.2: Explosive Hydrogen Burning During Classical Novae

Classical novae are intriguing astrophysical phenomena, and the study of these energetic explosions draws upon several different scientific disciplines—nuclear physics, astrophysics, computer science, and cosmochemistry [42]. Many stars do not spend their lives isolated and alone like our Sun, and in fact, binary star systems are quite common. Depending on the initial mass of each star, the system can evolve in interesting and unique ways. Many massive stars end their lives violently as core collapse supernovae, but as discussed above, lower mass stars, like our Sun, instead reach a point of instability during their life cycles and shed

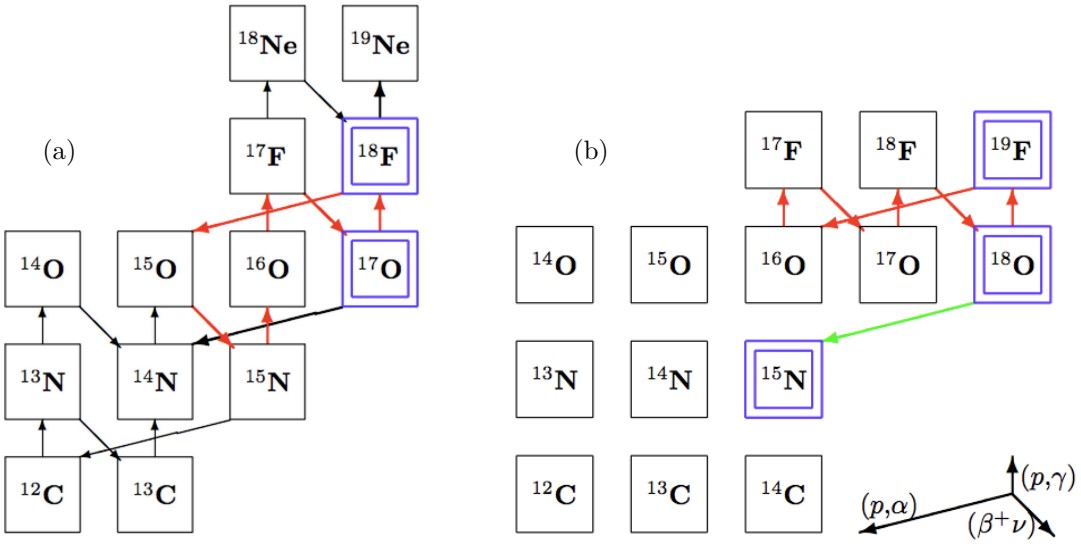

Figure 1.6: (a) The Hot CNO cycle is activated during explosive hydrogen burning in classical novae. The main reaction channels are (p,γ), (p,α), and $(\beta^+\nu)$. The Hot CNO cycle is shown with red arrows in this figure, and the ^{17}O$(p,\gamma)^{18}$F reaction is highlighted with blue squares. (b) Extreme ^{18}O depletion is possible if the CNO cycle is activated during cool bottom processing in low-mass asymptotic giant branch stars. The main destruction channels are the (p,γ) and (p,α) reactions. The CNO cycle of interest is shown with red arrows in this figure, and the ^{18}O$(p,\gamma)^{19}$F reaction is highlighted with blue squares. The competing ^{18}O$(p,\alpha)^{15}$N path is also shown with a green arrow, and ^{15}N is highlighted in blue.

layers of matter exposing a compact stellar *corpse*. These remnants, depending on the mass of the original star, are primarily carbon and oxygen. In a binary star system, this stellar corpse, referred to as a white dwarf star, can be reanimated by its companion. As the companion evolves, a parasitic white dwarf will begin to leach hydrogen-rich matter from the host main sequence star by Roche lobe overflow through the inner Lagrangian point of the binary system. An accretion disk can form around the white dwarf (if the magnetic field is weak), and layers of accreted hydrogen build up on the surface of the compact remnant. As more matter is accreted, compression will drive the underbelly of this hydrogen layer into a state of degeneracy. As stellar plasma temperatures rise, there is no longer a mechanism in place to cool the accreted material, and a thermonuclear runaway occurs [44, 42]. Thermonuclear reactions will proceed rapidly over a period of about 100 seconds, and during the outburst, the luminosity can increase by as much as a factor of 10,000 [45]. With luminosities between $10^{45}-10^{46}$ ergs [46], classical novae are only surpassed in luminosity by supernovae, hypernovae, and γ-ray bursts [42]. To put this in perspective, the AN602 hydrogen bomb (also known as *Tsar Bomba*), the most powerful nuclear weapon ever detonated, had an estimated yield of $\approx 2.38\times10^{24}$ ergs [47]. White dwarfs have diameters that are the same order of magnitude as the diameter of the planet Venus (but with masses closer to the mass of the Sun). Approximately ninety AN602 hydrogen

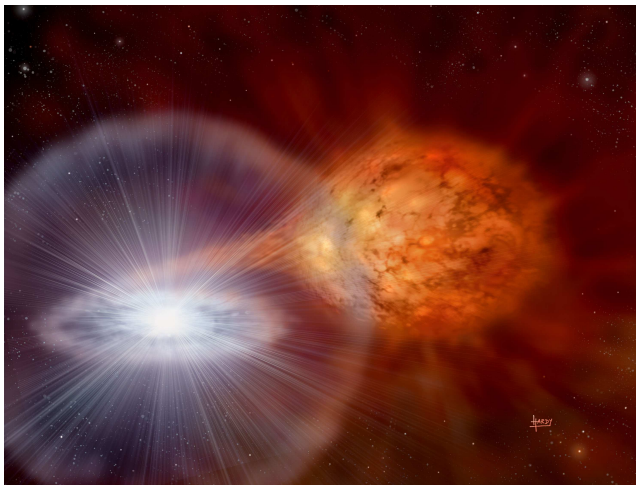

Figure 1.7: An artist's interpretation of a classical nova (© David A. Hardy/www.astroart.org [43]). It depicts a white dwarf accreting matter from a bloated main sequence star. Roche lobe overflow has formed an accretion disk around the white dwarf.

bombs would have to detonate on every square centimeter of Venus to match the output of a classical nova [48].

Unlike supernovae, classical novae are recurrent events—the star system is not disrupted and thermonuclear runaway can reoccur with a period of 10^4–10^5 years [45]. The most common classical novae involve a carbon-oxygen (CO) white dwarf that originated from a main sequence star ≤ 9–10 $M_\odot$. Heavier white dwarf stars from more evolved progenitors are classified as oxygen-neon (ONe) white dwarfs based on the nuclear ash accumulated during the progenitor's stellar evolution. Classical novae should not be confused with *dwarf novae* or *novae-like variables*; these recurrent variables are not thermonuclear burning sites. X-ray novae, on the other hand, are analogous to classical novae, but involve an accreting black hole or neutron star in a binary system instead of a white dwarf [42]. Classical novae occur in the Milky Way Galaxy at a rate of 35 ± 11 novae/year [49]. Figure 1.8 is an image taken of the recent nova, Nova Delphini 2013, with a PlaneWave 17" unit.

Spectroscopic studies of classical nova ejecta can reveal characteristics of the underlying white dwarf and elemental abundances produced during the nova event. Observed abundance profiles can provide considerable information about the thermonuclear runaway—peak temperature, envelope expansion timescale, and other constraints to stellar models [51]. In order for the observed abundances to be produced by this type of energetic event, CNO nuclei (provided by the underlying white dwarf core material) and a reservoir of protons (provided by the hydrogen-rich accreted matter) are required. Explosive hydrogen burning can proceed, and the *Hot* CNO cycle is the main nucleosynthesis mechanism at play during these events. The Hot CNO cycle (Fig. 1.6a) runs between the proton drip line and the line of stability, and the nucleosynthesis is limited to

Figure 1.8: An image taken with a PlaneWave 17" unit, after the average of 10, 10-seconds unfiltered exposures of Nova Delphini 2013. The classical nova is the bright object dominating the center of the frame [50].

(p,γ), (p,α), and ($\beta^+\nu$) paths [42]. Because the timescale—100 seconds—is so short, the CNO cycle never reaches equilibrium [44], and convection transports β^+ unstable nuclei to the surface of the envelope. These nuclei contribute the energy necessary to increase temperature and entropy to the point at which envelope degeneracy is lifted (the Fermi temperature), halt the thermonuclear runaway, and drive expansion and the ejection of the products of nucleosynthesis. They are also the slowest paths during the Hot CNO cycle and are essentially the nova nucleosynthesis *bottleneck* [42]. Classical nova peak temperatures range between 100−400 MK [52, 53, 54], and this defines the classical nova Gamow window—the temperature regime that needs to be probed experimentally.

Based on stellar models, reaction networks, and astronomical observations, novae are thought to be significant sources of Galactic ^{13}C, ^{15}N, and ^{17}O [55, 52, 54], and ≈1/3000 the Galaxy's disk dust and gas [42]. Classical novae also produce ^{7}Li, ^{19}F, and ^{26}Al, but CNO elements are the dominant products [53, 54]. One of the major elements created during the explosion is ^{18}F. It is not a stable fluorine isotope and decays by emitting a positron. When the positron encounters an electron, they annihilate producing radiation with a specific energy (511 keV) [56, 57]. Because the half-life of ^{18}F is ≈ 110 minutes, the 511 keV γ-ray is produced after the classical nova envelope has become transparent to γ-rays. Other β^+ unstable nuclei, like ^{13}N, decay while the envelope is opaque to γ-rays and their associated 511 keV γ-rays drive envelope expansion. The 511 keV signature from ^{18}F would be important to observe with an astronomical instrument like INTEGRAL, because detection could constrain classical nova models [58]. However, detectors like INTEGRAL would need to get lucky and be pointed at the right portion of the sky to detect these ^{18}F signature γ-rays—they do not coincide with the detection of optical frequencies.

Stellar models could also be constrained by studying nova presolar grains. Presolar grains could form in the cool, low-density envelope ejected by classical novae [42]. Infrared [59, 60] and ultraviolet [61] observations of nova light curves indicate dust formation, and suggest that CO-type novae are prolific dust creators [62, 63] while ONe-novae are not. This may be due to high-velocity ejecta from these novae and lower envelope densities. These grains should have anomalous carbon and nitrogen ratios [64], and oxygen isotopic ratios in these grains could constrain the type of nova that produced them, the mass of the white dwarf, and mixing processes between accreted and core matter [42]. Mixing occurs between core and accreted matter by some unknown mechanism [65]; candidate mixing methods include shear mixing [66, 67, 68, 69], elemental diffusion [70, 71], and the Kelvin-Helmholtz instability [72]. Grains that can be attributed to classical novae are rare (see Fig. 1.3b). The criteria are: (1) observation of ^{17}O enrichment with $^{17}O/^{16}O > 0.004$ and (2) *mild* ^{18}O depletion [7]. Alumina grain T54 [33] is one grain considered consistent with nova nucleosynthesis calculations [73]—$^{17}O/^{16}O = 1.41\times10^{-2}$ [11]. Grain C4-8 is another nova grain candidate with $^{17}O/^{16}O = 4.4\times10^{-2}$ (an order of magnitude higher than the concentration allowed by low-mass asymptotic giant branch models) [11]. Both grains are likely from CO-novae because $^{18}O/^{16}O$ abundance ratios are too high to attribute the grains to ONe-novae [11]. Nova grains are large compared to grains from the interstellar medium (ISM); nova grains are typically on the order of ≈ 0.5 μm [74]. The only known nova remnant that shows any indication of dust and molecules is GK Persei, but it is not thought that these grains are related to the 1901 nova event [74].

It is clear that thermonuclear reactions that create and destroy ^{18}F are extremely important and need to be studied experimentally. The most important ^{18}F production mechanism is the capture of a proton by ^{17}O (the rarest stable oxygen isotope). This reaction also affects the destruction of ^{17}O, and classical novae are thought to be the dominant source of ^{17}O in our Galaxy. However, there is evidence in the literature that hot bottom burning in asymptotic giant branch stars may also contribute to the synthesis of ^{17}O [15] where T = 30−100 MK [75].

The importance of ^{17}O proton capture—$^{17}O(p,\gamma)^{18}F$—is well established, and numerous studies have been performed to analyze this reaction experimentally [51, 76]. However, the temperature regime relevant to explosive hydrogen burning during a classical nova (100−400 MK) corresponds to very low proton bombarding energies (E_p^{cm} = 103−261 keV). At these low energies, the Coulomb barrier suppresses the reaction yield in the laboratory, and many accelerator facilities do not have the ability to overcome this limitation. Environmental backgrounds also dominate the detected signal, making it difficult to extract the γ-ray cascade produced when ^{17}O captures a proton. While other groups—Rolfs [77], Newton *et al.* [78], Hager *et al.* [79], Scott *et al.* [80], Kontos *et al.* [81], and Di Leva *et al.* [82] to name a few—had limited or no success making in-beam measurements within the energy region relevant to explosive hydrogen burning

during classical novae, the experimental tools at the LENA facility allow ^{17}O proton capture reaction rates to be constrained. In particular, direct capture is studied because reaction rate calculations indicate that direct capture dominates the rate at classical nova temperatures [75, 78]. This is a rare scenario because generally, narrow resonances at astrophysically relevant temperatures dominate the rate [78].

Section 1.2: Focus

In the following chapters, both (p,γ) experiments are described in detail. Chapter 2 outlines a majority of the underlying nuclear physics that affects how both experiments were designed and executed, and how data were analyzed. Chapter 3 describes the laboratory facility, the accelerators, and the detector system. Within chapter 3, relevant upgrades and modifications are discussed along with calibrations of the key equipment used in these studies. Target fabrication and characterization for both studies are discussed in Chapter 4. Then, Chapter 5 focuses specifically on the ^{18}O(p,γ)^{19}F experiment while Chapter 6 is dedicated to measurement, analysis, and results of the ^{17}O(p,γ)^{18}F direct capture study. The results presented in Chapter 5 were published in Buckner *et al.* (2012) [1]. Finally, a host of appendices document key aspects of these studies, from uncertainty analysis techniques (A) to reaction rate input (B) to angular correlation calculations (C) to Monte Carlo detector efficiencies (D) to spectra (E).

CHAPTER 2: NUCLEAR ASTROPHYSICS THEORY

The fundamental nuclear astrophysics concepts and equations outlined in this chapter are adapted from the text *Nuclear Physics of Stars* by C. Iliadis [4] and references therein. The equations presented in this chapter are used throughout the remainder of this dissertation and are key components to the analysis developed in this work and in preceding studies done at LENA. Note that stellar plasma energies, bombarding energies, and resonance energies discussed in this chapter are in the center-of-mass frame. In subsequent chapters, it should be assumed that all energies are in the laboratory frame.

Section 2.1: Thermonuclear Reaction Rates

Thermonuclear reaction rates are a quantitative measure of nuclear reaction probabilities in a stellar plasma. Thermonuclear reaction rate theory is discussed here as are the applications of this theory to the study of rare oxygen isotope proton captures.

The physical quantity at the heart of these studies, the main piece of nuclear physics information that these experiments are dedicated to measuring in the laboratory, is the nuclear cross section. This quantity, σ, is the probability that a nuclear interaction occurs between target nuclei and incident particles, and it can be defined as:

$$\sigma = \frac{interactions\ per\ unit\ time}{incident\ particles\ per\ unit\ time \times target\ nuclei\ per\ unit\ area}. \tag{2.1}$$

The cross section is expressed in units of barns (b) where

$$1\ \text{b} = 10^{-24}\ \text{cm}^2, \tag{2.2}$$

and as the units imply, this probability is essentially an area—the interaction area of target nuclei and incident particles. References to the cross section in this thesis will be limited to radiative proton capture. This means that the incident particles in the reactions discussed in this dissertation are protons, and when target nuclei capture these protons, electromagnetic radiation—a γ-ray—is emitted.

The reaction rate can be defined as the number of interactions per unit volume per unit time in a stellar plasma, and the incident particle and target nucleus have a temperature dependent velocity distribution,

ϕ(v). The reaction rate per particle pair is thus a convolution between the cross section and the velocity distribution where:

$$< \sigma \mathrm{v} >= \int_0^\infty \phi(\mathrm{v}) \mathrm{v} \sigma(\mathrm{v}) d\mathrm{v}. \tag{2.3}$$

The velocity distribution is assumed to be a Maxwell-Boltzmann distribution,

$$\phi(\mathrm{v}) = \left(\frac{\mu}{2\pi kT}\right)^{3/2} e^{-\mu \mathrm{v}^2/(2kT)} 4\pi \mathrm{v}^2, \tag{2.4}$$

if the reaction rate describes the interaction of non-degenerate, non-relativistic particles. Where

$$\mathrm{E} = \frac{\mu \mathrm{v}^2}{2} \tag{2.5}$$

and

$$\mu = \frac{\mathrm{M}_p \mathrm{M}_t}{\mathrm{M}_p + \mathrm{M}_t} \tag{2.6}$$

is the reduced mass of the target nucleus and incident particle (M_t and M_p, respectively), Eq. 2.3 can be rewritten as:

$$< \sigma \mathrm{v} >= \left(\frac{8}{\pi \mu}\right)^{1/2} \frac{1}{(kT)^{3/2}} \int_0^\infty \sigma(\mathrm{E}) \mathrm{E} e^{-\mathrm{E}/kT} d\mathrm{E}. \tag{2.7}$$

In this equation, the Boltzmann constant, k, is equal to 8.6173×10^{-8} keV/K. The thermonuclear reaction rate at a specific stellar plasma temperature can be calculated numerically with the following equation:

$$N_A < \sigma \mathrm{v} >= \frac{3.7318 \times 10^{10} \sqrt{\mu}}{T_9^{3/2}} \int_0^\infty \sigma(\mathrm{E}) \mathrm{E} e^{-11.605\mathrm{E}/T_9} d\mathrm{E} \ (\mathrm{cm}^3 \mathrm{mol}^{-1} \mathrm{s}^{-1}). \tag{2.8}$$

In this equation, E is the center-of-mass energy in units of MeV, T_9 is the temperature in GK, and the cross section is in barns. The nuclear masses are calculated from the atomic masses listed in Ref. [41] by subtracting the mass of electrons associated with the projectile and target atoms; all masses are in atomic mass units.

2.1.1: Non-Resonant Reaction Rates

A non-resonant reaction is a single-step process where a target nucleus captures a proton, emits a γ-ray, and forms a bound state of a final nucleus. No compound nucleus is formed because interaction with the electromagnetic field allows the proton to transition from an initial scattering state to a final bound state. This formalism is referred to as *direct capture*, and Fig. 2.1 shows a schematic drawing of a direct capture reaction from Ref. [83]. In the direct capture model, the target nucleus is approximated as an inert

core instead of a collection of individual nucleons; the reaction is not as sensitive to the nuclear interior and strong nuclear force as it is to the nuclear exterior and the electromagnetic force. The direct capture cross section varies smoothly as a function of energy because of this reaction mechanism's dependence on the electromagnetic force. The energies of direct capture primary transitions can be calculated with the equation:

$$\mathrm{E}_\gamma = \mathrm{Q}_{p\gamma} + \mathrm{E}_p - \mathrm{E}_x \tag{2.9}$$

where E_γ is the energy of a single direct capture primary, $\mathrm{Q}_{p\gamma}$ is the proton separation energy of the target nucleus for a (p,γ) reaction, E_p is the center-of-mass energy of the proton, and E_x is the bound state energy.

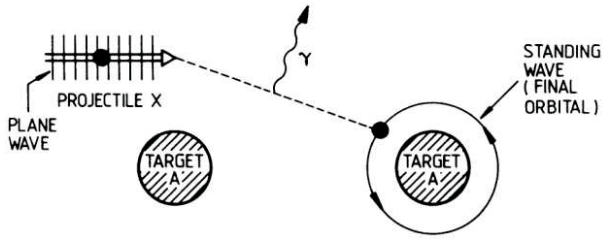

Figure 2.1: From *Cauldrons in the Cosmos* by Rolfs and Rodney [83], an incident particle capturing from an initial scattering state directly into a final bound state of nucleus "A."

The E1 transition is the dominant contribution to the direct capture cross section, and it can be described with the following equation:

$$\sigma_{\mathrm{calc}}(\mathrm{E1}) = 0.0716\mu^{3/2}\left(\frac{Z_p}{\mathrm{M}_p} - \frac{Z_t}{\mathrm{M}_t}\right)^2 \frac{\mathrm{E}_\gamma^3}{\mathrm{E}_p^{3/2}} \times \tag{2.10}$$

$$\frac{(2J_f+1)(2\ell_i+1)}{(2j_p+1)(2j_t+1)(2\ell_f+1)}(\ell_i 010|\ell_f 0)^2 R^2_{\ell_i 1 \ell_f}. \tag{2.11}$$

In this equation, Z_p, Z_t, M_p, and M_t are the charges and masses of the projectile and target, respectively; ℓ_i and ℓ_f are the scattering state initial orbital angular momentum and the bound state final orbital angular momentum, respectively; J_f, j_p, and j_t are the spins of the final state, projectile, and target, respectively; E_p and E_γ are the center-of-mass energy (in MeV) and transition γ-ray energy, respectively [84, 85]; $R_{\ell_i 1 \ell_f}$

is the radial integral where

$$R_{\ell_i 1 \ell_f} = \int_0^\infty u_c(r) \mathcal{O}_{\mathrm{E1}}(r) u_b(r) r^2 dr \tag{2.12}$$

and in this equation, $\mathcal{O}_{\mathrm{E1}}(r)$ is the radial part of the E1 electric dipole operator, and u_c and u_b are the continuum and bound state wave functions, respectively [84, 85].

The energy dependence of the direct capture cross section can be attributed to the radial integral, $R_{\ell_i 1 \ell_f}$, because the radial wave functions of the initial scattering and final bound states are sensitive to the energy. This means the scattering and bound state potentials selected to describe the nuclear potential are very important. If J_f, j_p, and j_t are known, the initial and final orbital angular momenta can be calculated. These values were calculated for both the ^{18}O$(p,\gamma)^{19}$F and ^{17}O$(p,\gamma)^{18}$F reactions, but as an example, ^{17}O$(p,\gamma)^{18}$F coupling calculations are discussed here:

$$^{17}\mathrm{O} + p + \ell_i \ \rightarrow \ ^{18}\mathrm{F} + \mathrm{E1}; \tag{2.13}$$

$$^{17}\mathrm{O} + p + \ell_f \ \rightarrow \ ^{18}\mathrm{F}. \tag{2.14}$$

Consider ^{17}O proton capture and the formation of a 3^+ state in ^{18}F. The proton and ^{17}O have angular momenta of $\frac{1}{2}^+$ and $\frac{5}{2}^+$, respectively, and they can couple to a total momentum of 2^+ or 3^+. The E1 multipolarity and ^{18}F have angular momenta of 1^- and 3^+, respectively, and they can couple to 2^-, 3^-, or 4^-. As a result, ℓ_i must be odd because the final parity is proportional to (-1)$^\ell$. The possible initial angular momenta are 1, 3, 5, or 7, but usually, all but the first two ℓ values are excluded from a coupling calculation.

Equation 2.14 can be solved for ℓ_f with a similar procedure. The formation of the final angular momentum, 3^+, requires that ℓ_f be even, and this allows $\ell_f = 0$ or 2; the final possible combinations are $\ell_i = 1$, 3 and $\ell_f = 0$, 2. The coupling calculations provide the quantities necessary to calculate the initial scattering and final bound state wave functions. The accepted ^{17}O$(p,\gamma)^{18}$F direct capture coupling calculation solutions are tabulated in Tab. 2.1.

Table 2.1: The $^{17}\mathrm{O} + p$ channel spin, total angular momentum of direct capture states, and the corresponding initial scattering state and final bound state orbital angular momenta.

s	J^π	ℓ_i	ℓ_f
2	0^+	(1,3)	2
3	1^+	(1,3)	2
2	2^+	(1,3)	(0,2)
3	3^+	(1,3)	(0,2)
2	4^+	(1,3)	2
3	5^+	(1,3)	2

For direct capture, the scattering state potential is set to zero [85], and the Woods-Saxon potential:

$$V_{WS}(r) = \frac{-V_0}{1 + e^{\frac{r-R}{a}}} \tag{2.15}$$

where $R = r_0 A_t^{1/3}$, $r_0 = 1.25$ fm, and $a = 0.65$ fm [85], is chosen for the bound state potential.

The assumption made in the direct capture formalism—that the target nucleus can be approximated as a single particle—is not entirely correct. Only a fraction of the total wave function exists as a single particle state. Spectroscopic factors are an empirical estimate of what fraction of the final state wave function can be described by a single particle bound in a potential well. The experimental cross section is related to the theoretical cross section by

$$\sigma_{\text{exp}} = \sum_{\ell_i, \ell_f} C^2 S(\ell_f) \sigma_{\text{theo}}(\ell_i, \ell_f). \tag{2.16}$$

The summation in this equation is over all possible initial and final state orbital angular momenta, ℓ_i and ℓ_f, and $C^2S(\ell_f)$ is the spectroscopic factor—the probability of arrangement into a residual nucleus and a single particle [4].

The smoothly varying direct capture cross section drops dramatically at low energies due to Coulomb suppression, and this exponential decline makes it difficult to visualize and understand the nuclear physics at the energies most relevant to nuclear astrophysics. Because of this, non-resonant cross sections are often rewritten in terms of the astrophysical S-factor, S(E). This representation of the cross section is easier to grasp conceptually and plot because it excludes the steep energy dependence (1/E) and the Coulomb barrier transmission probability. It isolates the nuclear contributions to the cross section from the electromagnetic contributions. This decomposition of the cross section can be expressed as:

$$\sigma(\text{E}) = \frac{\text{S(E)}}{\text{E}} e^{-2\pi\eta} \tag{2.17}$$

where $e^{-2\pi\eta}$ is the Gamow factor and η is the Sommerfeld parameter. The $2\pi\eta$ term in the Gamow factor can be written numerically as:

$$2\pi\eta = 0.98951013 \times \left(Z_p Z_t \sqrt{\frac{\mu}{\text{E}}} \right) \tag{2.18}$$

where E is the center-of-mass energy in units of MeV.

The thermonuclear reaction rate can be rewritten in terms of the astrophysical S-factor by substituting Eq. 2.17 into Eq. 2.7 and multiplying by Avogadro's number, N_A:

$$N_A < \sigma \text{v} > = \left(\frac{8}{\pi\mu} \right)^{1/2} \frac{N_A}{(kT)^{3/2}} \int_0^\infty \text{S(E)} e^{-2\pi\eta} e^{-\text{E}/kT} d\text{E}. \tag{2.19}$$

Within this integral is a very important quantity and concept in nuclear astrophysics, the Gamow peak. The product of the Gamow factor and the Maxwell-Boltzmann distribution, $e^{-2\pi\eta}e^{-\mathrm{E}/kT}$, describes an energy range and stellar plasma temperature regime that contains the non-resonant reactions that dominate the reaction rate. If the derivative of this product is set to zero, the maximum value, E_0 can be calculated:

$$\mathrm{E}_0 = 0.122 \times (Z_p^2 Z_t^2 \mu T_9^2)^{1/3} \text{ (MeV)}. \tag{2.20}$$

Assuming the Gamow peak is normally distributed, the $1/e$ width of the peak can be written as:

$$\Delta\mathrm{E} = 0.2368 \times (Z_p^2 Z_t^2 \mu T_9^5)^{1/6} \text{ (MeV)}. \tag{2.21}$$

In Fig. 2.2, the Gamow peak is solved and plotted at T = 50 MK (cool bottom processing), T = 125 MK (hot bottom burning), and T = 300 MK (classical novae).

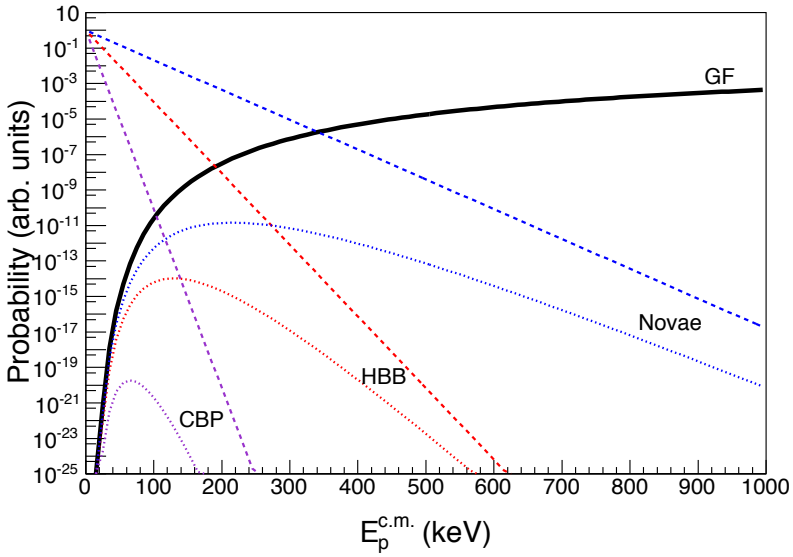

Figure 2.2: The products of the Gamow factor (solid black line) and the Maxwell-Boltzmann distributions (dashed lines) are plotted in this figure. The classical nova (blue), the hot bottom burning (red), and cool bottom processing (purple) Gamow peaks are shown as dotted lines. These peaks correspond to 300 MK, 125 MK, and 50 MK, respectively.

The astrophysical S-factor can be expanded in a Taylor series at E = 0 [86] because, with respect to energy, it is a slowly varying function:

$$\mathrm{S(E)} \approx \mathrm{S}(0) + \dot{\mathrm{S}}(0)\mathrm{E} + \frac{1}{2}\ddot{\mathrm{S}}(0)\mathrm{E}^2 \tag{2.22}$$

where $\dot{S}(0)$ and $\ddot{S}(0)$ are the first and second derivatives of S(E) at E = 0 keV, respectively. An analytical expression for the non-resonant reaction rate can be written as:

$$N_A < \sigma \mathrm{v} >= \left(\frac{4}{3}\right)^{3/2} \frac{\hbar N_A}{\pi \mu Z_p Z_t e^2} \mathrm{S}_{eff} \tau^2 e^{-\tau} \tag{2.23}$$

where

$$\tau = \frac{3\mathrm{E}_0}{kT} = 4.2487 \times \left(\frac{Z_p^2 Z_t^2 \mu}{T_9}\right)^{1/3} \tag{2.24}$$

and the effective S-factor [86] is

$$\mathrm{S}_{eff}(\mathrm{E}_0) = \mathrm{S}(0)\left[1 + \frac{5}{12\tau} + \frac{\dot{\mathrm{S}}(0)}{\mathrm{S}(0)}\left(\mathrm{E}_0 + \frac{35}{36}kT\right) + \frac{1}{2}\frac{\ddot{\mathrm{S}}(0)}{\mathrm{S}(0)}\left(\mathrm{E}_0^2 + \frac{89}{36}\mathrm{E}_0 kT\right)\right]. \tag{2.25}$$

If Eq. 2.22 diverges at high energies and fails to reproduce experimental data, the non-resonant reaction rate is multiplied by a cutoff function,

$$f_{\mathrm{cutoff}} \approx e^{-(T_9/T_{9,\mathrm{cutoff}})^2}, \tag{2.26}$$

to dampen its affect at these energies. In this equation,

$$T_{9,\mathrm{cutoff}} = 19.92 \times \left(\frac{\mathrm{E}_{\mathrm{cutoff}}^{3/2}}{\sqrt{Z_p^2 Z_t^2 \mu}}\right) \tag{2.27}$$

where $\mathrm{E}_{\mathrm{cutoff}}$ is in units of MeV.

2.1.2: Resonant Reaction Rates

Resonant captures, as opposed to direct captures, have energy-dependent cross sections—they do not vary smoothly. Variations in the cross section can span orders of magnitude over very narrow energy ranges. The total cross section thus resembles a smoothly varying background interspersed with spikes—resonances superimposed upon the direct capture cross section. Unlike direct capture, the nuclear interior plays a major role during resonant capture. At energies near the quasi-bound state potential energies, the matching of solutions to the interior and exterior wave function at the nuclear radius is favorable, and this produces a large wave function amplitude in the nuclear interior. This matching condition is satisfied when the sum of the resonance energy, E_{R}, (in the center-of-mass frame) and proton separation energy equals the excited state energy,

$$\mathrm{E}_{\mathrm{R}} + \mathrm{Q}_{p\gamma} = \mathrm{E}_x. \tag{2.28}$$

Narrow Resonances

Narrow resonances have constant partial widths (Γ_a,Γ_b) over the total width (Γ)—the sum of all partial widths—of the resonance. The total width of a narrow resonance is typically $\Gamma < 1{-}3$ keV. The Breit-Wigner equation can be used to express a resonant cross section where

$$\sigma_{BW}(\mathrm{E}) = \frac{\lambda^2}{4\pi}\omega\frac{\Gamma_a\Gamma_b}{(\mathrm{E}-\mathrm{E_R})^2+(\Gamma/2)^2} \tag{2.29}$$

and

$$\omega = \frac{2J+1}{(2J_p+1)(2J_t+1)}. \tag{2.30}$$

In these equations, J_p is the projectile spin, J_t is the target spin, J is the spin of the resonance state, $\mathrm{E_R}$ is the resonance energy in the center-of-mass frame, Γ_a is the entrance channel partial width, Γ_b is the exit channel partial width, Γ is the total resonance width, and λ is the de Broglie wavelength, defined as

$$\lambda = \frac{2\pi\hbar}{\sqrt{2\mu\mathrm{E}}}. \tag{2.31}$$

The single resonance reaction rate then becomes

$$N_A < \sigma\mathrm{v} >= N_A\frac{\sqrt{2\pi}\hbar^2}{(\mu kT)^{3/2}}\omega\int_0^\infty \frac{\Gamma_a\Gamma_b}{(\mathrm{E_R}-\mathrm{E})^2+\Gamma^2/4}e^{-\mathrm{E}/kT}d\mathrm{E} \tag{2.32}$$

when the Breit-Wigner cross section and de Broglie wavelength are substituted into Eq. 2.7 and then multiplied by Avogadro's number. If the Maxwell-Boltzmann distribution and partial widths are assumed to be constant, the narrow resonance reaction rate can be simplified further to

$$N_A < \sigma\mathrm{v} >= N_A\frac{\sqrt{2\pi}\hbar^2}{(\mu kT)^{3/2}}e^{-\mathrm{E}/kT}\omega\frac{2\Gamma_a\Gamma_b}{\Gamma}\int_0^\infty \frac{\Gamma/2}{(\mathrm{E_R}-\mathrm{E})^2+\Gamma^2/4}d\mathrm{E}. \tag{2.33}$$

This integral simplifies to π because

$$\int_{-\infty}^{\infty}\frac{a}{(\mathrm{E_R}-\mathrm{E})^2+a^2}d\mathrm{E} = \pi, \tag{2.34}$$

and an analytical expression for the narrow resonance reaction rate can be written as

$$N_A < \sigma\mathrm{v} >= N_A\left(\frac{\sqrt{2\pi}}{\mu kT}\right)^{3/2}\hbar^2 e^{-\mathrm{E}/kT}\omega\gamma \tag{2.35}$$

where the resonance strength is defined as

$$\omega\gamma = \omega\frac{\Gamma_a\Gamma_b}{\Gamma}. \tag{2.36}$$

Broad Resonances

The cross section of a broad resonance varies over wider energy ranges than are typical for narrow resonances. A good rule of thumb for resonances within the Gamow window is: if the total width, Γ, is a significant fraction of the Gamow peak width, the resonance is a broad resonance. Because of the inherent energy dependence of the broad resonance cross section, the partial widths, de Broglie wavelength, and the Maxwell-Boltzmann distribution can not be assumed to be constant, and the broad resonance reaction rate becomes

$$N_A < \sigma \mathrm{v} >= N_A\frac{\sqrt{2\pi}\hbar^2}{(\mu kT)^{3/2}}\omega\int_0^\infty \frac{\Gamma_a(\mathrm{E})\Gamma_b(\mathrm{E}+S_p-\mathrm{E}_f)}{(\mathrm{E_R}-\mathrm{E})^2+\Gamma(\mathrm{E})^2/4}e^{-\mathrm{E}/kT}d\mathrm{E}. \tag{2.37}$$

In this equation Γ_b corresponds to the partial width of a single exit channel transition and S_p is the proton separation energy. Multiple transitions sum incoherently with the cross section, and broad resonance tails are also included in the rate calculation. The energy dependence of the entrance channel partial width can be approximated by the penetration factor, $P_a(\mathrm{E})$—the transmission probability through the Coulomb and centripetal barriers:

$$\Gamma_a(\mathrm{E}) = \Gamma_a(\mathrm{E_R})\frac{P_a(\mathrm{E})}{P_a(\mathrm{E_R})}. \tag{2.38}$$

The exit channel partial width becomes:

$$\Gamma_b(\mathrm{E}) = \Gamma_b(\mathrm{E_R}+S_p-\mathrm{E}_f)\frac{P_b(\mathrm{E}+S_p-\mathrm{E}_f)}{P_b(\mathrm{E_R}+S_p-\mathrm{E}_f)}. \tag{2.39}$$

Assuming the exit channel is a γ-ray, as is the case in these experiments,

$$\Gamma_b(\mathrm{E}) = \Gamma_\gamma(\mathrm{E_R}+\mathrm{Q}_{p\gamma}-\mathrm{E}_f)\left[\frac{\mathrm{E}+\mathrm{Q}_{p\gamma}-\mathrm{E}_f}{\mathrm{E_R}+\mathrm{Q}_{p\gamma}-\mathrm{E}_f}\right]^{2L+1} \tag{2.40}$$

because $\Gamma_\gamma \approx \mathrm{E}_\gamma^{2L+1}$ (where L is the multipolarity of the emitted γ-ray). Here $S_p = \mathrm{Q}_{p\gamma}$. By making these substitutions, the Breit-Wigner cross section for a (p,γ) reaction becomes:

$$\sigma_{BW}(\mathrm{E}) = \frac{\pi\hbar^2\omega}{2\mu\mathrm{E}}\frac{\Gamma_a(\mathrm{E_R})\frac{P_a(\mathrm{E})}{P_a(\mathrm{E_R})}\Gamma_\gamma(\mathrm{E_R}+\mathrm{Q}_{p\gamma}-\mathrm{E}_f)\left[\frac{\mathrm{E}+\mathrm{Q}_{p\gamma}-\mathrm{E}_f}{\mathrm{E_R}+\mathrm{Q}_{p\gamma}-\mathrm{E}_f}\right]^{2L+1}}{(\mathrm{E_R}-\mathrm{E})^2+\Gamma(\mathrm{E})^2/4}. \tag{2.41}$$

For sub-threshold resonances ($\mathrm{E_R^{cm}} < 0$), the proton partial width is calculated with the spectroscopic

factor, C^2S, and the single particle reduced width, θ^2_{sp} [87]—the probability of a single nucleon appearing on the nuclear boundary. Spectroscopic factors are generally well documented in the literature by studies of stripping reactions—like (d,n) or (^{3}He,d). The particle partial width becomes

$$\Gamma_p(\mathrm{E}) = \frac{2\hbar^2}{\mu R^2} P(\mathrm{E}) C^2 S \theta^2_{sp} \tag{2.42}$$

where the majority of the energy dependence comes from the penetration factor.

Interfering Resonances

If two or more resonances have the same spin and parity, the amplitudes of these resonances can interfere either constructively or destructively. For two interfering resonances, the cross sections sum coherently where the total cross section is defined as

$$\sigma(\mathrm{E}) = \sigma_1(\mathrm{E}) + \sigma_2(\mathrm{E}) \pm 2\sqrt{\sigma_1(\mathrm{E})\sigma_2(\mathrm{E})} cos(\delta_1 - \delta_2) \tag{2.43}$$

and the phase shift of each resonance can be generalized as

$$\delta_i = arctan\left[\frac{\Gamma_i}{2(\mathrm{E} - \mathrm{E}_{\mathrm{R},i})}\right]. \tag{2.44}$$

The interference cross section can be substituted into Eq. 2.7, and this single reaction rate replaces the incoherent sum of the interfering resonances in the total reaction rate calculation. If the total widths of the interfering resonances are narrow ($\Gamma_i < 1$ eV), an argument can be made for ignoring the interference.

Finally, the total reaction rate is the incoherent sum of the non-resonant (NR), narrow resonance (RN), broad resonance (RB), and continuum (C) reaction rates:

$$N_A < \sigma \mathrm{v} >^{\mathrm{total}} = N_A < \sigma \mathrm{v} >^{NR} + \sum_i N_A < \sigma \mathrm{v} >_i^{RN} + \sum_j N_A < \sigma \mathrm{v} >_j^{RB} + N_A < \sigma \mathrm{v} >^{C} . \tag{2.45}$$

Section 2.2: Monte Carlo Reaction Rates

Reaction rates were calculated in this thesis with the Monte Carlo method developed by Ref. [88] with the code RatesMC [88]; the analysis description in Appendix A.1 explains why Monte Carlo techniques are growing in popularity. Each input parameter in the rate calculation is represented by a probability density function (PDF) that is sampled to construct a PDF for the reaction rate. As explained in more detail in Sec.

2.2.1, resonance energies are assumed to be normally distributed (Gaussian), resonance strengths, S-factors, and partial widths are lognormal distributions, and upper limits are treated as Porter-Thomas distributions. The final reaction rate probability density function is a lognormal distribution where the 0.16, 0.50, and 0.84 quantiles of the cumulative PDF are adopted as the low, median, and high reaction rates, respectively. The low and high rate are bounds that correspond to 68% coverage or 1σ, and can be referred to as the *uncertainty* in the rate. However, this uncertainty is used to describe the reaction rate probability density function—a continuum that the actual rate lies upon—and is not meant to be considered a *hard-cut-off*—the probability that the rate lies above the high rate or below the low rate is non-negligible.

2.2.1: Probability Density Functions

The quantities that factor into these Monte Carlo reaction rate calculations are associated with probability density functions. However, there are several key caveats that must be considered. Based on the nature and characteristics of an input parameter, an appropriate probability density function must be selected.

Resonance energies are assumed to be normally distributed (Gaussian), and in general, a Gaussian distribution is used when the uncertainty associated with a parameter can be considered the sum of many small contributions. For a continuous random variable x, the Gaussian function is defined as

$$f(x) = \frac{1}{\sigma\sqrt{2\pi}} e^{-\frac{1}{2}\left(\frac{x-\mu}{\sigma}\right)^2} \tag{2.46}$$

where μ is the mean and, in this case, expectation value, and σ is the standard deviation (the square-root of the variance). The expectation value and variance can be generalized as

$$E[x] = \int_{-\infty}^{\infty} x f(x) dx \tag{2.47}$$

and

$$V[x] = \int_{-\infty}^{\infty} (x - E[x])^2 f(x) dx, \tag{2.48}$$

respectively.

Resonance strengths, partial widths and direct capture S-factors are all represented as lognormal distributions. In general, a lognormal distribution is assumed when an input parameter is the product of many small contributions. Additionally, representing an input parameter as a Gaussian distribution implies that there is a finite probability that the parameter can be negative ($-\infty < x < \infty$). This scenario is often unphysical and undesirable, and it is instead necessary to represent the input parameter as a lognormal

distribution ($0 \leq \ x \ < \infty$). The lognormal distribution is defined as

$$f(x) = \frac{1}{\sigma\sqrt{2\pi}}\frac{1}{x}e^{-\frac{1}{2}\left(\frac{\ln(x)-\mu}{\sigma}\right)^2} \tag{2.49}$$

where

$$\mu = \ln(E[x]) - \frac{1}{2}\ln\left(1 + \frac{V[x]}{E[x]^2}\right) \tag{2.50}$$

and

$$\sigma = \sqrt{\ln\left(1 + \frac{V[x]}{E[x]^2}\right)}. \tag{2.51}$$

The geometric mean of a lognormal distribution is also the median where

$$\mu_g = e^{\mu}. \tag{2.52}$$

The geometric standard deviation is a lognormal distribution's factor uncertainty and is defined as

$$\sigma_g = e^{\sigma}. \tag{2.53}$$

Upper and lower bounds, providing 68% coverage, are given by $e^{\mu\pm\sigma}$.

Upper limits are often factored into calculations, and the Porter-Thomas distribution is relied upon when including an upper bound. More information on these functions and their applications in nuclear astrophysics can be found in Ref. [89] and Refs. [88, 90], respectively.

CHAPTER 3: ACCELERATORS AND DETECTORS

The Laboratory for Experimental Nuclear Astrophysics (LENA) is located on the campus of Duke University, Durham, NC and operates under the aegis of Triangle Universities Nuclear Laboratory (TUNL). LENA is a "sea-level" accelerator facility dedicated to the measurement of nuclear cross sections within the energy regime relevant to nuclear astrophysics. Nucleosynthesis occurs within a stellar environment at energies that most accelerator facilities are incapable of probing. The main problem is that at low bombarding energies, the cross section drops dramatically because of decreasing transmission probability through the Coulomb barrier. As a result, experimental count rates drop below detectable thresholds unless great lengths are taken to design an experiment that can reduce environmental backgrounds and boost the reaction yield. Figure 3.1, courtesy of Ref. [4] (with data from Ref. [91]), demonstrates this conundrum quite well. In the figure, the ^{16}O(p,γ)^{17}F cross section decreases by approximately four orders of magnitude over a narrow energy window ($\approx$ 500 keV). The impact this has on detecting the characteristic *fingerprint* of a reaction in the laboratory is staggering; however, LENA is equipped to tackle these complications with its advanced accelerators and detectors. Note that Fig. 3.1 also shows the astrophysical S-factor. As discussed in Sec. 2.1.1, the S-factor is related to the cross section; to calculate the S-factor, the energy dependence and transmission probability are removed from the cross section.

Figure 3.2 shows the layout of the LENA facility including the accelerators, beamline, quadrupole magnets (blue), analyzing magnet (yellow), and steerers (black). The quadrupoles and steerers are optical elements that allow the beam to be focused and repositioned, respectively. Beam produced by each accelerator is transmitted through two sets of quadrupoles and steerers with an analyzing magnet between them. The analyzing magnet—at least during JN operation—is a key component in a National Instruments LabVIEW controlled feedback system that uses beam current measurements on horizontal slits downstream from the magnet to adjust the JN terminal voltage. The following equation determines the calibrated magnetic field:

$$\mathrm{B} = \frac{k}{q}(2mc^2\mathrm{E} + \mathrm{E}^2)^{1/2} \tag{3.1}$$

where B is the field, E is the proton beam energy, q is the proton charge, m is the proton mass, c is the speed of light, and k is a calibration constant [83]. During ECR ion source operation, the proton beam is selected by adjusting the current through the analyzing magnet manually.

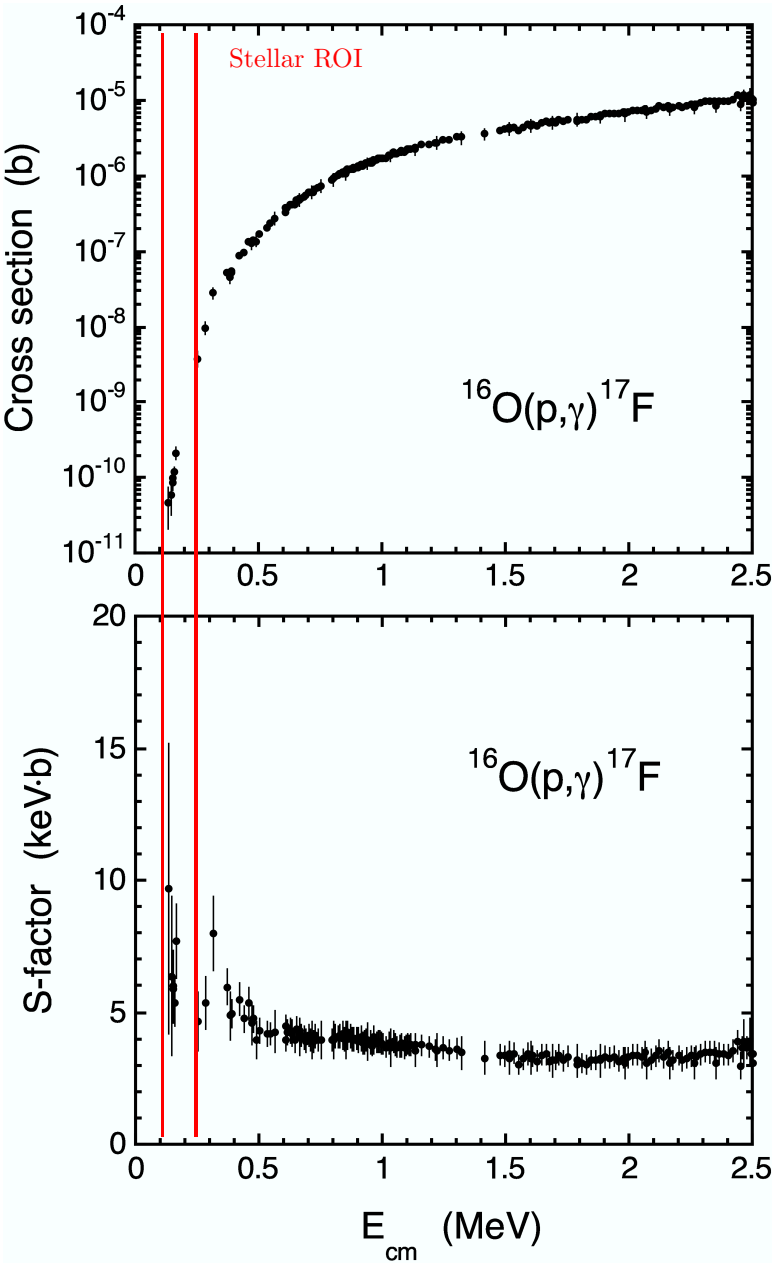

Figure 3.1: An illustration of the major challenge and motivation behind experimental nuclear astrophysics from Ref. [4] (with data from Ref. [91]). The ^{16}O$(p,\gamma)^{17}$F cross section and S-factor are shown from 0−2.5 MeV. The cross section drops at low energies due to Coulomb suppression; however, the low-energy regime corresponds to the stellar plasma temperatures at which nucleosynthesis occurs. Experiments must be designed carefully to boost reaction yield and suppress environmental backgrounds. A typical region of interest pertinent to stellar nucleosynthesis is highlighted in this figure with red bars.

The next few sections describe the accelerators and detectors and how they contribute to boosting signal-to-noise, making the energy regime pertinent to nuclear astrophysics experimentally accessible.

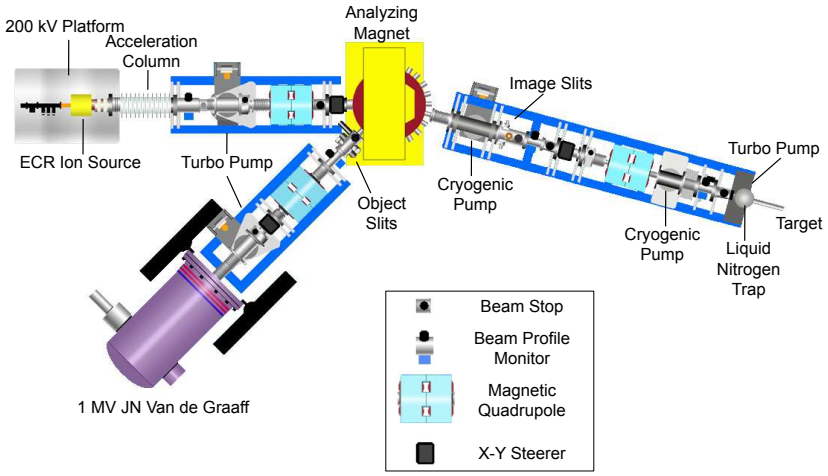

Figure 3.2: A schematic drawing of the Laboratory for Experimental Nuclear Astrophysics. The drawing shows the layout of the ECR Ion Source, the JN Van de Graaff, the beamline, optical elements, and the location of the target. Figure courtesy of A. E. Champagne.

Section 3.1: The Accelerators

3.1.1: 1 MV JN Van de Graaff

The JN Van de Graaff is an upgraded High Voltage Engineering Corporation (HVEC) 1 MV model capable of proton beams at the target with energies between $\approx$0.15$-$1.00 MeV. Several modifications were made to this accelerator since its introduction at LENA. These include a terminal that can accommodate a high-output ion source (and the necessary RF power supply), slit feedback circuitry, a modified generating voltmeter for improved stability, and a new acceleration column and charging belt. Beam currents at the target of $I_p \leq 150$ μA are achievable at a terminal voltage of 300 keV. The JN can typically be relied upon for beam energy resolution between 1$-$2 keV full width at half maximum (FWHM). The JN was used in both the $^{18}O(p,\gamma)^{19}F$ and $^{17}O(p,\gamma)^{18}F$ studies that are discussed within this thesis. In both studies, the JN was a valuable tool for probing and characterizing $Ta_2^{18}O_5$ and $Ta_2^{17}O_5$ anodized targets and was critical for

monitoring target degradation at well-established resonances. Additionally, for the $^{17}O(p,\gamma)^{18}F$ study, data were actually collected with JN beam. This will be discussed in more detail in Chapters 4 and 6.

Figure 3.3 is a photo of the plasma bottle secured to the original JN acceleration column and surrounded by permanent magnets. A radio frequency (RF) oscillator is coupled to the quartz bottle with a capacitor, and a remotely controlled gas leak injects H_2 into the bottle. The RF electric field excites electrons in the gas, and they gain kinetic energy as they collide with neutral gas particles; a hydrogen plasma is ignited when electrons have enough energy to ionize the gas. The permanent magnets produce a field that confines the plasma, and an electric potential from 0−5 kV between the probe tip and ion source base extracts proton beam.

The beam current was optimized at the target by remotely controlling the H_2 gas pressure and the extraction potential. During the experiments, the JN was run at high voltage in a tank pressurized with a mixture of N_2 and CO_2 in order to electrically insulate the terminal.

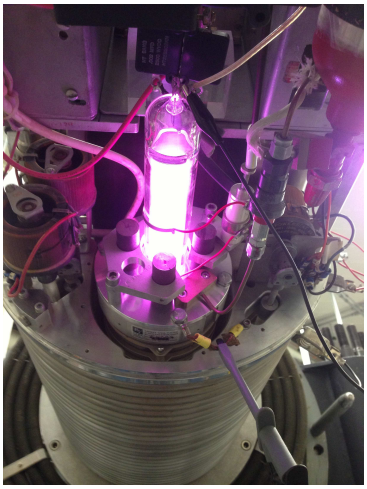

Figure 3.3: Photo of an optimized hydrogen plasma within the heart of the LENA JN Van de Graaff. The plasma bottle, permanent magnets, H_2 gas line, tuning capacitor, and the original acceleration column are shown.

3.1.2: ECR Ion Source

The 200 kV electron cyclotron resonance (ECR) ion source was introduced relatively recently to the LENA facility [92]. The ion source consists of a copper plasma chamber surrounded by a solenoidal permanent magnet array that produces regions of axial B = 87.5 mT magnetic field where electron cyclotron resonance is driven by $\nu = 2.45$ GHz input microwaves. The resulting hot electrons collide with and ionize the hydrogen (H_2) gas injected into the plasma chamber. The ECR ion source produced $E_p = 50-215$ keV beams with currents at the target of $I_p \leq 1.5$ mA after it was assembled and benchmarked [92]. High beam currents

are critical to the study of stellar nucleosynthesis because the low-energy regime can now be probed—high currents boost the reaction yield. However, high beam currents do not discriminate between reactive nuclei, and target purity can become a serious issue. Beam-induced backgrounds will be discussed in later chapters.

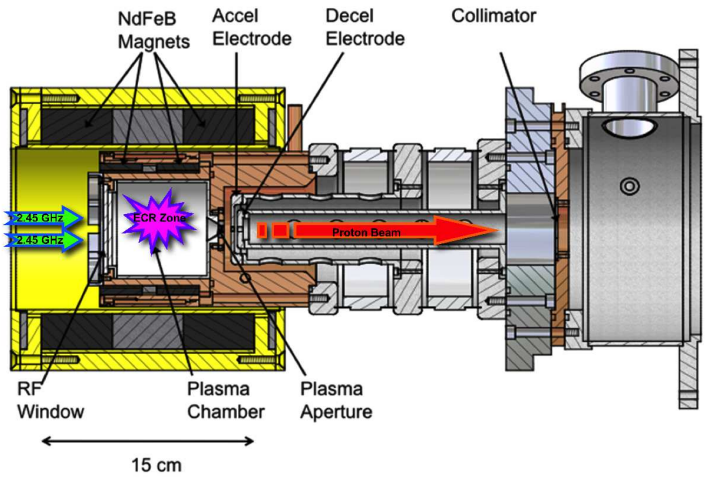

Figure 3.4: Schematic drawing of the LENA electron cyclotron resonance ion source courtesy of Ref. [92]. The beam direction down the pre-acceleration column is indicated with a red arrow, the ECR zone is shown in purple, and the input RF is depicted as green arrows. Other key features are labeled. H^+ beam is extracted with an *accel-decel* lens system and is then collimated before acceleration.

As can be seen in the schematic in Fig. 3.4, the beam is extracted from the plasma chamber by an extraction system composed of three main electrodes: the plasma aperture, the acceleration electrode, and the deceleration electrode. The plasma aperture is biased between 10−15 kV, the acceleration electrode is biased from -0.3 to -2.5 kV, and the deceleration electrode is grounded. The ECR ion source is mounted on an insulated high-voltage platform biased by a Glassman 200 kV, 8 kW power supply. The beam is transported to ground through a 24-gap air-insulated acceleration column manufactured by HVEC and optimized for 200 keV beam transport. The 200 kV electric potential is stepped down between gaps with 10 MΩ resistors, and at lower potentials, optimal beam focusing is achieved by shorting an appropriate number of downstream electrode gaps.

During the two experiments described in this dissertation, the ECR ion source was run in two very different modes—upgraded and deterioration modes.

ECRIS Deterioration Mode

The search for the $^{18}O(p,\gamma)^{19}F$ unobserved E_R = 95 keV resonance was performed in early 2011 at a time when the ECR ion source had few remote features, and manual recalibration at the source was a

constant necessity. At this time, a significant number of hours had already been logged, and the acceleration column was beginning to show signs of heat and radiation damage due to X-rays produced by bremsstrahlung radiation from back streaming electrons. Within the plasma chamber, a boron nitride dielectric window, bucket, and aperture—installed during source assembly—were beginning to exhibit signs of damage. Boron nitride, though a dielectric that effectively preserves ionization efficiency during electron cyclotron resonance, is not the optimal material to use if the source constantly needs to be vented to atmosphere for maintenance. It is hydrophilic and requires *baking-out* before stable, high-current beam can be achieved. Additionally, the 500 W Micro-Now Instrument Co., Inc. Model 420B1 Microwave Power Oscillator was unstable and would often drift during operation. Without remote control over this supply, drifting RF power often resulted in inconvenient downtime for source retuning.

One major upgrade was performed at this stage; remote National Instruments LabVIEW control was extended to the three-stub tuner. The 2.45 GHz microwaves necessary for electron cyclotron resonance are produced by the RF supply, and these microwaves are transmitted via a waveguide to a circulator. The circulator redirects reflected power to a water-cooled dummy load and sends direct power through a three-stub tuner and an additional waveguide to the plasma chamber. The brass rods within the three-stub tuner facilitate impedance matching for optimal RF transmission by manual tuning at the source. A new remote system to handle this tuning was conceived, designed, and installed. An aluminum box containing three Arcus Technology DMX-ETH model 381-105-0 stepper motors was mounted on the outside of the high-voltage cage that surrounds the ECR ion source. These motors at ground potential are connected by delrin rods to the three nubs of the three-stub tuner. Microwave transmission can now be tuned manually by the traditional method at the source before accelerating beam at high voltage; then at high voltage, a LabVIEW module, imbedded within the LENA control software allows remote three-stub tuning control. Remote control helped reduce downtime because any RF supply drift could be carefully corrected by adjusting the three-stub tuner from the control room, thereby reducing the reflected power.

This upgrade was a major step forward, but the ECR ion source was still on a deteriorating trajectory that would undoubtedly result in it ceasing to function as a viable tool for experimental nuclear astrophysics. With that said, during the $^{18}\mathrm{O}(p,\gamma)^{19}\mathrm{F}$ study an average current of $\mathrm{I}_p \approx 750$ μA was maintained at the target. However, continuing to operate in *deterioration mode* in future studies was clearly unsustainable and undesirable.

ECRIS Upgraded Mode

Before data acquisition began for the $^{17}O(p,\gamma)^{18}F$ study, a major overhaul of ECR ion source hardware and control mechanisms was performed. The first step involved replacing the old RF supply with a new, water-cooled, externally mounted 1200 W Alter Model TM-012-52 S/N 510 RF supply. This new supply is mounted on Thomson Industries, Inc. rods adjacent to the ECR ion source circulator and three-stub tuner. It was imperative to control this new RF supply both locally and remotely because of the intense X-ray radiation produced in the vicinity of the ion source—a maximum of ≈750 mrem was recorded during the $^{17}O(p,\gamma)^{18}F$ study at the analyzing magnet. A National Instruments Compact FieldPoint system was utilized to develop a hardware and software interface to communicate seamlessly between the RF supply, the LENA control room computer, and the LENA National Instruments LabVIEW virtual instrument (VI). This interface allows the RF supply to be controlled from a local, digital front panel at the source and from the LENA facility LabVIEW VI in the control room. It revolutionized how the LENA ECR ion source is controlled and operated, and several other key tuning parameters were added to the source front panel (local LabVIEW control) and passed to the LabVIEW control VI (remote LabVIEW control).

The existing three-stub tuner module was added to the new source interface, and additionally, local and remote LabVIEW control over the injection of H_2 into the plasma chamber was added. To achieve this, control over the ECR ion source mass flow controller was added to LabVIEW and to the new ion source front panel. The position of the 87.5 mT solenoidal magnetic field was manipulated previously to control the position of the *magnetic bottle* within the plasma chamber. A method of remotely tuning the position of the permanent magnet was developed, and an Arcus Technology DMX-ETH stepper motor was mounted adjacent to the plasma chamber. An aluminum sleeve was machined to connect the motor to a micrometer with set screws. The end of the micrometer was then fixed to the permanent magnet. Control of the magnet stepper motor was then added to the local and remote LabVIEW interface.

This substantial hardware and software upgrade to the ECR ion source led to high, sustainable beam current at the source, but it also caused tremendous heating of the thin Al_2O_3 window for the input microwave power. The power could not be dissipated without severely degrading the dielectric liner—a ceramic window, bucket, and aperture—internal to the plasma chamber or fracturing the Al_2O_3 window. The geometry of the RF waveguide, the plasma chamber, and the permanent magnet severely constrained solutions to the power dissipation issue. A heat sink was designed that would hug the end of the plasma chamber at the ceramic window and fit within the permanent magnet (see Fig. 3.5). This heat sink consists of a two-piece copper collar complete with chilled water channels and fins for both cooling and easy access to ion source assembly hardware. Copper pipe was soldered to each half of the cooling collar to connect chilled water

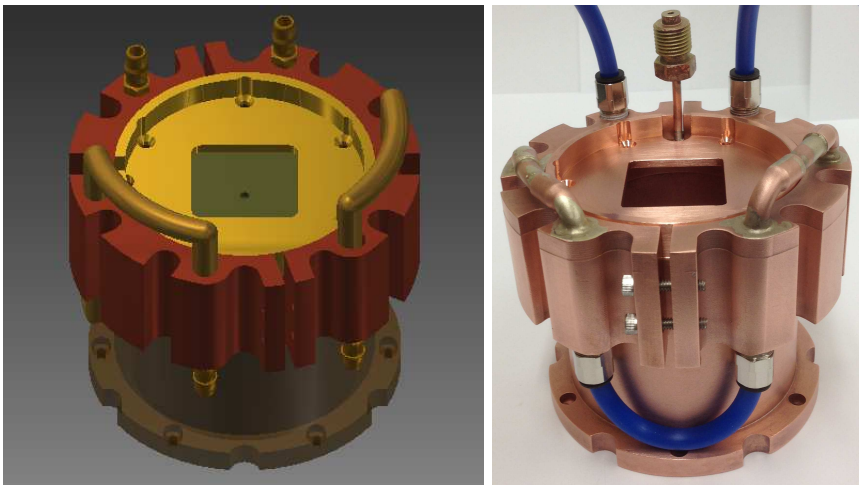

Figure 3.5: (Left) A 3D mock-up of the new ECR ion source plasma chamber heat sink was designed with Autodesk Inventor. This drawing shows the assembly of the plasma chamber (brown), the new copper mount for the RF/vacuum window (gold), the boron nitride window (green), and the new copper heat sink collar (red). (Right) A photo of the machined and assembled ECR ion source plasma chamber heat sink.

channels. Push-to-connect unions were fitted at the source and return of each half of the cooling collar and connected to the ECR ion source water manifold. An aluminum mount between the plasma chamber and the RF waveguide was replaced with a copper version of this component to improve the thermal conductivity of the new heat sink. The new heat sink effectively cools the plasma chamber RF vacuum window such that it no longer fails with typical incident RF power, $P_{RF} \approx 700$ W at 2.45 GHz.

Because the previous dielectric liner inside the plasma chamber was destroyed during initial tests of the upgraded ion source, it required replacement. Previous designs included BN components [92], and then Macor® versions. Both suffered significant damage from heating, and a new robust, durable liner was needed. An elegant and cost-effective solution was to replace the bucket and aperture with one complete component: a 2 mm thick aluminum bucket *with* an aperture (see Fig. 3.6). An aluminum oxide layer forms naturally on the interior of this new liner, and this insulating layer promotes plasma stability and prevents electron loss during electron cyclotron resonance [93], thus boosting ionization efficiency. The interior window at the RF/vacuum interface is boron nitride to allow 2.45 GHz microwaves to enter the chamber.

These substantial upgrades to the LENA ECR ion source led to a significant boost in target beam current. A maximum proton beam current of $I_p^{max} = 2.05$ mA was observed at the target with a current of $I_p = 4.25$ mA at the analyzing magnet beam stop at $E_p = 175$ keV. With $I_p = 2.9$ mA at the magnet, beam transmission to target was benchmarked for H^+ and H^{2+}, with $I_{H^+} = 1.375$ mA and $I_{H^{2+}} = 0.175$ mA respectively [94]. This boost in beam current was invaluable for the $^{17}O(p,\gamma)^{18}F$ experiment detailed in this dissertation.

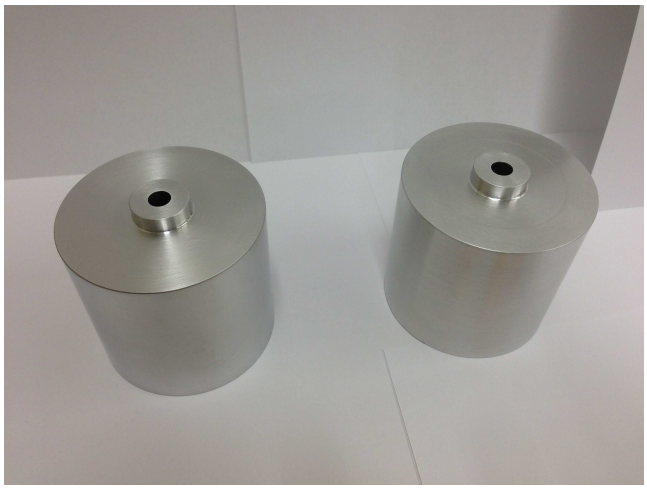

Figure 3.6: Two identical aluminum liners were machined by the UNC Department of Physics and Astronomy machine shop. These liners are 2 mm thick and simplify the separate ceramic bucket and aperture components into one cost-effective and easy-to-machine insert. The natural aluminum oxide layer that forms on the cup is a superb dielectric and maintains the plasma ionization efficiency during operation [93].

Degradation of the LENA ECR ion source continued during the $^{17}O(p,\gamma)^{18}F$ experiment and forced the proton beam energy upper limit on the accelerator to be downgraded to $E_p = 190$ keV because of conductive tracks within the acceleration column that resulted from use, age, and damage. This raised the electric field across the acceleration column gaps causing high-current discharges within the column (see Fig. 3.7). These disruptive events extinguished the plasma and damaged the column and electronics. To resolve this issue, accelerator column gaps were shorted on the ion source side. This remedy did not noticeably affect beam optics and instead allowed ECR ion source data collection to continue; however, with fewer gaps available, the beam energy upper limit on the ion source was truncated.

Section 3.2: New Beam Rastering System

During the $^{17}O(p,\gamma)^{18}F$ experiment, prior to ECR ion source data acquisition, a new beam rastering system was commissioned and installed between the final quadrupole magnet and the LN_2 cold trap. Focused, high-intensity beam (from either accelerator) can result in non-uniform target degradation regardless of target type. Target material can be sputtered away exposing the target substrate and leaving the surrounding target material unused. Also, the risk exists that high beam currents could cause significant target heating; if the target cooling system can not dissipate this power, the temperature gradient may be sufficient to melt the target substrate, flooding the beamline with cooling water and venting to atmosphere. The new beam rastering system moves focused, high-intensity beam continually over the full target area ensuring adequate heat dissipation and preserving the target surface.

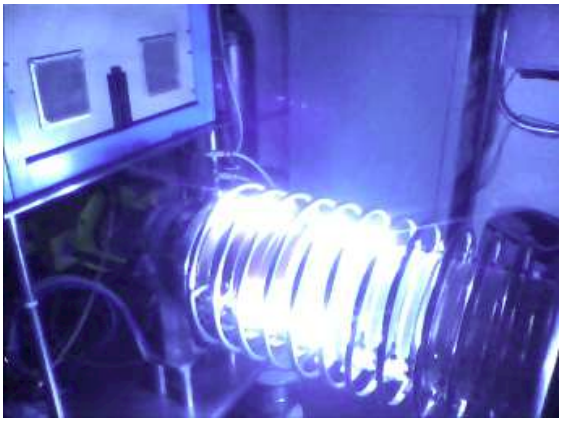

Figure 3.7: A massive spark along the ECR ion source acceleration column. Incessant sparks of this nature, at voltages and currents in excess of 175 kV and 6 mA, respectively, increased in frequency during data acquisition in July 2013. In order to continue the experiment, accelerator column gaps were grounded (on the ion source side) one after the other until the frequency of sparks decreased. Photo courtesy of S. Hunt.

An existing magnetic beam steerer was modified and mounted ≈2 m upstream from the target. Horizontal- and vertical-motion programmable power supplies are controlled remotely by FieldPoint modules and a National Instruments LabVIEW VI to vary the steerer coil currents and reposition the beam. During the $^{17}O(p,\gamma)^{18}F$ experiment, the rastering system was set to move the beam continuously across the target in 5-loop spirals with an angular frequency of 1°/100 ms. Ion source optics and transmission to target can vary between tunes, but generally, the beamspot diameter at the target is between 1.0 and 1.2 cm (determined by the target chamber collimator, see Fig. 3.9). Rastering allows even coverage of the target and ensures beam exposure is not disproportionately focused on small areas. The new rastering system allowed an average of 10 extra Coulomb of charge to be collected (in addition to the average 45 C per $Ta_2^{17}O_5$ target) during ECR ion source data acquisition with beam currents at the target that exceeded 2 mA [95].

Section 3.3: Preliminary Investigation into Beam Pulsing

During the summer of 2008, a modification began on the beam extraction system of the LENA ECR ion source with the goal of reducing experimental limitations introduced by background radiation. Modifications were aimed at trying to exploit the idea that the average current incident on the target would not change if the ECRIS extraction system is pulsed with a pulse period of 1 second and a pulse width of 100 milliseconds (a 10% duty cycle) while simultaneously increasing the intensity of the beam by a factor of ten. The detector system would be active only when the beam is pulsed. If properly implemented, this procedure could increase signal-to-noise over a shorter effective running time to increase measurement precision and sensitivity [96].

Several methods were investigated to pulse the ECRIS extraction system. First, an attempt was made to pulse the beam by pulsing the hydrogen gas flowing into the chamber of the ion source [97]. A remote pulsing circuit and a second circuit that powered a small valve were designed and connected with a fiber optic cable; the valve was pulsed with the required 10% duty cycle. The valve was attached to an unused scattering chamber at TUNL for tests of its pulsed performance. A vacuum of about 10^{-6} Torr was achieved, and bursts of nitrogen gas were pulsed into the chamber. The vacuum change within the chamber was monitored with a compact full range gauge, and output voltage pulses were compared on an oscilloscope with the pulses driving the valve. The pressure in the chamber rose sharply when the gas pulse was initiated but degraded slowly for 900 ms before the next pulse occurred; it did not mirror the rectangular pulse applied to the valve.

An attempt was also made to pulse the RF supply magnetron, but it was found that, at the time with the 500 W Micro-Now Instrument Co. Inc. Model 420B1 Microwave Power Oscillator, pulsing the RF quenched the ECRIS plasma.

The next approach to produce a pulsed beam was to directly pulse the ion source extraction voltages. The voltages applied to the ECR ion source plasma chamber and the acceleration electrode were pulsed with a programming voltage. Pulses were generated with the pulsing circuit originally developed to pulse the gas valve. This circuit, which incorporated 555 digital timers, was modified using AD5220 potentiometers to alter both the pulse width and pulse period. The potentiometers also facilitated remote pulse width and period control utilizing National Instruments LabVIEW hardware and software. Also, 5 V DC SPDT relays controlled by LabVIEW were included in the circuit design to allow the experimenter to switch remotely between constant and pulsed beam operation.

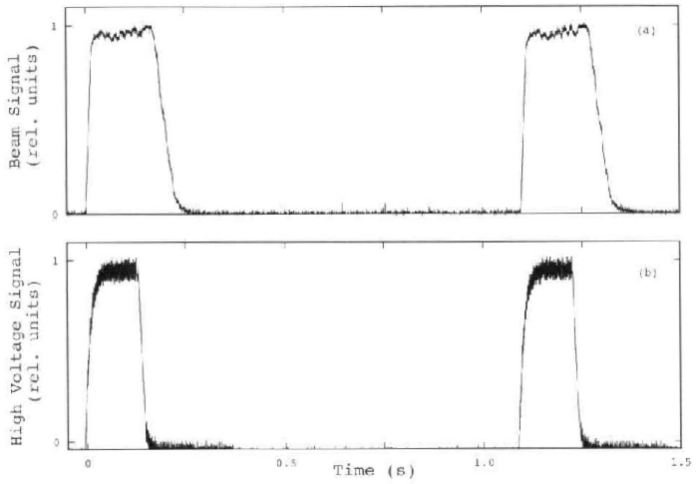

Figure 3.8: From Ref. [92], a comparison between (a) the pulsed ECR ion source proton beam (measured at the first beamstop) and (b) the signal applied to the ion source high voltage supplies.

To test the beam pulsing, the pulses sent to each power supply, and the pulsed target current produced by the ECR ion source were monitored together on an oscilloscope (see Fig. 3.8). The pulsed beam current profile matched the electronic pulse profile produced by the circuit very well. By modifying the voltages sent to the potentiometers remotely, beam pulse widths between 100 ms and 400 ms and periods between 780 ms and 1180 ms could be achieved. The 555 timer pulsing circuit was eventually substituted for a National Instruments Pulse Generating FieldPoint module. Additional testing and upgrades were performed at LENA and a major beam intensity upgrade is underway that is expected to enable pulsed H^+ beam operation [98].

Section 3.4: Target Chamber

The end of the LENA beamline and the attached target holder function as a Faraday cup for the measurement of charge accumulation on target and subsequent beam current integration. Targets are mounted in the chamber and then cooled by chilled water that flows behind the backing during data acquisition. Cooling the backings is extremely important when performing an experiment with beam currents in excess of $I_p \geq$ 1.0 mA. The target chamber is held under high vacuum ($\leq 5\times10^{-7}$ Torr) with a turbo pump backed by a scroll pump. This configuration helps ensure that the target chamber remains *oil-free* (and thus carbon free) because unlike a mechanical pump, a scroll pump does not require pump oil that can potentially contaminate the target chamber. Coupled with the liquid nitrogen cooled copper *cold trap* situated upstream from the target, minimal environmental contaminants should be present within the target chamber that could give rise to the detection of beam-induced backgrounds. Monitoring beam current on a 1.27 cm diameter copper collimator upstream from the target (downstream from the cold trap liquid nitrogen dewer) allows beam optics to be fine tuned by adjusting quadrupoles and steerers for optimal beam transmission through this aperture. A copper shroud biased to -300 V suppresses secondary electron emission from the target to improve the integrated beam current measurement. See Figure 3.9 for a schematic layout of the LENA target chamber system.

Section 3.5: Detectors

The detector system used during both the $^{18}O(p,\gamma)^{19}F$ and $^{17}O(p,\gamma)^{18}F$ experiments exploits $\gamma\gamma$-coincidence to isolate the reaction γ-cascades from environmental backgrounds. This detector array consists of one 135% coaxial high purity germanium (HPGe) detector, 16 thallium activated sodium iodide, NaI(Tl), scintillating detector segments, and five plastic scintillating paddles [99] (see Table 3.1 for detector dimensions from Refs. [100, 101]). In the $\gamma\gamma$-coincidence running geometry, the HPGe is oriented at 0°, with respect to the beam direction, with the detector end cap right up against the target chamber (1.1 cm from cap to target

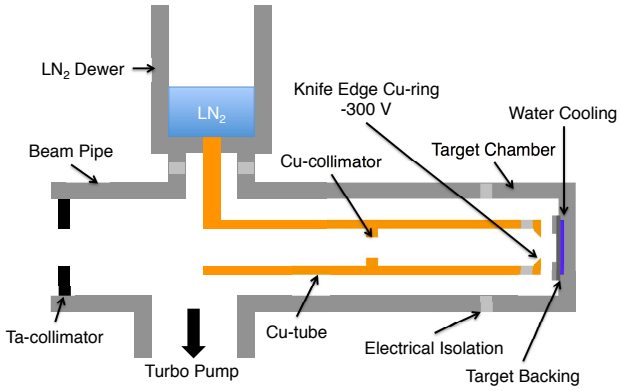

Figure 3.9: A schematic drawing of the LENA target chamber (*not to scale*). The target is directly cooled with chilled water (blue). The beamspot is defined by the 1.27 cm diameter collimator, and ceramic standoffs electrically isolate the Faraday cup from the accelerator beamline. Secondary electron suppression is provided by a knife-edge copper ring biased to -300 V. A turbo pump backed by a scroll pump ensures a high-vacuum, low-carbon environment, and a LN_2 cooled copper cold trap reduces contamination at the target.

surface). The NaI(Tl) scintillators are optically isolated and distributed in two annular eight-detector halves surrounding the target-HPGe geometry. An aluminum (Al) structure surrounds the target-HPGe-annulus configuration upon which 10 mm thick lead (Pb) plates are mounted to passively reduce environmental backgrounds. Thick plastic scintillating paddles (50 mm thick) surround the lead shield and actively veto muons produced by cosmic-rays. Figure 3.10 shows a GEANT4 [102, 103] rendering, drawn with the Fukui Renderer DAWN (Drawer for Academic WritiNgs) [104], of the coincidence spectrometer in the running geometry with the lead, aluminum, scintillator paddles, and HPGe pre-amp electronics removed.

3.5.1: HPGe Peak Efficiency

As will be demonstrated in Chapter 6, HPGe peak efficiencies were implicitly included during novel spectral analysis of $^{17}O(p,\gamma)^{18}F$ resonance and direct capture data. However, during the $^{18}O(p,\gamma)^{19}$ F study, the determination of experimental HPGe peak efficiencies was a critical component of the analysis. The methods described below were almost exclusively applied to the analysis of resonance and direct capture $^{18}O(p,\gamma)^{19}F$ data (discussed in Chapter 5). The comparison between simulated and experimental peak efficiencies is also relevant with respect to the $^{17}O(p,\gamma)^{18}F$ study; the solid black line labeled "Raw Simulation" in Fig. 3.11 is the implicit peak efficiency for the Monte Carlo template histograms discussed in Sec. 6.3.3.

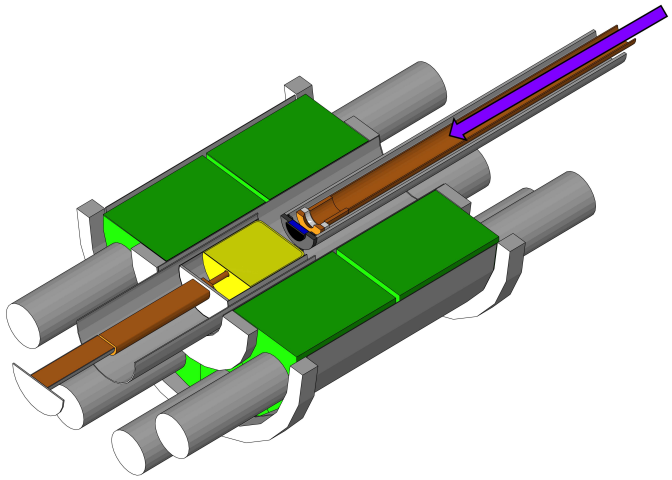

Figure 3.10: A GEANT4 rendering in DAWN [104] of the $\gamma\gamma$-coincidence spectrometer at LENA. The HPGe crystal is shown in yellow and the NaI(Tl) scintillator segments in green. The photomultiplier tubes attached to the NaI(Tl) scintillators are shown, as are the HPGe cold finger and end cap. The target chamber, knife-edge copper electron suppressor, copper collimator, and beamline are also shown. The target is located upstream from the blue strip at the end of the beamline—the location of chilled cooling-water. The beam direction is shown coming from the right of the figure as a thick purple arrow. Figure courtesy of C. Howard.

The first step in calculating the peak efficiency of the high purity germanium detector is to use a ^{60}Co radioactive source and a procedure called the *sum-peak method*. This technique removes dependence on the source activity from the efficiency measurement, and produces an absolute efficiency [105]. For a two-

Table 3.1: Dimensions of the LENA 135% HPGe detector and the NaI(Tl) annulus. These dimensions, from Refs. [100, 101], are incorporated into LENA GEANT4 simulations.

HPGe parameters	Dimension (mm)
End cap outer diameter	107.95(2)
Distance end cap-crystal	6.2(5)
Crystal length	91.6(10)
Crystal diameter	89.0(5)
Bulletizing radius	7.1(5)
Central hole diameter	8.5(10)
Central hole length	79.1
Central hole bottom radius	4.7
Vertical crystal displacement	-1.5(5)
Contact pin diameter	6.9(5)
Contact layer thickness	1.2
NaI(Tl) annulus parameters	**Dimension**
Inner radius	118.0(5) mm
Outer radius	357.0(5) mm
Crystal length	330.0(5) mm
Segment spanning angle	43.0(5)°

step decay, like the dominant decay in ^{60}Co($\beta^+\overline{\nu}_e$)^{60}Ni, the detection of both γ-rays in a close geometry is indistinguishable from the detection of a single γ-ray with an energy equal to the sum of the decay energies. Nearly 100% of the time, a single ^{60}Co decay produces a two-γ cascade where E_γ^{21} = 1173.228(3) keV and E_γ^{10} = 1332.492(4) keV [106].

During a source efficiency measurement, the source, housed in a mylar puck, is placed in the beamline at atmosphere, with the foil side of the puck centered against a tantalum blank mounted in the target chamber. The NaI(Tl) annulus and the HPGe detector are then positioned in the close, $\gamma\gamma$-coincidence running geometry. For ^{60}Co data acquisition in this geometry, the two photons *sum-in* producing a E_γ^{20} = 2505.720(5) keV peak in the HPGe spectrum. The *sum-peak method* from Ref. [105] can now be applied.

If the ^{60}Co decay is represented by the following 2-step decay, 2→1→0, where 2→1 is the primary and 1→0 is the secondary, the peak and total efficiencies can be calculated. The necessary equations are:

$$\eta_{21}^{Ge,P} = \frac{1}{\mathrm{W}(\theta)}\sqrt{\frac{N_{21}N_{20}^2}{N_{10}N_{20}N_t + N_{21}N_{10}^2}}, \tag{3.2}$$

$$\eta_{10}^{Ge,P} = \frac{1}{\mathrm{W}(\theta)}\sqrt{\frac{N_{10}N_{20}^2}{N_{21}N_{20}N_t + N_{10}N_{21}^2}}, \tag{3.3}$$

and

$$\eta^{Ge,T} = \frac{1}{\mathrm{W}(\theta)} - \frac{1}{\mathrm{W}(\theta)}\sqrt{\frac{N_{21}N_{10}}{N_{20}N_t + N_{21}N_{10}}} \tag{3.4}$$

where N_{21}, N_{10}, and N_{20} are the primary, secondary, and sum-peak background-subtracted intensities; N_t is the total intensity; W(θ) is the angular correlation if θ is the angle between the two γ-rays, $\eta_{21}^{Ge,P}$ is the primary germanium peak efficiency; $\eta_{10}^{Ge,P}$ is the secondary germanium peak efficiency; $\eta^{Ge,T}$ is the germanium total efficiency at $(E_\gamma^{21} + E_\gamma^{10})/2$ [99]. The angular correlation was calculated with the following equation [107]:

$$\mathrm{W}(\theta) = 1 + \frac{5}{49}Q_2^{10}Q_2^{21}P_2(cos\theta) + \frac{4}{441}Q_4^{10}Q_4^{21}P_4(cos\theta) \tag{3.5}$$

where $P_k(cos\theta)$ is the Legendre polynomial and Q_k^{ij} is the solid angle attenuation factor for each γ-ray, γ_{ij}. The Q-coefficients and their associated uncertainties were calculated with a post-processing code that was applied to GEANT4 simulations of the detector geometry and the ^{60}Co decay. This code, from Ref. [99], solves the following equation [100]:

$$Q_k^{ij} = \frac{1}{N}\sum_{l=0}^{N} P_k(cos\theta_l) \tag{3.6}$$

where N is the number of detected events in a peak and θ is the emission angle of the l^{th} detected γ-ray.

Uncertainty associated with the Q-coefficients was calculated by varying the source position within the mylar puck during subsequent GEANT4 simulations of the ^{60}Co decay. The diameter of the HPGe crystal was also varied during this sensitivity study. The systematic uncertainty associated with the Q_2 attenuation factor amounted to 2% and the uncertainty in the Q_4 coefficient was 10%. Adding the systematic and statistical uncertainties in quadrature yields the uncertainties on the attenuation factors in Table 3.2. From Eq. 3.5, the angular correlation is $W(\theta) = 1.0276 \pm 0.0010$.

Table 3.2: The calculated sum-peak attenuation factors for ^{60}Co at E_γ^{21} = 1173.228(3) keV and E_γ^{10} = 1332.492(4) keV. The secondary attenuation factors agree very well with the factors presented in Ref. [108]. Differences in the primary attenuation factors are likely due to significant improvements in the LENA GEANT4 detector geometry.

Coefficient	1173 (keV)	1332 (keV)
Q_1	0.804 ± 0.019	0.83 ± 0.02
Q_2	0.495 ± 0.012	0.546 ± 0.013
Q_3	0.209 ± 0.005	0.267 ± 0.006
Q_4	0.029 ± 0.003	0.069 ± 0.007

Peak and total efficiencies were then calculated, and a GEANT4 normalization was applied between simulated source intensity and beam intensity at E_γ^{10} = 1332.5 keV. This normalization is performed because the GEANT4 assembly (target, detectors, etc.) differs slightly if a radioactive source or a beamspot is simulated. For the radioactive source, a mylar puck and a source volume are included. For a beamspot simulation, γ-rays are emitted from a two-dimensional surface on the target. Since the experimental peak efficiencies are for beam-induced reactions, the absolute ^{60}Co efficiency is adjusted by the ratio $N_{1332}^{\text{beamspot}}/N_{1332}^{\text{source}}$. The new absolute peak and total efficiencies were found to be:

$$\eta^{Ge,P}(1173) = 0.0406 \pm 0.0008\ (2\%), \tag{3.7}$$

$$\eta^{Ge,P}(1332) = 0.0383 \pm 0.0008\ (2\%), \tag{3.8}$$

and

$$\eta^{Ge,T}(1253) = 0.189 \pm 0.004\ (2\%). \tag{3.9}$$

Mono-energetic γ-rays emitted from a 1.2 cm diameter beamspot at the target surface were simulated with GEANT4 (the solid line in Fig. 3.11), normalized to the ^{60}Co sum-peak efficiency (Eq. 3.8), and plotted alongside the ^{60}Co peak efficiencies (see Figs. 3.11). The normalized simulated efficiency is the dashed line in Fig. 3.11 and differs from the raw, GEANT4 peak efficiency curve by 5%. The next steps involve comparing

experimental relative peak efficiencies to the absolute peak efficiency and the simulated efficiency curve. The traditional matrix method of Refs. [109, 99] was used to sum-correct experimental peak intensities.

The sum-correction matrix method from Ref. [109] relies on repeatedly solving the following equation for the corrected peak efficiency:

$$\frac{S_{ji}}{I_{ji}} - \frac{D_{ji}}{[\mathbf{N^{(0)}c}]_{ji}} = \epsilon_{ji}^{P} \tag{3.10}$$

where ϵ_{ji}^{P} is the peak efficiency for the deexcitation from level j to level i; S_{ji} is the peak intensity in the presence of coincidence summing; I_{ji} is the γ-ray emission rate; $[\mathrm{N}^{(0)}\mathrm{c}]_{ji}$ is a quantity related to the decay path where c is the branching ratio matrix and $\mathrm{N}^{(0)}$ is a feeding fraction matrix; D_{ji} corrects for coincidence summing. Reference [109] also explains that the following equation can be solved for the number of disintegrations:

$$S_{ji} = R_{ji}[\mathbf{N^{(0)}A^{(0)}} + \mathbf{D}]_{ji} \tag{3.11}$$

where R_{ji} is the disintegration rate and $\mathrm{A}^{(0)}$ contains branching ratio and peak efficiency information. The codes *sump.c* and *sum.c*, developed by R. Longland, solve Eq. 3.10 and Eq. 3.11 respectively, and they are described and benchmarked in Ref. [99].

Data were collected with the $\gamma\gamma$-coincidence spectrometer for radioactive sources and beam-induced reactions. A ^{56}Co source was used along with the $\mathrm{E_R}$ = 278 keV ^{14}N(p,γ)^{15}O resonance [110, 111], the $\mathrm{E_R}$ = 151 keV ^{18}O(p,γ)^{19}F resonance [40, 112], and the $\mathrm{E_R}$ = 406 keV ^{27}Al(p,γ)^{28}Si resonance [110, 113]. The ^{14}N(p,γ)^{15}O and ^{56}Co data were fit independently with the following analytical function from Ref. [114]:

$$\eta(\mathrm{E}) = e^{a+bln(\mathrm{E})+cln(\mathrm{E})^2}. \tag{3.12}$$

The ^{56}Co data were first normalized with GEANT4 to account for the conversion from a source efficiency to a beamspot efficiency, and the collection of efficiencies was then translated along the y-axis to match the ^{60}Co sum-peak absolute efficiency at E_γ = 1332 keV. The ^{14}N(p,γ)^{15}O data were also shifted along the y-axis to match the absolute sum-peak result. This collection of sum-peak-shifted data was then used to adjust the remaining reaction data. The final experimental peak efficiencies are plotted in Fig. 3.11 and labeled "Data" in the figure. A systematic uncertainty of 5% is adopted for HPGe peak efficiencies based on the agreement between raw Monte Carlo efficiencies and the experimental efficiencies.

3.5.2: NaI(Tl) Total Efficiency

Like the HPGe peak efficiencies, NaI(Tl) total efficiencies are taken into account implicitly by the analysis of ^{17}O(p,γ)^{18}F data described in Chapter 6. The analysis performed during the ^{18}O(p,γ)^{19}F study is very

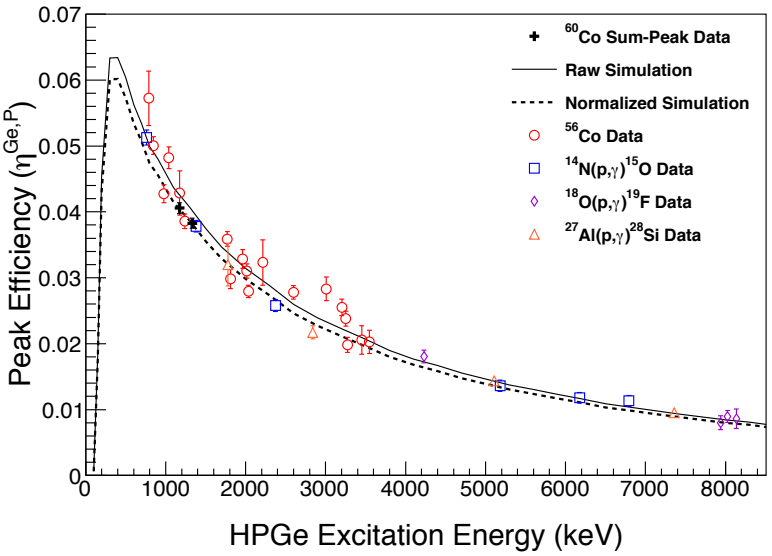

Figure 3.11: The absolute ^{60}Co peak efficiency was determined with the sum-peak method from Ref. [105] (black crosses). The matrix method (Refs. [109, 99]) was used to sum-correct ^{56}Co, ^{14}N(p,γ)^{15}O E_R = 278 keV, ^{18}O(p,γ)^{19}F E_R = 151 keV, and ^{27}Al(p,γ)^{28}Si E_R = 406 keV experimental efficiencies. The *raw simulation* (solid line) was determined from GEANT4 mono-energetic γ-ray simulations. This simulated efficiency curve was normalized to the absolute ^{60}Co peak efficiency to produce the dashed line. The raw and normalized simulated efficiencies differ by 5%.

different from the ^{17}O(p,γ)^{18}F analysis (see Chapter 5)—no ^{19}F deexcitations were detected. The treatment of the NaI(Tl) total efficiencies presented below was applied exclusively to the analysis of ^{18}O(p,γ)^{19}F resonance and direct capture data. A separate characterization of NaI(Tl) gated total efficiencies is presented in Appendix D.2 but is not used in either the ^{18}O(p,γ)^{19}F or ^{17}O(p,γ)^{18}F analyses. A systematic uncertainty of 5% on the gated total efficiency is derived from this assessment.

The NaI(Tl) annulus is composed of 16 scintillating detector segments, and each is connected to photo-multiplier tubes (PMTs). During these studies, initial biases for each PMT were selected carefully and tested because NaI(Tl) detectors have notoriously low energy resolution and calibrations can be very non-linear over wide energy ranges. Several radioactive sources, ^{60}Co, ^{22}Na, and ^{137}Cs, were used to determine what bias voltage would provide the best resolution, the best linear energy calibration, and to gain-match the signal from each PMT. Though the resolution of the annulus is inferior to the resolution of the HPGe detector, it has better absolute efficiency. The annulus was used as a coincidence counter in these experiments; events within a software gate would be recorded in a coincidence spectrum if annulus events coincided with events detected by the HPGe detector. The γ-cascade produced by a beam-induced reaction should be detected partially in both detectors within reasonable timing and energy windows. These gates can be selected to exclude a majority of environmental background counts.

In Fig. 3.12, if a simple, two-step cascade from level 2→1→0 of a hypothetical deexcitation is assumed, two photons will be produced—γ_{21} and γ_{10}. If the yellow volume in the figure, the HPGe detector, detects γ_{10} and the green volume, the annulus, detects γ_{21}, and the gating condition $E_{low} \leq E_{\gamma_{10}}^{Ge} + E_{\gamma_{21}}^{NaI(Tl)} \leq E_{high}$ is satisfied, a coincidence spectrum will be populated with an $E_{\gamma_{10}}$ count. This is of course the simplest of scenarios, but it is easy to imagine how this can be extrapolated to complex decay schemes. The $\gamma\gamma$-coincidence spectrometer allows isolation of the characteristic fingerprint of the beam-induced reaction of interest from the environmental background. The environmental background is unlikely to satisfy the timing and energy constraints necessary to populate a coincidence spectrum [115].

During these experiments, ^{60}Co and ^{22}Na sources were used every day data were acquired to energy-calibrate the NaI(Tl) detectors. A code was written to determine quickly the bin number of the peak intensities detected from these two sources and write an energy calibration file that the JAM [116] data acquisition system could read. Because the annulus is the secondary counter and it is necessary that some fraction of the reaction γ-cascade be detected to fill coincidence histograms, it is important to be able to characterize the NaI(Tl) total efficiency. Monte Carlo techniques are the primary method used to calculate annulus total efficiencies.

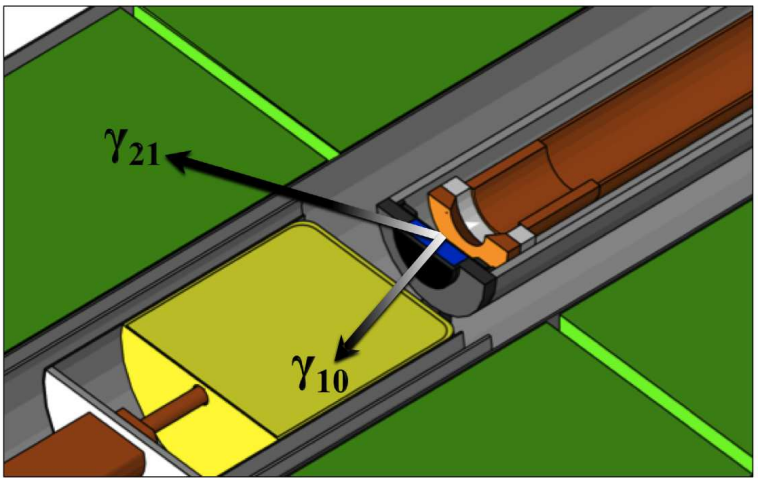

Figure 3.12: From the DAWN [104] schematic of the LENA $\gamma\gamma$-coincidence spectrometer in Fig. 3.10, the scenario where two coincident γ-rays can be detected by the spectrometer is shown. The HPGe detector (yellow) detects the photon labeled γ_{10} and the NaI(Tl) annulus (green) detects the photon labeled γ_{21}.

The ^{18}O$(p,\gamma)^{19}$F study discussed in this thesis was performed with the LENA $\gamma\gamma$-spectrometer at 0° (with respect to the beam). In this configuration, shown in Figs. 3.10 and 3.12, a coincidence correction factor, $f_\gamma(B, \eta, \mathrm{W})$, must be calculated where B represents branching ratios for γ-rays detected in the annulus, η is the total efficiency of the annulus at these γ-ray energies, and W is the associated angular correlation. For the simple case described above where the cascade proceeds from hypothetical levels 2→1→0, the peak

intensity of γ_{10} in the coincidence spectrum can be expressed as:

$$N_{10}^{c} = N_{\mathrm{R}} \eta_{10}^{Ge,P} B_{10} B_{21} [1 - (1 - \eta_{21}^{NaI(Tl),T})] \tag{3.13}$$

where N_{10}^{c} is the γ_{10} intensity in the coincidence spectrum, N_{R} is the number of disintegrations, $\eta_{10}^{Ge,P}$ is the peak efficiency of γ_{10}, B_{10} is the branching ratio of the 1→0 transition, B_{21} is the branching ratio of the 2→1 transition, and $\eta_{21}^{NaI(Tl),T}$ is the total efficiency of γ_{21}. This equation can be generalized to:

$$N_{lm}^{c} = N_{\mathrm{R}} \eta_{lm}^{Ge,P} B_{lm} f_{\gamma}(B_{l'm',n}, \eta_{l'm',n}^{NaI(Tl),T}) \tag{3.14}$$

where the $l \rightarrow m$ transition is detected by the HPGe detector, and from Refs. [4, 117], the coincidence correction factor, f_{γ}, is defined as:

$$f_{\gamma}(B_{l'm',n}, \eta_{l'm',n}^{NaI(Tl),T}) = \sum_{n} \left\{ \left[\prod_{l'>m'} B_{l'm',n} \right] \left[1 - \prod_{\substack{l'>m' \\ l \nrightarrow m}} \left(1 - \eta_{l'm',n}^{NaI(Tl),T} \right) \right] \right\}. \tag{3.15}$$

In Eq. 3.15, B is the branching ratio for a $l' \rightarrow m'$ transition detected by the annulus, and $\eta^{NaI(Tl),T}$ is the total efficiency for the same transition. It is assumed here that W = 1. In this dissertation, the correction factor will be referred to as f_{γ}.

For very complex decay schemes, Eq. 3.15 can become intractable. Since the number of disintegrations is set manually during a GEANT4 simulation and all efficiencies are a product of the simulation (the user defined geometry), a new *PrimaryGeneratorAction.cc* class was written for the LENA GEANT4 simulation to generate resonance and direct capture γ-cascades. The input file for this new class reads in a list of energy levels and decay logic (including branching ratios) for the deexcitation of interest. The contents of the ROOT tree generated by GEANT4 can be sorted with the ROOT sort routine, *sort.cxx*. This sort routine bins simulated Monte Carlo data into histograms that mirror the spectra created during data acquisition with JAM [116] (see Sec. 6.3.1 for more information on sorting data with ROOT and the code *sort.cxx*). Coincidence logic was carefully coded into *sort.cxx*, and the coincidence spectra generated with the ROOT sort routine agree with spectra generated during data acquisition (see Refs. [101] and [1]). Armed with this tool, for a single decay of interest—the 1→0 transition for example—f_{γ} can be isolated without having to calculate meticulously each term in Eq. 3.15. The only stipulation is that the branching ratios and decay scheme included in the GEANT4 input file be well known. The following equation, from Ref. [1], can then be solved for f_{γ}:

$$N_{10}^{c} = N_{\mathrm{R}}' \eta_{10}^{Ge,P} B_{10} f_{\gamma} \tag{3.16}$$

where N_{10}^{c} is the simulated peak intensity of the 1→0 transition, $N_{\mathrm{R}}^{\prime}$ is the simulated (user defined) number of disintegrations, $\eta_{10}^{Ge,P}$ is the experimental peak efficiency of the 1→0 transition in the HPGe detector, B_{10} is the branching ratio for this transition, and f_{γ} contains the remaining branching ratio and total efficiency terms for the γ-rays coincident with 1→0 but detected by the NaI(Tl) annulus.

During the $^{18}\mathrm{O}(p,\gamma)^{19}\mathrm{F}$ study, handling the NaI(Tl) annulus total efficiency in this manner was sufficient because the resonance of interest was not detected and the decay scheme was unknown. Instead, f_{γ} was used as the basis of a complex argument that constrained the upper limit on the resonance strength for the $\mathrm{E_R}$ = 95 keV resonance. This analysis is discussed in Chapter 5 of this dissertation.

3.5.3: Scintillating Muon Veto Paddles

When the HPGe detector and NaI(Tl) annulus are placed in the running geometry, the entire $\gamma\gamma$-coincidence spectrometer is surrounded on five sides by lead sheets and plastic scintillating muon veto paddles—10 mm and 50 mm thick, respectively. The lead sheets provide passive shielding of low-energy environmental background radiation, and the scintillating paddles actively veto cosmic-ray induced muons. The muon veto is configured by setting a software anticoincidence condition during data acquisition between the paddles and the HPGe detector. These events are thus excluded from the analysis.

3.5.4: $\gamma\gamma$-Coincidence Electronics

Between the 16 individual NaI(Tl) crystals, the HPGe detector, and the five muon veto paddles, the $\gamma\gamma$-coincidence spectrometer has a total of 22 energy and timing signals that must be processed. Nuclear Instrument Modules (NIM) and VME-bus modules were used to process these signals. The HPGe detector has an on-board pre-amplifier; a spectroscopy amplifier and a timing filter amplifier (TFA) receive preamplified signals straight from the detector. The energy signal from the spectroscopy amplifier is sent to an analog-to-digital converter (ADC). The timing signal leaves the TFA and is then discriminated by a constant fraction discriminator (CFD). A gate-delay generator downstream from the CFD converts the discriminated timing signal into the master timing gate. A pulser is used to inject a pulse signal into the HPGe's preamplifier to monitor deadtime. Meanwhile, the signals from the annulus are amplified by a spectroscopy amplifier for energy and a fast amplifier for timing. The energy signals are sent to an ADC while the timing signals are sent to a CFD and a 500 ns delay before proceeding to a time-to-digital converter (TDC). The master gate set by the HPGe timing signal is used to start the TDC while the annulus signals stop it. Wide TDC gates were used during both experiments. The $^{19}\mathrm{F}$ nucleus deexcites preferentially through the 197 keV second excited state, and this level has a τ_m = 128.8 ± 1.5 ns lifetime [40]. Narrow TDC gates, on the order of 20

ns, would prevent the detection of the 197 keV γ-ray by the $\gamma\gamma$-coincidence spectrometer. The TDC gate was widened by an additional ≈400 ns prior to the TDC peak. Likewise, in the ^{18}F nucleus, the fourth excited state, 1121 keV, has a $\tau_m = 234 \pm 10$ ns lifetime [40], and narrow TDC gates could not be used during data acquisition. The TDC gate was widened by an additional ≈700 ns after the TDC peak.

The scintillator paddle signals are also sent to a spectroscopy amplifier and an ADC; however, their timing signals go to a leading-edge discriminator (LED). A time-to-amplitude converter (TAC) is used to set up the anticoincidence condition between the paddles and the HPGe detector. The HPGe master gate is the start condition, and the LED's 'or' signal is used as the stop. A detailed electronics schematic is shown in Fig. 3.13. The NaI(Tl) annulus ADC and TDC are CAEN devices. They are installed in a VME-bus crate and queried by a VME single board computer. The data acquisition system JAM [116] is used to process the signals from the electronics system, and data are stored event-by-event. Coincidence and anticoincidence conditions are governed by a JAVA sort routine that runs during data acquisition but can also be run offline to resort data or to modify timing, and a record of raw ADC and TDC intensities (by channel number) is saved to a text file. This file can then be parsed and sorted with the ROOT sort routine, *sort.cxx*, to sort experimental data into the same histogram hierarchy that GEANT4 data are sorted. This histogram hierarchy mirrors the gating and logic structure assembled in JAM during data acquisition, and sorted JAM histograms match sorted *sort.cxx* histograms. See Sec. 6.3.1 for more details on the JAM to ROOT conversion.

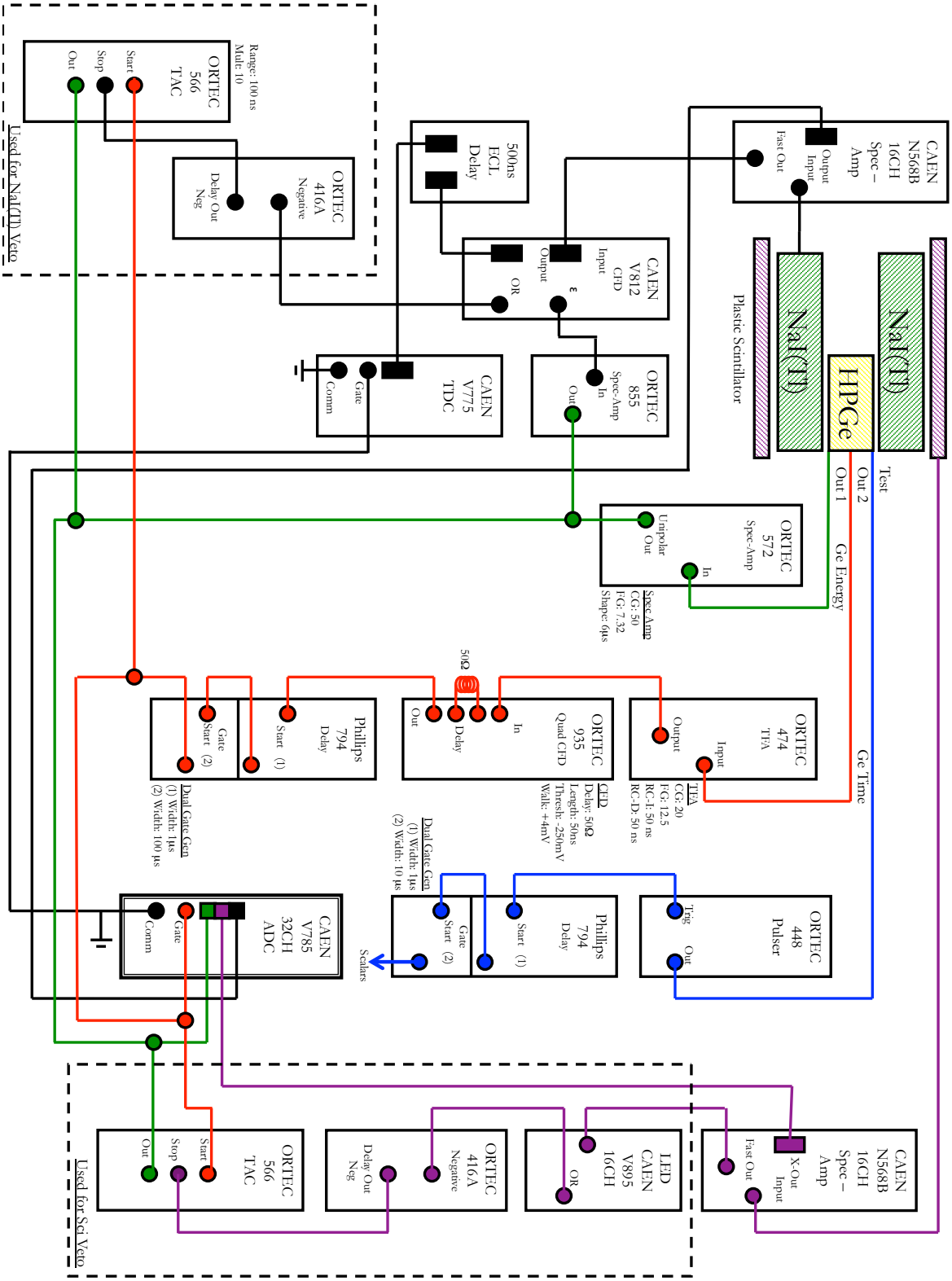

Figure 3.13: Electronics diagram for the $\gamma\gamma$-coincidence spectrometer. The HPGe detector is the primary counter and the NaI(Tl) annulus is the secondary counter. The electronics necessary for the scintillator muon veto are also shown.

CHAPTER 4: OXYGEN ENRICHED TARGETS

To boost the signal-to-noise ratio and extract the signature γ-cascade for the nuclear reaction of interest, LENA features the accelerators and detectors necessary to perform these experiments at "sea-level." However, beam-induced background contaminants are another potentially overwhelming source of noise that could hinder or prevent detection. Steps were taken to reduce these potential sources of background, but several contaminants were unavoidable for reasons that will soon be apparent. Contaminant reactions observed during the present studies are listed in Table 4.1. As Ref. [80] pointed out, ^{19}F contamination in anodized targets is unavoidable—this is because fluorine is used during the production of thin tantalum foils. Another unavoidable contaminant is ^{18}O, because it is not possible to buy isotopically pure $H_2^{17}O$. The $^{18}O(p,\gamma)^{19}F$ resonance at $E_R = 150.82 \pm 0.09$ keV [118] is a strong resonance, $\omega\gamma = 0.97 \pm 0.05$ meV [4] (the weighted average of strengths reported by Refs. [112], [119] and [120]), and at low beam energies, this contaminant will show up. For both of these cases, ^{19}F and ^{18}O, the experiment must be tailored to avoid these resonances. The beam energies selected for the $^{17}O(p,\gamma)^{18}F$ study were selected in order to be as far off resonance as possible. This will be discussed further later in Chapter 6.

Table 4.1: The contaminants that were observed during the $^{17}O(p,\gamma)^{18}F$ study. The $^{18}O(p,\gamma)^{19}F$ study was significantly less affected by beam-induced backgrounds because it was conducted at beam energies well below contaminant Q-values.

Reaction	Type	E_p (keV)	Q-value (keV)	Source
$^{11}B(p,\gamma)^{12}C$	Resonance	162.5(9)[1]	15956.9(4)	Vacuum System
$^{12}C(p,\gamma)^{13}N$	Direct Capture	175−325[2]	1943.49(27)	Vacuum System
$^{14}N(p,\gamma)^{15}O$	Resonance	278.4(7)[1]	7296.8(5)	Previous Experiment
$^{16}O(p,\gamma)^{17}F$	Direct Capture[3]	175−325[2]	600.27(25)	Enriched Water
$^{18}O(p,\gamma)^{19}F$	Resonance	150.82(9)[4]	7993.6(0)[5]	Enriched Water
$^{19}F(p,\alpha\gamma)^{16}O$	Resonance	340.46(4)[6]	8113.61(0)[5]	Ta Foil Production

[1] Calculated from Refs. [41] and [121].
[2] $^{17}O(p,\gamma)^{18}F$ study energy range.
[3] Ref. [122].
[4] Resonance energy reported in Ref. [118].
[5] Q-value uncertainty less than significant figures in Ref. [41].
[6] Resonance energy reported in Ref. [123].

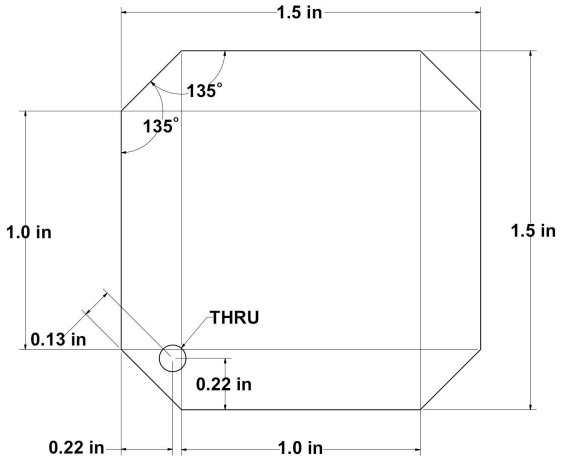

Figure 4.1: A schematic drawing of the target substrates machined from thin tantalum foils, typically 0.5 mm thick, for the rare oxygen isotope studies discussed in this thesis. The major improvement over previous target fabrication was the inclusion of a small hole in the target backing that allowed easy retrieval during acid etching. This hole was placed just outside the perimeter of the target chamber o-ring seal. As can be seen from the drawing, initial tantalum substrate dimensions are ≈1.5"×1.5".

Section 4.1: Target Preparation

Figure 4.1 shows a typical target backing used at LENA, regardless of the substrate material. Target backings are machined carefully from sheets of ≈ 0.5 mm thick foils into 1.5"×1.5" pieces. A hole is drilled well outside the diameter of the target chamber o-ring seal to make it easier to chemically etch the substrate material. For the studies discussed in this dissertation, ultra-pure tantalum (Ta) was used for all target backings because tantalum is stable, resistant to corrosion, capable of being chemically etched to remove surface contaminants, will not interact with the beam at the experimental energies, and can be anodized to produce oxide targets. The anodic oxidation of tantalum targets was first outlined by Ref. [124]. The anodization process allows target thicknesses to be reproduced consistently, and it also allows the production of robust oxygen targets that remain stable when exposed to intense H^+ beam. Additionally, the stoichiometry of the oxide produced by anodization, Ta_2O_5, is well established [125].

4.1.1: Chemical Etching

Thin tantalum foils were ordered from *Alfa Aesar* and were 0.5 mm thick at a purity of annealed 99.95% metal basis excluding niobium. Target backings were machined from this foil at the Duke University machine shop to the specifications shown in Fig. 4.1. Before a target backing makes it to the anodization stage, the machined tantalum substrate is acid etched in a bath. The tantalum acid etching recipe used in these experiments comes from Ref. [126] and is tailored specifically for the preparation of anodized oxide films.

The acid bath consists of 5 parts 95% H_2SO_4, 2 parts 70% HNO_3, and 2 parts 50% HF. Typical batch volumes were 75 mL H_2SO_4, 30 mL HNO_3, and 30 mL HF. Acids were combined carefully under a fume hood in a teflon beaker. This beaker was placed in a ice bath during etching because the etching process is exothermic. Each target backing was dipped in the acid bath three times for a period of 20 seconds. Backings were dipped in distilled water in between etching sessions and after three dips, backings were cleaned in ethanol and allowed to dry. Typically three targets were etched in each batch of acid with an average final target thickness of 0.3 mm.

Figure 4.2: All tantalum backings were etched in an acid bath of 5 parts 95% H_2SO_4, 2 parts 70% HNO_3, and 2 parts 50% HF. Etching was performed in a teflon beaker under a fume hood. The necessary safety precautions were taken while etching backings and handling acids.

Tefzel® ethylene tetrafluoroethylene (ETFE) tongs were ordered specifically for these rounds of acid etching because the acid bath proved too caustic for TUNL's supply of teflon tongs. One end of the new Tefzel® ETFE tongs was drilled and tapped for a replaceable teflon screw. The combination of the tongs and the screw made it easy to dip targets in the acid bath by hooking the screw through the hole in the tantalum backing (shown in Fig. 4.1) without losing the backing in the acid bath. Additionally, the new tongs are longer than the previous generation of teflon tongs allowing the experimenter to safely distance hands from the acid bath without sacrificing dexterity.

Etched backings were stored in a lucite target chamber under high vacuum (typically 50 mbar) until the next stage in the target production process.

4.1.2: Resistive Heating

The next step in the contamination reduction process is resistive heating in a vacuum. A new, oil-free evaporation chamber was built by J. M. Cesaratto and is discussed in detail in Ref. [108]. The etched backings were secured between copper electrodes within the evaporation station and a bell jar was placed over the system. The volume was evacuated with a scroll pump and a cryogenic vacuum pump to achieve high vacuum ($<10^{-6}$ Torr). The vacuum pump selection was an important, conscious decision made to reduce contamination. Other evaporation stations use diffusion and mechanical pumps to achieve high vacuum, but these pumps require pump oil that can potentially contaminate the chamber. If these contaminants come in contact with the target, observed ^{11}B, ^{12}C, and ^{19}F concentrations could reach unacceptable levels. However, this evaporation chamber is intentionally an oil-free environment, thus preserving the contaminant reduction achieved by etching and the additional reduction gained by outgassing the target.

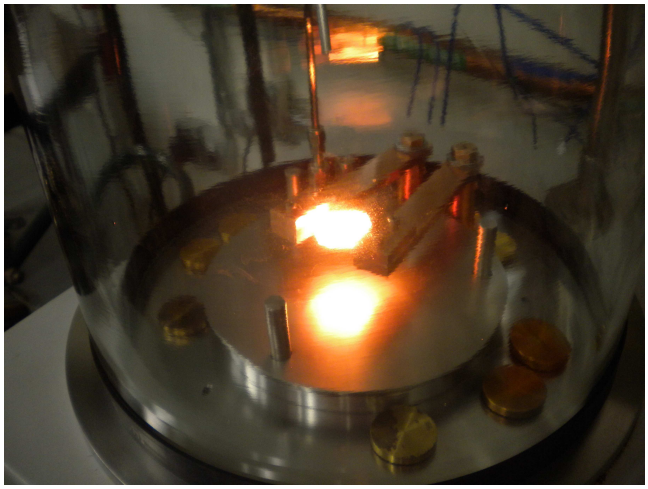

Figure 4.3: After acid etching, tantalum backings are resistively heated under high vacuum to further reduce contamination.

Under high vacuum, a current is applied across the target backing. This current is raised gradually until the tantalum backing starts to glow *red hot* (typically ≈275 A). Current and the observed blackbody color are monitored because, if the target becomes *white hot*, the tantalum backing may approach and exceed its melting point. A spike in vacuum pressure indicates that contaminants are boiling off the target surface. The vacuum system removes these contaminants from the evaporation chamber, and after several minutes, the chamber pressure decreases. Backings are typically resistively heated for 15 minutes after the initial outgassing event. The current is then decreased gradually and the backing is allowed to cool for an hour. Outgassed backings are then anodized immediately.

4.1.3: Anodic Oxidation

Anodization is a well-understood and well-established process, and it produces stable targets with known stoichiometry. During this process, isotopically enriched water is dissociated, and the O^{2-} ions combine with the ionized metal (Ta). The chemical reaction is [127]:

$$2\mathrm{Ta} + 5\mathrm{H_2O} = \mathrm{Ta_2O_5} + 5\mathrm{H_2}. \tag{4.1}$$

A new anodization chamber was designed and assembled for the measurements described in this thesis according to the description in Ref. [128] (see Figs. 4.4 and 4.5). The impetus behind designing a new chamber as opposed to using the existing chamber featured in Ref. [129] was to achieve improved retention of expensive, rare oxygen isotope enriched water ($2535 per gram for $H_2^{17}O$ enriched to 88 atom %). The new design features a tantalum anode (target) and cathode (blank) sealed with o-rings and held in place by bolting copper electrodes to both surfaces. Entry and exit holes were bored through the top of the lucite chamber to allow displaced air and the products of disassociation to escape. These holes also allow enriched water to be easily inserted and reconstituted from the chamber. A switch was added between the chamber

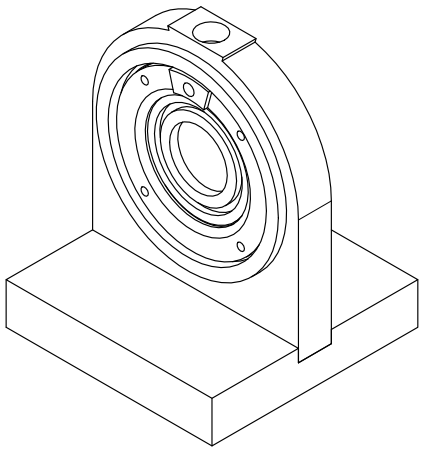

Figure 4.4: A schematic drawing of the new anodization chamber assembly. This new chamber streamlines the injection of rare oxygen isotope enriched water and optimizes the recovery of water after anodization. The average loss of enriched water per target was reduced to <0.5 mL/target. Previous anodization chambers lost as much as 1.0−1.5 mL/target. This new design is based on the chamber described in Ref. [128].

and the high voltage supply to avoid any voltage and current perturbations that might be introduced as the high voltage supply is biased. During anodization, a positive voltage is applied to an etched and outgassed

tantalum backing secured to the target chamber anode. Electrons are pulled off the target surface forming Ta^{5+} ions, and the anodizing voltage also dissociates the isotopically enriched water within the chamber producing O^{2-} ions. The tantalum and oxygen ions combine to form the well-defined compound, Ta_2O_5. Potassium iodide crystals were added to the enriched water before anodization to boost current flow from the anode to the cathode. The following equation was used to tune the target thickness produced by anodization [129]:

$$\Delta E = 1.5347 + 0.26565 \times V \tag{4.2}$$

where ΔE is the target thickness in keV and V is the anodizing voltage in volts. This equation was determined by former LENA post-doctoral associate C. Fox, and it is a sufficient method to determine approximate ^{17}O and ^{18}O target thicknesses before collecting a yield curve.

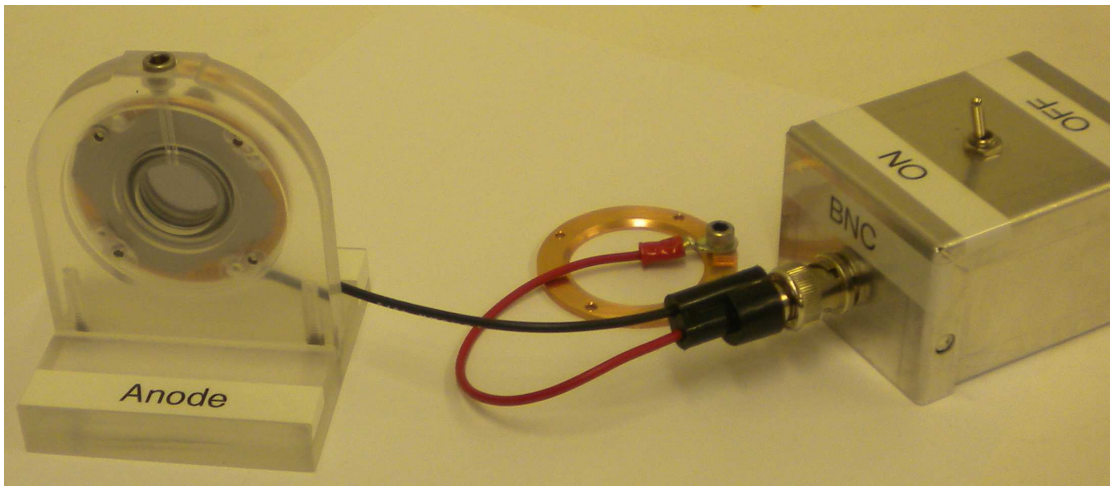

Figure 4.5: A photo of the new anodization chamber designed and assembled for these experiments. The key feature of this new chamber is the high retention of rare oxygen isotope enriched water between anodic oxidation sessions. Copper electrodes clamp down on the anode (the target backing) and the cathode (a tantalum blank). Compression allows o-rings to seal the chamber. Two holes in the top of the chamber allow enriched water to be injected—or extracted—with a syringe and displaced air—or the products of dissociation—to escape the chamber.

Target thicknesses near the experimental laboratory energies were estimated with well-known $^{18}O(p,\gamma)^{19}F$ and $^{17}O(p,\gamma)^{18}F$ resonances and the relationship [4]:

$$\frac{\Delta E(\text{resonance})}{\epsilon_{eff}(\text{resonance})} = \frac{\Delta E(E_p)}{\epsilon_{eff}(E_p)} \tag{4.3}$$

where ΔE is the measured target thickness in keV, and ϵ_{eff} is the effective stopping power, derived from

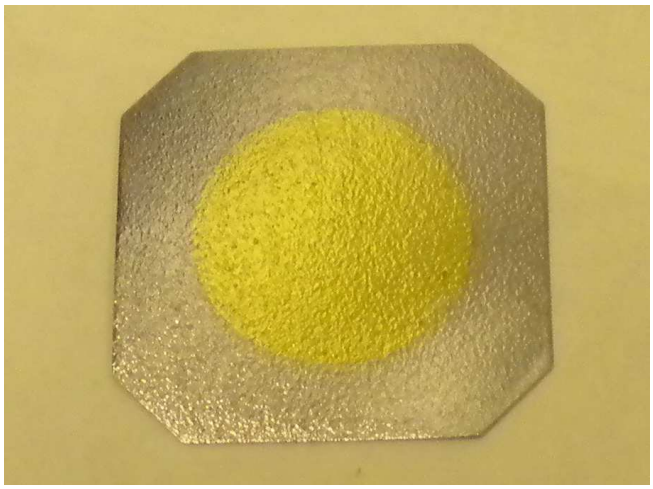

Figure 4.6: A photo of a pristine anodized target. The yellow/gold region is a thin film of Ta_2O_5 produced by anodic oxidation within the anodization chamber shown in Fig. 4.5. Target thickness as a function of stopping power (keV) is dependent upon the voltage used during anodization.

Bragg's rule [75, 4]:

$$\epsilon_{eff} = \frac{M_{x_O}}{M_p + M_{x_O}} \left(\frac{N_O}{N_{x_O}} \epsilon_{x_O} + \frac{N_{Ta}}{N_{x_O}} \epsilon_{Ta} \right) \tag{4.4}$$

where M_p and M_{x_O} are the mass of the proton and the oxygen isotope of interest (either ^{17}O or ^{18}O), ϵ_{x_O} and ϵ_{Ta} are the laboratory stopping powers of protons in the oxygen isotope of interest and tantalum (calculated with SRIM [130]), respectively, and N_i are number densities ($N_O = N_{^{16}O} + N_{^{17}O} + N_{^{18}O}$).

Section 4.2: ^{18}O Targets

For the ^{18}O study, 2 grams of ^{18}O-enriched water were purchased from *Icon Isotopes* with the following enrichments: 99.3 atom % ^{18}O, 0.5 atom % ^{16}O, and 0.2 atom % ^{17}O.

Excitation functions were collected during the $^{18}O(p,\gamma)^{19}F$ experiment at the well-known $E_R = 150.82 \pm 0.09$ keV [118] resonance with the LENA 1 MV JN Van de Graaff. Target thicknesses were estimated with Eq. 4.4. It was found that targets could withstand proton accumulations of $Q > 45$ C without significant degradation at $I_p^{ECRIS} = 0.5{-}1.0$ mA.

Targets produced for the $^{18}O(p,\gamma)^{19}F$ study are listed in Tab. 4.2. This table includes their initial thicknesses with respect to the 151 keV resonance and the amount of charge accumulated on- and off-resonance. A Markov Chain Monte Carlo (MCMC) code written by R. Longland in R, *YCurveFit.R*, was used to analyze the yield curves collected on each target. Based on the excitation function, this code can calculate parameters such as thickness, resonance energy, straggling constant, and beam width; it converges on a fit to the target profile through a minimization procedure. Excitation functions collected for each target

used during the $^{18}O(p,\gamma)^{19}F$ study are shown in Fig. 4.7 and labeled by target designation from Tab. 4.2. Excitation functions were produced by monitoring and recording the intensity of the R→3908 transition in ^{19}F from E_p = 148−172 keV.

Table 4.2: The ^{18}O targets fabricated for the $^{18}O(p,\gamma)^{19}F$ study and the target thicknesses at the E_R = 151 keV resonance. Charge accumulation on- and off-resonance (the E_R = 95 keV resonance), pertinent to the $^{18}O(p,\gamma)^{19}F$ experiment, are also shown.

Target Designation	Thickness (keV)	On-Res. Charge (C)	Off-Res. Charge (C)
$\alpha 1$	18.1 ± 0.2	44.8	–
$\alpha 2$	18.1 ± 0.2	3.1	16.0
$\alpha 3$	17.69 ± 0.19	21.0	24.0
$\alpha 4$	17.63 ± 0.17	11.1	–

Section 4.3: ^{17}O Targets

During the ^{17}O study, 2 grams of ^{17}O-enriched water were purchased from Icon Isotopes with the following enrichments: 87.7 atom % ^{17}O, 11.6 atom % ^{16}O, and 0.7 atom % ^{18}O. Of the stable oxygen isotopes, ^{17}O is the rarest; the abundance percentage, $^{17}O/^{16}O$, is 0.038% in our Solar system [131]. The scarcity of this isotope increases the cost of ^{17}O-enriched water dramatically—$2535 per gram.

Yield curves were gathered during the $^{17}O(p,\gamma)^{18}F$ direct capture study at the well-known E_R = 518.3 ± 1.2 keV (see Tab. B.2) resonance (Γ = 0.24 ± 0.03 keV [121]). However, mechanical complications associated with the JN Van de Graaff during the experiment required that yield curves during ECR ion source data acquisition be taken at E_R = 151 keV with the $^{18}O(p,\gamma)^{19}F$ resonance. These yield curves reduced target longevity because 0.5 C was necessary to collect decent statistics at each point along the excitation function. High charge accumulations were necessary because the anodized ^{17}O targets were depleted in ^{18}O (see above). For this reason, the yield curves were sparsely populated intentionally to reduce target wear. Enough points were collected to assess degradation and for the Markov Chain Monte Carlo code to calculate target parameters. Target thicknesses were calculated with Eq. 4.4 but thicknesses were then converted carefully from the $^{18}O(p,\gamma)^{19}F$ center-of-mass frame to the $^{17}O(p,\gamma)^{18}F$ center-of-mass frame. With the additional target longevity afforded by rastering the beam (see Sec. 3.2), it was found targets could withstand proton accumulations of Q > 55 C at I_p^{ECRIS} = 2.0 mA without losing the maximum yield (ideal for resonance experiments). However, degradation (between 0.07−0.22 keV per Coulomb) proved to be significant enough to require some additional steps during the analysis of direct capture data. Target thicknesses decreased, on average, from 15.7−11.6 keV at E_R = 151 keV over approximately 30 C. To account for degradation, the

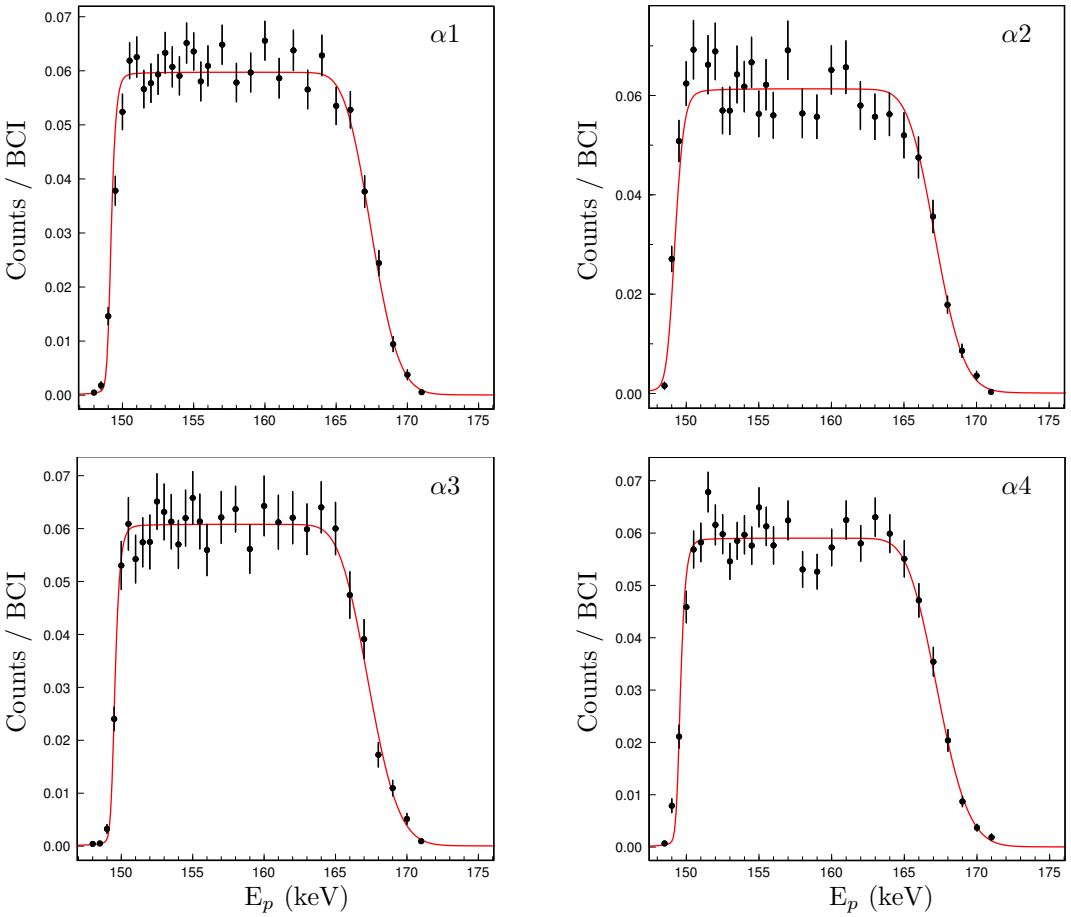

Figure 4.7: Yield curves were collected at the well-known ^{18}O(p,γ)^{19}F resonance E$_R$ = 151 keV with the LENA JN Van de Graaff accelerator. The MCMC fit is shown in red in these figures. The x-axis is the H$^+$ bombarding energy in keV in the laboratory frame, and the y-axis is in units of Counts/BCI (beam charge integration). In these experiments, beam charge integration results in units of 10^{-6} C. Each figure is labeled by target designation and can be cross-referenced with Tab. 4.2 for additional target information. The R→3908 primary transition was used to generate these excitation functions.

target thickness determined from yield curve measurements was corrected by the amount of charge collected on a particular target, and this allowed a mean thickness to be calculated. The mean target thickness during data acquisition at E_p = 190 keV was $\Delta\overline{E}$ = 11.9 keV, and during E_p = 175 keV data acquisition, the mean thickness was $\Delta\overline{E}$ = 13.4 keV. A systematic uncertainty in the mean thickness of 3.2% was determined based on the maximum degradation rate and the uncertainty in the target thickness associated with the Markov Chain Monte Carlo code. It was only necessary to account for target degradation while collecting direct capture data with the ECR ion source. Targets exposed to JN beam did not exhibit any observable degradation because the beam current at the target was over an order of magnitude lower. Data were collected at the $^{17}O(p,\gamma)^{18}F$ resonance E_R = 193.2 ± 0.9 keV [75] with the ECR ion source at E_p = 200 keV with a charge accumulation of Q = 14 C. No degradation was observed during this period of ECRIS data acquisition because beam currents were relatively low, predominantly 800−1000 μA.

Table 4.3: The ^{17}O targets fabricated for the $^{17}O(p,\gamma)^{18}F$ study and the target thicknesses at the E_R = 518 keV resonance. These "βx" targets were monitored with the JN Van de Graaff accelerator for target thickness and degradation. The "γx" targets were monitored with the ECR ion source for target thickness and degradation at the $^{18}O(p,\gamma)^{19}F$ resonance E_R = 151 keV. Yield curves collected with the ECR ion source were *expensive* with respect to accumulated charge—0.5 C per point. The yield curves were sparsely populated to reduce degradation due to collection. The total charge accumulated on each target is also listed.

Target Designation	Thickness (keV)	Off-Res. Charge (C)	On-Res. Charge (C)
β1	12.20 ± 0.10	8.0	–
β2	10.8 ± 0.5	10.0	–
β3	11.15 ± 0.16	15.0	14.0
γ1	15.9 ± 0.3	38.7	–
γ2	15.7 ± 0.3	30.3	–
γ3	15.5 ± 0.3	25.7	–
γ4	15.8 ± 0.3	29.4	–
γ5	15.8 ± 0.3	29.7	–

Targets probed during the JN portion of the experiment are itemized in the top portion of Tab. 4.3 while targets used during ECRIS data acquisition are listed in the bottom portion. Both tables include initial target thicknesses and the total accumulated charge on each target. The JN target thicknesses in Tab. 4.3 are with respect to the $^{17}O(p,\gamma)^{18}F$ resonance E_R = 518 keV, and the ECRIS thicknesses are with respect to the $^{18}O(p,\gamma)^{19}F$ resonance E_R = 151 keV. Excitation functions collected near 518 keV with the JN Van de Graaff accelerator are shown in Fig. 4.8 while yield curves collected with the ECR ion source near 151 keV are shown in Fig. 4.9. The yield curves are labeled by the target designations listed in Tabs. 4.3 for the JN and ECRIS portions of the experiment, respectively. Note that the ECRIS yield curves are sparsely populated to reduce target degradation due to the high-intensity H^+ beam. For the JN yield curves,

excitation functions were produced by monitoring and recording the intensity of the R→1121 transition in ^{18}F from E$_p$ = 517−538 keV. For the ECRIS yield curves, the same transition and energy range probed during the ^{18}O(p,γ)^{19}F study were used. It is clear from Figs. 4.8 and 4.9 that the energy resolution of the ECR ion source is superior to the energy resolution of the JN Van de Graaff.

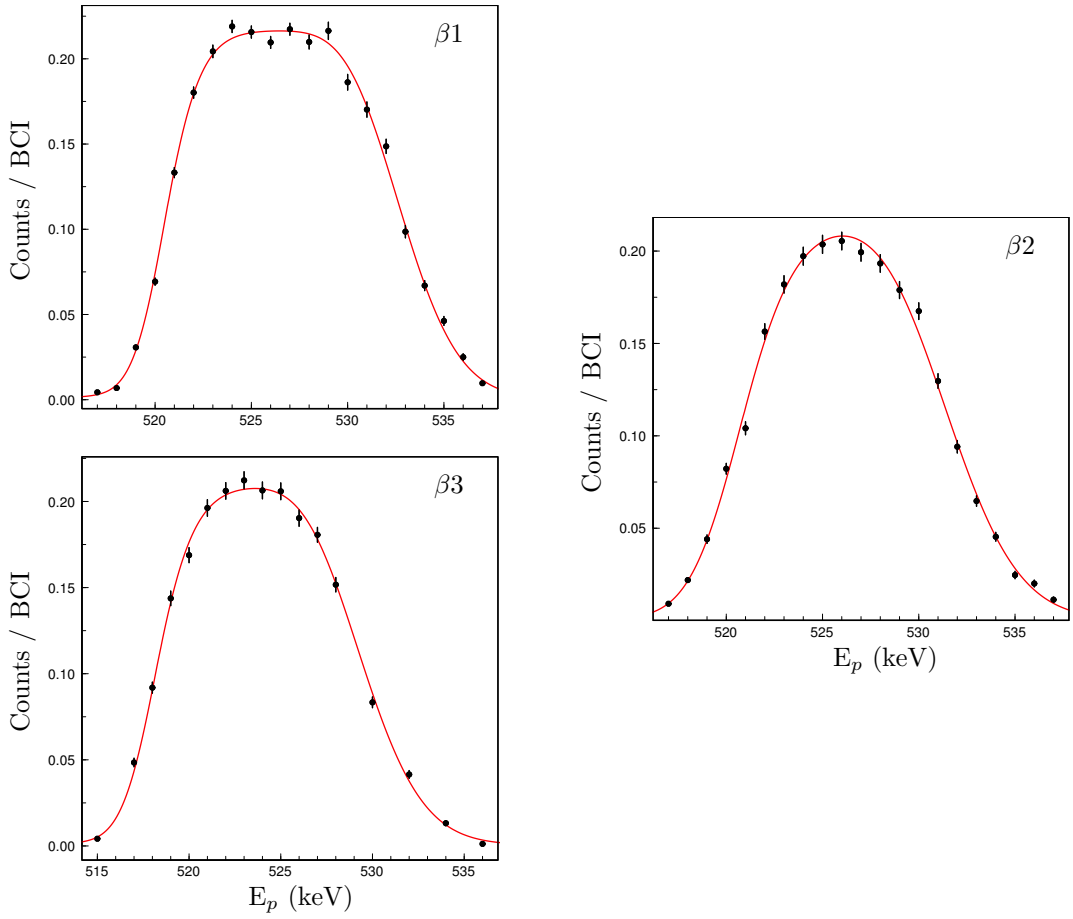

Figure 4.8: Yield curves were collected at the well-known ^{17}O(p,γ)^{18}F resonance, E$_R$ = 518 keV, with the LENA JN Van de Graaff accelerator. The MCMC fit is shown in red in these figures. The x-axis is the laboratory beam energy in keV, and the y-axis is in units of Counts/BCI. Each figure is labeled by target designation and can be cross-referenced with Tab. 4.3 for additional target information. The R→1121 primary was used to generate these excitation functions. The energy resolution of the JN Van de Graaff accelerator is clearly inferior to the energy resolution of the ECR ion source (compare with Fig. 4.9).

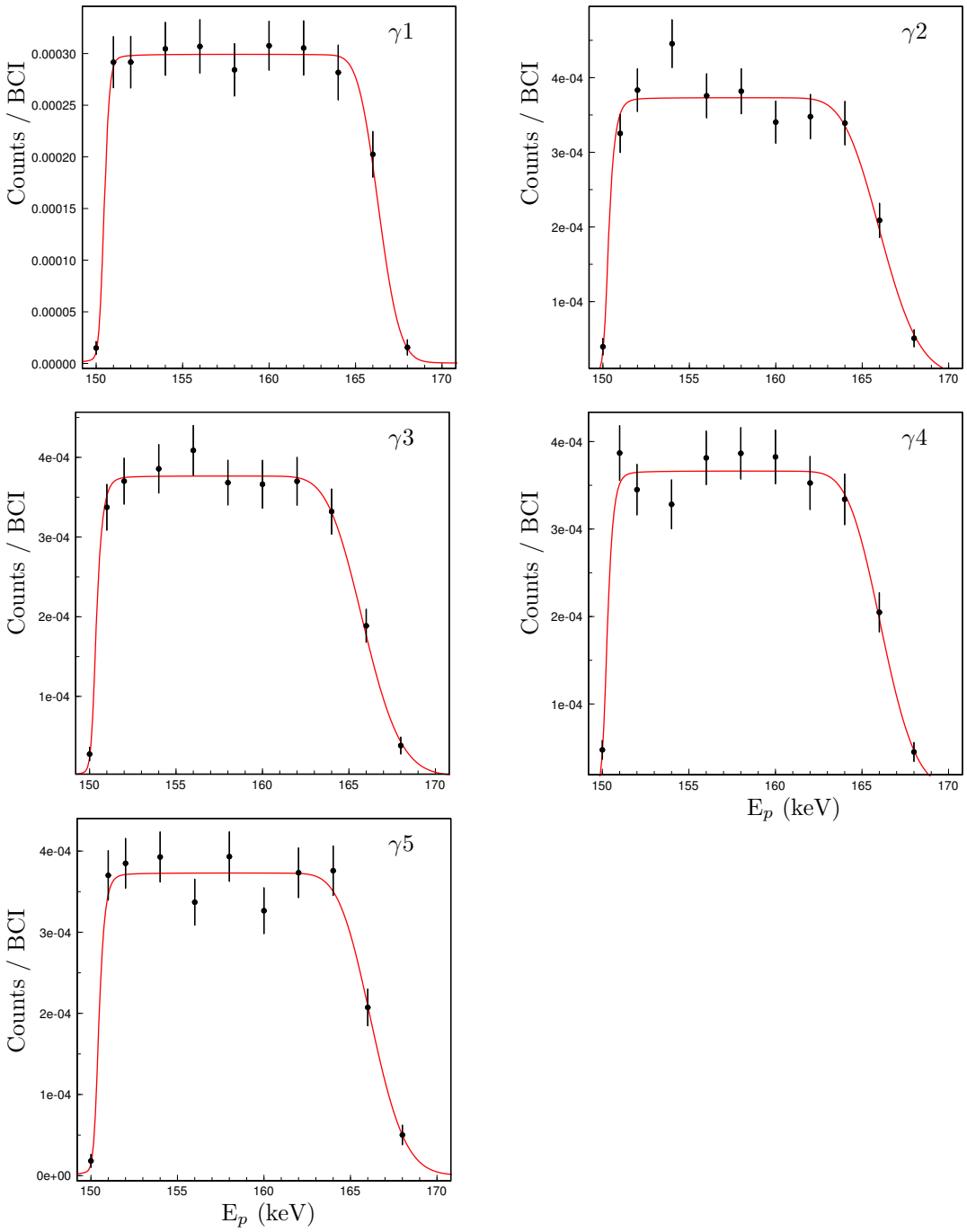

Figure 4.9: Yield curves were collected during the ^{17}O study at the well-known ^{18}O(p,γ)^{19}F resonance E$_R$ = 151 keV with the ECR ion source. The MCMC fit is shown in red in these figures. The x-axis is the laboratory beam energy in keV, and the y-axis is in units of Counts/BCI. Each figure is labeled by target designation identifier and can be cross-referenced with Tab. 4.3 for additional target information. The R→3908 primary was used to generate these excitation functions.

CHAPTER 5: ^{18}O(p,γ)^{19}F PROTON CAPTURE

Section 5.1: Previous Experiments

Within the cool bottom processing temperature regime in asymptotic giant branch stars (≈50 MK), the ^{18}O(p,γ)^{19}F reaction rate may be influenced by an unobserved, low-energy resonance at $E_R = 95 \pm 3$ keV [40, 41] (see Fig. 5.1). In the competing ^{18}O(p,α)^{15}N reaction, a strength of $\omega\gamma_{p\alpha} = (1.6 \pm 0.5)\times10^{-7}$ eV at $E_R = 95$ keV was measured directly by Lorenz-Wirzba *et al.* (1979) [133]. Ref. [133] used two silicon (Si) surface barrier detectors positioned 7 cm from the target at 90° and 135°. Their tantalum pentoxide targets were enriched to 99.9 atom % ^{18}O, and they collected data at the University of Münster using a 350 keV accelerator. In the ^{18}O(p,γ)^{19}F reaction, the $E_R = 95$ keV resonance has never been observed, and none of the γ-ray decays from the resonance level are known. Upper limits were placed on the resonance strength in the past, first by Wiescher *et al.* (1980) [112] with $\omega\gamma_{p\gamma} \leq 5\times10^{-8}$ eV and then by Vogelaar *et al.* (1990) [120] with $\omega\gamma_{p\gamma} \leq 4\times10^{-8}$ eV.

The Wiescher *et al.* (1980) [112] experiment spanned a wide energy range, $E_p = 80-2200$ keV, but the portion pertinent to the 95 keV resonance was performed at the University of Münster using a 350 keV accelerator with beam currents between $I_p = 250-300$ μA. They produced $Ta_2^{18}O_5$ targets enriched to 99 atom % in ^{18}O, and their detector array was a 40 cm^3 Ge(Li) detector with no active or passive shielding. To calculate their upper limit, Ref. [112] assumed a 100% deexcitation through the ^{19}F second excited state—the $E_x = 197$ keV level.

The Vogelaar *et al.* (1990) [120] experiment used Ta targets anodized in 97 atom % ^{18}O-enriched water. They used four 15×15×25 cm^3 NaI scintillators stacked in a 4π geometry, cosmic-ray veto paddles, and lead (5 cm thick) and paraffin (20 cm thick) shielding. They collected 400 mC of charge with ≈ 40 μA beam over 2.9 hours of data acquisition.

With a proton separation energy of $Q_{p\gamma} = 7993.5994 \pm 0.0011$ keV [41], the $E_R = 95$ keV resonance corresponds to the $E_x = 8084 \pm 3$ keV [40] level in the ^{19}F nucleus. The previous experimental information regarding the structure of this compound nucleus level is summarized in Tab. 5.1. From the ^{18}O(^{3}He,d)^{19}F experiment performed by Ref. [134], it is clear that the proton orbital angular momentum transfer for the 8084 keV level is restricted to $\ell_p = (2,3)$ (see Fig. 5.2a). In Ref. [39], the *Trojan Horse Method* was used to investigate this level with the ^{2}H(^{18}O,α^{15}N)n reaction. They determined that $J = 3/2$ and $\ell_\alpha = 1$ (see Fig.

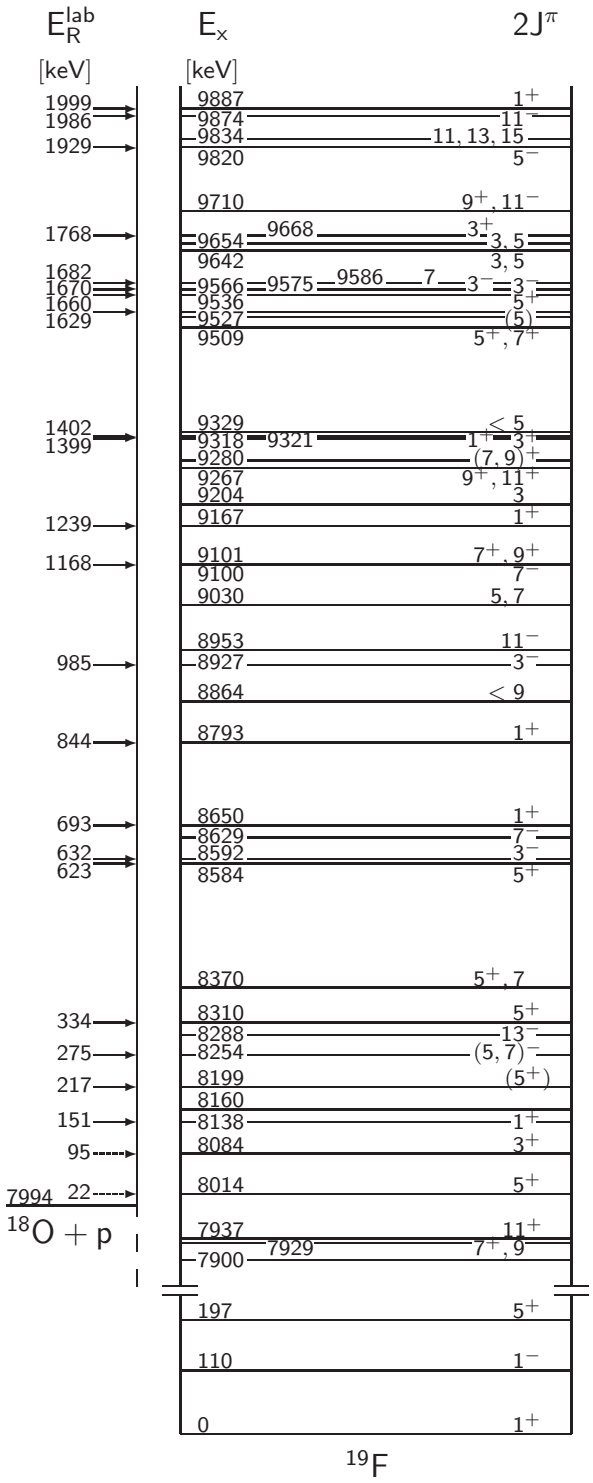

Figure 5.1: The ^{19}F level diagram and ^{18}O + p resonances [132, 133, 112, 120, 40, 118] through E_R = 1999 keV. The E_R = 95 keV resonance corresponds to the E_x = 8084 keV excited state. Dashed arrows indicate unobserved resonances and solid arrows indicate observed resonances with known γ-ray decays. The proton threshold, $Q_{p\gamma}$ = 7994 keV, was taken from Ref. [41].

5.2b). Consequently, based on the angular momentum coupling rules, the spin-parity and orbital angular momentum amount to $J^\pi = (3/2)^+$ and $\ell_p = 2$, respectively. An incorrect spin and parity of $J^\pi = (3/2)^-$ was assumed previously for this level in Ref. [135].

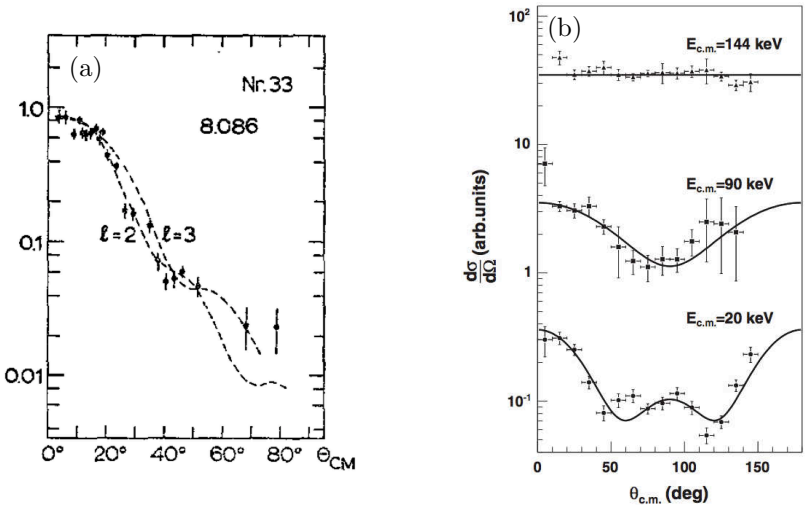

Figure 5.2: (a) From Ref. [134], the angular distribution of the ^{18}O(^{3}He,d)^{19}F reaction for the 8084 keV ^{19}F energy level (8.086 MeV). The fits shown are from distorted-wave Born approximation (DWBA) curves. (b) From Ref. [39], the angular distribution of the ^{18}O(p,α)^{15}N reaction for the E_R^{cm} = 20, 90, and 144 keV resonances. The fit of the 90 keV resonance gives a $\ell_\alpha = 1$ angular momentum for the exit channel.

Table 5.1: E_x = 8084 keV level parameters.

Parameter	Value (eV)	Reference
$\omega\gamma_{p\alpha}$	$1.6\times10^{-7}(5)$	[133]
$\omega\gamma_{p\gamma,UL}$	$\leq 4.0\times10^{-8}$	[120]
$\omega\gamma_{p\gamma,LL}$	$\geq 1.3\times10^{-11}$	present
Γ_γ	$6.0\times10^{-1}(25)$ [1]	[112]
Γ	$\leq 3.0\times10^{3}$ [2]	[133]

[1] Private communication from K. Allen quoted in Ref. [112].
[2] Total width determined from slope of front edge of thick-target yield curve.

The remainder of this chapter documents a new search for the E_R = 95 keV resonance in ^{18}O(p,γ)^{19}F with significantly improved sensitivity compared to previous studies, Refs. [112, 120]. New reaction rates are reported in Sec. 5.4.

Section 5.2: Measurement

From April to May 2011, an $^{18}O(p,\gamma)^{19}F$ study was conducted at the Laboratory for Experimental Nuclear Astrophysics (LENA) with high-intensity proton beam from the lab's ECR ion source. In order to search for the $E_R = 95$ keV resonance, 80 C of charge was accumulated *on-resonance* at a bombarding energy of $E_p = 105$ keV, and 40 C were accumulated *off-resonance* at $E_p = 85$ keV. The average beam current on target amounted to $I_p = 754$ μA during the on-resonance portion of the experiment and $I_p = 695$ μA during the off-resonance phase. Tab. 4.2 shows additional target details. Yield curves collected with the LENA 1 MV JN Van de Graaff are shown in Fig. 4.7.

Gates were constructed in JAM [116] to produce $\gamma\gamma$-coincidence spectra, uncover the γ-ray decay fingerprint of the resonance, and reduce background contributions. Note that the second excited state in the ^{19}F nucleus, 197 keV, has a $\tau_m = 128.8 \pm 1.5$ ns lifetime [40], and narrow TDC gates were not used during data analysis. In Fig. 5.3, the on-resonance (ungated) singles HPGe spectrum is shown in blue and the coincidence gated spectrum is in red from $E_\gamma = 85-575$ keV. For the latter spectrum, only events in the HPGe detector that are coincident with events in the NaI(Tl) counter of energy 4.25 MeV $\leq E_\gamma^{NaI(Tl)} \leq 10.0$ MeV are accepted. It can be seen in Fig. 5.3 that this condition suppresses the environmental background by two orders of magnitude. The prominent peak in the figure is the 511 keV background associated with e^+e^--annihilation. Most ^{19}F levels decay by $\gamma\gamma$-cascades through the first (110 keV) excited state, and all ^{19}F levels (with known decay schemes) deexcite through the second (197 keV) excited state. In Fig. 5.3, vertical dashed lines indicate anticipated locations of the γ-rays originating from the deexcitation of the first excited state (110 keV) and second excited state (197 keV). Note that because of their low energy, the 110 keV photons would be attenuated significantly. No peaks were observed for these two secondary decays. In fact, although a considerably improved detection sensitivity compared to previous studies (by about half an order of magnitude; see below) was achieved, no γ-rays from the decay of the $E_R = 95$ keV resonance were observed in any of the singles or coincidence spectra. This means that the strength of this resonance is much smaller than previously thought. Comparisons between the on-resonance and off-resonance coincidence data confirm this assertion.

Section 5.3: Analysis

Since no direct observation of the $^{18}O(p,\gamma)^{19}F$ resonance was made, complex analysis steps were taken to constrain the resonance strength and place an upper limit on the direct capture astrophysical S-factor. These constraints were made on coincidence spectra collected at 0°, and the f_γ correction played an important role in this analysis (see Sec. 3.5.2 and Eqs. 3.13, 3.14, and 3.15).

5.3.1: Resonant Capture

An improved upper limit on the resonance strength of the unobserved $E_R = 95$ keV resonance was determined relative to the strength of the well-known resonance at $E_R = 151$ keV. The resonance strength is given by Refs. [136, 4]:

$$\omega\gamma = \frac{2\epsilon_{eff}}{\lambda^2}\frac{N_{\max}}{N_p B_\gamma \eta \mathrm{W}} \tag{5.1}$$

where ϵ_{eff} is the effective stopping power at the resonance energy as defined in Eq. (4.4); λ is the de Broglie wavelength, where [4]:

$$\frac{\lambda^2}{2} = \frac{4.125 \times 10^{-18}}{\mu E_R^{\mathrm{cm}}}\ (\mathrm{cm}^2); \tag{5.2}$$

$N_{\max}$ is the total number of detected γ-rays if the target is considered infinitely thick; N_p is the number of incident protons:

$$N_p = \frac{Q}{e} \tag{5.3}$$

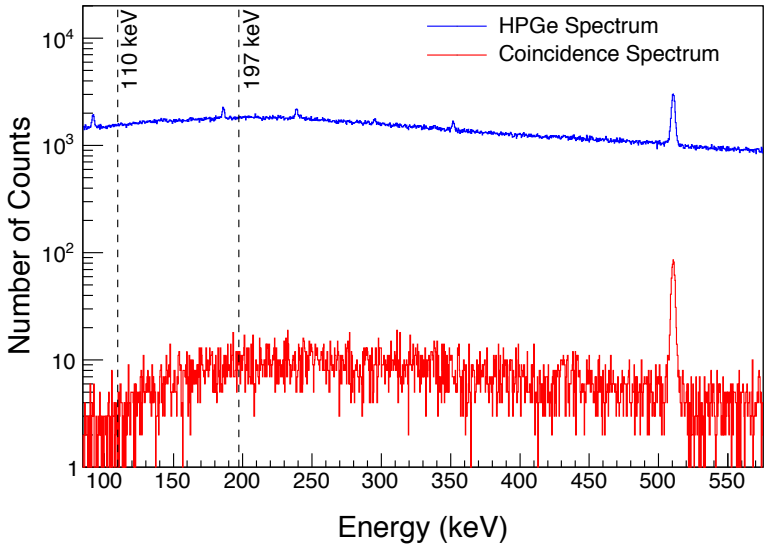

Figure 5.3: Measured HPGe singles spectrum (blue) and $\gamma\gamma$-coincidence spectrum (red) from the $^{18}O(p,\gamma)^{19}F$ study. Background reduction amounts to a factor of 100. The prominent background peak at 511 keV arises from the annihilation of pair-produced positrons. Dashed lines indicate the anticipated locations of the $1 \rightarrow 0$ (110 keV) and $2 \rightarrow 0$ (197 keV) transitions in ^{19}F. The spectra shown represent on-resonance data, with a total charge accumulation of 80 C at $E_p = 105$ keV. Based on these spectra, clearly a detection was not achieved and steps must be taken to constrain the (p,γ) strength upper limit.

where Q is the accumulated charge on target and e is the unit charge in Coulomb; B_γ is the branching ratio; η is the efficiency of the detector; W is the angular correlation. The ratio of resonance strengths is then [4]:

$$\frac{\omega\gamma_{95}}{\omega\gamma_{151}} = \left(\frac{\epsilon_{eff}N_{\max}}{\lambda^2 N_p B_\gamma \eta \mathrm{W}}\right)_{95} \times \left(\frac{\epsilon_{eff}N_{\max}}{\lambda^2 N_p B_\gamma \eta \mathrm{W}}\right)^{-1}_{151}. \tag{5.4}$$

In this equation, the resonance strength, $\omega\gamma_{151} = (9.7 \pm 0.5)\times10^{-4}$ eV [4], comes from the weighted mean of the resonance strengths reported in Refs. [112, 119, 120]. All ^{19}F levels decay through the second excited state ($2 \rightarrow 0$), and the possibility that the 8084 keV level decays with a substantial primary ground state branch was also included in the analysis. Therefore, the following expression was used to estimate an upper limit for the number of ^{19}F compound nuclei produced [115, 4]:

$$\left(\frac{N_{\max}}{B_\gamma \eta \mathrm{W}}\right)_{95} = \frac{N_{R0}}{\eta_{R0}^{Ge,P}} + \frac{N_{20}}{\eta_{20}^{Ge,P} f_\gamma} \tag{5.5}$$

where N_{R0} is the upper limit on the intensity of the ground state transition in the singles HPGe spectrum; N_{20} is the upper limit on the intensity of the decay from the ^{19}F second excited state to the ground state ($2 \rightarrow 0$; see Fig. 5.1) in the coincidence-gated HPGe spectrum; $\eta_{R0}^{Ge,P}$ is the HPGe peak efficiency for the ground state transition; $\eta_{20}^{Ge,P}$ is the HPGe peak efficiency of the $2 \rightarrow 0$ transition; f_γ is a $\gamma\gamma$-coincidence correction factor that depends on the γ-ray decay scheme and the coincidence gate selected.

To calculate the correction factor, f_γ, a GEANT4 simulation was run that, for a given energy level, used known branching ratios to predict the total number of detected γ-rays arising from the $2 \rightarrow 0$ transition for a variety of coincidence gates. The new experimental upper limit was extracted by requiring a rectangular energy gate of 4.25 MeV $\leq \mathrm{E}_\gamma^{NaI(Tl)} \leq$ 10.0 MeV in the two-dimensional NaI(Tl) vs. HPGe coincidence energy spectrum. The simulated coincidence histograms could then be sorted with the same energy gates and conditions that were used to analyze the experimental data. The correction factor, f_γ, was calculated by solving Eq. 3.16 for the $2\rightarrow0$ transition. This procedure was tested at the $\mathrm{E_R}$ = 151 keV resonance, where the simulated intensities agreed with the experimental values within uncertainty (4% for the $2\rightarrow0$ decay in a rectangular coincidence spectrum).

The $\mathrm{E_R}$ = 95 keV resonance has no known decay scheme. Therefore, the decays that are known for all other ^{19}F states were analyzed. The results were then used to estimate the possible decays of the $\mathrm{E_R}$ = 95 keV resonance. This procedure relies on statistical analysis and is reasonable, considering the lack of information regarding this resonance. The f_γ correction factor was calculated, according to the procedure described above, for all bound and unbound ^{19}F levels with known decay schemes [40]. A reasonable average from the ensemble of values was adopted. The statistical analysis was restricted to levels with $J < 9/2$

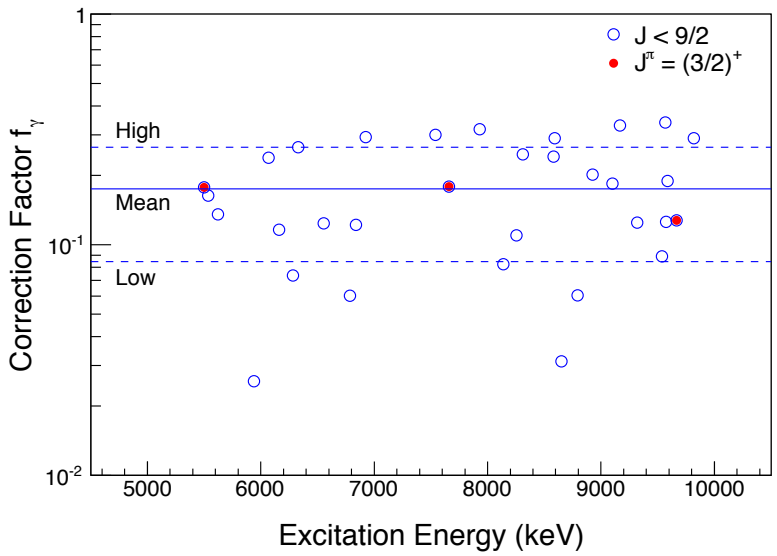

Figure 5.4: The $\gamma\gamma$-coincidence correction factors (f_γ) for all ^{19}F energy levels with $J < 9/2$ (open blue circles) and $E_x \geq 5500$ keV; levels with high ground state decay modes were excluded. Additionally, correction factors for levels with $J^\pi = (3/2)^+$ are indicated by solid red circles. These correction factors were estimated with GEANT4 simulations that were gated with the 4.25 MeV $\leq E_\gamma^{NaI(Tl)} \leq$ 10.0 MeV condition. The mean f_γ value for the entire distribution, $f_\gamma = 0.17 \pm 0.09$, is represented by the solid blue line. The two dashed blue lines represent the uncertainty (in this instance, the standard deviation).

(open blue circles in Fig. 5.4) and $E_x \geq 5500$ keV. The constraint on the spin was chosen to associate the calculated mean f_γ value with low-spin states, while the energy threshold was set so that the f_γ values were associated with complex γ-ray decay routes to the ^{19}F second excited state. As an additional constraint, no level with a ground state branching ratio that exceeded the total probability of emission to the ^{19}F second excited state was included in the analysis. This final constraint was added because the ground state decay mode is already included in the strength upper limit calculation—see Eq. 5.5. Results of this analysis for a 4.25 MeV $\leq E_\gamma^{NaI(Tl)} \leq$ 10.0 MeV gate are shown in Fig. 5.4. An average value of $f_\gamma = 0.17 \pm 0.09$ represents a reasonable $\gamma\gamma$-coincidence correction factor estimate for the $E_R = 95$ keV resonance. The quoted uncertainty of the mean correction factor is the standard deviation of the distribution. In Fig. 5.4, the $J^\pi = (3/2)^+$ levels (levels with the same spin and parity as the $E_R = 95$ keV resonance level) are indicated with solid red circles. The $J^\pi = (3/2)^+$ levels agree with the mean value.

The peak intensity upper limit for the 2→0 transition (197 keV) was obtained from the HPGe coincidence spectrum using the Bayesian statistical approach outlined in Ref. [137]. According to this method, conditional, non-informative posterior probability density functions (PDFs) were generated for each energy

region, and peak intensity upper limits were calculated. The conditional PDF is assembled so that

$$p(n|s) = e^{-(s+b)} \frac{(s+b)^n}{n!} \tag{5.6}$$

where s is the unknown number of signal events, b is the number of background events, and n is the total number of events. A non-informative prior PDF is constructed so that

$$\pi(s) \propto \frac{1}{(s+b)^m}, \ s \geq 0, \ 0 \leq m \leq 1 \tag{5.7}$$

where $m = 0.5$ leads to a versatile choice for the prior that provides reasonable mean coverage for the confidence interval and upper limit. Next, a conditional, non-informative posterior PDF is constructed where

$$h(s|m) = \frac{(s+b)^{n-m} e^{-(s+b)}}{\Gamma(n-m+1, b)} \tag{5.8}$$

where Γ(n−m+1,b) is an incomplete gamma function defined as

$$\Gamma(x, b) = \int_b^\infty s^{x-1} e^{-s} ds, \ x > 0, \ b > 0. \tag{5.9}$$

A separate conditional PDF that includes background uncertainty can be assembled so that

$$q(n|s) = \int_0^\infty p(n|s)_{b'} f_{b'}(b, \sigma_b) db' \tag{5.10}$$

where $f_{b'}(b, \sigma_b)$ is the background component and $p(n|s)_{b'}$ is the conditional PDF in Eq. 5.6. The final posterior is

$$h(s|n) = \frac{q(n|s)_b \pi(s)}{\int_0^\infty q(n|s)_b \pi(s) ds}. \tag{5.11}$$

The upper limit on the unobserved 197 keV coincidence peak intensity can be found by solving

$$1 - \alpha = \int_0^{S_{UP}} h(s|n) ds \tag{5.12}$$

where S_{UP} is the upper limit and $1 - \alpha$ is the confidence level. A code written in R by R. Longland was used to calculate the $E_x = 197$ keV peak intensity upper limit from the on-resonance, 4.25 MeV $\leq E_\gamma^{NaI(Tl)} \leq$ 10.0 MeV coincidence spectrum. This code reads in spectra and solves Eq. 5.12 for the peak intensity upper limit. Modifications were made to the original code to randomly sample the background bounding the region of interest [108].

Armed with intensity upper limit PDFs, the $E_R = 95$ keV resonance strength upper limit was determined by generating normally distributed probability density functions for all of the other quantities that entered into the resonance strength calculation—Eqs. (5.2−5.5). All probability density functions were then randomly sampled (see the description of Monte Carlo analysis in Appendix A.1), and this process produced a resonance strength probability density function that was then integrated to the 90% confidence level (see Fig. 5.5). Figure 5.5 shows a truncated probability distribution for the resonance strength calculated with the Monte Carlo analysis code. The intensity upper limit, from the Bayesian statistical analysis discussed above, produces a truncated intensity PDF (emphasizing the point that there was no detection), and this structure propagates through the analysis to the resonance strength PDF [89]. A new resonance strength upper limit of

$$\omega\gamma_{95} \;\leq\; 7.8 \times 10^{-9} \text{ eV (90\% CL)} \tag{5.13}$$

was obtained for the $E_R = 95$ keV resonance in the $^{18}O(p,\gamma)^{19}F$ reaction. This new upper limit improves upon the upper limit presented in Ref. [120] by about a factor of 5.

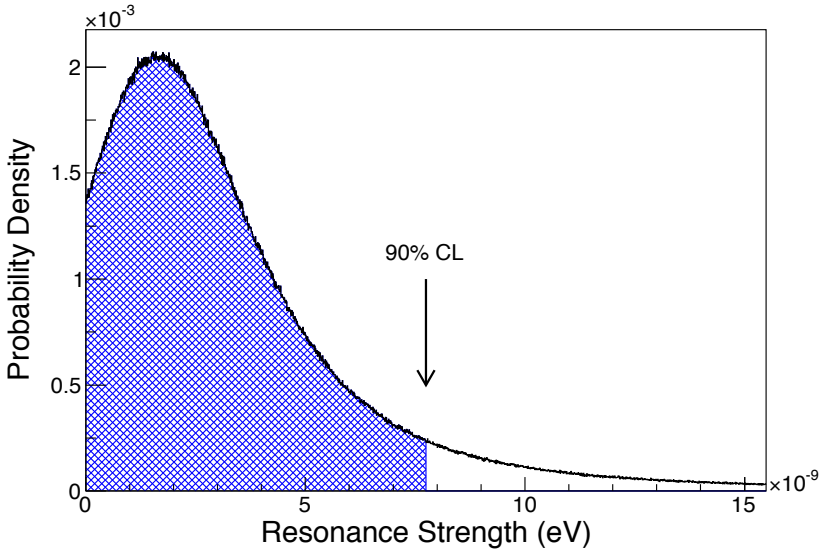

Figure 5.5: The resonance strength probability density function generated by solving repeatedly the resonance strength equation and populating a histogram. Normal distributions were constructed for each value that entered into the strength calculation; these distributions were then randomly sampled. The histogram created was then integrated to the 90% confidence level, and a new upper limit of $\omega\gamma \leq 7.8\times10^{-9}$ eV was extracted.

5.3.2: Direct Capture

Data collected during this study at $E_p = 105$ keV are also important for obtaining improved estimates for the direct capture cross section of $^{18}O(p,\gamma)^{19}F$. The experimental $^{18}O(p,\gamma)^{19}F$ direct capture cross section at $E_p = 1850$ keV was measured previously by Ref. [112].

While the second excited state transition f_γ estimation explained in Sec. 5.3.1 relied upon a statistical argument, this assumption was not necessary to determine the direct capture coincidence correction factor, f_γ^{DC}, because branching ratios can be estimated. These branching ratios must first be determined in order to calculate f_γ^{DC} with GEANT4 [102, 103] (see Sec. 5.3.1). To calculate the branching ratios, the experimental cross section was extrapolated to $E_p = 105$ keV for all direct capture transitions observed in Ref. [112]. Two different direct capture codes were used; the code TEDCA [138] was used to compute the direct capture cross section for a zero scattering potential. The bound state and scattering state potential parameters used were adopted from Ref. [85]. The code DIRCAP [85] was utilized to perform the same calculation with a hard-sphere scattering potential. The calculated cross sections (from $E_p^{cm} = 0.03-1.99$ MeV) were normalized to the measured direct capture cross sections at $E_p = 1850$ keV [112].

Though no direct capture transitions were observed in the singles or coincidence spectra populated at $E_p = 105$ keV, the spectra are more sensitive than any previous measurements. It is interesting to compare the measured upper limit values with direct capture model calculations. An experimental upper limit on the total direct capture cross section was obtained from [4]:

$$Y = \frac{N_{20}}{N_p \eta^{Ge,P} f_\gamma^{DC}} = \frac{1}{\epsilon_{eff}} \int_{E_p^{cm}-\Delta E}^{E_p^{cm}} \sigma_{DC}(E)\, dE \tag{5.14}$$

where Y is the measured yield upper limit; N_{20} is the intensity upper limit of the $2 \rightarrow 0$ transition from the Bayesian treatment discussed in Sec. 5.3.1; $\eta^{Ge,P}$ is the experimental HPGe peak efficiency; $\sigma_{DC}(E)$ is the direct capture cross section. This expression assumes that the effective stopping power is approximately constant over the target thickness, because the target was relatively thin. The cross section can be rewritten in terms of the astrophysical S-factor with Eq. 2.17. It was assumed that the S-factor was nearly constant over the target thickness because the non-resonant direct capture S-factor varies very slowly with energy. With these conditions, the yield equation can be integrated numerically to extract $\sigma(E)$ or $S(E)$. This set of calculations was performed for the same $\gamma\gamma$-coincidence gate used in Sec. 5.3.1. For the total experimental astrophysical S-factor, an upper limit of

$$S_{DC}(105) \leq 8.1 \text{ keV b (90\% CL)}, \tag{5.15}$$

corresponding to a direct capture cross section upper limit of

$$\sigma_{DC}(105) \;\leq\; 1.8 \text{ pb (90\% CL)}. \tag{5.16}$$

Note that these values are nearly independent (within 2%) of the direct capture code used to calculate the branching ratios at $E_p = 105$ keV.

The experimental total S-factor upper limit (90% CL) at $E_p = 105$ keV is shown in Fig. 5.6, along with the values corresponding to the 95% and 99% confidence levels. The black solid curve represents the total S-factor reported by Ref. [112], while the red and blue solid lines were calculated in the present work using the codes TEDCA [138] and DIRCAP [85], respectively. The latter two were normalized to the previously measured direct capture cross section at $E_p = 1850$ keV [112]. At $E_p = 105$ keV, the measured upper limits are smaller than the prediction of Ref. [112] by about a factor of 2. The DIRCAP S-factor (blue line) was only marginally consistent with the experimental upper limit (90% CL) while the extrapolation derived from the code TEDCA (red line) fell within the 90% confidence level. Previous reaction rates used the Wiescher *et al.* (1980) [112] direct capture S-factor which is off by a factor of 2 at $E_p = 105$ keV.

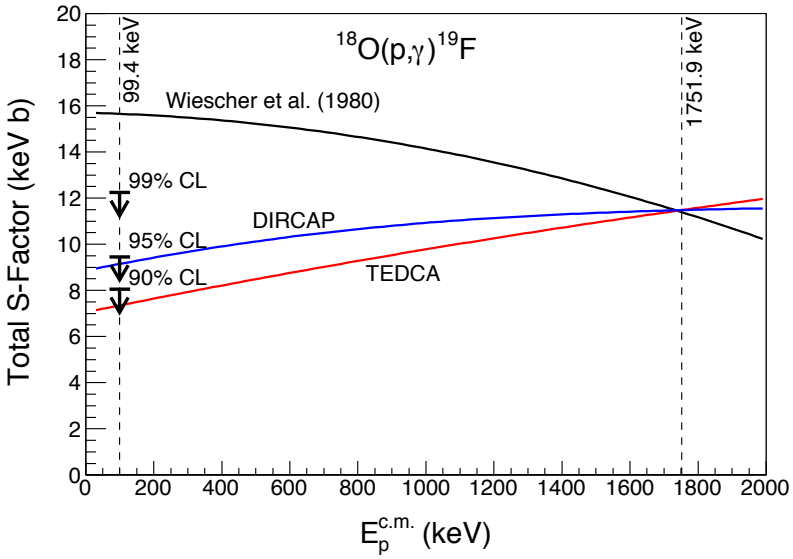

Figure 5.6: The total direct capture S-factor for ^{18}O(p,γ)^{19}F. The solid lines represent direct capture model calculations: (black) Ref. [112]; (blue) using the code DIRCAP [85]; (red) using the code TEDCA [138]; the latter two results are normalized to the measured direct capture cross section at $E_p = 1850$ keV [112]. The measured upper limits (90%, 95%, 99% confidence levels) at $E_p^{cm} = 99.4$ keV ($E_p = 105$ keV) are displayed as three black arrows.

Section 5.4: Reaction Rates

Thermonuclear reaction rates for ^{18}O(p,γ)^{19}F were calculated with the Monte Carlo method of Ref. [88] (see Sec. 2.2). In the Monte Carlo calculation, the nuclear physics input from Ref. [139] was adopted, except for the E_R = 95 keV resonance strength, the total direct capture S-factor, the separation energy [41], and the resonance energies.

Based on Ref. [85], the TEDCA extrapolation of the total direct capture S-factor, normalized at E_p = 1850 keV [112], was used. For bombarding energies below E_p^{cm} = 2.0 MeV, the adopted total S-factor was expanded around E = 0, with the result:

$$\begin{aligned} S(E) &\approx S(0) + \dot{S}(0)E + \frac{1}{2}\ddot{S}(0)E^2 \\ &= 7.06 + 2.98\times10^{-3}E - 2.60\times10^{-7}E^2 \text{ (keV b)}, \end{aligned} \tag{5.17}$$

where E is the center-of-mass energy. At low energies, the new direct capture S-factor is significantly smaller than the result reported in Ref. [112]. Note that the $\dot{S}(0)$ coefficient presented in Ref. [112] was reported incorrectly and should in fact be $\dot{S}(0) = -0.34\times10^{-3}$ b [140]. This correction is already applied to the black line in Fig. 5.6.

In the present work, an improved upper limit of the E_R = 95 keV resonance strength is reported, $\omega\gamma \leq 7.8\times10^{-9}$ eV (90% CL). For this particular ^{19}F level, a lower limit on the resonance strength can be estimated based on the available resonance properties (see Tab. 5.1). The ratio of resonance strengths in the (p,γ) and (p,α) channels, according to Eq. (2.36), is given by:

$$\frac{\omega\gamma_{p\gamma}}{\omega\gamma_{p\alpha}} = \frac{\Gamma_\gamma}{\Gamma_\alpha}. \tag{5.18}$$

The (p,α) strength was measured by Ref. [133], with the result $\omega\gamma_{p\alpha} = (1.6 \pm 0.5)\times10^{-7}$ eV. An upper limit for the total width of $\Gamma < 3\times10^3$ eV was obtained from the slope of the low-energy edge of the thick-target yield curve [133], implying an upper limit of $\Gamma_\alpha < 3\times10^3$ eV for the α-particle partial width. Finally, a value of $\Gamma_\gamma = (6.0 \pm 2.5)\times10^{-1}$ eV was reported for the γ-ray partial width in Ref. [112]. With these input values and their associated uncertainties, from Eq. 5.18, a *lower limit* on the (p,γ) strength of $\omega\gamma_{p\gamma} \geq 1.3\times10^{-11}$ eV was calculated.

Since both an upper and a lower limit on the strength were calculated, a recommended value and a factor

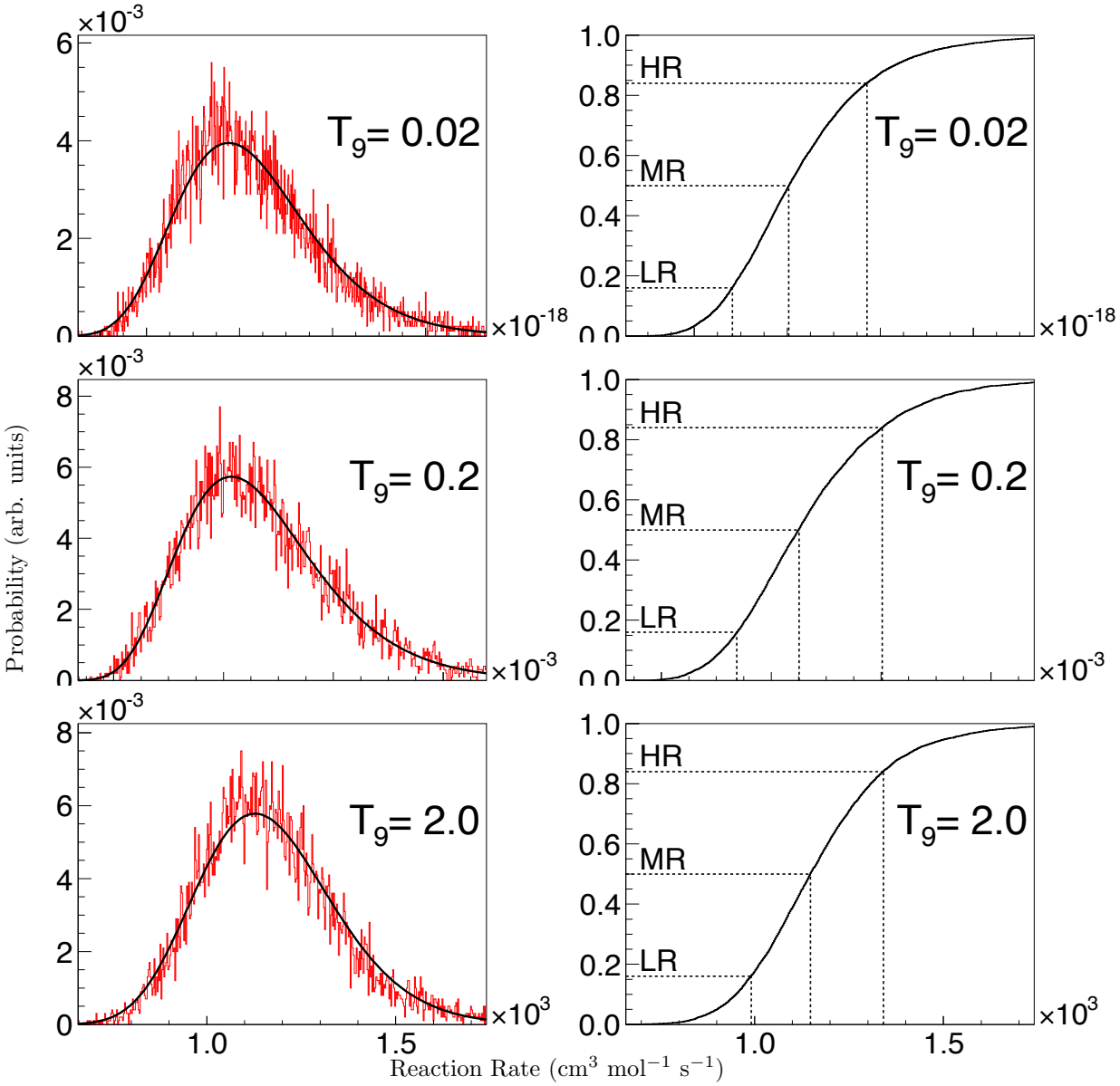

Figure 5.7: (Left) the reaction rate probability density functions (red) for ^{18}O(p,γ)^{19}F at 0.02 GK, 0.2 GK, and 2.0 GK populated with the RatesMC Monte Carlo code [88]. The lognormal approximations are overlaid in black. (Right) The corresponding cumulative probability functions used to define the low, median, and high rates as 0.16, 0.5, and 0.84 quantiles, respectively. These histograms were generated with a 10,000-sample calculation.

uncertainty were estimated using the following equations [88]:

$$\omega\gamma = \sqrt{\omega\gamma_{LL} \times \omega\gamma_{UL}} = 3.2 \times 10^{-10} \text{ eV}, \tag{5.19}$$

$$f.u. = \sqrt{\frac{\omega\gamma_{UL}}{\omega\gamma_{LL}}} = 25. \tag{5.20}$$

The Monte Carlo reaction rate code, RatesMC [88], was used to calculate the rate contribution of the E_R = 95 keV resonance strength by randomly sampling a lognormal distribution constructed from the mean value and factor uncertainty (see Sec. 2.2.1).

The new low, median, and high $^{18}O(p,\gamma)^{19}F$ reaction rates (corresponding to 0.16, 0.50, and 0.84 quantiles, respectively, of the cumulative reaction rate distribution) are tabulated in Tab. 5.2 over a stellar plasma temperature range of 0.01−10.00 GK. Reaction rate probability density functions at a few sample temperatures (0.02, 0.2, 2.0 GK) are displayed as red histograms in Fig. 5.7 (left panel), with the lognormal approximations shown as black solid lines. On the right, the corresponding cumulative probability functions are shown with the dashed lines indicating the low, median, and high rates. It can be seen that a lognormal function approximates the actual Monte Carlo distribution well.

Figure 5.8 compares the new reaction rate with the one published by Ref. [139]. The new (solid lines) and previous (dotted lines) high and low rates are normalized to the previous recommended rate [139]. Note that the previous rates contained two small mistakes: (1) an erroneous assignment of $J^\pi = (3/2)^-$, and (2) the incorrectly reported value of $\dot{S}(0) = 0.34\times10^{-3}$ b from Ref. [112]. The dashed vertical line at 50 MK indicates the location of the temperature region at which, according to Ref. [10], cool bottom processing can occur in AGB stars. The vertical dashed line at 5.5 GK represents the stellar temperature beyond which the rates must be found with the aid of Hauser-Feshbach calculations. This cutoff is necessary because in many reactions, there is an energy upper limit beyond which no more measurements can be made. This is due to high level densities beyond this energy threshold. This threshold was computed based on the methodology outlined by Ref. [141]. Reaction rates above 5.5 GK were matched to theoretical rates from BRUSLIB [142]. The matched rates are included in Tab 5.2. The lognormal-μ and -σ for each reaction rate probability density function are also listed; Anderson-Darling statistics, A−D, are included in the table and represent the agreement between the PDF generated by the Monte Carlo and a lognormal probability density function with the listed lognormal-μ and -σ [88].

The difference in Fig. 5.8 between new and previous rates at temperatures below 50 MK can be explained by the lower estimates both for the contributions from direct capture and the resonance at E_R = 95 keV. Since the new rates are smaller at cool bottom processing threshold temperatures compared to the previous results, it is even less likely that the $^{18}O(p,\gamma)^{19}F$ reaction contributes significantly to the depletion of ^{18}O

observed in stellar atmospheres and presolar grain samples. The slight increase in the rate near 50 MK is dependent upon the calculated E_R = 95 keV strength upper limit and can not account for observed ^{18}O depletions. The difference at temperatures in excess of 5 GK is caused solely by the treatment of the direct capture contribution: the S-factor expansion was cut off artificially at E_p^{cm} = 1.0 MeV in previous work [112, 139], while in the present work the S-factor is calculated up to energies of E_p^{cm} = 2.0 MeV (Fig. 5.6), resulting in a much higher cutoff value and a significantly increased direct capture contribution. In Fig. 5.9, the new rate (solid black line) is plotted alongside the old rate (dashed black line); the low, median, and high rates normalized separately to the median rate. The new (solid black line) high rate uncertainty increases by as much as 5% at cool bottom processing temperatures. In this case, the new recommended value and factor uncertainty in Eq. 5.19 were used to calculate the E_R = 95 keV rate contribution analytically—Eq. 2.35. In this work, the new upper limit (and thus an analytical solution for the E_R = 95 keV rate contribution) is adopted instead of performing the numerical calculation—Eq. 2.8—from Ref. [135] for the E_R = 95 keV resonance rate contribution.

The fractional contributions to the total $^{18}O(p,\gamma)^{19}F$ reaction rates are shown in Fig. 5.10. These contributions were calculated during the RatesMC rate calculation. During a reaction rate Monte Carlo calculation, a contribution from a single resonant or non-resonant reaction is divided by the total contribution

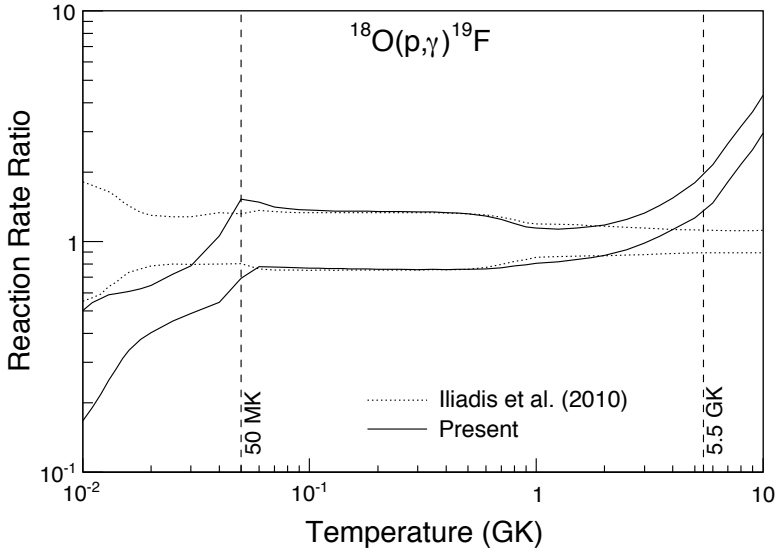

Figure 5.8: The present (solid lines) and previous [139] (dotted lines) high and low reaction rates, normalized to the recommended previous rates. The vertical dashed line at 50 MK represents the plasma temperature of circulated material during cool bottom processing in low-mass AGB stars according to Ref. [10]. The vertical dashed line at 5.5 GK represents the temperature at which the experimental rates need to be extrapolated with the aid of BRUSLIB Hauser-Feshbach results [142].

(the sum of all contributions). Each fractional rate populates a probability density function until the Monte Carlo calculation finishes (in this case, after 10,000 samples). The low (0.16 quantile), median (0.5 quantile), and high (0.84 quantile) fractions are then calculated for each of these PDFs. The colored bands in Fig. 5.10 represent the region bounded by the low and high fractional rate. The labels in this figure are the center-of-mass energies of the resonances and the direct capture contribution ("A-Rate 1"). The dotted black line is the sum of fractional rates that contribute less than 15% to the total rate. In Fig. 5.10, it can be seen that the lower estimate for the direct capture process (yellow solid line) contributes significantly (>10%) at temperatures of 0.011−0.05 GK. The high estimate for the $E_R = 95$ keV resonance (maroon solid line) contributes as much as 45%. This means the present work reduced the importance of the unobserved resonance to less than 50% of the total reaction rate. If a direct measurement is made, the $E_R = 95$ keV resonance will not increase the rate enough to effect cool bottom processing in low-mass AGB stars.

The ratio of $^{18}O(p,\alpha)^{15}N$ (from Ref. [143]) and $^{18}O(p,\gamma)^{19}F$ high and low rates is shown in Fig. 5.11. The dotted lines are based on the results of Ref. [143] alone, while the solid lines incorporate the new $^{18}O(p,\gamma)^{19}F$ rates. This figure does not account for correlations between the (p,α) and (p,γ) rates—the ratio is calculated but disregards the relationship between the nuclear physics input to both rate calculations. For the temperature region relevant to cool bottom processing, the established (p,α) rate [143] exceeds the (p,γ) rate by a factor of 5100−1700 over the temperature range 0.03−0.05 GK. The improved $E_R = 95$ keV

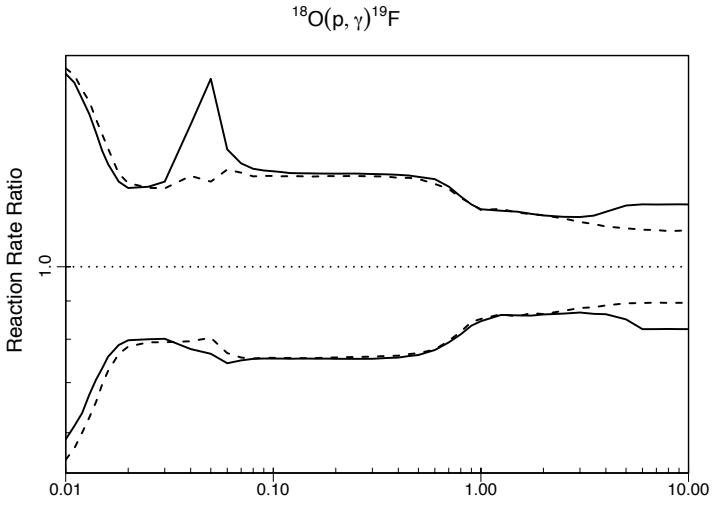

Figure 5.9: The reaction rate from this work (solid line) is compared to the rate from the 2010 reaction rate compilation, Ref. [143]. The uncertainty in the rate increases by as much as 5% at cool bottom processing temperatures. The difference comes from how the two rates are calculated; the new reaction rate includes an analytic calculation (Eq. 2.35) of the rate contribution from $E_R = 95$ keV (with the results of this work) while Ref. [135] calculated this contribution numerically (Eq. 2.8).

resonance strength upper limit and the refined direct capture S-factor support the conclusion that the (p,γ) reaction does not contribute significantly to the overall ^{18}O destruction at temperatures suggested for cool bottom processing to occur in low-mass AGB stars. Therefore, future efforts to study ^{18}O depletion by cool bottom processing in asymptotic giant branch stars should focus on direct measurement of the ^{18}O$(p,\alpha)^{15}$N reaction at low energies.

Table 5.2: Experimental Monte Carlo-based ^{18}O$(p,\gamma)^{19}$F reaction rates (in units of cm^{3}mol^{-1}s^{-1}). For T $\geq$ 5.5 GK, rates were matched to BRUSLIB Hauser-Feshbach results [142] according to the procedure described in Ref. [141]. The lognormal-μ and -σ for the reaction rate probability density functions are also tabulated. The Anderson-Darling, A−D, statistics are shown [88].

T (GK)	Low Rate	Median Rate	High Rate	Lognormal μ	Lognormal σ	A−D
1.000×10^{-02}	2.923×10^{-24}	4.967×10^{-24}	8.785×10^{-24}	$-5.363\times10^{+01}$	5.487×10^{-01}	$7.333\times10^{+00}$
1.100×10^{-02}	2.581×10^{-23}	4.222×10^{-23}	7.344×10^{-23}	$-5.149\times10^{+01}$	5.179×10^{-01}	$1.118\times10^{+01}$
1.200×10^{-02}	1.719×10^{-22}	2.676×10^{-22}	4.468×10^{-22}	$-4.964\times10^{+01}$	4.784×10^{-01}	$1.634\times10^{+01}$
1.300×10^{-02}	9.299×10^{-22}	1.370×10^{-21}	2.181×10^{-21}	$-4.800\times10^{+01}$	4.284×10^{-01}	$2.330\times10^{+01}$
1.400×10^{-02}	4.223×10^{-21}	5.973×10^{-21}	8.985×10^{-21}	$-4.653\times10^{+01}$	3.832×10^{-01}	$2.600\times10^{+01}$
1.500×10^{-02}	1.709×10^{-20}	2.321×10^{-20}	3.309×10^{-20}	$-4.519\times10^{+01}$	3.395×10^{-01}	$2.099\times10^{+01}$
1.600×10^{-02}	6.180×10^{-20}	8.151×10^{-20}	1.113×10^{-19}	$-4.393\times10^{+01}$	3.014×10^{-01}	$1.471\times10^{+01}$
1.800×10^{-02}	6.283×10^{-19}	8.027×10^{-19}	1.041×10^{-18}	$-4.166\times10^{+01}$	2.542×10^{-01}	$6.808\times10^{+00}$
2.000×10^{-02}	4.820×10^{-18}	6.045×10^{-18}	7.721×10^{-18}	$-3.964\times10^{+01}$	2.403×10^{-01}	$6.734\times10^{+00}$

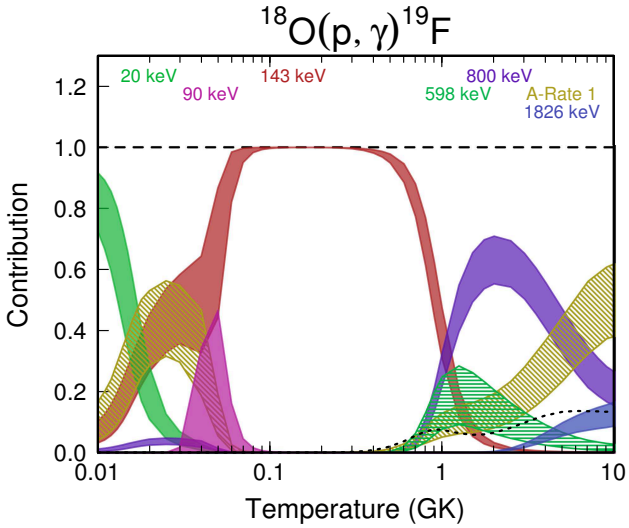

Figure 5.10: The fractional contribution of non-resonant and resonant reactions. The colored bands represent the region bounded by the low and high fractional rate. The high bound on the E_R = 95 keV resonance contribution is as much as 45%. This work reduced the importance of the unobserved resonance to less than 50% of the total rate and excludes the possibility that the resonance will increase the rate enough to effect cool bottom processing. The center-of-mass energies of the resonances are shown. "A-Rate 1" refers to the direct capture contribution to the rate. The contribution shown as a dotted black line is the sum of fractional reaction rates that contribute less than 15% to the total rate.

Table 5.2 – continued

T (GK)	Low Rate	Median Rate	High Rate	Lognormal μ	Lognormal σ	A−D
2.500×10^{-02}	3.235×10^{-16}	4.041×10^{-16}	5.168×10^{-16}	$-3.543\times10^{+01}$	2.441×10^{-01}	$1.467\times10^{+01}$
3.000×10^{-02}	8.728×10^{-15}	1.093×10^{-14}	1.402×10^{-14}	$-3.212\times10^{+01}$	3.294×10^{-01}	$2.409\times10^{+02}$
4.000×10^{-02}	1.206×10^{-12}	1.555×10^{-12}	2.340×10^{-12}	$-2.701\times10^{+01}$	7.516×10^{-01}	$1.057\times10^{+03}$
5.000×10^{-02}	9.349×10^{-11}	1.227×10^{-10}	2.056×10^{-10}	$-2.259\times10^{+01}$	8.583×10^{-01}	$1.066\times10^{+03}$
6.000×10^{-02}	9.553×10^{-09}	1.274×10^{-08}	1.818×10^{-08}	$-1.809\times10^{+01}$	5.776×10^{-01}	$5.999\times10^{+02}$
7.000×10^{-02}	3.573×10^{-07}	4.764×10^{-07}	6.503×10^{-07}	$-1.452\times10^{+01}$	4.144×10^{-01}	$2.160\times10^{+02}$
8.000×10^{-02}	5.495×10^{-06}	7.304×10^{-06}	9.891×10^{-06}	$-1.181\times10^{+01}$	3.462×10^{-01}	$5.981\times10^{+01}$
9.000×10^{-02}	4.553×10^{-05}	6.049×10^{-05}	8.137×10^{-05}	$-9.706\times10^{+00}$	3.179×10^{-01}	$1.740\times10^{+01}$
1.000×10^{-01}	2.437×10^{-04}	3.239×10^{-04}	4.347×10^{-04}	$-8.031\times10^{+00}$	3.053×10^{-01}	$6.392\times10^{+00}$
1.100×10^{-01}	9.505×10^{-04}	1.263×10^{-03}	1.692×10^{-03}	$-6.673\times10^{+00}$	2.992×10^{-01}	$2.813\times10^{+00}$
1.200×10^{-01}	2.921×10^{-03}	3.880×10^{-03}	5.191×10^{-03}	$-5.551\times10^{+00}$	2.958×10^{-01}	$1.391\times10^{+00}$
1.300×10^{-01}	7.484×10^{-03}	9.946×10^{-03}	1.330×10^{-02}	$-4.610\times10^{+00}$	2.938×10^{-01}	8.234×10^{-01}
1.400×10^{-01}	1.663×10^{-02}	2.211×10^{-02}	2.957×10^{-02}	$-3.812\times10^{+00}$	2.926×10^{-01}	5.508×10^{-01}
1.500×10^{-01}	3.300×10^{-02}	4.386×10^{-02}	5.867×10^{-02}	$-3.127\times10^{+00}$	2.918×10^{-01}	4.284×10^{-01}
1.600×10^{-01}	5.970×10^{-02}	7.942×10^{-02}	1.062×10^{-01}	$-2.533\times10^{+00}$	2.912×10^{-01}	3.574×10^{-01}
1.800×10^{-01}	1.581×10^{-01}	2.102×10^{-01}	2.814×10^{-01}	$-1.560\times10^{+00}$	2.905×10^{-01}	3.073×10^{-01}
2.000×10^{-01}	3.388×10^{-01}	4.507×10^{-01}	6.033×10^{-01}	-7.970×10^{-01}	2.901×10^{-01}	2.947×10^{-01}
2.500×10^{-01}	$1.274\times10^{+00}$	$1.694\times10^{+00}$	$2.266\times10^{+00}$	5.265×10^{-01}	2.894×10^{-01}	2.872×10^{-01}
3.000×10^{-01}	$2.932\times10^{+00}$	$3.903\times10^{+00}$	$5.212\times10^{+00}$	$1.360\times10^{+00}$	2.886×10^{-01}	2.796×10^{-01}
3.500×10^{-01}	$5.153\times10^{+00}$	$6.853\times10^{+00}$	$9.134\times10^{+00}$	$1.923\times10^{+00}$	2.874×10^{-01}	2.714×10^{-01}
4.000×10^{-01}	$7.695\times10^{+00}$	$1.020\times10^{+01}$	$1.360\times10^{+01}$	$2.322\times10^{+00}$	2.855×10^{-01}	2.688×10^{-01}
4.500×10^{-01}	$1.037\times10^{+01}$	$1.370\times10^{+01}$	$1.819\times10^{+01}$	$2.616\times10^{+00}$	2.826×10^{-01}	2.732×10^{-01}
5.000×10^{-01}	$1.303\times10^{+01}$	$1.715\times10^{+01}$	$2.269\times10^{+01}$	$2.842\times10^{+00}$	2.786×10^{-01}	2.909×10^{-01}
6.000×10^{-01}	$1.841\times10^{+01}$	$2.387\times10^{+01}$	$3.123\times10^{+01}$	$3.175\times10^{+00}$	2.657×10^{-01}	3.858×10^{-01}
7.000×10^{-01}	$2.464\times10^{+01}$	$3.121\times10^{+01}$	$3.988\times10^{+01}$	$3.445\times10^{+00}$	2.431×10^{-01}	7.541×10^{-01}
8.000×10^{-01}	$3.356\times10^{+01}$	$4.137\times10^{+01}$	$5.129\times10^{+01}$	$3.727\times10^{+00}$	2.144×10^{-01}	$1.303\times10^{+00}$
9.000×10^{-01}	$4.759\times10^{+01}$	$5.709\times10^{+01}$	$6.938\times10^{+01}$	$4.050\times10^{+00}$	1.906×10^{-01}	$3.356\times10^{+00}$
$1.000\times10^{+00}$	$6.916\times10^{+01}$	$8.167\times10^{+01}$	$9.819\times10^{+01}$	$4.412\times10^{+00}$	1.787×10^{-01}	$1.133\times10^{+01}$
$1.250\times10^{+00}$	$1.719\times10^{+02}$	$2.000\times10^{+02}$	$2.380\times10^{+02}$	$5.312\times10^{+00}$	1.732×10^{-01}	$3.372\times10^{+01}$
$1.500\times10^{+00}$	$3.630\times10^{+02}$	$4.213\times10^{+02}$	$4.975\times10^{+02}$	$6.053\times10^{+00}$	1.683×10^{-01}	$2.349\times10^{+01}$
$1.750\times10^{+00}$	$6.403\times10^{+02}$	$7.430\times10^{+02}$	$8.726\times10^{+02}$	$6.619\times10^{+00}$	1.631×10^{-01}	$1.335\times10^{+01}$
$2.000\times10^{+00}$	$9.921\times10^{+02}$	$1.149\times10^{+03}$	$1.342\times10^{+03}$	$7.053\times10^{+00}$	1.580×10^{-01}	$8.269\times10^{+00}$
$2.500\times10^{+00}$	$1.842\times10^{+03}$	$2.129\times10^{+03}$	$2.487\times10^{+03}$	$7.668\times10^{+00}$	1.519×10^{-01}	$4.135\times10^{+00}$
$3.000\times10^{+00}$	$2.798\times10^{+03}$	$3.230\times10^{+03}$	$3.769\times10^{+03}$	$8.086\times10^{+00}$	1.529×10^{-01}	$7.123\times10^{+00}$
$3.500\times10^{+00}$	$3.777\times10^{+03}$	$4.369\times10^{+03}$	$5.130\times10^{+03}$	$8.389\times10^{+00}$	1.550×10^{-01}	$1.054\times10^{+01}$
$4.000\times10^{+00}$	$4.758\times10^{+03}$	$5.507\times10^{+03}$	$6.507\times10^{+03}$	$8.625\times10^{+00}$	1.632×10^{-01}	$2.026\times10^{+01}$
$5.000\times10^{+00}$	$6.600\times10^{+03}$	$7.729\times10^{+03}$	$9.353\times10^{+03}$	$8.968\times10^{+00}$	1.796×10^{-01}	$2.771\times10^{+01}$
$6.000\times10^{+00}$	$8.727\times10^{+03}$	$1.056\times10^{+04}$	$1.277\times10^{+04}$	$9.265\times10^{+00}$	1.903×10^{-01}	–
$7.000\times10^{+00}$	$1.167\times10^{+04}$	$1.411\times10^{+04}$	$1.707\times10^{+04}$	$9.555\times10^{+00}$	1.903×10^{-01}	–
$8.000\times10^{+00}$	$1.452\times10^{+04}$	$1.757\times10^{+04}$	$2.125\times10^{+04}$	$9.774\times10^{+00}$	1.903×10^{-01}	–
$9.000\times10^{+00}$	$1.718\times10^{+04}$	$2.078\times10^{+04}$	$2.514\times10^{+04}$	$9.942\times10^{+00}$	1.903×10^{-01}	–
$1.000\times10^{+01}$	$2.032\times10^{+04}$	$2.458\times10^{+04}$	$2.974\times10^{+04}$	$1.011\times10^{+01}$	1.903×10^{-01}	–

The unobserved ^{18}O(p,γ)^{19}F resonance, E_R = 95 keV, was studied at LENA with high-intensity ECR ion source beam and a $\gamma\gamma$-coincidence detector configuration. With these tools, data were collected at E_p = 105 keV (on-resonance) and E_p = 85 keV (off-resonance). The upper limit on the E_R = 95 keV resonance was constrained further to $\omega\gamma_{95} \leq 7.8\times10^{-9}$ eV (90% CL)—a factor of 5 improvement over the result from

Ref. [120]. A new upper limit was also calculated for the direct capture astrophysical S-factor that was a factor of 2 lower than the result from Ref. [112]. From the literature [39, 134], it was found that the parity of the $E_R = 95$ keV resonance level had been reported incorrectly in Ref. [135]. Also, $\dot{S}(0)$ from Ref. [112] was found to have been reported with the incorrect sign.

The new reaction rates determined in this work were published in Buckner *et al.* (2012) [1]. From these rates, it was determined that the $^{18}O(p,\gamma)^{19}F$ resonance, $E_R = 95$ keV, can not account for ^{18}O depletion during cool bottom processing in low-mass asymptotic giant branch stars.

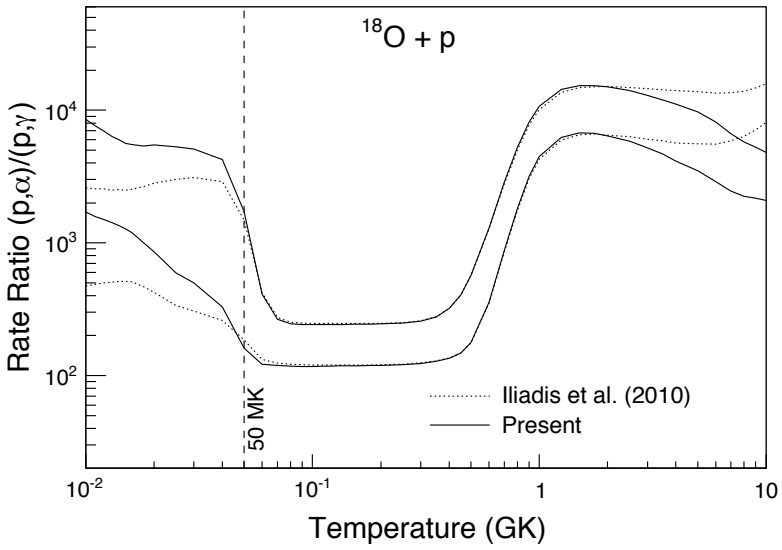

Figure 5.11: The ratios between (p,α) low and high reaction rates from Ref. [139] and the present (p,γ) high and low reaction rates, respectively (solid black lines). The corresponding ratios based solely on the previous rates [139] are shown as dotted lines. The vertical dashed line at 50 MK represents the plasma temperature of circulated material during cool bottom processing in low-mass AGB stars according to Ref. [10]. It should be noted that correlations between the (p,α) and (p,γ) rates are not taken into account.

CHAPTER 6: ^{17}O(p,γ)^{18}F DIRECT CAPTURE

Section 6.1: Previous Experiments

Over the past several decades, numerous experiments were performed dedicated to studying ^{17}O(p,γ)^{18}F direct capture. Table 6.1 summarizes these experiments and they are described below. Careful examination of this table reveals the narrative that unfolded in the literature over the past forty years. The study performed by Ref. [77] presented an astrophysical S-factor that disagreed dramatically with future observations made by other groups; while Ref. [77] observed a constant S-factor, others noticed a distinct energy dependence. Fox *et al.* (2005) [75] asserted, and then verified, that this energy dependence is influenced by the tails of broad resonances, specifically the E_R^{cm} = 556 keV and 676 keV resonances. The model calculations presented in Ref. [75] verified this hypothesis and experimental data accumulated by numerous groups over the past decade supported this conclusion.

One of the first, recent studies of the ^{17}O(p,γ)^{18}F reaction was performed at LENA by Fox *et al.* (2004) [51]. They were able to tune I_p = 100 μA beam from the LENA 1 MV JN Van de Graaff accelerator to target. With targets enriched to 83.8 atom % in ^{17}O, they made the first observation of the E_R = 193.2 ± 0.9 keV resonance and provided the first strength reported in the literature for this resonance, $\omega\gamma$ = 1.2 ± 0.2 μeV.

Chafa *et al.* (2005) [76] probed ^{17}O and ^{18}O targets implanted in 0.3 mm tantalum sheets for the ^{17}O(p,γ)^{18}F reaction near 194.1 keV (lab). They used activation techniques by placing targets bombarded for ≈ 5 hours with I_p = 70 μA proton beam between two germanium detectors. Beam was supplied by the PAPAP electrostatic accelerator at the CSNSM Laboratory (Orsay). Reference [144] arrived at a E_R = 193 keV resonance strength of $\omega\gamma$ = 2.2 ± 0.4 μeV. The strength was reported originally as $\omega\gamma$ = 3.4 ± 0.6 μeV in Ref. [76], but after accounting for a coincident summing correction, the strength was revised in Ref. [145].

A more recent study at LENA was performed by Newton *et al.* (2010) [78] with the 1 MV JN Van de Graaff accelerator. They used a 55° detector configuration (with respect to the beam) and the LENA 140% (updated recently to 135% [101]) HPGe detector. With 91.2 atom % enriched ^{17}O targets and I_p = 120 μA, they arrived at a direct capture S-factor of $S_{DC}(0)$ = 4.6 ± 1.1 keV b. Reaction rates calculated during this study indicated that the direct capture rate dominates the total reaction rate at classical nova temperatures.

An experiment was performed in inverse kinematics—^{1}H(^{17}O,^{18}F)γ—on the DRAGON recoil separator

at ISAC at TRIUMF in Vancouver, Canada by Hager *et al.* (2012) [79]. A hydrogen gas target at 7 Torr ± 3% was used, and ^{17}O beam was supplied by the Supernanogan ECR ion source (I^{max} = 1.5×10^{12} particles/second). A 30 BGO (bismuth germanate) detector array was set up, and a direct capture astrophysical S-factor of $S_{DC}(0)$ = 5.3 ± 0.8 keV b was calculated from their total S-factor by the Notre Dame group, Ref. [81].

At Notre Dame, Kontos *et al.* (2012) [81] studied the ^{17}O(p,γ)^{18}F reaction from E_p = 600−1800 keV using their 4 MV KN Van de Graaff accelerator and E_p = 365−700 keV using their 1 MV JN Van de Graaff accelerator. They manually rastered (by steering the beamspot back and forth across the target) their H^+ beam at currents between 20−40 μA at the target. Their targets were anodized with water enriched in ^{17}O to 90.1 atom %. Reference [81] arrived at a direct capture astrophysical S-factor of $S_{DC}(0)$ = 4.9 ± 1.1 keV b.

The Laboratory for Underground Nuclear Astrophysics (LUNA) at Laboratori Nazionali del Gran Sasso [80] performed an underground experiment with both activation and prompt γ-ray measurements. They used the LUNA 400 kV accelerator and achieved 200 μA H^+ beam at the target. Their targets were enriched in 66 atom % ^{17}O and 4 atom % ^{18}O. The LUNA detector array consisted of a 115 % HPGe detector in a 55° configuration. Their initial claim in the Scott *et al* (2012) [80] publication was a E_R = 193 keV resonance strength of $\omega\gamma$ = 1.70 ± 0.14 μeV with the addition of one new primary transition (Fox *et al.* [75] only observed two transitions) from prompt γ-ray measurements. Activation techniques gave LUNA a strength of $\omega\gamma$ = 1.65 ± 0.13 μeV. They reconciled their results to $\omega\gamma$ = 1.67 ± 0.12 μeV and calculated a direct capture S-factor of $S_{DC}(0)$ = 4.4 ± 0.4 keV b. Di Leva *et al.* (2014) [82] reiterates most of the previous LUNA results but reports a total S-factor of S(0) = 4.8 ± 0.4 keV b. They also claim that they observe nine E_R = 193 keV resonance primary transitions.

The total S-factors from the literature are plotted in Fig. 6.1. In the figure, the grey, cross-hatched energy region (E_p^{cm} = 103−261 keV) is the classical nova Gamow window. The LUNA total S-factors are plotted in blue. Note that their lowest energy data points come from the activation portion of their analysis. A summary of previous experiments can be found in Tab. 6.1.

Section 6.2: Measurement

For the ^{17}O(p,γ)^{18}F direct capture study presented in this thesis, the experiment was performed at LENA, a "sea-level" accelerator facility. Underground experiments dramatically reduce cosmic-ray induced environmental backgrounds; however, the Laboratory for Experimental Nuclear Astrophysics has the tools to perform these studies above ground (see Sec. 3). High current, low-energy accelerators and $\gamma\gamma$-coincidence

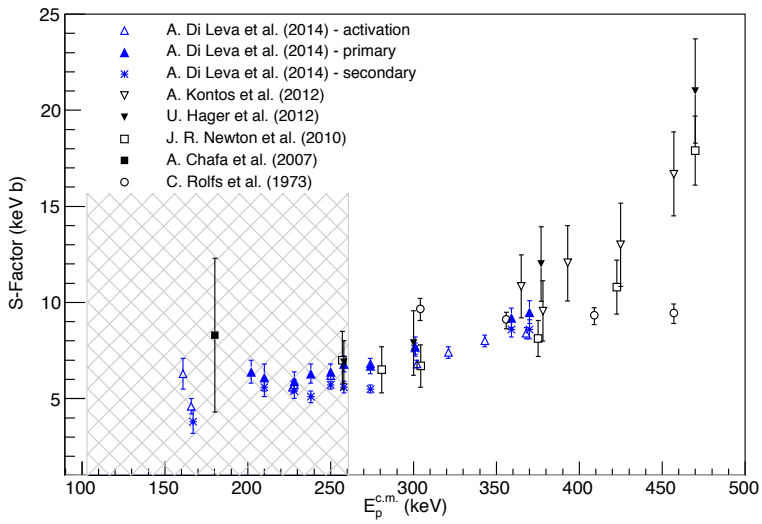

Figure 6.1: Total S-factors from the literature. The classical nova Gamow window is highlighted by the grey, cross-hatched energy region (E_p^{cm} = 103−261 keV). Contributions made by LUNA are in blue; a combination of prompt γ-ray and activation measurements. Note that their lowest energy data points are activation measurements. See Table 6.1 for more details on previous S-factor measurements.

techniques allow the γ-cascade of interest to be isolated and studied and environmental backgrounds to be reduced. Additionally, a novel spectral analysis method was developed (see Sec. 6.3).

The ^{17}O(p,γ)^{18}F experiment was performed between March and August 2013 at the Laboratory for

Table 6.1: Previous ^{17}O(p,γ)^{18}F measurements from the literature. Previous approaches include in-beam, activation, and inverse kinematics measurements. Activation studies were performed by several research groups. It is important to note the beam energy ranges probed (the classical nova Gamow window is 103−261 keV) and the beam currents available to these different research groups.

Reference	Facility	Accelerator	E_p (keV)	I_p (μA)
[77][1]	University Toronto	1 MV JN Van de Graaff	270−440	120
	McMaster University	3MV JN Van de Graaff	880−1780	150−200
[75][1]	LENA−TUNL	1 MV JN Van de Graaff	180−540	100
[76][2]	CSNSM Orsay	Electrostatic PAPAP	$<$ 250	$\approx$ 70
[78][1]	LENA−TUNL	1 MV JN Van de Graaff	275−500	75
[79][3]	TRIUMF	DRAGON	260−505	—
[81][1]	NSL−Univ. Notre Dame	1 MV JN Van de Graaff	365−700	20−40
		4 MV JN Van de Graaff	600−1800	20−40
[80][1,2]	LUNA−Gran Sasso	400 kV LUNA II	212−392	200
[82][1,2]	LUNA−Gran Sasso	400 kV LUNA II	169−392	200

[1] prompt γ-ray
[2] activation
[3] inverse kinematics

Experimental Nuclear Astrophysics. The experiment was split into two parts: the higher energy portion and the lower energy portion. Beam was supplied by the 1 MV JN Van de Graaff accelerator during the higher energy portion. Target thickness and longevity were monitored with the JN Van de Graaff by collecting ^{17}O(p,γ)^{18}F yield curves at the E_R = 518.3 ± 1.2 keV resonance (see Sec. 4.3). See Tab. 6.2 for laboratory energies, beam current range, charge accumulation, and live time. The beam energies, E_p = 250, 275, 300 and 325 keV, were selected to overlap with the Newton *et al.* (2010) [78] study and to avoid the strong ^{19}F(p,$\alpha\gamma$)^{16}O resonance at E_R = 340 keV [123]. On-resonance data were collected with the ECR ion source at E_p = 200 keV for the E_R = 193 keV resonance with a total charge accumulation of Q = 14 C. The final two direct capture sets of data were also collected with high-intensity ECR ion source beam. The beam was rastered with the new rastering system (see Sec. 3.2). Major ion source upgrades responsible for the boost in ECR ion source H^+ current at the target are discussed in Sec. 3.1.2. JN Van de Graaff accelerator issues, discussed in Sec. 4.3, lead to ^{17}O targets being monitored with the ECR ion source during this phase of the experiment. Target thickness and degradation were assessed with the well-known ^{18}O(p,γ)^{19}F resonance E_R = 150.82 ± 0.09 keV [118]. See Tab. 6.2 for bombarding energies, ECR ion source currents at the target, accumulated charge, and acquisition live time. The direct capture beam energies, E_p = 175 and 190 keV, were selected to avoid the ^{18}O(p,γ)^{19}F resonance at E_R = 151 keV and the ^{17}O(p,γ)^{18}F resonance at E_R = 193 keV.

Table 6.2: Laboratory bombarding energies, target beam currents, charge accumulation, and live time are listed in the top portion of this table for the sets of data collected with ECR ion source beam. Data were collected on-resonance for the E_R = 193 keV resonance at E_p = 200 keV. The same parameters are tabulated in the bottom portion for the sets of data collected with H^+ beam from the JN Van de Graaff.

E_p (keV)	I_p^{min} (μA)	I_p^{mean} (μA)	I_p^{max} (μA)	T^{live} (hrs)	Q (C)
175	809	1186	2047	23	100
190	789	1125	1851	13	54
200	796	1030	1360	4	14
250	46	85	116	49	15
275	28	53	64	53	10
300	66	78	86	18	5
325	42	67	80	12	3

The ^{18}F level diagram in Fig. 6.2 shows all of the known energy levels and their associated spins and parities. The γ-ray transitions and intensities observed and attributed to ^{18}F deexcitations for each direct capture laboratory energy are listed in Tab. 6.3. Both the HPGe singles intensities (including the muon veto condition) and the $\gamma\gamma$-coincidence intensities are tabulated; these intensities were determined with a code written specifically for extracting net areas from ROOT histograms (see Appendix A.3). Spectra with peak

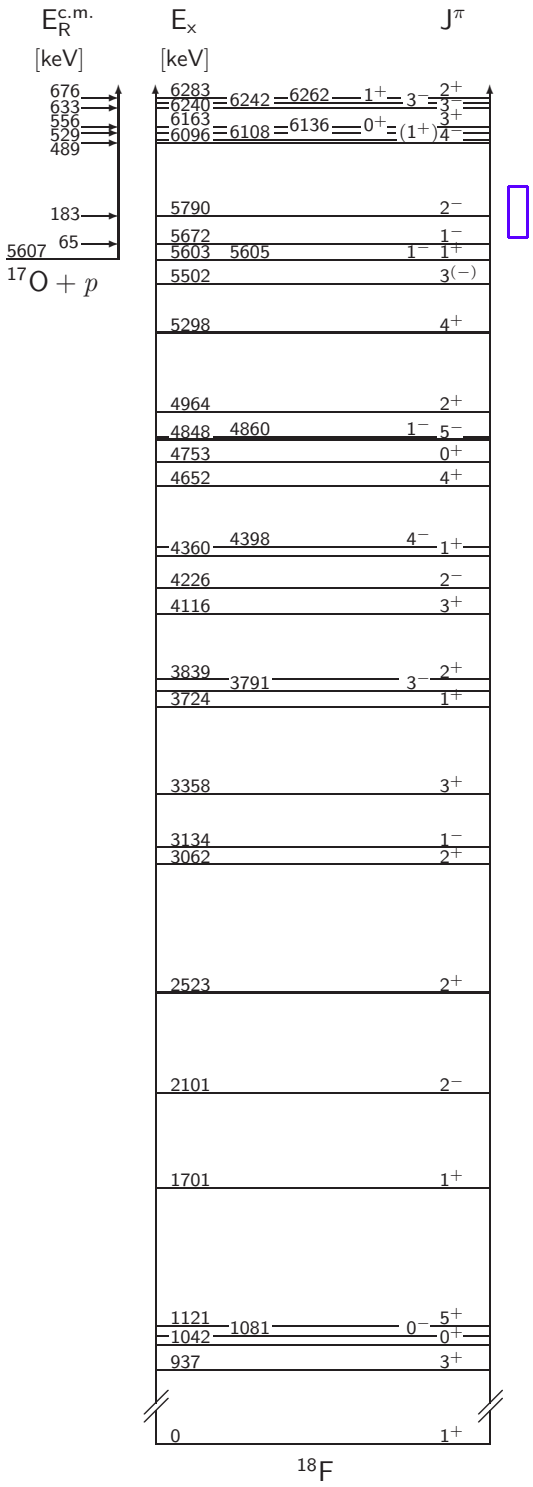

Figure 6.2: Truncated ^{18}F level diagram and ^{17}O + p resonances [40, 144] through E_R^{cm} = 676 keV. The proton threshold, $Q_{p\gamma}$ = 5607 keV, was taken from Ref. [41]. The classical nova Gamow window is shown right of the diagram in blue.

labels can be found in Appendix E along with a table of observed environmental backgrounds.

Table 6.3: Intensities for the observed ^{18}F transitions in both the muon-vetoed HPGe singles spectrum and the gated coincidence spectrum (3.5 MeV $\leq E_\gamma^{Ge} + E_\gamma^{NaI(Tl)} \leq$ 9.0 MeV). The muon veto condition was also applied to the coincidence spectrum.

	Intensity (cts) by E_p (keV)					
Transition	175	190	250	275	300	325
HPGe Singles Intensities						
937→0	1300(200)	1120(190)	4100(200)	5000(200)	4720(140)	5370(120)
1042→0	–	–	–	–	–	470(110)
1081→0	–	–	–	–	–	290(90)
1121→937	–	–	–	–	–	–
2101→0	–	–	–	–	–	–
2101→937	–	–	–	–	–	–
2523→0	–	–	–	–	–	100(30)
3062→0	–	41(16)	180(20)	210(20)	220(20)	210(20)
3062→937	240(50)	730(60)	1040(80)	930(80)	740(70)	740(40)
3791→2101	–	–	–	180(60)	–	–
3839→0	–	–	120(16)	160(20)	160(20)	220(20)
3839→937	–	–	–	51(17)	41(15)	63(14)
3839→3062	–	–	–	–	380(130)	610(120)
4116→3062	–	–	480(180)	–	380(100)	–
4652→1121	–	–	–	–	61(14)	54(14)
4964→0	–	30(10)	94(15)	148(17)	160(20)	144(13)
R/DC→0	49(12)	25(7)	124(18)	170(19)	142(18)	410(30)
R/DC→937	93(16)	112(14)	450(30)	550(30)	540(20)	590(40)
R/DC→1121	–	23(8)	132(18)	210(20)	180(30)	210(30)
R/DC→2523	–	–	–	90(20)	116(19)	–
R/DC→3062	–	–	180(30)	170(40)	190(30)	150(20)
R/DC→3791	–	–	–	–	–	111(12)
R/DC→3839	–	110(40)	–	340(110)	410(80)	400(70)
R/DC→4116	–	–	–	–	350(40)	160(50)
R/DC→4652	–	–	–	–	–	–
R/DC→4964	–	–	–	–	–	–
$\gamma\gamma$-Coincidence Intensities						
937→0	420(30)	470(30)	1770(50)	2310(50)	2180(50)	2610(50)
1042→0	–	31(10)	–	91(17)	42(15)	82(18)
1081→0	–	–	–	–	–	–
1121→937	–	–	119(19)	120(20)	110(20)	200(20)
2101→0	–	–	–	–	63(14)	–
2101→937	–	–	–	–	–	36(12)
2523→0	–	–	51(13)	–	72(16)	54(14)
3062→0	–	48(13	146(18)	155(17)	165(18)	172(18)
3062→937	82(14)	97(14)	310(20)	390(20)	390(30)	410(20)
3791→2101	–	–	–	44(12)	51(15)	53(16)
3839→0	–	–	85(13)	126(16)	94(17)	149(19)
3839→937	–	–	–	46(12)	34(12)	53(11)
3839→3062	70(30)	50(14)	210(20)	250(30)	250(20)	250(30)
4116→3062	46(12)	49(12)	140(20)	210(20)	184(19)	226(19)
4652→1121	–	–	–	–	44(12)	–
4964→0	–	–	59(11)	87(13)	124(15)	94(11)

Table 6.3 – continued

Transition	Intensity (cts) by E_p (keV) 175	190	250	275	300	325
R/DC→0	–	–	–	–	–	–
R/DC→937	43(11)	64(10)	260(20)	310(20)	314(18)	350(30)
R/DC→1121	–	–	80(14)	108(17)	94(19)	130(20)
R/DC→2523	–	–	–	70(18)	90(16)	49(16)
R/DC→3062	–	–	100(20)	110(20)	140(20)	96(17)
R/DC→3791	–	–	–	64(16)	47(13)	59(7)
R/DC→3839	59(12)	41(10)	160(20)	200(20)	240(20)	260(20)
R/DC→4116	36(11)	–	100(20)	80(20)	39(12)	119(18)
R/DC→4652	–	–	–	–	73(19)	–
R/DC→4964	–	–	130(20)	130(30)	50(13)	–

Section 6.3: Analysis

Previous direct capture studies were performed at 55° [129, 78] because at this angle, angular correlation effects are suppressed—$P_2[\cos(55°)] = 0$. During this experiment, ultra-pure tantalum targets were used in a carbon-free target chamber to reduce beam-induced backgrounds (see Sec. 4). The $\gamma\gamma$-coincidence spectrometer was used to isolate the direct capture γ-cascade and reduce environmental background contributions to the analyzed spectra (see Sec. 3.5.2). Utilizing coincidence requires that the experiment be performed at 0°, and as a result, angular correlations can not be neglected. Sensitivity calculations were performed and are documented in Appendix C to assess what ^{18}F transitions would produce anisotropic angular correlations. These anisotropies were finally built into the GEANT4 [102, 103] analysis and are discussed here in Sec. 6.3.6.

A novel spectral analysis technique was developed and implemented to extract partial and total reaction numbers from HPGe singles and coincidence spectra. This analysis method relies on ROOT's *TFractionFitter* class. A C++ code, *solver.cxx*, was written that accepts data sorted into singles or coincidence histograms with ROOT. Environmental backgrounds (experimental), beam-induced backgrounds (simulated), and in this case, ^{18}F deexcitations (simulated) were sorted into *template* histograms. The *TFractionFitter* class determines the fractional contribution of each template to the data histogram.

Section 6.3.1 introduces sorting experimental and simulated data with ROOT. Using the ^{56}Co$(\beta^+\nu_e)^{56}$Fe decay as an example, Sec. 6.3.2 introduces the derivation of total reaction numbers through the comparison of simulated and experimental spectra. Section 6.3.3 describes the *TFractionFitter* class in detail and provides an example calculation of the total number of ^{56}Co disintegrations. In Sec. 6.3.4, the analysis code, *solver.cxx* is introduced. In this section, ^{18}F deexcitation templates are simulations of individual ^{17}O$(p,\gamma)^{18}$F primaries (and the secondaries associated with each primary). The E_R = 193 and 518 keV resonances are used to test

the new analysis method before it is applied to direct capture data in Sec. 6.3.7.

6.3.1: Sorting Data with ROOT

The data analysis for this experiment started at the data acquisition stage. To streamline data analysis, data collected with JAM [116] had to be transferred from JAM user interface and event files into a format that could be analyzed with computer codes written in C++ and ROOT. To accomplish this, several lines were added to the JAM sort routine—a code written in JAVA that governs how signals from the data acquisition electronics are sorted into spectra (histograms). These extra lines of code in the sort routine fill a text file with ADC (analog-to-digital converter) and TDC (time-to-digital converter) intensities by channel number (see Sec. 3.5.4) from the $\gamma\gamma$-coincidence spectrometer—the HPGe detector, the NaI(Tl) annulus, and the scintillator paddles. Note that the fourth excited state in the ^{18}F nucleus, 1121 keV, has a $\tau_m = 234 \pm 10$ ns lifetime [40], and narrow TDC gates were not used during data analysis. JAM allows data to be sorted online and offline, and these text files can also be created online and offline if necessary. A new sort routine, *sort.cxx*, was written in C++ and ROOT to sort the data into spectra and store them as ROOT histograms. Detector energy calibrations were collected and stored each day data were collected, and these calibrations were applied to the new ROOT spectra. The ROOT spectra were also binned the same way JAM bins spectra—all spectra have 4,096 bins. The new spectra stored in ROOT files were compared to spectra created by JAM and the JAVA sort routine; because the binning and energy calibrations agreed, the ROOT sort routine reproduced the JAM spectra.

Additional functionality was added to *sort.cxx* so that GEANT4 simulations of γ-cascades in the LENA $\gamma\gamma$-spectrometer (also stored in ROOT files) could be sorted the same way experimental data were sorted. The gating logic applied to data to fill coincidence spectra could also be applied to the histograms produced by the Monte Carlo to simulate coincidence spectra. The GEANT4 simulations have no energy resolution, so the Monte Carlo spectra are convolved with a Gaussian function to match simulated spectra to experimental spectra. The *full width at half maximum* (FWHM) of a direct capture primary depends on the target thickness and will be affected by Doppler-broadening; as a result, a separate Gaussian function must be used to match simulated and measured direct capture primaries and their associated first and second escape peaks. The FWHM of an observed primary or secondary was determined with JAM, and then Gaussian-σ, the standard deviation, was calculated where [146]:

$$\text{FWHM} = 2\sigma\sqrt{2ln(2)}. \tag{6.1}$$

As an example, Fig. 6.3 shows the two resolution fits determined for the direct capture data at $E_p = 250$

keV. The red squares represent the standard deviation for direct capture primaries and the blue circles are the secondaries; they are plotted versus excitation energy. The red dashed line is the adopted fit used to convolve simulated direct capture primaries and the blue dashed line is the fit applied to all other simulated peaks (direct capture secondaries and beam-induced backgrounds). Linear resolution functions were also

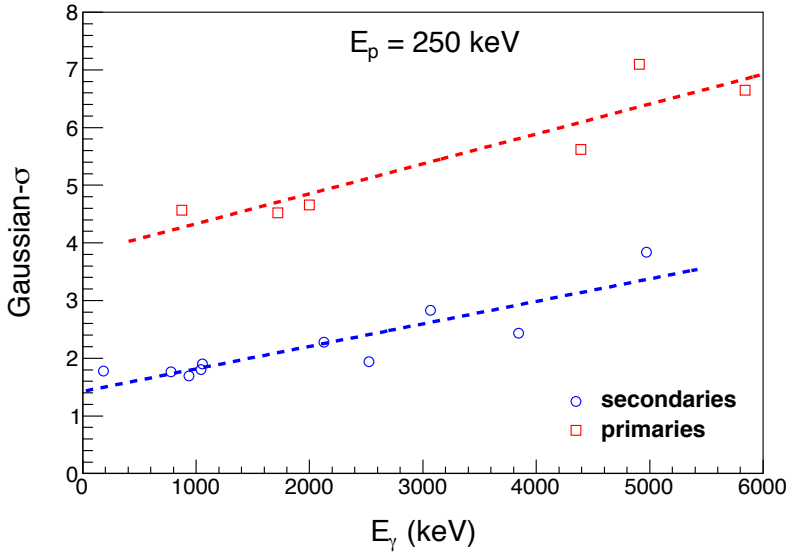

Figure 6.3: Separate resolution functions for E_p = 250 keV direct capture primaries (red dashed line) and secondaries (blue dashed line) were applied to convolve simulated spectra. The full width at half maximum was determined with JAM for each primary and secondary, and Gaussian-σ, the standard deviation, was calculated with Eq. 6.1. The standard deviation is plotted versus excitation energy for direct capture primaries (red squares) and secondaries (blue circles).

determined for each of the sixteen NaI(Tl) energy spectra. The ^{22}Na energy calibrations that were collected each day data were accumulated were summed and fit for each experimental data set. Simulated NaI(Tl) energy spectra were then convolved with these Gaussian functions.

The flowchart in Figure 6.4 summarizes the JAM to ROOT conversion and the steps taken to sort Monte Carlo histograms into simulated spectra.

6.3.2: Total Number of Reactions from Normalized Histograms

The next step in the analysis was to compare simulated radioactive source and beam-induced reactions with experimental data in order to calculate the number of disintegrations (reactions), N_{R}. A radioactive source, ^{56}Co, with an initial activity of A_i = 37,851 Bq and a current activity of A_f = 1461 Bq was placed within the target chamber (at atmosphere) against the surface of the target. The LENA $\gamma\gamma$-coincidence spectrometer was placed in the running geometry, and data were acquired for a live time of t_{live} = 7469

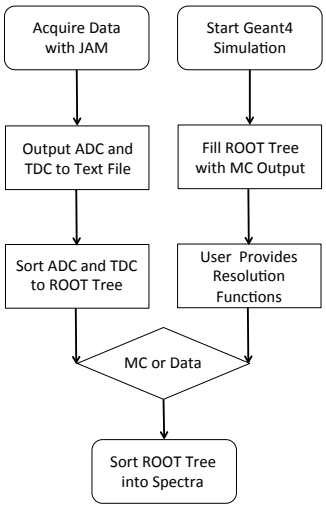

Figure 6.4: To analyze experimental data with ROOT and C++, ADC (analog-to-digital converter) and TDC (time-to-digital converter) intensities were sorted with the JAM data acquisition system but were also written to text files for analysis with ROOT. A new ROOT and C++ sort routine, *sort.cxx*, was written to sort ADC and TDC signals into spectra. Analogous logic was used to sort GEANT4 Monte Carlo histograms with *sort.cxx* to assemble simulated spectra.

seconds. The number of disintegrations was calculated from the activity with the equation:

$$N_{\mathrm{R}} = \mathrm{A}_f t_{\mathrm{live}} e^{-\frac{ln(2)t_{\mathrm{live}}}{t_h}} \tag{6.2}$$

where t_h is the half-life of ^{56}Co. From Ref. [147], $t_h = 77.31 \pm 19$ days for ^{56}Co. The number of disintegrations was found to be $N_{\mathrm{R}}(^{56}\mathrm{Co}) = (10.90 \pm 0.16)\times 10^6$.

Next, seventy-five million ^{56}Co disintegrations were simulated with GEANT4 and the Monte Carlo histogram was sorted into a HPGe singles spectrum. From Ref. [148], γ-ray and β-decay branching ratios were used in the simulation. The collected ^{56}Co experimental data and environmental background data were also sorted into HPGe singles spectra. Scalars collected during data acquisition (real time, pulser area, and the number of pulser gates) were used to calculate the live times for both experimental data sets. The background spectrum was then normalized to the ^{56}Co live time. After this step, the background singles spectrum was subtracted from the experimental ^{56}Co HPGe singles spectrum. Then the areas of the background subtracted ^{56}Co spectrum and the Monte Carlo singles spectrum were calculated between 800−1500 keV. These areas were used to normalize the Monte Carlo spectrum to the background subtracted ^{56}Co spectrum. Finally, the number of disintegrations was calculated from these areas and the simulated number

of disintegrations:

$$N_{\mathrm{R}}^{\mathrm{data}} = \frac{N_{\mathrm{R}}^{\mathrm{MC}} A^{\mathrm{sub}}}{A^{\mathrm{MC}}} \tag{6.3}$$

where $N_{\mathrm{R}}^{\mathrm{MC}}$ is the user specified number of Monte Carlo disintegrations, A^{sub} is the area (from 800−1500 keV in this case) of the background subtracted ^{56}Co singles spectrum, and A^{MC} is the area (from 800−1500 keV in this case) of the simulated ^{56}Co singles spectrum. This calculation yielded $N_{\mathrm{R}}(^{56}\mathrm{Co}) = (11.0 \pm 0.2)\times10^{6}$ disintegrations, and this result agrees well with the number of disintegrations calculated above from the source activity.

6.3.3: Total Number of Reactions from a *TFractionFitter* Code

A new code was written to test the ROOT class *TFractionFitter*. The idea was, that instead of background subtracting the experimental data, the *TFractionFitter* class could be used to determine what fraction of the data were contributions from the reaction of interest. The *TFractionFitter* class accepts a histogram that contains experimental data and then a user specified number of *template* histograms. These templates can be an environmental background spectrum, Monte Carlo simulations of beam-induced backgrounds that have been sorted into histograms, or a GEANT4 simulation of the reaction of interest that has also been sorted. For primary transitions, Doppler and recoil shifts affect the γ-ray energy emitted by a recoiling nucleus. The LENA GEANT4 simulation does not automatically include these effects; therefore, in addition to the decay scheme, the centroids of shifted primary transitions must be provided as input to the GEANT4 simulations; otherwise, the *TFractionFitter* class will not be able to match Monte Carlo templates to data histograms.

The *TFractionFitter* class relies on a standard likelihood fit using Poisson statistics. The template histograms are varied within statistics, and produce additional contributions to the overall likelihood. Many fit parameters are included in the analysis (one per bin per template), but an analytical approach to the minimization—with respect to these additional parameters—is favored instead of introducing them as formal fit parameters. The *TFractionFitter* routine calls the HMCMLL subroutine [149], and it is this subroutine that fits the data with this binned maximum likelihood approach. The HMCMLL subroutine uses MINUIT [150]—a numerical minimization code—to perform a log-likelihood fit and return the fraction with its associated uncertainty. The uncertainty from *TFractionFitter* takes both Monte Carlo and experimental statistical uncertainties into account. Two conditions are applied when comparing template histograms to an experimental data histogram with the *TFractionFitter* class to produce, according to Ref. [151], unbiased fit uncertainties: (1) the number of events in the template (or templates) must be sufficiently large enough that Poisson uncertainties can be ignored; and (2) template bin content exceeds the bin content of the experimental data histogram.

A code that calls *TFractionFitter* must read in a sorted data histogram as well as the template histograms. The templates are normalized to the data with the ratio $A^{\rm data}/A_i^{\rm temp}$ where $A^{\rm data}$ is a user specified area in the data histogram (from some low energy to some higher energy), and $A_i^{\rm temp}$ is the area of the same energy range in the i^{th} template histogram. The data histogram and the normalized template histograms are then passed to ROOT's *TFractionFitter* class. The energy range used to normalize the templates is also supplied to *TFractionFitter*—this range limits what bins will be assessed in each histogram. When the calculation is complete, the fractional contribution of each template histogram to the experimental data histogram is returned, where $V_i^{\rm temp}$ is the fractional contribution of the i^{th} template histogram—a scaling factor. Before plotting the histograms, the normalized templates must all be scaled by their respective fractions, $V_i^{\rm temp}$.

If a template is the sorted histogram from a Monte Carlo simulation, an initial number of disintegrations, $N_{\rm R}^{\rm MC}$, was specified by the user when the simulation was performed. The template was normalized to the data, so to determine the number of experimental disintegrations, $N_{\rm R}^{\rm MC}$ is normalized by the same ratio—$A^{\rm data}/A_i^{\rm temp}$. Before the normalized template was plotted, it was scaled by its associated fractional contribution scaling factor, $V_i^{\rm temp}$, and as a result, $N_{\rm R}^{\rm MC}$ is multiplied by $V_i^{\rm temp}$. Therefore, to calculate the number of experimental disintegrations with *TFractionFitter*:

$$N_{\rm R}^{\rm data} = \frac{N_{\rm R}^{\rm MC} A^{\rm data} V_i^{\rm temp}}{A_i^{\rm temp}}. \tag{6.4}$$

This equation is very similar to Eq. 6.3 except now $A^{\rm sub} = A^{\rm data}V_i^{\rm temp}$; the area of the experimental data histogram is scaled by the fractional contribution of the i^{th} template, and the total number of experimental disintegrations can be calculated.

The sorted ^{56}Co data were analyzed with a new *TFractionFitter* code. A HPGe data histogram, an environmental background template histogram, and a ^{56}Co GEANT4 simulated template histogram (sorted into a HPGe singles spectrum) were passed to ROOT's *TFractionFitter* class. From Eq. 6.4, the calculation yielded $N_{\rm R}^{\rm data}(^{56}{\rm Co}) = (10.90 \pm 0.14)\times10^6$ disintegrations. This result agrees well with the results from Sec. 6.3.2—the source activity and the number of reactions calculated by normalizing histograms. This agreement lends some credence to using ROOT's *TFractionFitter* class to calculate the number of reactions. Rigorous tests with beam-induced reactions at established resonance energies are presented in the next section.

6.3.4: Partial Number of Reactions from a *TFractionFitter* Code

The type of *TFractionFitter* code described thus far provides one way to calculate the total number of experimental reactions, but the code described above requires a well-known decay scheme with known branching ratios in order to produce a template histogram that can be matched to the data. The $^{17}{\rm O}(p,\gamma)^{18}{\rm F}$

direct capture reaction does not have a well-known decay scheme, and the branching ratios are expected to change with bombarding energy. Additionally, the tails of broad resonances, E_R^{cm} = 556 keV and 676 keV, contaminate the direct capture signal with resonance contributions. A modified *TFractionFitter* code, *solver.cxx*, that makes no assumptions about the decay scheme other than what primary transitions are theoretically possible, was written. Model calculations, for the direct capture, and Breit-Wigner calculations, for the broad resonance contributions, were performed to estimate the expected primary transition branching ratios; however, *solver.cxx* relies on GEANT4 simulations of each primary transition decay chain (including the secondaries associated with each primary) independently, and it assigns a 100% branching ratio to each primary—no prior knowledge of the branching ratio is assumed or necessary.

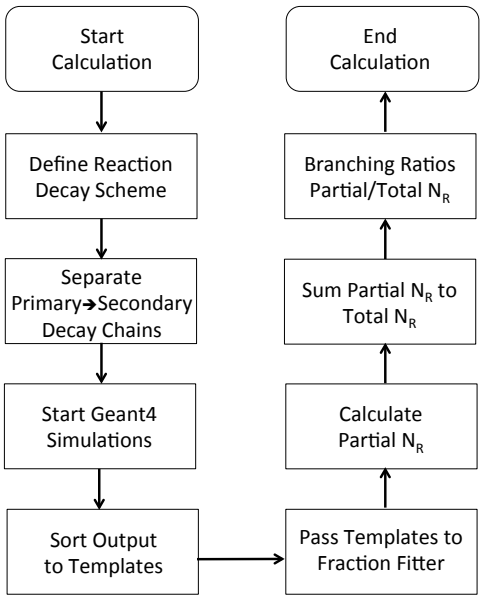

Figure 6.5: A flowchart of how *solver.cxx* operates. The code fits all possible *primary→secondary* templates to the data histogram. The scaling factors returned by the fitter are used to derive the partial number of reactions associated with each primary transition. These partial values are summed to the total number of reactions. The ratio between each partial number of reactions and the total number of reactions is a primary branching ratio.

Now, instead of fitting one Monte Carlo template of interest to the data histogram (along with background templates), all possible decay channels are simulated independently, and these *primary→secondary* templates are passed, with the backgrounds, to the *TFractionFitter* class. The scaling factors, V_i^{temp}, returned by *TFractionFitter* can then be used to calculate the partial number of experimental reactions. Equation 6.4

described above still holds except the calculated N_R^{data} is the number of reactions associated with a single primary transition. For "n" primaries, the total number of reactions is calculated by summing the partial reaction numbers:

$$N_R^{total} = N_{R,1}^{partial} + N_{R,2}^{partial} + ... + N_{R,n}^{partial}. \quad (6.5)$$

Branching ratios can then be calculated where, for example, the branching ratio, B_1, of primary "1" is:

$$B_1 = \frac{N_{R,1}^{partial}}{N_R^{total}}. \quad (6.6)$$

A flowchart that summarizes the operation of the *solver.cxx* code is shown in Fig. 6.5.

This new analysis technique was tested with the $^{17}O(p,\gamma)^{18}F$ resonances at E_R = 518 keV and E_R = 193 keV. Data collected at E_p = 525 keV during a E_R = 518 keV yield curve on target $\beta 1$ (see Fig. 4.8) were sorted into coincidence and singles data histograms. This data—charge accumulation of Q = 0.02 C—were then compared to simulated *primary→secondary* templates and overnight background templates. Angular correlations were built into the GEANT4 simulations of the *primary→secondary* deexcitation chains. Theoretical angular correlations are listed for each primary transition in Tab. 6.4. Mixed angular correlations for the primaries R→3791 and R→4398 were excluded from the simulations but are listed in the Tab. 6.4 along with their associated γ-ray multipolarities. Partial reaction numbers were determined with Eq. 6.4

Table 6.4: Theoretical angular correlations were calculated for the $^{17}O(p,\gamma)^{18}F$ resonance E_R = 518 keV. The R→3791 and R→4398 primaries have mixed emission patterns. For both transitions, the M1 and E2 angular correlations are opposite in sign and will not impact significantly the intensity of these two low-branching ratio primaries at 0°. The R→3791 and R→4398 angular correlations were not included in the GEANT4 simulations used to calculate the partial reaction numbers in Tab. 6.5.

Transition	Theoretical W(θ)	γ mult.
R→937	$1 - 0.196P_2(\cos\theta)$	
R→1121	$1 - 0.100P_2(\cos\theta)$	
R→2101	$1 - 0.281P_2(\cos\theta)$	
R→3791	$1 - 0.196P_2(\cos\theta)$	M1
R→3791	$1 + 0.028P_2(\cos\theta)$	E2
R→4116	$1 - 0.196P_2(\cos\theta)$	
R→4398	$1 + 0.275P_2(\cos\theta)$	M1
R→4398	$1 - 0.165P_2(\cos\theta)$	E2
R→4652	$1 + 0.275P_2(\cos\theta)$	

for the seven resonance primaries with both coincidence and singles data histograms. The total number of reactions was then calculated with Eq. 6.5, and these results are shown in Tab. 6.5. New branching ratios were then calculated with Eq. 6.6 based on *primary→secondary* templates fit independently to singles and

Table 6.5: Seven $^{17}O(p,\gamma)^{18}F$ resonance $E_R = 518$ keV template histograms—the resonance's constituent primaries and their associated secondaries—were simulated. These *primary→secondary* templates were passed, along with an environmental background template, to ROOT's *TFractionFitter* class. Results from the coincidence and singles spectra are shown. Theoretical angular correlations were built into the GEANT4 simulation (see Tab. 6.4).

	$N_R^{partial}$	
Transition	coincidence	singles
R→937	41000(2000)	46000(3000)
R→1121	423000(7000)	485000(8000)
R→2101	196000(4000)	200000(3000)
R→3791	9400(900)	16500(1000)
R→4116	12000(900)	15500(800)
R→4398	6100(800)	9100(1000)
R→4652	40400(1600)	42800(1400)
N_R^{total}	728000(9000)	815000(9000)

coincidence data histograms with ROOT's *TFractionFitter* class. These branching ratios are listed in Tab. 6.6 alongside the $E_R = 518$ keV branching ratios from Kontos *et al.* (2012) [81] and Tilley *et al.* (1995) [40]. The resonance strength was then calculated with the total number of reactions, N_R^{total}, from the coincidence and singles data histograms in Tab. 6.5 and the following expression:

$$\omega\gamma = \frac{2\epsilon_{eff}}{\lambda^2}\frac{N_R^{total}}{N_p} \tag{6.7}$$

where λ, the de Broglie wavelength, was defined in Eq. 5.2; ϵ_{eff} is the effective stopping power defined in Eq. 4.4; N_p is the number of incident particles defined in Eq. 5.3. Systematic uncertainties adopted during

Table 6.6: Branching ratios for the $^{17}O(p,\gamma)^{18}F$ resonance, $E_R = 518$ keV, primary transitions were calculated from the partial and total number of reactions in Tab. 6.5. They are compared here to the branching ratios from Kontos *et al.* (2012) [81] and Tilley *et al.* (1995) [40]. Independent results from the coincidence and singles spectra are shown.

	Branching Ratio (%)			
Transition	Ref. [81]	Ref. [40]	coincidence	singles
R→937	4.2(5)	4.9(9)	5.7(3)	5.7(4)
R→1121	58.6(23)	55(3)	58.1(12)	59.5(11)
R→2101	25.1(11)	27(2)	26.9(6)	24.5(5)
R→3791	1.3(2)	1.4(3)	1.29(13)	2.02(13)
R→4116	1.8(3)	1.8(3)	1.65(12)	1.90(10)
R→4398	2.2(3)	0.7(3)	0.83(11)	1.12(12)
R→4652	6.8(3)	8.7(7)	5.6(2)	5.25(18)

this calculation are listed in Tab. 6.7. New resonance strengths for the $E_R = 518$ keV resonance are listed

Table 6.7: The systematic uncertainties present during the $^{17}O(p,\gamma)^{18}F$ direct capture study.

Source	Uncertainty (%)
GEANT4[1]	1.3
^{17}O-enriched water	3.0
Charge integration[2]	3.0
Target degradation[3]	3.2
Stopping power[4]	4.0
HPGe peak efficiency	5.0
NaI(Tl) total efficiency	5.0

[1] From Ref. [101].
[2] In agreement with Ref. [152].
[3] From maximum degradation rate and target thickness uncertainty.
[4] From Ref. [153].

in Tab. 6.8 from the coincidence and singles data histograms. They are tabulated alongside the literature strengths from Kontos *et al.* (2012) [81] , Newton *et al.* (2010) [78], Fox *et al.* (2005) [75], and Rolfs, Charlesworth, and Azuma (1973) [77]. The weighted mean of the literature resonance strengths and the new

Table 6.8: The resonance strength, $\omega\gamma$, for the $^{17}O(p,\gamma)^{18}F$ resonance $E_R = 518$ keV was determined from the total number of reactions in Tab. 6.5. This strength is compared to the strength from Kontos *et al.* (2012) [81], Newton *et al.* (2010) [78], Fox *et al.* (2005) [75], and Rolfs, Charlesworth, and Azuma (1973) [77].

$E_R = 518$ keV Resonance Strength (meV)					
Ref. [81]	Ref. [78]	Ref. [75]	Ref. [77]	coincidence	singles
13.0(15)	13.7(22)	12(3)	13.0(17)	12.9(9)	14.5(10)

strength from the coincidence spectrum, $\omega\gamma = 12.9 \pm 0.9$ meV, was found to be

$$\omega\gamma = 13.0 \pm 0.7 \text{ meV}; \tag{6.8}$$

the weighted mean was adopted for the reaction rate calculations reported at the end of this chapter (see Tab. B.2).

At the beginning of ECR ion source data acquisition, on-resonance charge accumulation, $Q = 14$ C, on target $\beta 3$ was performed at $E_p = 200$ keV. Coincidence and singles spectra are shown in Appendix E, Fig. E.7; the observed primaries, secondaries, and escape peaks are labeled. These $E_R = 193$ keV resonance data were also used to test the *TFractionFitter* analysis technique. Based on the observed primary transitions, the resonance γ-cascade was decomposed into ten *primary*→*secondary* Monte Carlo template histograms.

Theoretical angular correlations were built into the GEANT4 simulation for the resonance primaries (see Tab. 6.9), but a direct capture primary, R/DC→3839, was also observed. The angular correlation calculations presented in Appendix C and discussed further in Sec. 6.3.6 were used to include the anisotropic emission pattern for this direct capture primary. Mixed angular correlations for the R→2101, R→3134, and R→3791 resonance primaries were excluded from the analysis. The total number of reactions from the coincidence data histogram differed by ≈0.7% if all transitions were assumed to have an isotropic emission pattern. The total number of reactions from the singles data histogram differed by ≈1.2% if isotropy was assumed. Partial reaction numbers were determined with Eq. 6.4 for the nine resonance primaries and the one (hypothesized) direct capture primary with both coincidence and singles data histograms. The total number of reactions was then calculated with Eq. 6.5. However, at E_p = 200 keV the observed direct capture primary, R/DC→3839, has not previously been associated with the E_R = 193 keV resonance (according to Ref. [82]). The partial number of direct capture reactions at E_p = 200 keV must be calculated. The total S-factor at E_p = 190 keV, discussed in the next few sections, was used to calculate the partial number of reactions that contaminate the E_R = 193 keV spectra. To calculate the partial number of direct capture (and broad resonance)—DCBR—reactions for the i^{th} primary at E_p = 200 keV, $N_{R,i}^{DCBR}(200)$ is defined as:

$$N_{R,i}^{DCBR}(200) = N_p(200)\frac{\Delta E(200)}{\epsilon_{eff}(200)}\frac{S^{total}(190)}{E(200)}B_{\gamma,i}(190)e^{-2\pi\eta(200)}. \tag{6.9}$$

In this equation, $N_p(200)$, $\Delta E(200)$, $\epsilon_{eff}(200)$, $E(200)$, and $2\pi\eta(200)$ are the number of incident particles, the target thickness, the effective stopping power, the center-of-mass bombarding energy, and the Sommerfeld parameter, respectively, at E_p = 200 keV. However, $S^{total}(190)$ and $B_{\gamma,i}(190)$ are the total S-factor and the branching ratio of the i^{th} primary, respectively, at E_p = 190 keV. The total S-factor can be found in Tab. 6.20 and the branching ratios of the primaries are listed in Tab. 6.19. The partial number of direct capture (and broad resonance) reactions was then subtracted from the partial number of reactions determined with *TFractionFitter* where the partial number of resonance reactions is:

$$N_{R,i}^{Resonance} = N_{R,i}^{TFF} - N_{R,i}^{DCBR} \tag{6.10}$$

where TFF stands for *TFractionFitter*. The R→0, R→937, R→1042, R→2523, and R/DC→3839 primaries were found to have contributions from direct capture (and the E_R^{cm} = 556 and 676 keV broad resonances). These contributions were subtracted according to Eq. 6.10. These results are tabulated in Tab. 6.10. The coincidence and singles total resonance reaction numbers, partial resonance reaction numbers, and Eq. 6.6 were used to calculate the E_R = 193 keV branching ratios. These branching ratios are tabulated alongside

the Rolfs, Charlesworth, and Azuma (1973) [77] and Di Leva *et al.* (2014) [82] branching ratios in Tab. 6.11. The coincidence and singles total resonance reaction numbers, and Eq. 6.7 were used to calculate the E_R = 193 keV resonance strength. The results are tabulated alongside the Di Leva *et al.* (2014) [82], Chafa *et al.* (2007) [144], and Fox *et al.* (2005) [75] resonance strengths in Tab. 6.12. Systematic uncertainties

Table 6.9: Theoretical angular correlations were calculated for the $^{17}O(p,\gamma)^{18}F$ resonance $E_R = 193$ keV. The R→2101, R→3134, and R→3791 primaries have mixed emission patterns. The mixed angular correlations were not included in the GEANT4 simulations used to calculate the partial reaction numbers in Tab. 6.10.

Transition	Theoretical W(θ)	γ mult.
R→0	$1 - 0.1000P_2(\cos\theta)$	
R→937	$1 - 0.0285P_2(\cos\theta)$	
R→1042	$1 + 0.1428P_2(\cos\theta)$	
R→1081	$1 + 0.1428P_2(\cos\theta)$	
R→2101	$1 + 0.1000P_2(\cos\theta)$	M1
R→2101	$1 - 0.0306P_2(\cos\theta)$	E2
R→2523	$1 + 0.1000P_2(\cos\theta)$	
R→3134	$1 - 0.1000P_2(\cos\theta)$	M1
R→3134	$1 + 0.0714P_2(\cos\theta)$	E2
R→3358	$1 - 0.0285P_2(\cos\theta)$	
R→3791	$1 - 0.0285P_2(\cos\theta)$	M1
R→3791	$1 - 0.0816P_2(\cos\theta)$	E2

Table 6.10: The $^{17}O(p,\gamma)^{18}F$ resonance $E_R = 193$ keV *primary→secondary* templates were passed, along with an environmental background template, to ROOT's *TFractionFitter* class (TFF). The template scaling factors were used to calculate the partial number of reactions for each primary transition. These were then summed to determine the total number of $E_R = 193$ keV reactions. Results from the coincidence and singles spectra are shown. The direct capture S-factor at $E_p = 190$ keV, discussed later, was used to determine the direct capture (and broad resonance) component to these measured partial reaction numbers (DCBR); these direct capture reactions were subtracted from the measured partial reaction numbers to arrive at the partial number of resonance reactions.

$N_R^{partial}$	TFF		DCBR	Resonance	
Transition	coincidence	singles	Eq. 6.9	coincidence	singles
R→0	4500(600)[1]	4500(600)	1000(300)	3500(700)	3500(700)
R→937	42300(1400)	43700(1500)	12000(2000)	30000(3000)	31000(3000)
R→1042	4100(500)	4200(600)	1000(400)	3100(700)	3300(800)
R→1080	57100(1600)	53800(1400)	–	57100(1600)	53800(1400)
R→2101	12800(1000)	13400(1000)	–	12800(1000)	13400(1000)
R→2523	9400(700)	8600(600)	800(400)	8700(800)	7900(700)
R→3133	5700(700)	4800(600)	–	5700(700)	4800(600)
R→3356	3100(600)	3700(700)	–	3100(600)	3700(700)
R→3791	6900(700)	6900(900)	–	6900(700)	6900(900)
R→3839	9200(900)	7400(1100)	6700(1500)	2500(1700)	–
N_R^{total}	155000(3000)	151000(3000)	22000(3000)	133000(4000)	129000(4000)

[1] Adopted from g.s. transition fit in HPGe singles spectrum.

adopted during this calculation are listed in Tab. 6.7. The weighted mean of the LUNA resonance strength,

Table 6.11: Branching ratios for the $^{17}O(p,\gamma)^{18}F$ resonance, $E_R = 193$ keV, primary transitions were isolated from direct capture contributions and calculated from the partial and total number of reactions in Tab. 6.10. They are compared here to the branching ratios from Rolfs, Charlesworth and Azuma (1973) [77] and Di Leva *et al.* (2014) [82]. Results from the coincidence and singles spectra are shown.

	Branching Ratio (%)			
Transition	Ref. [77]	Ref. [82]	coincidence	singles
R→0	–	2.9(4)	2.7(5)	2.8(6)
R→937	40(8)	24.5(8)	22(2)	24(2)
R→1042	–	3.4(4)	2.3(5)	2.5(6)
R→1080	60(8)	40.8(7)	42.9(18)	41.9(16)
R→2101	–	11.8(8)	9.6(8)	10.4(8)
R→2523	–	5.5(6)	6.5(7)	6.1(6)
R→3133	–	4.3(4)	4.2(5)	3.8(5)
R→3356	–	2.3(3)	2.3(4)	2.9(6)
R→3791	–	4.5(4)	5.2(5)	5.3(7)
R→3839	–	–	1.8(13)	–

Table 6.12: The resonance strength, $\omega\gamma$, for the $^{17}O(p,\gamma)^{18}F$ resonance $E_R = 193$ keV was determined from the total number of reactions in Tab. 6.10. This strength is compared to the strength from Di Leva *et al.* (2014) [82], Chafa *et al.* (2007) [144], and Fox *et al.* (2005) [75].

$E_R = 193$ keV Resonance Strength (μeV)				
Ref. [82]	Ref. [144]	Ref. [75]	coincidence	singles
1.67(12)	2.2(4)[1]	1.2(2)	1.89(15)	1.82(14)

[1] Strength from Ref. [76], $\omega\gamma = 3.4(6)$ μeV, revised in Refs. [145, 144].

$\omega\gamma = 1.67 \pm 0.12$ μeV, and the new strength determined from the coincidence spectrum, $\omega\gamma = 1.89 \pm 0.15$ μeV, was found to be

$$\omega\gamma = 1.76 \pm 0.09\ \mu eV; \tag{6.11}$$

the weighted mean was adopted for the reaction rate calculations reported at the end of this chapter (see Tab. B.2).

The remaining $^{17}O(p,\gamma)^{18}F$ data at $E_p = 175$, 190, 250, 275, 300, and 325 keV have both direct capture and broad resonance components that must be taken into account. The branching ratios were first approximated based on direct capture model and Breit-Wigner calculations. These calculations are discussed next in Sec. 6.3.5. Anisotropic angular correlations may also affect the observed peak intensities. Calculation and assessment of $^{17}O(p,\gamma)^{18}F$ angular correlations are presented in Appendix C. Anisotropies could result from

interference between the resonances and the direct capture reaction (see Appendix C.1), different bound state orbital angular momenta (see Appendix C.2), or interference between different scattering state orbital angular momenta (see Appendix C.3). The results were written into the GEANT4 simulations producing ^{17}O(p,γ)^{18}F *primary→secondary* template histograms for the *solver.cxx* code. This is discussed in more detail in Sec. 6.3.6.

6.3.5: Estimated Direct Capture and Broad Resonance Branching Ratios

The code TEDCA [138] was used to perform direct capture model calculations, and *reacnumeric.f* [154] was used for the Breit-Wigner calculations. The direct capture model calculations were based on the decay scheme observed by Ref. [84] at E_p = 1625 keV. The decay schemes of the two broad resonances come from Refs. [40, 81]. Figure 6.6a shows the direct capture decay scheme from Ref. [84] as thick red arrows. The decay scheme for the E_R^{cm} = 556 keV resonance from Refs. [40, 81] is shown in Fig. 6.6b. The thick black and red arrows are the ^{18}F decays due to the resonance; however, the red arrows indicate that certain E_R^{cm} = 556 keV resonance decays are also direct capture decays. Figure 6.6c shows a decay scheme for the E_R^{cm} = 676 keV resonance from Refs. [40, 81]. Again, the thick black and red arrows are due to the resonance, but the red arrows mean that some of the resonance decays are also direct capture decays. The hatch marks in the three level diagrams are meant to represent an arbitrary proton bombarding energy. The direct capture primaries will have γ-ray energies $E_\gamma = Q_{p\gamma} + E_p - E_x$ (as discussed in Sec. 2.1.1), but so will the primaries from the broad resonance tails. The branching ratios of the broad resonances are listed in Tab. 6.13, and differences between the emission probabilities presented in Refs. [40, 81] were reconciled with the procedure discussed in Appendix A.2. The partial widths used in the Breit-Wigner calculations are tabulated in Appendix B.1.1, Tab. B.2. Coupling calculations (an example calculation is discussed in Sec. 2.1.1) were performed for ^{17}O(p,γ)^{18}F direct capture, and the orbital angular momenta (listed in Tab. 2.1) were used as input to TEDCA [138]. A zero scattering state potential and the bound state potential parameters, r_0 = 1.25 fm and a = 0.65 fm [85], were also used as TEDCA input. The model calculations were computed for each experimental bombarding energy, and the TEDCA cross sections were multiplied by the spectroscopic factors, C^2S, according to Eq. 2.16 in Sec. 2.1.1. The spectroscopic factors used from Refs. [155, 156, 81] are listed in Tab. 6.14. Differences between the literature values were reconciled with the procedure outlined in Appendix A.2. The direct capture model S-factor, calculated with TEDCA [138] is shown in Fig. 6.7 as a dashed black line. The broad resonance contribution to the S-factor is plotted as a dotted black line, and the incoherent sum of the two calculations is a solid black line (the total S-factor).

From the direct capture model and Breit-Wigner calculations, estimates of the *convolved* branching ratios

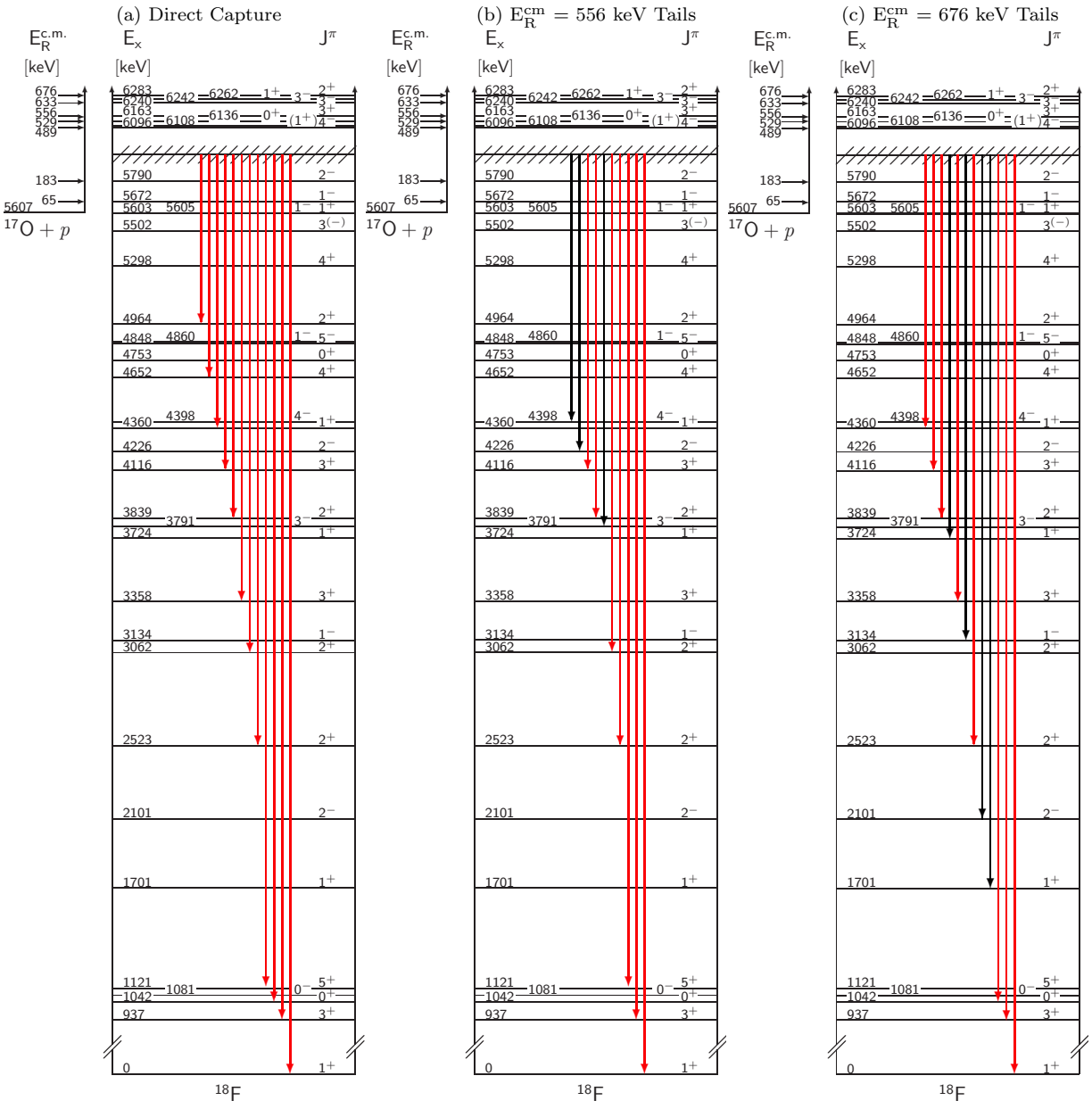

Figure 6.6: (a) Direct capture [84], (b) $E_R^{cm} = 556$ keV, and (c) $E_R^{cm} = 676$ keV broad resonance tail [40, 81] decay schemes. In the broad resonance tail level diagrams, transitions that can also be attributed to direct capture are red arrows. Transitions that are just from the broad resonance tails are black arrows. The hatch marks above $E_p^{cm} = 183$ keV in all three diagrams represents an arbitrary proton bombarding energy where $E_\gamma = Q_{p\gamma} + E_p - E_x$

Table 6.13: Discrepancies between broad resonance branching ratios presented in Refs. [40, 81] are resolved by calculating weighted and reconfigured means. Branching ratios are tabulated as percentages (%).

Transition	E_R^{cm} = 556 keV			E_R^{cm} = 676 keV		
	[81]	[40]	adopted	[81]	[40]	adopted
R → 0	–	0.2(2)	0.2(2)	0.38(2)	0.3(1)	0.38(2)[1]
R → 937	50.3(6)	51(3)	51(2)[1]	65.73(35)	67(3)	66.2(17)[1]
R → 1042	–	–	–	0.69(7)	1.3(1)	1.0(3)[2]
R → 1121	2.1(2)	1.0(1)	1.5(6)[2]	–	–	–
R → 1701	–	–	–	5.67(13)	5.7(6)	5.67(13)[1]
R → 2101	–	–	–	1.74(9)	1.2(3)	1.5(3)[2]
R → 2523	7.0(2)	5.5(4)	6.3(8)[2]	0.73(6)	0.3(2)	0.6(2)[2]
R → 3062	2.3(1)	1.3(3)	1.8(5)[2]	–	–	–
R → 3134	–	–	–	1.29(6)	0.7(3)	1.1(3)[2]
R → 3358	–	–	–	2.10(5)	2.3(3)	2.11(5)[1]
R → 3724	–	–	–	2.51(5)	1.4(5)	2.1(5)[2]
R → 3791	10.2(2)	11.6(13)	10.3(4)[2]	–	–	–
R → 3839	22.0(3)	25.0(16)	23.1(14)[2]	13.28(10)	15.8(14)	14.2(12)[2]
R → 4116	2.2(3)	1.5(3)	1.9(4)[2]	3.73(6)	3.9(2)	3.74(6)[1]
R → 4226	1.4(2)	0.9(3)	1.2(2)[2]	–	–	–
R → 4360	–	–	–	2.14(6)	0.5(4)	1.4(8)[2]
R → 4398	2.5(1)	2.0(2)	2.3(3)[2]	–	–	–

[1] Weighted mean.
[2] Reconfigured mean.

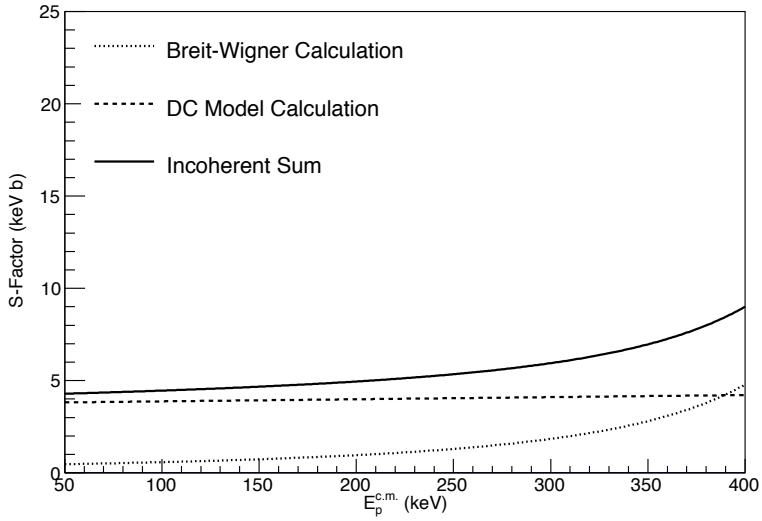

Figure 6.7: Direct capture model calculations were performed with the code TEDCA [138] and the result is shown here as a dashed black line. The Breit-Wigner calculation performed with the code *reacnumeric.f* [154] is shown as a dotted black line. The incoherent sum of the two is a solid black line. Spectroscopic factors and partial widths used in these calculations can be found in Tables 6.14 and B.2, respectively.

Table 6.14: Spectroscopic factors presented in Refs. [155, 156, 81] were reconciled with the procedure discussed in Appendix A.2. Spectroscopic factors from Refs. [155, 156] were determined from transfer reactions, and the spectroscopic factors from Ref. [81] were calculated from R-matrix fits.

E_x (keV)	ℓ_f	C^2S [155]	C^2S [156]	C^2S [81]	C^2S adopted
0	2	0.62(16)[1]	–	–	0.62(16)
937	0	0.27(7)[1,2]	0.102(15)[3]	–	0.17(8)[4]
937	2	–	0.306(46)[3]	–	0.31(5)
1042	2	0.96(24)[1]	0.96(14)[3]	–	0.96(12)[5]
1121	2	0.83(21)[1]	0.89(13)[3]	–	0.87(11)[5]
1701	2	–	0.035(5)[3]	–	0.035(5)
2523	0	0.021(5)[1,2]	0.014(2)[3]	–	0.017(8)[4]
2523	2	–	0.0110(17)[3]	–	0.0110(17)
3062	0	0.13(3)[1]	0.21(3)[3]	0.32(16)[6]	0.18(4)[4]
3062	2	0.61(15)[1]	0.62(9)[3]	0.37(19)[6]	0.58(7)[5]
3358	0	–	0.014(2)[3]	–	0.014(2)
3358	2	–	–	–	0.040(10)[7]
3839	0	0.41(10)[1,2]	–	0.42(21)[6]	0.42(9)[5]
3839	2	–	–	0.19(10)[6]	0.19(10)
4116	0	0.11(3)[1]	0.17(3)[3]	–	0.14(3)[4]
4116	2	0.63(16)[1]	0.68(10)[3]	–	0.66(9)[5]
4360	2	–	0.074(11)[3]	–	0.074(11)
4652	2	0.8(2)[1]	1.04(16)[3]	1.6(8)[6]	0.97(12)[5]
4753	2	–	0.18(3)[3]	–	0.18(3)
4964	0	0.18(5)[1]	0.17(3)[3]	0.17(9)[6]	0.17(2)[5]
4964	2	0.41(10)[1]	0.51(8)[3]	0.5(3)[6]	0.47(6)[5]
5298	2	–	0.120(18)[3]	–	0.120(18)
5603	2	–	0.120(18)[3]	–	0.120(18)

[1] 25% uncertainty adopted from Ref. [85].
[2] Mean of upper and lower limit.
[3] 15% uncertainty adopted from Ref. [85].
[4] Reconfigured mean.
[5] Weighted mean.
[6] 50% uncertainty adopted from Ref. [81].
[7] Extrapolated from direct capture cross section at $E_p = 1625$ keV in Ref. [84].

(the direct capture branching ratios with the broad resonance contributions included) at each bombarding energy were calculated with the following equation:

$$B_{ij} = \frac{\sigma_{ij}^{556} + \sigma_{ij}^{676} + \sigma_{ij}^{DC}}{\sigma_{\text{total}}^{556} + \sigma_{\text{total}}^{676} + \sigma_{\text{total}}^{DC}}. \tag{6.12}$$

In this equation, B_{ij} is the branching ratio for transition $i \rightarrow j$; σ_{ij}^{556} is the cross section of the $i \rightarrow j$ transition in the $E_R^{cm} = 556$ keV resonance; σ_{ij}^{676} is the cross section of the $i \rightarrow j$ transition in the $E_R^{cm} =$ 676 keV resonance; σ_{ij}^{DC} is the cross section of the $i \rightarrow j$ transition in the direct capture reactions; $\sigma_{\text{total}}^{556}$ is the total cross section of $E_R^{cm} = 556$ keV resonance; $\sigma_{\text{total}}^{676}$ is the total cross section of the $E_R^{cm} = 676$ keV resonance; $\sigma_{\text{total}}^{DC}$ is the total cross section of the direct capture reaction. The estimates of the convolved

branching ratios for every possible transition are listed in Tab. 6.15.

Table 6.15: The incoherent sum of the computed cross sections is used to calculate the branching ratios for all possible $^{17}O(p,\gamma)^{18}F$ direct capture and broad resonance levels (see Eq. 6.12). These calculations were performed for each experimental bombarding energy, and branching ratios are tabulated as percentages (%). These branching ratios are estimates and are not used by the *solver.cxx* analysis code.

	Branching Ratio (%) by E_p (keV)					
Transition	175	190	250	275	300	325
R/DC→0	4.2(11)	4.1(11)	4.0(10)	3.8(10)	3.7(9)	3.6(9)
R/DC→937	26(4)	26(4)	28(4)	29(4)	30(4)	32(3)
R/DC→1042	1.17(16)	1.16(16)	1.11(15)	1.08(15)	1.05(14)	1.01(13)
R/DC→1121	11.1(14)	11.0(14)	10.5(14)	10.2(13)	9.9(13)	9.5(12)
R/DC→1701	0.21(2)	0.22(2)	0.26(3)	0.28(3)	0.30(3)	0.32(3)
R/DC→2101	0.054(12)	0.057(13)	0.067(15)	0.073(16)	0.078(17)	0.083(18)
R/DC→2523	1.6(4)	1.7(4)	1.9(4)	2.1(4)	2.2(4)	2.4(4)
R/DC→3062	10.2(16)	10.1(16)	9.6(14)	9.3(14)	9.0(13)	8.6(13)
R/DC→3134	0.035(10)	0.036(11)	0.044(13)	0.048(14)	0.051(15)	0.056(16)
R/DC→3358	1.17(16)	1.16(16)	1.11(15)	1.08(14)	1.05(13)	1.00(13)
R/DC→3724	0.058(15)	0.061(16)	0.074(19)	0.08(2)	0.09(2)	0.10(2)
R/DC→3791	1.16(10)	1.24(11)	1.66(14)	1.92(16)	2.18(17)	2.51(19)
R/DC→3839	19(3)	19(3)	19(3)	19(3)	19(3)	19(2)
R/DC→4116	11.6(18)	11.5(18)	10.9(17)	10.5(16)	10.2(15)	9.7(14)
R/DC→4226	0.12(2)	0.13(2)	0.17(3)	0.20(4)	0.23(4)	0.27(5)
R/DC→4360	0.17(3)	0.17(3)	0.17(3)	0.17(3)	0.17(3)	0.17(4)
R/DC→4398	0.21(3)	0.23(3)	0.31(5)	0.37(6)	0.42(6)	0.50(7)
R/DC→4652	4.0(6)	3.9(5)	3.8(5)	3.7(5)	3.5(5)	3.4(4)
R/DC→4964	7.8(9)	7.6(9)	7.0(8)	6.6(8)	6.3(7)	5.9(7)

6.3.6: Accounting for Anisotropic Angular Correlations

The $^{17}O(p,\gamma)^{18}F$ direct capture study was performed at $\theta = 0°$ with respect to the beam direction. The $\gamma\gamma$-coincidence spectrometer can only be used at this angle. Previous studies performed this experiment at $\theta = 55°$ because the $P_2(\cos\theta)$ Legendre polynomial is zero at this angle and angular correlation calculations can be simplified. References [84, 157] outline how to calculate angular correlations for resonant and direct capture reactions. Three possible scenarios were considered: (1) the broad resonance tails and direct capture interfere, *R,D interference*, and the angular correlation for a transition is the coherent sum of resonance and direct capture components; (2) the direct capture scattering state orbital angular momenta interfere, and the angular correlation contains a coherent sum due to this interference; (3) the direct capture bound state orbital angular momenta contribute a component to the incoherent sum of angular correlations for each transition. Appendix C documents each of these three scenarios and the assessment of their impact on the total angular correlation. After careful assessment, the angular correlations calculated for R,D interference

and scattering state orbital angular momenta interference were excluded from the final analysis because they do not introduce anisotropies, and the terms computed are consistent with unity. For each known direct capture primary [84], an expression for the included angular correlations was calculated, and these expressions are tabulated in Tab. 6.16. In this table, the angular correlations are defined as [84]:

$$\mathrm{W}_{\ell_{f^*}}(\theta) = \mathrm{W}_{\ell_i}(\theta) = \mathrm{W}_{p\to d}(\theta) = 1 - \frac{1}{10}P_2(cos\theta), \tag{6.13}$$

$$\mathrm{W}_{\ell_f}(\theta) = \mathrm{W}_{p\to s}(\theta) = 1 - P_2(cos\theta), \tag{6.14}$$

and

$$\mathrm{W}_{\ell_{i^*}}(\theta) = \mathrm{W}_{f\to d}(\theta) = 1 - \frac{2}{5}P_2(cos\theta). \tag{6.15}$$

In these equations p and f refer to p-wave ($\ell_i = 1$) and f-wave ($\ell_{i^*} = 3$) formation, respectively; d refers to the d-shell ($\ell_{f^*} = 2$) orbital; s refers to the s-shell ($\ell_f = 0$) orbital. A z-factor and y-factor are defined as [84]:

$$z = \frac{\sigma_{p\to d}(E)}{\sigma_{p\to s}(E)}, \tag{6.16}$$

and

$$y = \frac{\sigma_{f\to d}(E)}{\sigma_{p\to d}(E)}. \tag{6.17}$$

The z-factor is the ratio between the ($p \to d$) and ($p \to s$) cross sections for a particular direct capture transition, and the y-factor is the ratio between the ($f \to d$) and ($p \to d$) cross sections.

It can be assumed that the angular correlations of direct capture secondaries are isotropic due to the detector geometry—the NaI(Tl) annulus provides nearly 4π coverage. As a result, contributions to the angular correlation by direct capture secondaries are not included in the final analysis.

These angular correlation terms can now be incorporated into GEANT4 reaction simulations for ^{17}O(p,γ)^{18}F. From Sec. C, $\sigma_{\ell_{f^*}}$(E), σ_{ℓ_f}(E), $\sigma_{\ell_{i^*}}$(E), σ_{556}(E), and σ_{676}(E) are calculated with a direct capture model code (TEDCA [138]) and a Breit-Wigner code (*reacnumeric.f* [154]) at each experimental beam energy. In GEANT4, the angular correlation is constructed so that:

$$\mathrm{W(E},\theta) = \frac{\sigma_{556}(\mathrm{E})\mathrm{W}_{556}(\theta) + \sigma_{676}(\mathrm{E})\mathrm{W}_{676}(\theta) + \sigma_{\ell_{f^*}}(\mathrm{E})\mathrm{W}_{\ell_{f^*}}(\theta) + \sigma_{\ell_f}(\mathrm{E})\mathrm{W}_{\ell_f}(\theta) + \sigma_{\ell_{i^*}}(\mathrm{E})\mathrm{W}_{\ell_{i^*}}(\theta)}{\sigma_{\mathrm{tot}}(\mathrm{E})} \tag{6.18}$$

where

$$\sigma_{\mathrm{tot}}(\mathrm{E}) = \sigma_{556}(\mathrm{E}) + \sigma_{676}(\mathrm{E}) + \sigma_{\ell_{f^*}}(\mathrm{E}) + \sigma_{\ell_f}(\mathrm{E}) + \sigma_{\ell_{i^*}}(\mathrm{E}). \tag{6.19}$$

Note that according to Ref. [84], $\mathrm{W}_{556}(\theta) = 1$ and $\mathrm{W}_{676}(\theta) = 1$ because all ^{17}O(p,γ)^{18}F resonances with

Table 6.16: The angular correlation terms considered for each ^{17}O(p,γ)^{18}F transition. As demonstrated in Sections C.1 and C.3, interference between resonances and direct capture is negligible, and interference between scattering state orbital angular momenta is negligible.

E_x (keV)	bound state W(θ)	scattering state W(θ)
0	$W_{\ell_{f^*}}(\theta)$	$\frac{1}{1+y}\left(W_{\ell_i}(\theta)+yW_{\ell_{i^*}}(\theta)\right)$
937	$\frac{1}{1+z}\left(W_{\ell_f}(\theta)+zW_{\ell_{f^*}}(\theta)\right)$	$\frac{1}{1+y}\left(W_{\ell_i}(\theta)+yW_{\ell_{i^*}}(\theta)\right)$
1042	$W_{\ell_{f^*}}(\theta)$	$\frac{1}{1+y}\left(W_{\ell_i}(\theta)+yW_{\ell_{i^*}}(\theta)\right)$
1121	$W_{\ell_{f^*}}(\theta)$	$\frac{1}{1+y}\left(W_{\ell_i}(\theta)+yW_{\ell_{i^*}}(\theta)\right)$
2523	$\frac{1}{1+z}\left(W_{\ell_f}(\theta)+zW_{\ell_{f^*}}(\theta)\right)$	$\frac{1}{1+y}\left(W_{\ell_i}(\theta)+yW_{\ell_{i^*}}(\theta)\right)$
3062	$\frac{1}{1+z}\left(W_{\ell_f}(\theta)+zW_{\ell_{f^*}}(\theta)\right)$	$\frac{1}{1+y}\left(W_{\ell_i}(\theta)+yW_{\ell_{i^*}}(\theta)\right)$
3358	$\frac{1}{1+z}\left(W_{\ell_f}(\theta)+zW_{\ell_{f^*}}(\theta)\right)$	$\frac{1}{1+y}\left(W_{\ell_i}(\theta)+yW_{\ell_{i^*}}(\theta)\right)$
3839	$\frac{1}{1+z}\left(W_{\ell_f}(\theta)+zW_{\ell_{f^*}}(\theta)\right)$	$\frac{1}{1+y}\left(W_{\ell_i}(\theta)+yW_{\ell_{i^*}}(\theta)\right)$
4116	$\frac{1}{1+z}\left(W_{\ell_f}(\theta)+zW_{\ell_{f^*}}(\theta)\right)$	$\frac{1}{1+y}\left(W_{\ell_i}(\theta)+yW_{\ell_{i^*}}(\theta)\right)$
4360	$W_{\ell_{f^*}}(\theta)$	$\frac{1}{1+y}\left(W_{\ell_i}(\theta)+yW_{\ell_{i^*}}(\theta)\right)$
4652	$W_{\ell_{f^*}}(\theta)$	$\frac{1}{1+y}\left(W_{\ell_i}(\theta)+yW_{\ell_{i^*}}(\theta)\right)$
4964	$\frac{1}{1+z}\left(W_{\ell_f}(\theta)+zW_{\ell_{f^*}}(\theta)\right)$	$\frac{1}{1+y}\left(W_{\ell_i}(\theta)+yW_{\ell_{i^*}}(\theta)\right)$

spin $J \leq 3$ give rise to isotropic emission patterns.

GEANT4 spectra generated with the theoretical angular correlations built into the Monte Carlo were compared with spectra that assumed that every ^{18}F transition is isotropic. For the primaries, this ratio $N_\gamma^{corr.}/N_\gamma^{no\ corr.}$ is equal to the experimental angular correlation associated with the transition. Experimental angular correlations are derived from the integral of theoretical angular correlations over the finite solid angle subtended by the detector. In general, expressions for the theoretical angular correlations remain the same except for the inclusion of attenuation coefficients, Q_n. For example, the experimental angular correlation becomes [4]:

$$W_{\rm exp}(\theta) = \frac{1}{a_0}\sum_{n=0}^{n_{\rm max}} a_n Q_n P_n(cos\theta) \tag{6.20}$$

as opposed to the theoretical expression:

$$W_{\rm theo}(\theta) = \frac{1}{a_0}\sum_{n=0}^{n_{\rm max}} a_n P_n(cos\theta). \tag{6.21}$$

Peak intensities were calculated from GEANT4 spectra for both scenarios, $N_\gamma^{corr.}$ and $N_\gamma^{no\ corr.}$, and the intensity ratio was plotted for each bombarding energy. Figure 6.8 shows the ratio between Monte Carlo HPGe singles peak intensities collected from spectra with the ^{18}F angular correlations included and without the correlations for each experimental beam energy. Only the ratios for observed γ-rays (see Tab. 6.3) are shown. The conclusion that $N_\gamma^{corr.}/N_\gamma^{no\ corr.} = W(\theta)$ can be verified by comparing the order of magnitude of the primary experimental angular correlations in Fig. 6.8 with experimental direct capture primary angular

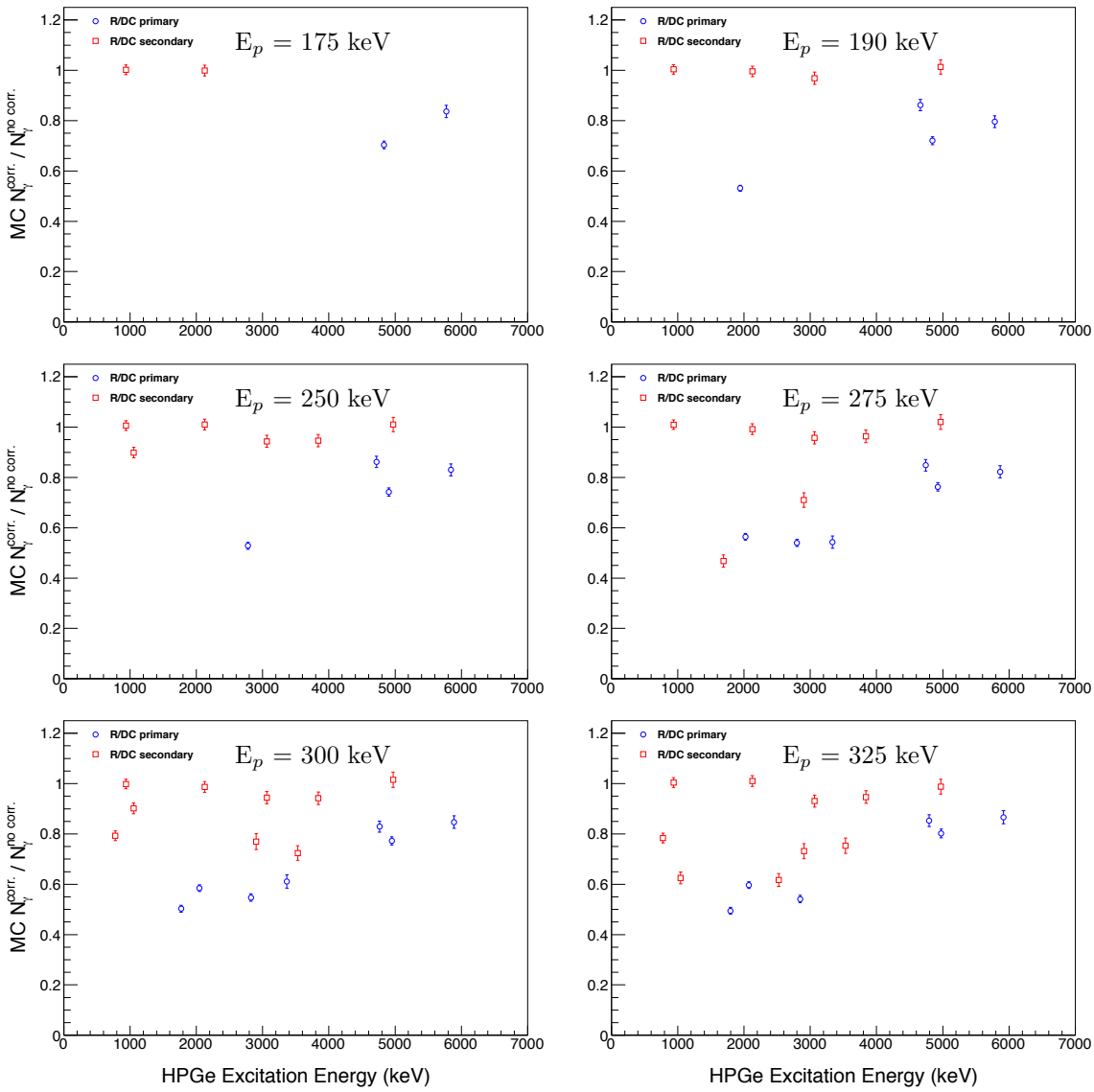

Figure 6.8: Ratios of ^{18}F HPGe singles peak intensities from spectra generated with GEANT4. Simulated intensities from the deexcitation of the ^{18}F nucleus with theoretical angular correlations included were compared to simulated intensities where all transitions were assumed to be isotropic. Primaries are shown as open blue circles and secondaries are shown as open red squares in these figures. For the primaries, the ratio is equivalent to the experimental angular correlation of that particular primary transition and can be compared to the preliminary experimental angular correlations due to different direct capture bound state orbital angular momenta in Fig. C.6. Only ratios for observed γ-rays (see Tab. 6.3) are plotted.

correlations in Appendix C.2, Fig. C.6. As discussed in Appendix C, the incoherent sum of angular correlations due to different bound state orbital angular momenta is the primary source of anisotropic emission patterns. At all six bombarding energies, the experimental angular correlation amounts to ≈ 0.5 for the seven transitions that contribute to the direct capture portion of the emission (see Tab. 6.16). Incorporating the theoretical angular correlations in Fig. C.6 into Eq. 6.19 yields theoretical *convolved* angular correlations. Experimental convolved angular correlations can be calculated from the detector geometry or by performing GEANT4 simulations. The deviations between the experimental angular correlations in Fig. C.6 and Fig. 6.8 are justified by the geometry of the simulated GEANT4 $\gamma\gamma$-coincidence spectrometer and the convolution of the direct capture and broad resonance angular correlations (Eq. 6.19).

6.3.7: Direct Capture ^{17}O(p,γ)^{18}F Partial Reaction Numbers

The convolved direct capture and broad resonance decay scheme, a combination of the broad resonance contributions in Tab. 6.13 and Figs. 6.6b and 6.6c from Refs. [40, 81] and the direct capture contributions in Fig. 6.6a from Ref. [84], can be decomposed into nineteen *primary→secondary* template histograms. The total, convolved, branching ratio estimates are listed in Tab. 6.15, and this table shows the nineteen contributions that the *solver.cxx* code passes to ROOT's *TFractionFitter* class. In addition to environmental background templates, assembled from overnight background runs after each day data were acquired, beam-induced background templates were included in the analysis where applicable. The centroids of beam-induced background primaries and secondaries were used to produce GEANT4 simulated spectra that were then passed to *TFractionFitter*. Resolution functions, separate from the functions used for ^{17}O(p,γ)^{18}F primaries and secondaries, were applied to the beam-induced background simulations by *sort.cxx* before they were sorted into singles and coincidence template spectra. Table 6.17 shows what beam-induced background templates were considered at each direct capture bombarding energy.

Table 6.17: Beam-induced template histograms included by the *TFractionFitter* analysis code, *solver.cxx*. A "×" indicates that a template was included at a particular bombarding energy while "–" means it was excluded.

	Beam-Induced Templates by E_p (keV)					
Reaction	175	190	250	275	300	325
^{11}B(p,γ)^{12}C	×	×	–	–	–	–
^{14}N(p,γ)^{15}O	–	–	–	×	×	×
^{18}O(p,γ)^{19}F	×	–	–	–	–	–
^{19}F(p,$\alpha\gamma$)^{16}O	–	–	×	×	×	×

The analysis code, *solver.cxx*, was used to fit simulated ^{17}O(p,γ)^{18}F *primary→secondary* templates,

along with environmental and beam-induced background templates, to coincidence and HPGe singles data histograms. The partial number of reactions for each primary transition at each direct capture bombarding energy is listed in Tab. 6.18. The fitting routine had difficulty converging if the *TFractionFitter* energy threshold was set below E_{min} = 2650 keV for the HPGe singles histograms. Slight variations in the environmental background templates, the sum of several overnight background runs collected daily after data were acquired, are responsible for these fitting issues at low energies in the singles spectra. Environmental backgrounds are suppressed significantly in the coincidence spectra, and the fitting routine was able to converge over wide energy regions (≈200−8000 keV). As a result, the inclusion of partial reaction numbers from the analysis of HPGe singles spectra is kept to a minimum, and they were sparingly used for the ground state transition (a γ-ray that will not be in coincidence with the other constituents of the γ-cascade). At E_p = 275, 300, and 325 keV, strong first and second escape peaks associated with the ground state transition were present in the coincidence spectra and the HPGe singles histogram was ignored completely. At E_p = 190 and 250 keV, the HPGe singles spectrum was analyzed in order to determine the number of ground state reactions; the ground state transition and its associated escape peaks fall within the 2650−6000 keV *TFractionFitter* energy region. The analysis code did not identify a ground state contribution appreciably above background at E_p = 175 keV. Therefore, a majority of the partial reaction numbers listed in Tab. 6.18 are from the analysis of coincidence spectra with the coincidence condition 3.5 MeV ≤ $E_\gamma^{Ge} + E_\gamma^{NaI(Tl)}$ ≤ 9.0 MeV. Any exceptions that rely on the analysis of HPGe singles spectra are noted.

At E_p = 325 keV, an abnormal enhancement in the number of ground state reactions was observed. The trend in the relative intensity of the ground state transition (see Tab. 6.3) and the observation of strong first and second escape peaks in the coincidence spectrum corresponding to this transition (see Fig. E.6) indicate that this enhancement is physical and not an artifact of the analysis. No narrow $^{17}O(p,\gamma)^{18}F$ resonances are known at this energy and no beam-induced background could be identified that might be responsible for this enhancement. As a result, the number of ground state reactions measured at E_p = 325 keV were excluded from the final analysis. The total number of reactions was calculated for each direct capture bombarding energy with Eq. 6.5 and are tabulated in Tab. 6.18. The number of incident protons at each beam energy is also shown in Tab. 6.18. As an illustration, Fig. 6.9 shows the E_p = 250 keV coincidence spectrum (data are black) with the sum of all template histograms (red) overlaid with each *primary→secondary* template identified as a contribution to the data histogram (varying shades of blue).

The total number of reactions at each bombarding energy can now be used to calculate the astrophysical S-factor because the reaction yield can be expressed in terms of the total number of reactions, N_R in this

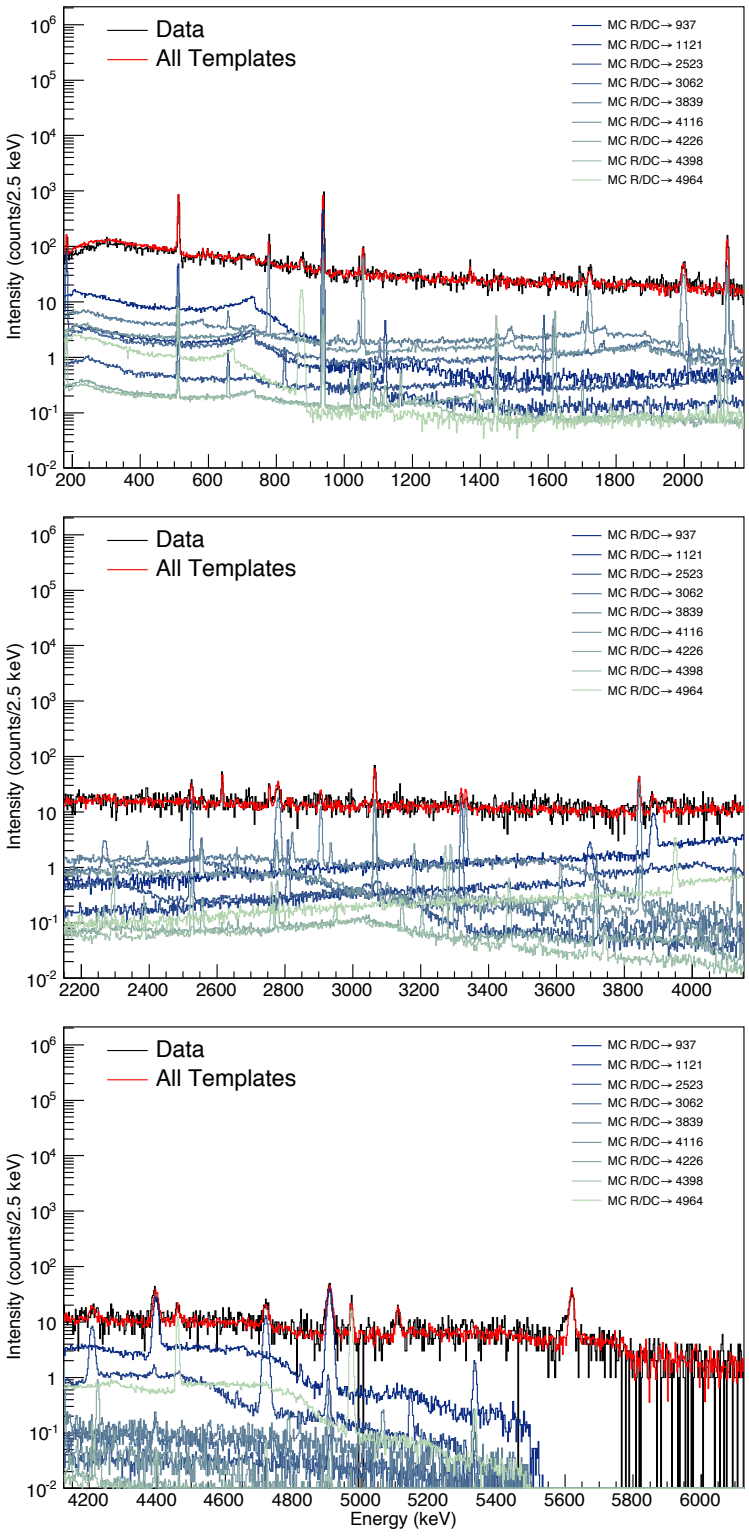

Figure 6.9: The code *solver.cxx* was used to fit nineteen *primary→secondary* ^{17}O(p,γ)^{18}F template histograms to coincidence data collected at E$_p$ = 250 keV. Environmental background and ^{19}F(p,$\alpha\gamma$)^{16}O templates are included but are not shown separately here. The black spectrum is the data, the red spectrum is the sum of all templates, and the blue spectra are the ^{17}O(p,γ)^{18}F templates that were found to contribute at E$_p$ = 250 keV. The partial and total number of ^{17}O(p,γ)^{18}F reactions are tabulated in Tab. 6.18. Branching ratios are listed in Tab. 6.19. The coincidence condition 3.5 MeV $\leq$ E$_\gamma^{Ge}$ + E$_\gamma^{NaI(Tl)}$ $\leq$ 9.0 MeV was applied to the data and template histograms.

expression, and the cross section:

$$Y = \frac{N_R}{N_p} = \int_{\mathrm{E}_p^{\mathrm{cm}}-\Delta\mathrm{E}}^{\mathrm{E}_p^{\mathrm{cm}}} \frac{\sigma(\mathrm{E})}{\epsilon_{eff}(\mathrm{E})} d\mathrm{E} \tag{6.22}$$

where Y is the yield, $\mathrm{E}_p^{\mathrm{cm}}$ is the center-of-mass H^+ bombarding energy, ΔE is the target thickness, σ(E) is the cross section, and ϵ_{eff}(E) is the effective stopping power. The cross section can be replaced with the astrophysical S-factor as shown in Sec. 2.1.1, Eq. 2.17. The code *sfactor.cxx* uses Eq. 6.22 and 2.17 to solve for the astrophysical S-factor at each experimental beam energy. The calculation of the effective beam energy is also discussed in Sec. 6.3.8.

Table 6.18: Each ^{17}O(p,γ)^{18}F Monte Carlo spectrum was decomposed into nineteen individual *primary→secondary* templates. These templates were then fit to each coincidence data histogram along with environmental and beam-induced background templates. The scaling factor returned for each *primary→secondary* template was used to calculate the partial number of ^{17}O(p,γ)^{18}F reactions. These partial values were summed to determine the total number of reactions. Unless noted otherwise, the ground state transition contribution was also determined from coincidence spectra. The number of incident protons, N_p are also listed. An enhancement in the ground state transition at E_p = 325 keV was excluded from the analysis.

	Partial Number of Reactions by E_p (keV)					
Transition	175	190	250	275	300	325
R/DC→0	–	900(300)[1]	6200(1100)[1]	9000(2000)	7000(1900)	29000(4000)[2]
R/DC→937	11900(1200)	11900(1000)	44000(2000)	59000(2000)	66000(2000)	77000(3000)
R/DC→1042	–	900(400)	–	1200(800)	1100(500)	400(300)
R/DC→1121	2400(1000)	1400(800)	11500(1600)	18000(2000)	11600(1600)	17000(2000)
R/DC→1701	700(500)	–	–	1100(600)	–	–
R/DC→2101	1100(600)	–	–	–	700(600)	1500(700)
R/DC→2523	–	700(400)	4200(700)	4400(900)	7000(900)	5800(800)
R/DC→3062	2800(1000)	3100(800)	11900(1500)	11500(1700)	12600(1500)	10400(1700)
R/DC→3134	–	–	–	1000(600)	700(600)	1600(600)
R/DC→3358	–	–	–	2300(900)	1400(800)	1400(700)
R/DC→3724	1000(500)	–	–	1100(600)	1500(500)	1800(500)
R/DC→3791	–	–	–	5000(900)	7100(800)	7000(1000)
R/DC→3839	7800(1100)	6500(900)	22300(1600)	29400(1700)	34200(16000	37500(1700)
R/DC→4116	4000(800)	3000(700)	11000(1200)	15300(1200)	14900(1100)	17000(1200)
R/DC→4226	–	–	1200(700)	1300(700)	1100(600)	–
R/DC→4360	–	–	–	–	–	800(500)
R/DC→4398	–	–	1000(700)	2500(800)	2000(600)	2800(700)
R/DC→4652	–	1000(500)	–	1800(700)	5100(800)	3200(600)
R/DC→4964	1000(500)	500(500)	7200(900)	10000(1000)	8400(900)	2800(900)
$\mathrm{N_R^{total}}$	33000(3000)	30000(2000)	120000(4000)	174000(5000)	183000(5000)	188000(5000)
N_p ($\times 10^{20}$)	6.23(19)	3.37(10)	0.93(3)	0.624(19)	0.312(9)	0.187(6)

[1] Adopted from g.s. transition fit in HPGe singles spectrum.
[2] Ground state transition enhancement excluded from the analysis.

Table 6.19: Branching ratios were calculated from the partial and total number of reactions in Tab. 6.18. Each partial value was divided by the total number of reactions to determine the branching ratio.

	Branching Ratio (%) by E_p (keV)					
Transition	175	190	250	275	300	325
R/DC→0	–	3.1(10)	5.1(9)	5.0(11)	3.9(10)	–
R/DC→937	37(5)	40(5)	36(2)	33.8(17)	36.2(16)	40.9(19)
R/DC→1042	–	3.1(13)	–	0.7(4)	0.6(3)	0.2(1)
R/DC→1121	7(3)	5(3)	9.6(14)	10.6(12)	6.4(9)	9.2(11)
R/DC→1701	2.2(16)	–	–	0.6(3)	–	–
R/DC→2101	3.3(19)	–	–	–	0.4(3)	0.8(4)
R/DC→2523	–	2.3(15)	3.5(6)	2.5(5)	3.9(5)	3.1(4)
R/DC→3062	9(3)	10(3)	9.9(13)	6.6(10)	6.9(9)	5.6(9)
R/DC→3134	–	–	–	0.5(3)	0.4(3)	0.8(3)
R/DC→3358	–	–	–	1.3(5)	0.8(5)	0.7(4)
R/DC→3724	3.0(14)	–	–	0.6(4)	0.8(3)	0.9(2)
R/DC→3791	–	–	–	3.0(5)	3.9(4)	3.7(6)
R/DC→3839	24(4)	22(3)	18.6(14)	16.9(11)	18.7(10)	19.9(10)
R/DC→4116	12(3)	10(2)	9.1(10)	8.8(7)	8.2(6)	9.0(7)
R/DC→4226	–	–	1.0(6)	0.8(4)	0.6(3)	–
R/DC→4360	–	–	–	–	–	0.4(3)
R/DC→4398	–	–	0.8(6)	1.5(4)	1.1(3)	1.5(4)
R/DC→4652	–	3.5(15)	–	1.1(4)	2.8(4)	1.7(3)
R/DC→4964	3.0(16)	1.6(15)	6.0(8)	5.7(6)	4.6(5)	1.5(5)

6.3.8: Astrophysical S-Factor Calculations

The analysis code, *sfactor.cxx*, uses the Monte Carlo technique described in Appendix A.1 to solve an analytical expression of the astrophysical S-factor at each experimental energy. All input parameters are defined as probability density functions. To accomplish this calculation, an analytical expression for the S-factor must be derived from the numerical equations, Eq. 6.22, with the substitution from Eq. 2.17:

$$\sigma(\mathrm{E}) = \frac{\mathrm{S(E)}}{\mathrm{E}} e^{-2\pi\eta}. \tag{6.23}$$

This is accomplished through the calculation of effective energies (described below). The code *sfactor.cxx* solves for the effective energy utilizing the formalism explained by Ref. [158]. In this paper, the authors make the case that a generalized energy deconvolution procedure can be derived if adjustments to the experimental cross section are considered in addition to the energy [158]:

$$\sigma_{exp}(\mathrm{E}_{eff}) = \frac{Y(\mathrm{E}_0)}{fn\Delta x} \tag{6.24}$$

where E_{eff} is the effective energy, f is the adjustment factor, n is the number density of target atoms, Δx is the linear target thickness, E_0 is the incident beam energy in the center-of-mass frame, and Y is the reaction yield. The effective energy is the energy at which the following expression is true [159]:

$$\sigma(E_{eff}) \int_{E_0-\Delta E}^{E_0} \frac{dE}{\epsilon(E)} = \int_{E_0-\Delta E}^{E_0} \frac{\sigma(E)}{\epsilon(E)} dE \tag{6.25}$$

where ΔE is the target thickness and $\epsilon(E)$ is the effective stopping power. The authors of Ref. [158] go on to present several acceptable deconvolution procedures and their analytical expressions; however, the procedure that best resembles the technique described by Ref. [4] is the *median energy*. Within this dissertation, the effective beam energy is in fact the median energy according to the deconvolution procedure outlined by Ref. [158] and $E_{eff} = E_m$. To calculate the median energy, the energy dependence of the cross section is assumed to be at most quadratic. The median energy is then defined as:

$$E_{eff} = E_m = E_0 - \frac{1}{2}\Delta E + \frac{[1 + R_1^2(\Delta E)^2/4]^{1/2} - 1}{R_1} \tag{6.26}$$

where R_1 is defined as:

$$R_1 = \frac{1}{\sigma_h}\left(\frac{d\sigma}{dE}\right)_{E_h}. \tag{6.27}$$

In this equation, $E_h = E_0 - \Delta E/2$ and $\sigma_h = \sigma(E_h)$ where it is assumed (based on the observed energy dependence in the literature) that the cross section is quadratic. The median adjustment factor can be calculated with the following equation [158]:

$$f_m^{-1} = [1 + \frac{1}{4}R_1^2(\Delta E)^2]^{1/2}. \tag{6.28}$$

Equation 6.24 can then be rewritten in terms of the effective stopping power, the target thickness, and the astrophysical S-factor as:

$$S(E_{eff}) = \frac{Y(E_0)\epsilon(E_0)E_{eff}e^{2\pi\eta}}{f_m \Delta E(E_0)} \tag{6.29}$$

where the number density of target atoms and linear target thickness was written as $n\Delta x = \Delta E(E_0)/\epsilon(E_0)$ and f_m is the median adjustment factor. This expression assumes the effective stopping power is constant and the cross section does not vary drastically (e.g. narrow resonances) over the target thickness [4].

Next, the $E_R^{cm} = 556$ and 676 keV resonance parameters listed in Tabs. B.2 and 6.13 are inputed into the Breit-Wigner code *reacnumeric.f* [154]. All input parameters are assigned probability density functions and the Breit-Wigner equation is solved by sampling these PDFs. This procedure gives the S-factor for each broad resonance at each beam energy. The Breit-Wigner code was imbedded within the *sfactor.cxx*

analysis code to extract the resonance S-factors. Because the total S-factor is the incoherent sum of the direct capture S-factors and the broad resonance S-factors, the difference between a total S-factor and the broad resonance S-factor yields the direct capture S-factor at each bombarding energy. The total astrophysical S-factor calculated at each beam energy is listed in Tab. 6.20 alongside the effective (median) energy. These S-factors are plotted as solid red circles in Fig. 6.10 along with the literature values from Fig. 6.1.

Table 6.20: The effective (median [158]) energy is tabulated for each laboratory bombarding energy alongside the corresponding total astrophysical S-factor and direct capture S-factor. S-factors were calculated with the analysis code *sfactor.cxx*.

E_p (keV)	E^{cm}_{eff} (keV)	S_{total} (keV b)	S_{DC} (keV b)
175	160.1(10)	5.2(6)	4.4(6)
190	174.5(15)	4.9(6)	4.1(6)
250	228.1(19)	6.0(5)	4.9(5)
275	255.1(13)	6.1(5)	4.8(5)
300	276.4(19)	6.7(5)	5.2(6)
325	300.7(16)	6.9(5)	5.0(5)

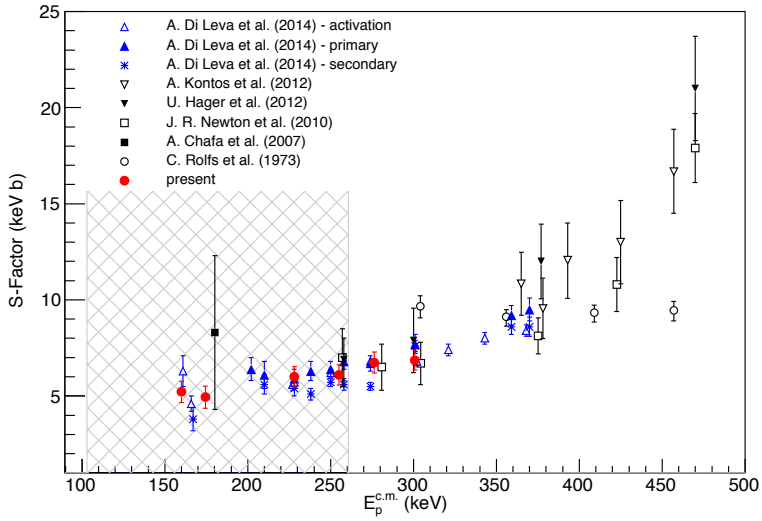

Figure 6.10: The new total S-factors are added to the plot of the literature values shown in Fig. 6.1. The Gamow window for classical novae is shown as a grey, cross-hatched energy region (103−261 keV). The experimental total S-factors from the present work are shown as solid red circles. Note that energy data points from the present work are prompt γ-ray measurements, and the present work contains the lowest in-beam measurement within the classical nova Gamow window.

The direct capture S-factor is also tabulated at each experimental energy in Tab. 6.20 and plotted as solid black squares in Fig. 6.11. In Fig. 6.11, the black dotted line represents the resonance tail contribution from the $E^{cm}_R = 556$ and 676 keV resonances. The total S-factors are represented by solid red circles. Based on the

assertion of Ref. [75], it was assumed that the direct capture S-factor is constant, and this assumption was bolstered by direct capture model calculations performed with the code TEDCA [138]. A new direct capture S-factor curve, the solid purple line in Fig. 6.11, was determined from the average of the extracted direct capture S-factor data points.

The uncertainty in this new S-factor curve has three contributions: statistical, systematic, and broad resonance uncertainties. Statistical uncertainties arise from experimental and Monte Carlo counting statistics. Systematic uncertainties come from GEANT4, stopping powers, charge integration, target thickness, peak and total efficiencies, and the ^{17}O-enriched water (see Tab. 6.7 for the accepted systematic uncertainty percentages).

Broad resonance S-factor uncertainties were calculated by the *reacnumeric.f* [154] code imbedded within *sfactor.cxx*, as discussed above. The input to this new code, partial widths and branching ratios, can be found in Tabs. B.2 and 6.13, respectively. The accepted partial widths and branching ratios were reconciled from the literature with the reconfigured mean procedure detailed in Appendix A.2 (unless otherwise noted). Partial widths were associated with lognormal probability distributions according to the prescription outlined in Section 2.2.1. For more information on calculating uncertainties with a Monte Carlo approach, see Appendix A.1.

The statistical uncertainty on each of the six direct capture data points was used to weight the new direct capture S-factor. The average of the systematic uncertainties and of the broad resonance tail uncertainties for each data point were added in quadrature with the uncertainty on the weighted average. This gives a final, constant direct capture S-factor value at low energies of:

$$S_{DC}(0) = (4.82 \pm 0.41) \text{ keV b} \tag{6.30}$$

for $E_{eff}^{cm} < 305$ keV. This corresponds to an uncertainty of 8.6% on the new direct capture S-factor.

Section 6.4: Reaction Rates

The goal of this research was to reduce the uncertainty on the ^{17}O(p,γ)^{18}F thermonuclear reaction rate at stellar plasma temperatures that correspond to explosive hydrogen burning during classical novae. Additionally, it was anticipated that rate might improve within the temperature regime relevant to *hot bottom burning* in asymptotic giant branch (AGB) stars. New reaction rates were calculated with the Monte Carlo method developed by Ref. [88]; this method is based on the analysis argument discussed in Appendix A.1 and described in more detail in Section 2.2. Figure 6.12 shows some of the histograms (in red) populated by

RatesMC during this reaction rate calculation. The black line in each panel is not a fit but is in fact the lognormal probability density function corresponding to lognormal-μ and lognormal-σ calculated by the Monte Carlo code at each temperature. These values were calculated with Eqs. 2.49−2.51. Histograms and probability density functions are shown for $T_9 = 0.04$, 0.07, 0.1, 0.25, 0.4, and 0.7 to provide a decent sample of RatesMC output over the classical nova and hot bottom burning AGB star Gamow windows.

Input to the reaction rate Monte Carlo code, RatesMC, can be found in Appendix B.2.2 where resonance parameters were reconciled from the literature with the procedure explained in Appendix A.2 and tabulated in Tabs. B.1 and B.2.

The computed Monte Carlo reaction rates were examined carefully because Di Leva *et al.* (2014) [82] asserts that the LUNA collaboration was able to improve the reaction rate presented by Refs. [143, 78] within the classical nova Gamow window by a factor of 4. This requires some clarification that is not provided by the authors in Ref. [82]. In Iliadis *et al.* (2010) [135], the $E_R = 193$ keV resonance interference is taken into account; the 193 keV resonance interferes with the 1098 keV (lab) resonance because both levels have spin and parity of $J^\pi = 2^-$. The rate is sampled over the unknown interference sign. The reaction rate code, RatesMC, integrates numerically, Eqs. 2.8 and 2.43, to solve for the reaction rate if interference

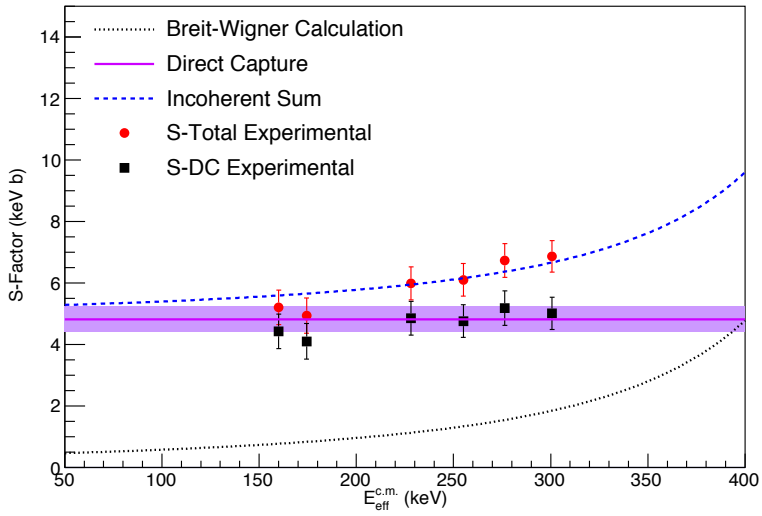

Figure 6.11: Broad resonance S-factor contributions from resonances at $E_R^{cm} = 556$ and 676 keV were calculated with a Breit-Wigner code (dotted black line). These S-factors were subtracted from the total experimental S-factor (solid red circles) to arrive at the experimental direct capture S-factors (solid black squares). The mean of the six experimental direct capture S-factors, weighted by their statistical uncertainty, was calculated (purple line). Systematic, statistical and broad resonance uncertainties were added in quadrature to calculate the pink error band. The total S-factor (dashed blue line) is shown to illustrate the energy dependence of the total S-factor—first proposed by Ref. [75].

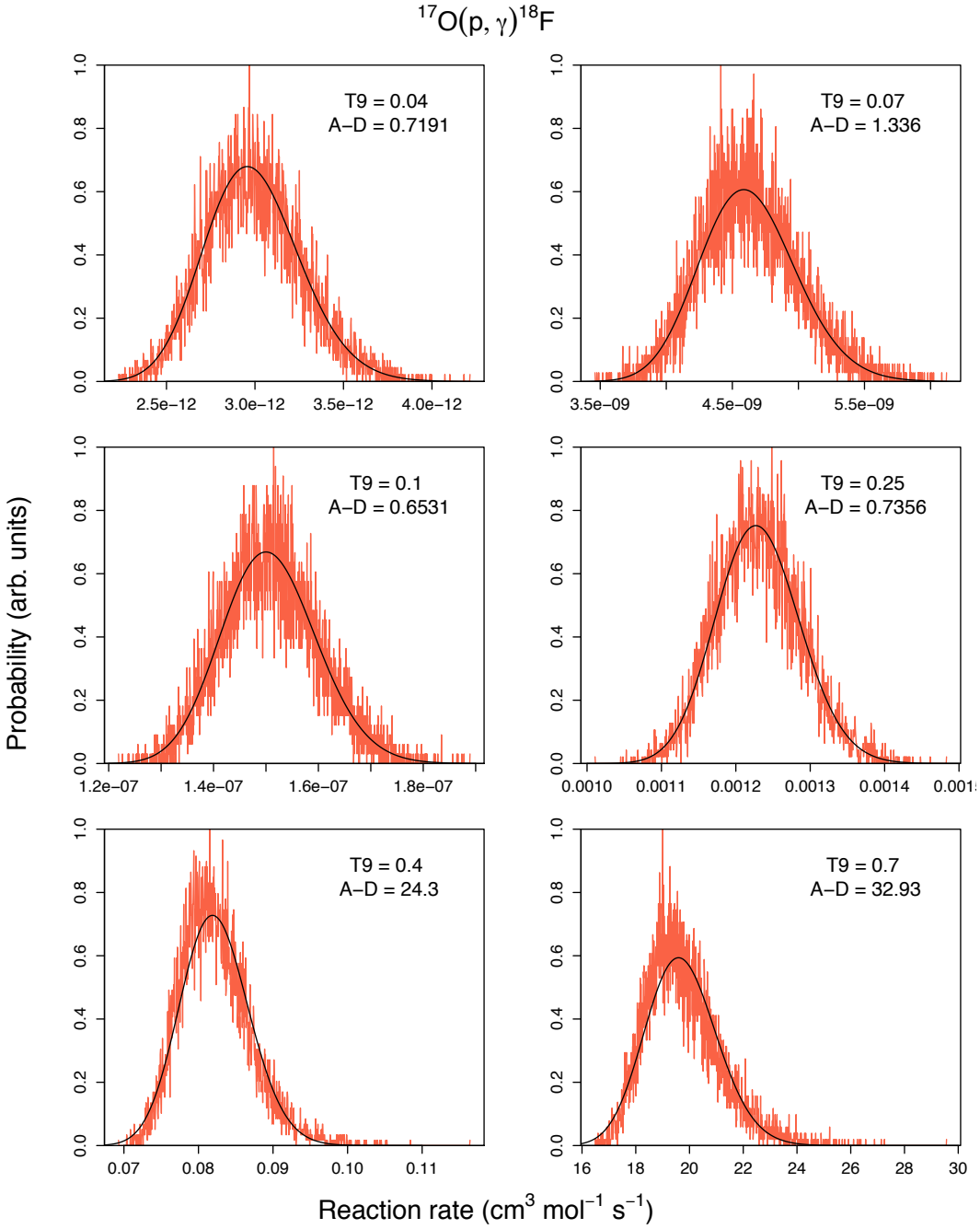

Figure 6.12: Reaction rate probability density functions calculated by the reaction rate Monte Carlo code, RatesMC [88], at T = 0.04, 0.07, 0.1, 0.25, 0.4, and 0.7 GK. The red histograms are the Monte Carlo rates and the solid black lines are lognormal probability density functions (not fits to the histograms). Anderson-Darling statistics are shown in each figure.

considerations are included. There is no option to solve for the rate analytically (Eq. 2.35) if the strength of one of the resonances is known. The resonance strength of the $E_R = 193$ keV resonance was first determined by Ref. [51] to be $\omega\gamma = 1.2 \pm 0.2$ μeV by in-beam measurement. Reference [76] used activation techniques to arrive at a final resonance strength of $\omega\gamma = 2.2 \pm 0.4$ μeV [145, 144]; these strengths are excluded from the analysis. The recent publication by Ref. [82] identified nine primary transitions associated with the 193 keV resonance (as opposed to the two transitions identified by Ref [75] that Ref. [82] argues only contribute 65% of the total strength). The strength determined by the LUNA collaboration in Refs. [80, 82] was $\omega\gamma = 1.67 \pm 0.12$ μeV. The authors then claim they utilized a Monte Carlo method similar to the calculations performed here with RatesMC to determine the reaction rate. Though little is known about the LUNA analysis code, it must be assumed they solved for the rate analytically with their new resonance strength, but it is not clear if they accounted for interference between the 193 keV and 1098 keV resonances. This means that their claim that their reaction rate is an improvement of a factor of 4 over the Iliadis *et al.* (2010) reaction rate is an *error of omission*; LUNA is not comparing rates that are calculated the same way—Ref. [135] solved numerically for the rate, accounted for interference and used all partial widths (with their associated uncertainties) while Ref. [82] solved for the rate analytically with a resonance strength that has a 7% uncertainty associated with it. This difference alone accounts for the factor of 4 decrease in the reaction rate uncertainty within the classical nova Gamow window.

To proceed with the reaction rate calculation here, the sensitivity of the rate to the interference between the 193 and 1098 keV resonances must be assessed with RatesMC. The reaction rate was calculated numerically with the partial widths and their associated uncertainties two different ways: (1) assuming that the interference affects the rate, and (2) assuming that the interference between the 193 and 1098 keV resonances has a negligible impact on the total rate. Fig. 6.13 shows the result of this sensitivity assessment. The top plot shows the ratio between the median rate and the high and low rate for each case. The solid black line represents the reaction rate ratio where the interference between the two resonances is not assumed to affect the rate, and the dashed line assumes that interference should be considered. The bottom plot shows the ratio between the two rates—the low, median, and high rates without interference are compared to the recommended rate with interference. As the figures show, the rates do not differ significantly, and any observed difference is within the uncertainty associated with the Monte Carlo calculation ($< 1\%$). The 193 and 1098 keV resonances interference is ignored here because it does not affect the total reaction rate appreciably.

Next, the assertion made above, that it is illegitimate to compare the reaction rate presented in Refs. [143, 139] with the rate in Ref. [82], was assessed. The reaction rate was again calculated twice: (1) the 193 keV contribution was calculated numerically with the available partial widths listed in Tab. B.2 and (2)

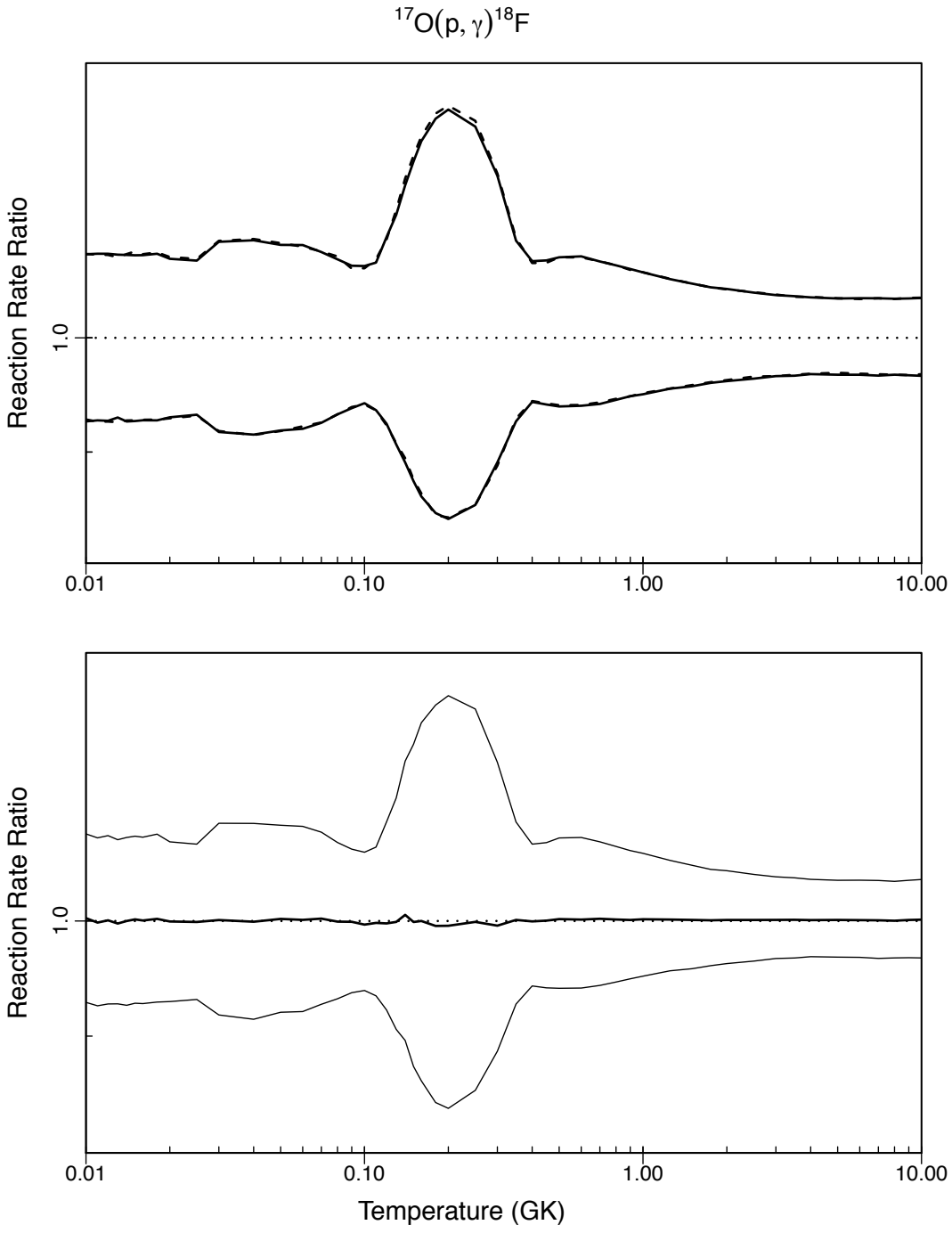

Figure 6.13: A comparison between the reaction rate ratios if the interference between the $E_R = 193$ and 1098 keV resonances is assumed to have an appreciable impact on the reaction rate (dashed line) and if interference between these resonances does not influence the rate dramatically (solid line). Reaction rates calculated with and without this interference condition are indistinguishable within the uncertainty of the RatesMC Monte Carlo code. Interference between these two $J^\pi = 2^-$ resonances was not included in the final rate calculation. The top figure shows the high and low rates normalized to the median rate in each scenario. The bottom figure represents the ratio between the rate calculated without this interference and the rate calculated with this interference.

the 193 keV contribution was calculated analytically with $\omega\gamma = 1.76 \pm 0.09$ μeV, the weighted mean of the strength determined in the present work and the strength from Refs. [80, 82]. The normalized uncertainty in the rate decreases by as much as 15% within the classical nova Gamow window if the resonance strength is used instead of solving for the rate contribution numerically with partial widths and their associated uncertainties. This confirms that it is disingenuous to claim a factor of 4 reduction in the reaction rate between Refs. [143, 135, 139] and Ref. [82] without first clarifying that the rates are being calculated very differently and certain experimental uncertainties are either being included or excluded. Figure 6.14 compares the reaction rate calculated with the 193 keV resonance strength (analytically, Eq. 2.35) or with the partial widths associated with this level (numerically, Eq. 2.8). The solid black line in the top figure represents the ratio between the rate limits and the median rate where the 193 keV resonance strength is used. The dashed black line is the reaction rate ratio if the 193 keV resonance partial widths are used and the contribution to the total rate is calculated numerically. The bottom plot shows the ratio between the rate calculated with the strength versus without it. The reaction rate calculated with the weighted mean of the present and LUNA 193 keV resonance strengths was adopted here for this analysis.

The new ^{17}O(p,γ)^{18}F reaction rate was then compared to the NACRE reaction rate from Ref. [91]. This was included because surprisingly, many in the nuclear astrophysics community still use and cite this dated rate compilation. It is important to clarify and emphasize how out of date NACRE rates are. The new rates presented in this thesis improve upon the NACRE rates with a 30% reduction in the normalized rate uncertainty within the classical nova Gamow window and a reduction of 23% in this uncertainty within the AGB hot bottom burning Gamow window. Figure 6.15 shows the ratio between the uncertainties and median recommended rate for both the new rate (solid line) and the NACRE rate (dashed line) in the top plot. In the bottom plot, the ratio between the new low, high, and median rates and the recommended NACRE rate are shown. There is a slight spike in the new ^{17}O(p,γ)^{18}F reaction rate within the hot bottom burning temperature regime compared to the NACRE rate (see the bottom plot in Fig. 6.15). Reference [15] studied the evolution of isotopic ratios in the solar neighborhood with detailed stellar models. In this paper, the authors likely used the NACRE ^{17}O(p,γ)^{18}F reaction rate, and they observed an overproduction of ^{17}O by their AGB stellar models that disagrees with solar abundances. While direct measurement of the E_R^{cm} = 65 keV resonance will likely improve the reaction rate uncertainty, the new rates presented in this thesis clearly improve the rate uncertainty over the NACRE rates. This improvement comes from the assessment of the literature partial widths discussed in Appendix B.1.1 and listed in Tab. B.2. As will be shown later in Fig. 6.19, direct capture also contributes to that rate at hot bottom burning temperatures. The increase in the reaction rate observed at hot bottom burning stellar plasma temperatures could account for observed solar abundances that Ref. [15] could not reconcile with the reaction rates they had at the time; an increase

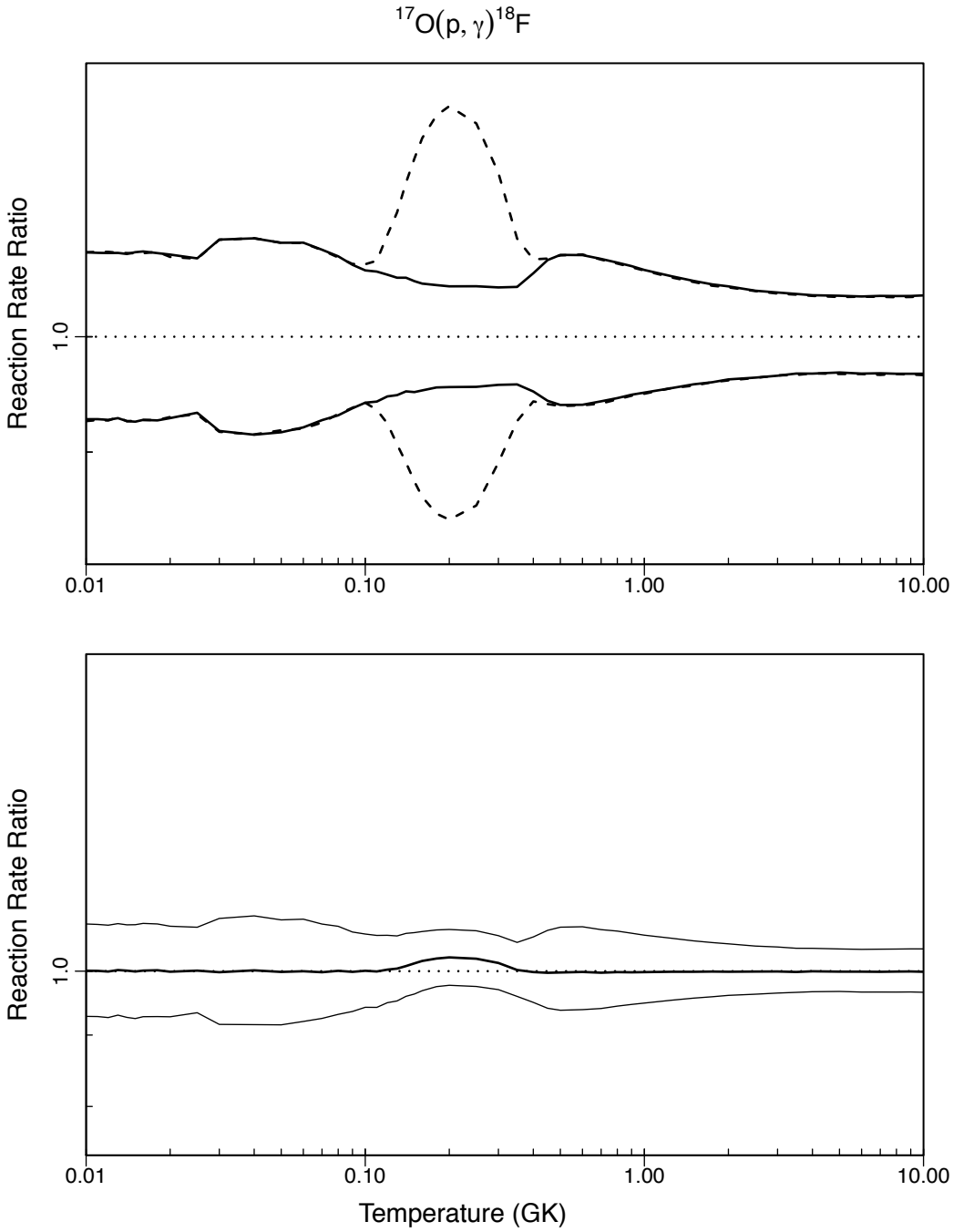

Figure 6.14: Monte Carlo reaction rates were compared for two scenarios; in the first scenario, the $E_R = 193$ keV and 1098 keV resonances are assumed to interfere and the calculation was performed numerically with Eq. 2.8 (dashed line). The second scenario disregards the interference and uses the strength from Eq. 6.11 to calculate the rate analytically with Eq. 2.35 (solid line). Uncertainty in the normalized rate decreases by 15% if the analytical calculation is performed. This is because fewer terms with inherent uncertainties are being used in the rate calculation. The top figure shows the high and low rates normalized to the median rate in each scenario. The bottom figure represents the ratio between the rate calculated analytically and the median rate calculated numerically.

in the rate destroys ^{17}O and decreases the ^{17}O contribution made by this class of AGB star.

It is important to compare the new reaction rates from this thesis with the original rates from the 2010 LENA rate compilation, Refs. [88, 143, 135, 139], because this was the introduction of RatesMC and the first time Monte Carlo techniques were used to calculate thermonuclear reaction rates. Input to the reaction rate Monte Carlo code was updated for these new calculations based on the literature (see Tab. B.2), the direct capture astrophysical S-factor measured during this experiment, and the E_R = 193 and 518 keV resonance strengths measured in this study. It was discussed numerous times in this dissertation how the resonance input was reconciled from the literature and the new direct capture S-factor can be found in Eq. 6.30. The new E_R = 193 and 518 keV resonance strengths can be found in Eqs. 6.11 and 6.8, respectively. With all of these changes and improvements accounted for, the normalized rate uncertainty improves by 18% in the classical nova Gamow window (note that as explained above, Ref. [135] used a numerical calculation of the 193 keV resonance contribution to the rate while an analytical calculation is performed here). The uncertainty in the normalized rate decreased by 7% in the temperature regime relevant to hot bottom burning in AGB stars. Figure 6.16 shows the ratio between the uncertainties and median value for both the new rate (solid line) and the 2010 LENA rate (dashed line) in the top plot. In the bottom plot, the ratio between the new low, median, and high rate and the recommended LENA rate are shown.

Finally, the new rate from this dissertation is compared to the rate from the recent papers by the LUNA collaboration [82, 80]. By using the weighted mean of the present and LUNA resonance strength for the E_R = 193 keV resonance, the new normalized reaction rate uncertainty presented here is as much as 2% lower than the LUNA rate within the classical nova Gamow window at *high* temperatures (near 400 MK). The new rate from the present study features a reduction in the normalized reaction rate uncertainty by as much as 6% at temperatures relevant to hot bottom burning in AGB stars. Fig. 6.17 shows the ratio between the uncertainties and median value for both the new rate (solid line) and the LUNA rate (dashed line) in the top plot. In the bottom plot, the ratio between the new low, median, and high rates and the recommended LUNA rate are shown.

Figure 6.18 plots the new, normalized ^{17}O(p,γ)^{18}F thermonuclear reaction rate from 0.01−10 GK. A *black-red-yellow* color scheme is used to differentiate between the different quantiles of this two-dimensional probability density function (reaction rate versus temperature). The reaction rate is normalized to the median rate. The 1σ contour is shown as a thick black line and the 2σ contour is a thin black line. The low, median, and high rates with their associated lognormal-μ and lognormal-σ are tabulated in Tab. 6.21. Anderson-Darling statistics, a measure of how well the Monte Carlo reproduces a particular probability density function (in this case a lognormal distribution) [88], are also tabulated. The experimental data determine the rates over the full temperature range of 0.01−10 GK, and no extrapolations using nuclear

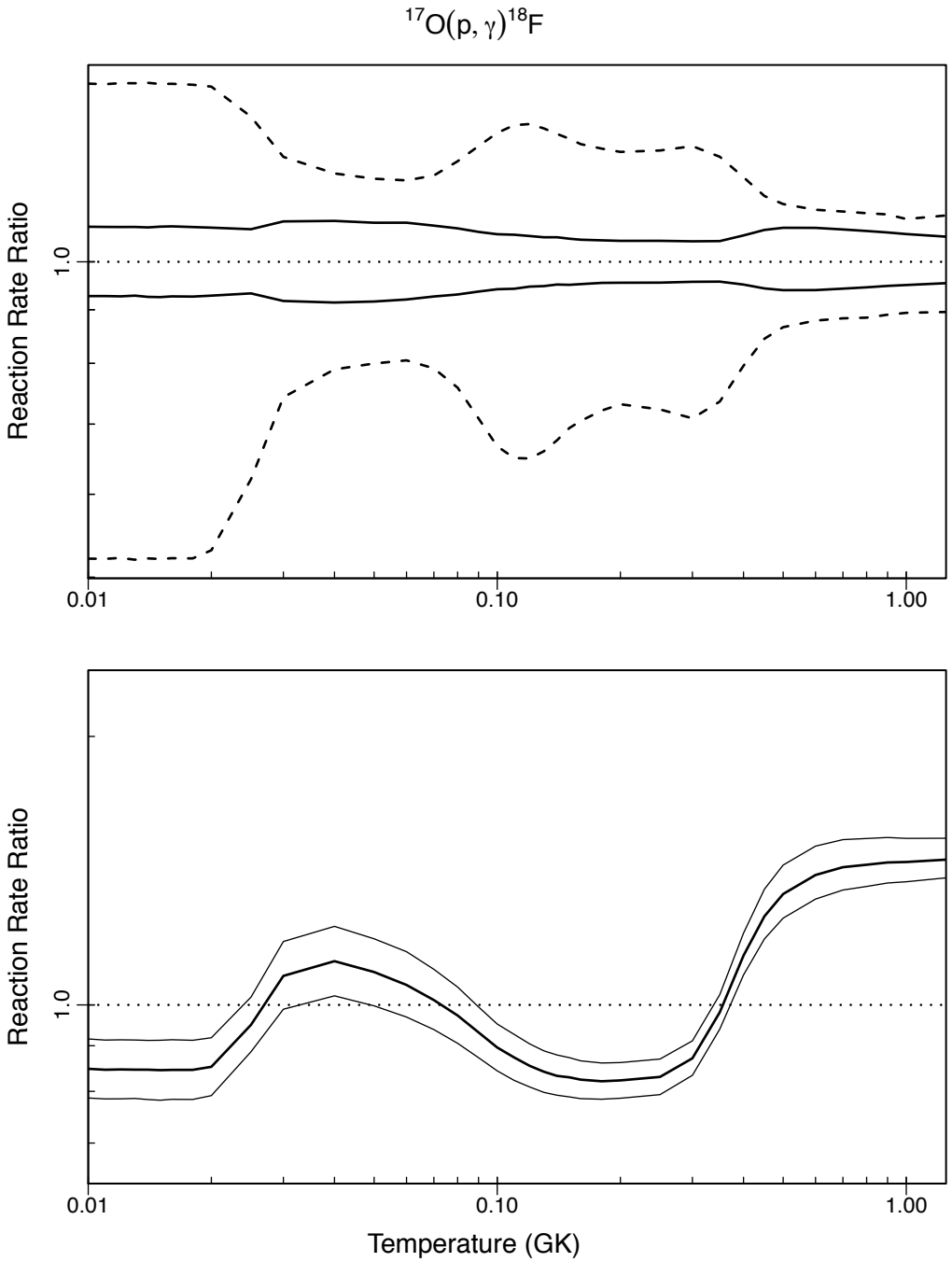

Figure 6.15: The reaction rate from this work (solid line) is compared to the rate from the NACRE reaction rate compilation, Ref. [91]. The uncertainty in the normalized rate decreases by as much as 30% within the classical nova Gamow window (0.1−0.4 GK) and 23% within the hot bottom burning Gamow window (0.03−0.1 GK). The top figure shows the rate normalized to the median rate from the present study and the NACRE recommended rate [91]. The bottom figure represents the ratio between the new low, median, and high rates and the NACRE recommended rate.

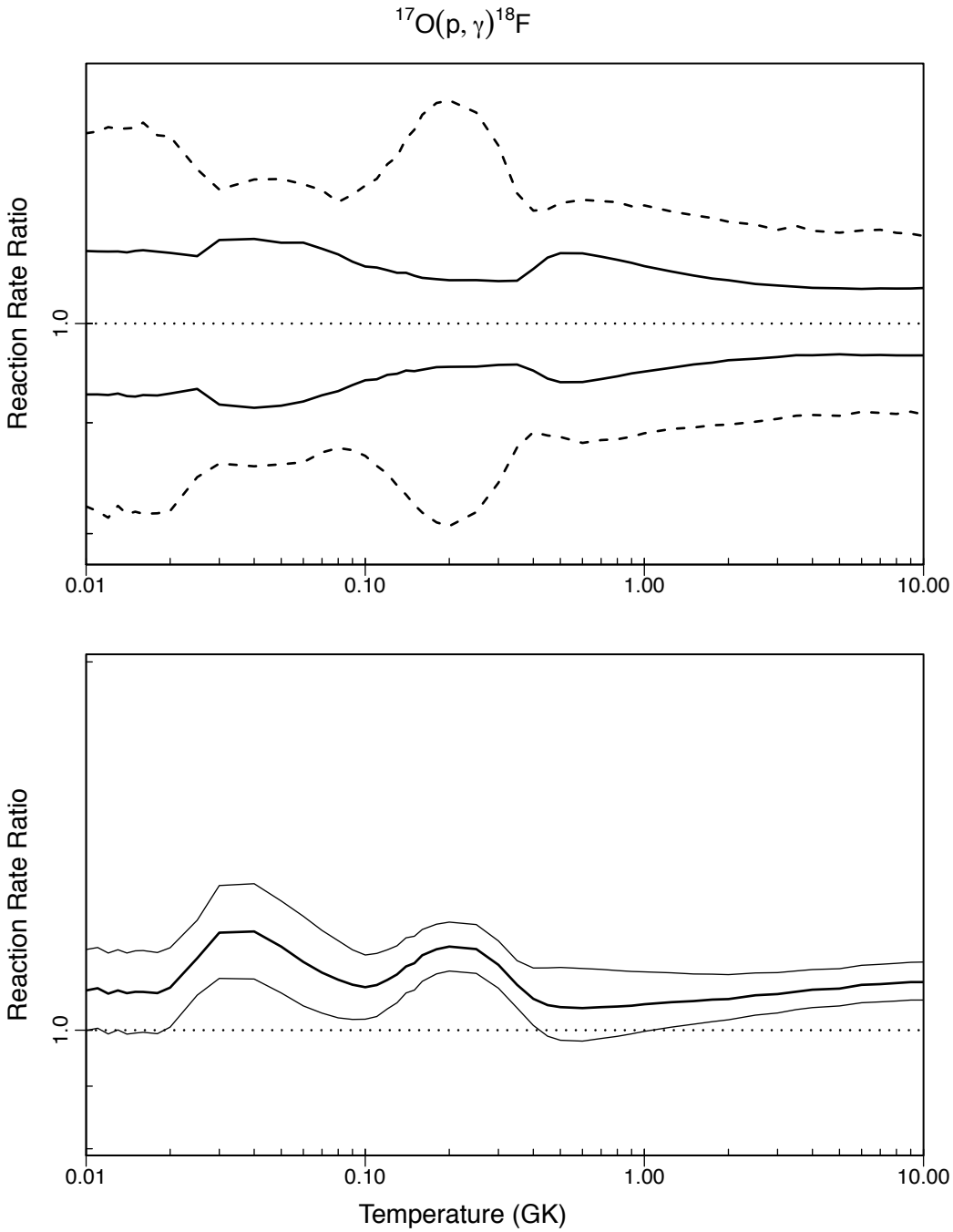

Figure 6.16: The reaction rate from this work (solid line) is compared to the rate from the 2010 LENA reaction rate compilation, Refs. [88, 143, 135, 139]. The uncertainty in the normalized rate decreases by as much as 18% within the classical nova Gamow window (0.1−0.4 GK) and 7% within the hot bottom burning AGB star Gamow window (0.03−0.1 GK). The top figure shows the rate normalized to the median rate for the present study (solid line) and the 2010 LENA rate (dashed line) [143, 90]. The bottom figure represents the ratio between the new low, median, and high rates and the recommended LENA rate.

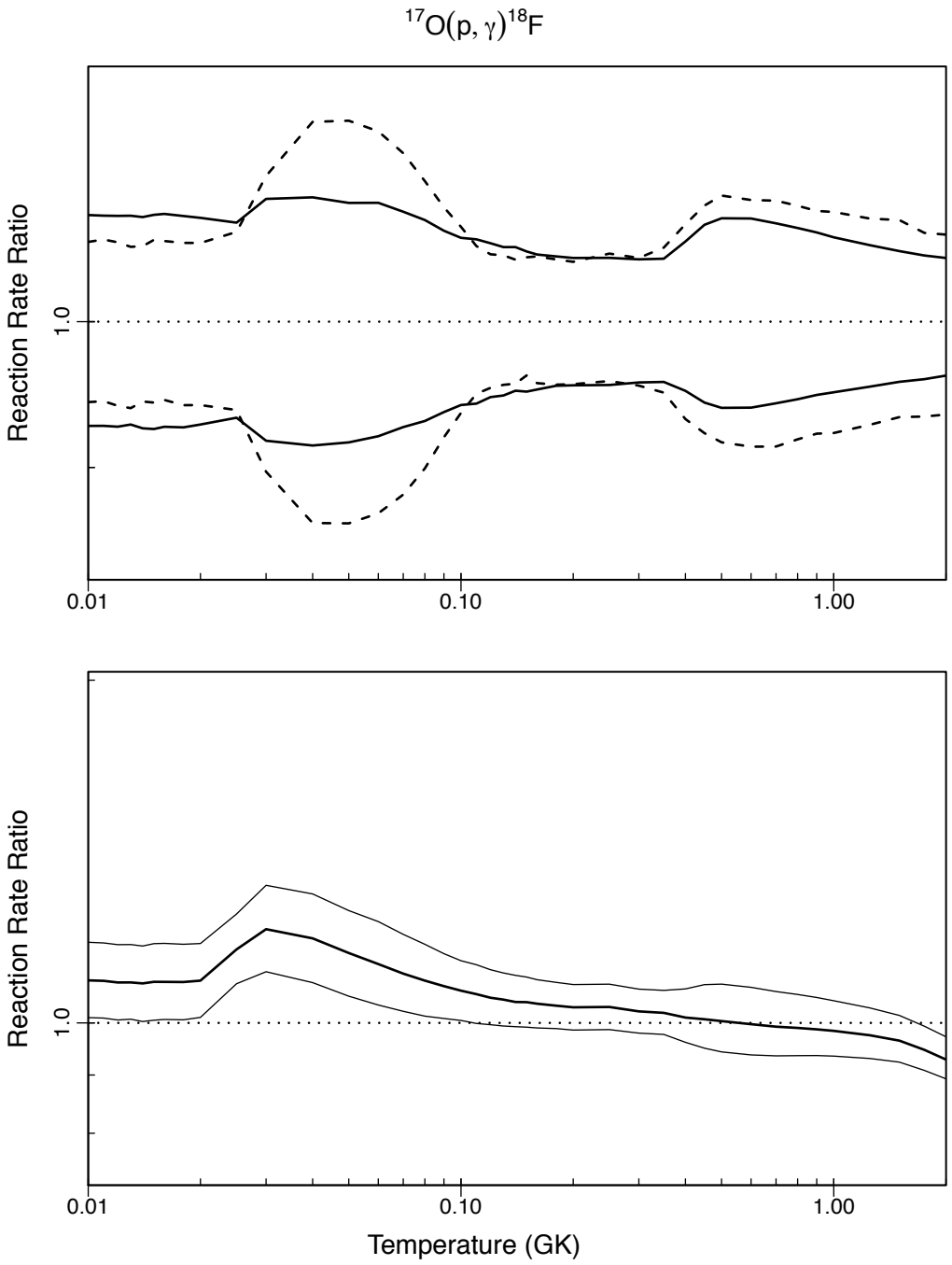

Figure 6.17: The reaction rate from this work (solid line) is compared to the LUNA reaction rate, Refs. [80, 82]. The uncertainty in the normalized rate is as much as 2% lower within the classical nova Gamow window (0.1−0.4 GK) in this work. Within the hot bottom burning AGB star Gamow window (0.03−0.1 GK) the normalized rate uncertainty is as much as 6% lower than the recent LUNA rate. The top figure shows the rate normalized to the median rate for the present study (solid line) and the LUNA experiment (dashed line) [82]. The bottom figure represents the ratio between the new low, median, and high rate and the recommended LUNA rate.

theory were necessary.

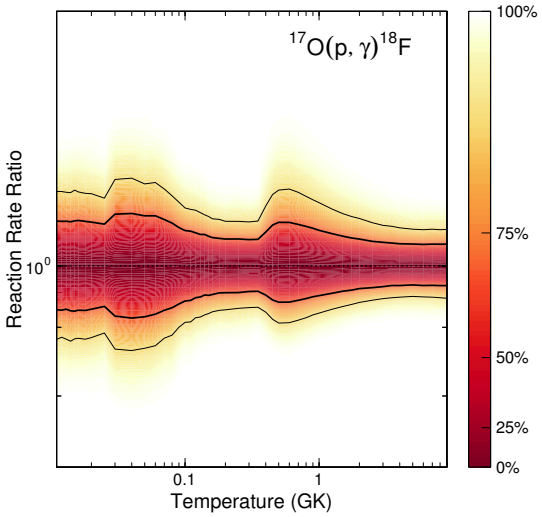

Figure 6.18: The reaction rate probability density as a function of temperature. The *black-red-yellow* color scheme is meant to illustrate that the high and low rates are not hard cutoffs. The low, median, and high rates represent the 0.16, 0.5, and 0.84 quantiles of the probability density function, respectively. The thick black lines represent 1σ coverage and the thin black lines represent 2σ coverage.

The reaction rate can also be broken up into its fractional contributions—the direct capture and individual resonant contributions to the total rate. Figure 6.19 shows the contribution from each resonance and from direct capture (labeled "A-Rate 1" in this figure). The high and low rate contributions (0.16 to 0.84 quantiles or 1σ) are plotted producing the colored bands shown in the figure. In Fig. 6.19, the interference contribution from the $E_R^{cm} = 65$ and -2 keV resonances ($J^\pi = 1^-$) is labeled *Intf 1*. The interference between $E_R^{cm} = 676$ and 778 keV resonances ($J^\pi = 2^+$) is labeled *Intf 2*. The reaction rate is still clearly dominated by the direct capture contribution at classical nova temperatures. This confirms the assessment of rate contributions made by Newton *et al.* (2010) [78]. Also, in the figure it is clear that direct capture, though not the dominant contribution, contributes almost 20% of the total reaction rate at hot bottom burning temperatures.

Table 6.21: The final ^{17}O(p,γ)^{18}F reaction rates from this study calculated with the reaction rate Monte Carlo code, RatesMC [88].

T (GK)	Low Rate	Median Rate	High Rate	Lognormal μ	Lognormal σ	A−D
1.000×10^{-02}	3.578×10^{-25}	3.858×10^{-25}	4.167×10^{-25}	$-5.621\times10^{+01}$	7.738×10^{-02}	3.922×10^{-01}
1.100×10^{-02}	3.797×10^{-24}	4.094×10^{-24}	4.420×10^{-24}	$-5.385\times10^{+01}$	7.675×10^{-02}	3.013×10^{-01}
1.200×10^{-02}	3.068×10^{-23}	3.310×10^{-23}	3.573×10^{-23}	$-5.176\times10^{+01}$	7.633×10^{-02}	7.062×10^{-01}
1.300×10^{-02}	1.995×10^{-22}	2.149×10^{-22}	2.320×10^{-22}	$-4.989\times10^{+01}$	7.620×10^{-02}	1.837×10^{-01}
1.400×10^{-02}	1.073×10^{-21}	1.159×10^{-21}	1.250×10^{-21}	$-4.821\times10^{+01}$	7.720×10^{-02}	4.710×10^{-01}

Table 6.21 – continued

T (GK)	Low Rate	Median Rate	High Rate	Lognormal μ	Lognormal σ	A−D
1.500×10^{-02}	4.957×10^{-21}	5.357×10^{-21}	5.787×10^{-21}	$-4.668\times10^{+01}$	7.744×10^{-02}	7.944×10^{-01}
1.600×10^{-02}	2.014×10^{-20}	2.173×10^{-20}	2.349×10^{-20}	$-4.528\times10^{+01}$	7.697×10^{-02}	3.988×10^{-01}
1.800×10^{-02}	2.405×10^{-19}	2.596×10^{-19}	2.802×10^{-19}	$-4.280\times10^{+01}$	7.654×10^{-02}	3.651×10^{-01}
2.000×10^{-02}	2.073×10^{-18}	2.233×10^{-18}	2.407×10^{-18}	$-4.064\times10^{+01}$	7.534×10^{-02}	2.710×10^{-01}
2.500×10^{-02}	2.100×10^{-16}	2.251×10^{-16}	2.418×10^{-16}	$-3.603\times10^{+01}$	7.061×10^{-02}	2.853×10^{-01}
3.000×10^{-02}	1.068×10^{-14}	1.164×10^{-14}	1.272×10^{-14}	$-3.208\times10^{+01}$	8.782×10^{-02}	6.060×10^{-01}
4.000×10^{-02}	2.723×10^{-12}	2.978×10^{-12}	3.258×10^{-12}	$-2.654\times10^{+01}$	8.993×10^{-02}	7.191×10^{-01}
5.000×10^{-02}	8.170×10^{-11}	8.915×10^{-11}	9.714×10^{-11}	$-2.314\times10^{+01}$	8.639×10^{-02}	2.877×10^{-01}
6.000×10^{-02}	8.015×10^{-10}	8.707×10^{-10}	9.488×10^{-10}	$-2.086\times10^{+01}$	8.447×10^{-02}	7.617×10^{-01}
7.000×10^{-02}	4.269×10^{-09}	4.607×10^{-09}	4.988×10^{-09}	$-1.919\times10^{+01}$	7.836×10^{-02}	$1.336\times10^{+00}$
8.000×10^{-02}	1.612×10^{-08}	1.732×10^{-08}	1.864×10^{-08}	$-1.787\times10^{+01}$	7.284×10^{-02}	2.855×10^{-01}
9.000×10^{-02}	5.035×10^{-08}	5.375×10^{-08}	5.740×10^{-08}	$-1.674\times10^{+01}$	6.549×10^{-02}	3.780×10^{-01}
1.000×10^{-01}	1.417×10^{-07}	1.505×10^{-07}	1.599×10^{-07}	$-1.571\times10^{+01}$	6.010×10^{-02}	6.531×10^{-01}
1.100×10^{-01}	3.736×10^{-07}	3.964×10^{-07}	4.207×10^{-07}	$-1.474\times10^{+01}$	5.925×10^{-02}	3.326×10^{-01}
1.200×10^{-01}	9.386×10^{-07}	9.912×10^{-07}	1.049×10^{-06}	$-1.382\times10^{+01}$	5.609×10^{-02}	$1.377\times10^{+00}$
1.300×10^{-01}	2.226×10^{-06}	2.348×10^{-06}	2.478×10^{-06}	$-1.296\times10^{+01}$	5.415×10^{-02}	9.502×10^{-01}
1.400×10^{-01}	4.982×10^{-06}	5.237×10^{-06}	5.527×10^{-06}	$-1.216\times10^{+01}$	5.256×10^{-02}	$1.321\times10^{+00}$
1.500×10^{-01}	1.041×10^{-05}	1.095×10^{-05}	1.152×10^{-05}	$-1.142\times10^{+01}$	5.038×10^{-02}	6.370×10^{-01}
1.600×10^{-01}	2.049×10^{-05}	2.152×10^{-05}	2.259×10^{-05}	$-1.075\times10^{+01}$	4.872×10^{-02}	7.693×10^{-01}
1.800×10^{-01}	6.663×10^{-05}	6.979×10^{-05}	7.316×10^{-05}	$-9.570\times10^{+00}$	4.707×10^{-02}	7.577×10^{-01}
2.000×10^{-01}	1.784×10^{-04}	1.868×10^{-04}	1.956×10^{-04}	$-8.585\times10^{+00}$	4.638×10^{-02}	5.905×10^{-01}
2.500×10^{-01}	1.174×10^{-03}	1.229×10^{-03}	1.287×10^{-03}	$-6.701\times10^{+00}$	4.595×10^{-02}	7.356×10^{-01}
3.000×10^{-01}	4.986×10^{-03}	5.210×10^{-03}	5.450×10^{-03}	$-5.256\times10^{+00}$	4.461×10^{-02}	7.121×10^{-01}
3.500×10^{-01}	1.954×10^{-02}	2.041×10^{-02}	2.136×10^{-02}	$-3.890\times10^{+00}$	4.466×10^{-02}	$2.987\times10^{+00}$
4.000×10^{-01}	7.779×10^{-02}	8.178×10^{-02}	8.666×10^{-02}	$-2.499\times10^{+00}$	5.612×10^{-02}	$2.430\times10^{+01}$
4.500×10^{-01}	2.822×10^{-01}	2.992×10^{-01}	3.209×10^{-01}	$-1.201\times10^{+00}$	6.602×10^{-02}	$3.034\times10^{+01}$
5.000×10^{-01}	8.695×10^{-01}	9.254×10^{-01}	9.972×10^{-01}	-7.115×10^{-02}	7.014×10^{-02}	$3.145\times10^{+01}$
6.000×10^{-01}	$5.099\times10^{+00}$	$5.426\times10^{+00}$	$5.846\times10^{+00}$	$1.698\times10^{+00}$	7.047×10^{-02}	$3.329\times10^{+01}$
7.000×10^{-01}	$1.843\times10^{+01}$	$1.955\times10^{+01}$	$2.099\times10^{+01}$	$2.980\times10^{+00}$	6.725×10^{-02}	$3.293\times10^{+01}$
8.000×10^{-01}	$4.820\times10^{+01}$	$5.098\times10^{+01}$	$5.455\times10^{+01}$	$3.938\times10^{+00}$	6.389×10^{-02}	$3.231\times10^{+01}$
9.000×10^{-01}	$1.011\times10^{+02}$	$1.066\times10^{+02}$	$1.137\times10^{+02}$	$4.675\times10^{+00}$	6.074×10^{-02}	$3.129\times10^{+01}$
$1.000\times10^{+00}$	$1.814\times10^{+02}$	$1.909\times10^{+02}$	$2.029\times10^{+02}$	$5.257\times10^{+00}$	5.792×10^{-02}	$3.110\times10^{+01}$
$1.250\times10^{+00}$	$5.053\times10^{+02}$	$5.296\times10^{+02}$	$5.597\times10^{+02}$	$6.276\times10^{+00}$	5.272×10^{-02}	$2.715\times10^{+01}$
$1.500\times10^{+00}$	$9.699\times10^{+02}$	$1.013\times10^{+03}$	$1.066\times10^{+03}$	$6.924\times10^{+00}$	4.878×10^{-02}	$2.636\times10^{+01}$
$1.750\times10^{+00}$	$1.508\times10^{+03}$	$1.572\times10^{+03}$	$1.649\times10^{+03}$	$7.363\times10^{+00}$	4.604×10^{-02}	$2.276\times10^{+01}$
$2.000\times10^{+00}$	$2.063\times10^{+03}$	$2.145\times10^{+03}$	$2.246\times10^{+03}$	$7.675\times10^{+00}$	4.402×10^{-02}	$2.353\times10^{+01}$
$2.500\times10^{+00}$	$3.075\times10^{+03}$	$3.192\times10^{+03}$	$3.329\times10^{+03}$	$8.071\times10^{+00}$	4.089×10^{-02}	$1.992\times10^{+01}$
$3.000\times10^{+00}$	$3.863\times10^{+03}$	$4.003\times10^{+03}$	$4.168\times10^{+03}$	$8.297\times10^{+00}$	3.874×10^{-02}	$1.606\times10^{+01}$
$3.500\times10^{+00}$	$4.414\times10^{+03}$	$4.565\times10^{+03}$	$4.747\times10^{+03}$	$8.429\times10^{+00}$	3.741×10^{-02}	$1.473\times10^{+01}$
$4.000\times10^{+00}$	$4.756\times10^{+03}$	$4.919\times10^{+03}$	$5.109\times10^{+03}$	$8.503\times10^{+00}$	3.647×10^{-02}	$1.318\times10^{+01}$
$5.000\times10^{+00}$	$5.000\times10^{+03}$	$5.166\times10^{+03}$	$5.363\times10^{+03}$	$8.552\times10^{+00}$	3.546×10^{-02}	$1.212\times10^{+01}$
$6.000\times10^{+00}$	$4.905\times10^{+03}$	$5.073\times10^{+03}$	$5.263\times10^{+03}$	$8.533\times10^{+00}$	3.546×10^{-02}	$8.505\times10^{+00}$
$7.000\times10^{+00}$	$4.682\times10^{+03}$	$4.841\times10^{+03}$	$5.025\times10^{+03}$	$8.487\times10^{+00}$	3.558×10^{-02}	$8.726\times10^{+00}$
$8.000\times10^{+00}$	$4.419\times10^{+03}$	$4.571\times10^{+03}$	$4.744\times10^{+03}$	$8.429\times10^{+00}$	3.565×10^{-02}	$6.461\times10^{+00}$
$9.000\times10^{+00}$	$4.155\times10^{+03}$	$4.298\times10^{+03}$	$4.461\times10^{+03}$	$8.367\times10^{+00}$	3.576×10^{-02}	$5.858\times10^{+00}$
$1.000\times10^{+01}$	$3.897\times10^{+03}$	$4.031\times10^{+03}$	$4.186\times10^{+03}$	$8.303\times10^{+00}$	3.595×10^{-02}	$5.770\times10^{+00}$

The lowest energy in-beam measurement of the ^{17}O(p,γ)^{18}F direct capture reaction was performed at

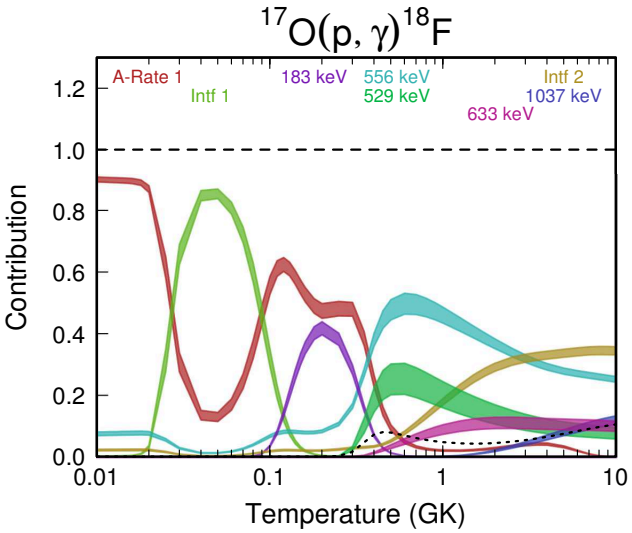

Figure 6.19: The fractional contributions made by ^{17}O(p,γ)^{18}F resonances and direct capture (labeled "A-Rate 1") to the total reaction rate. The contribution ranges (low to high) are shown as thick *uncertainty* bands. Direct capture (red in this figure) clearly dominates the rate over broad resonance tails and the narrow E_R^{cm} = 183 keV (E_R = 193 keV) resonance within the classical nova Gamow window (0.1−0.4 GK). The combined rate contribution from interfering resonances are labeled *Intf*.

LENA, and a new direct capture S-factor of $S_{DC}(0) = 4.82 \pm 0.41$ keV b was measured. The novel spectral analysis techniques applied to direct capture data also allowed E_R = 193 and 518 keV resonance strengths to be determined—$\omega\gamma = 1.89 \pm 0.15$ μeV and $\omega\gamma = 12.9 \pm 0.9$ meV, respectively. Combined with partial widths and resonance strengths reconciled from the literature, new reaction rates were calculated with this direct capture S-factor and these new strengths. The new reaction rates determined in this thesis will be prepared for publication.

CHAPTER 7: CONCLUSION

Two proton capture studies involving the destruction of rare oxygen isotopes were performed at the LENA accelerator facility with high-intensity, low energy beam. Improved thermonuclear reaction rates were calculated for both the ^{18}O destruction mechanism—^{18}O(p,γ)^{19}F—and ^{17}O destruction mechanism—^{17}O(p,γ)^{18}F.

For the ^{18}O(p,γ)^{19}F reaction, a new resonance strength upper limit of $\omega\gamma \leq 7.8\times10^{-9}$ eV (90% CL) for the E_R = 95 keV resonance was measured; it improves upon the previous (p,γ) upper limit published by Ref. [120] by about half an order of magnitude. The data also allow for a significant improvement of the total direct capture S-factor prediction. At $S_{DC}(105) \leq 8.1$ keV b (90% CL), this S-factor amounts to about half of the previously accepted value at low energies [112]. The combination of this new experimental information allowed improved Monte Carlo-based reaction rates for ^{18}O(p,γ)^{19}F to be determined. It was found that the new reaction rates in the hypothesized cool bottom processing temperature regime are even smaller than assumed previously. It is clear that ^{18}O depletion in low-mass AGB stellar atmospheres and some presolar oxide grains is dominated by the competing ^{18}O(p,α)^{15}N reaction.

For the ^{17}O(p,γ)^{18}F reaction, the lowest energy in-beam measurement of the total astrophysical S-factor was achieved. From the measured total S-factors, an improved direct capture S-factor of $S_{DC}(0) = 4.82 \pm 0.41$ keV b was determined. Additionally, the analysis techniques developed for the direct capture study allowed a new E_R = 193 keV resonance strength, $\omega\gamma = 1.89 \pm 0.15$ μeV, and a new E_R = 518 keV resonance strength, $\omega\gamma = 12.9 \pm 0.9$ meV, to be determined. Based on this new S-factor and these new strengths, updated reaction rates were calculated that showed an improvement in uncertainties at stellar temperatures relevant to ^{17}O destruction in AGB stars and during classical novae. At classical nova temperatures, the uncertainty in the rate improves with respect to the NACRE [91], LENA [88, 143, 135, 139], and LUNA [80, 82] recommended rates. This study demonstrates that an experiment can be designed and executed at a "sea-level" facility to probe low-energy reactions suppressed by the Coulomb barrier. High-intensity proton beam to boost signal-to-noise, $\gamma\gamma$-coincidence techniques to reduce environmental backgrounds, and a sophisticated new spectral analysis toolkit, allow the fingerprints of the reactions that synthesize the elements found in Nature to be uncovered in the laboratory.

Thermonuclear reaction rates of proton captures by rare oxygen isotopes allow us to improve our understanding of Galactic chemical evolution and how the isotopic abundances observed in our Solar neighborhood

came about, but they also allow us to learn a little bit more about ourselves. **"The atoms of our bodies are traceable to stars that manufactured them in their cores and exploded these enriched ingredients across our Galaxy, billions of years ago. For this reason, we are biologically connected to every other living thing in the world. We are chemically connected to all molecules on Earth. And we are atomically connected to all atoms in the Universe. We are not figuratively, but literally stardust." —Neil deGrasse Tyson**

APPENDIX A: UNCERTAINTY ANALYSIS

Appendix A.1: Monte Carlo Uncertainty Analysis

Propagation of uncertainty is historically handled a number of different ways. These different approaches include (i) differential analysis, (ii) variance decomposition procedures, (iii) response surface methodology, (iv) fast probability integration, and (v) Monte Carlo, sampling-based, techniques [160].

In sampling-based procedures, the uncertainty analysis formalism involves generating and exploring a probabilistic map between analysis input and results [161, 162, 163, 164, 165, 166, 167, 168, 169, 170, 171]. Probability density functions (PDFs) are constructed for all parameters inputted into a calculation. These functions are then randomly sampled and a histogram with the sampled solution to the calculation is populated. This procedure allows a new probability density function—the solution—to be constructed. The final PDF is assessed based upon key characteristics (such as skewness) to determine what type of PDF it can be classified as (see section 2.2.1). The adopted value and uncertainty hinges upon this randomly assembled PDF's classification.

Monte Carlo uncertainty analysis is a popular and appealing technique because it is easy to understand and implement, and it disregards intermediate models. However, it can be computationally expensive depending on which sampling formalism is applied [160]. Regardless, myriad applications of these techniques have found their way into the literature, and Monte Carlo uncertainty analysis procedures are now utilized in numerous scientific fields [171]. These techniques were applied recently to calculations relevant to nuclear astrophysics; these include the determination of thermonuclear reactions rates [88, 143, 135, 139, 90], resonance strengths and direct capture S-factors [1], and reduced widths [172].

Appendix A.2: Reconciling Differences in the Literature

When trying to resolve disparities between conflicting observations, a simple weighted average often skews the final result towards the measurement with the highest precision. If measurements are separated by several sigma, this average is unreasonable—it is not representative of either of the observations. To solve this problem, it is common to expand the weighted uncertainty by a factor of $\sqrt{\chi^2/\nu}$; however, the mean value is predisposed to favor measurements with narrow uncertainties and will remain unchanged. Another technique is postulated by Ref. [173] specifically to address the controversy in the world average of the neutron lifetime. This technique assumes that for all measurements i of quantity x, there exists an unknown, identical systematic uncertainty σ_u, which is added in quadrature to each reported uncertainty

σ_i, such that:

$$\sigma_i' = \sqrt{\sigma_u^2 + \sigma_i^2} \tag{A.1}$$

where σ_i' is the expanded uncertainty for measurement i. Then the weighted average, $\overline{x}$, and its uncertainty, $\overline{\sigma}$, become an implicit function of the unknown uncertainty:

$$\overline{x}(\sigma_u) = \frac{\sum_i x_i/\sigma_i'^2}{\sum_i 1/\sigma_i'^2} \quad ; \quad \overline{\sigma}(\sigma_u) = \sqrt{\frac{1}{\sum_i 1/\sigma_i'^2}} \tag{A.2}$$

χ^2/ν is then also a function of σ_u:

$$\frac{\chi^2}{\nu}(\sigma_u) = \Big(\sum_i \frac{(x_i - \overline{x}(\sigma_u))^2}{\sigma_i'^2} \Big) / (n-1) \tag{A.3}$$

where n is the number of measurements. An iterative process determines what value of σ_u reduces χ^2/ν to 1. This methodology produces a more realistic uncertainty that is representative of the data spread, and it also prevents dominant, high-precision measurements from skewing the average. This process produces what will be referred to in this thesis as the *reconfigured mean* [90, 174].

Appendix A.3: Net Areas—Calculating Peak Intensities with ROOT

Peak intensity can be calculated by selecting background and peak areas in the JAM [116] user interface, and JAM then calculates the net area of the peak. However, JAM can not be used to determine peak intensities in spectra generated with the *sort.cxx* sort routine discussed in Sec. 6.3.1—a ROOT and C++ code. A net area code, *fitter.c* from Ref. [175], was tested and adapted to calculate net areas in spectra sorted with *sort.cxx*.

There is some background contribution within the gross area of a peak, and the rate of the background flux needs to be estimated. Usually the background is assumed to be a constant; *fitter.c* assumes the background is a linear function. To determine the coefficients of this 1^{st} order polynomial, a region before and after the peak are used to estimate the background. If the background rate is constant on both sides of this function, the 1^{st} order polynomial will reduce to a 0-order polynomial. However, usually this function is linear, and a slope and intercept can be calculated. The areas of the two background regions are found with the following equations:

$$B_1 = \int_{c_1}^{c_2} (mx + b) dx \tag{A.4}$$

and

$$B_2 = \int_{c_3}^{c_4} (mx + b)dx. \tag{A.5}$$

In these equations, B_1 and B_2 are the areas of the background regions on either side of the peak; m is the slope of the linear function; b is the intercept of the linear function; c_1 and c_2 are the lower and upper bound channel numbers on B_1, respectively; c_3 and c_4 are the lower and upper bound channel numbers on B_2, respectively. When ROOT solves these equations, it is summing the bin content of each background region. Equations A.4 and A.5 are integrated to solve for the slope and intercept, and this yields:

$$B_1 = \frac{m}{2}(c_2^2 - c_1^2) + b(c_2 - c_1) \tag{A.6}$$

and

$$B_2 = \frac{m}{2}(c_4^2 - c_3^2) + b(c_4 - c_3). \tag{A.7}$$

These equations can then be rearranged to solve for the slope and intercept:

$$b = \frac{B_1 - \frac{m}{2}(c_2^2 - c_1^2)}{c_2 - c_1}, \tag{A.8}$$

$$b = \frac{B_2 - \frac{m}{2}(c_4^2 - c_3^2)}{c_4 - c_3}, \tag{A.9}$$

and

$$m = \frac{2(B_1 - uB_2)}{v} \tag{A.10}$$

where

$$u = \frac{c_2 - c_1}{c_4 - c_3} \tag{A.11}$$

and

$$v = (c_2^2 - c_1^2) - u(c_4^2 - c_3^2). \tag{A.12}$$

The estimate of the background contribution to the peak is calculated with an equation analogous to Eqs. A.6 and A.7:

$$N_{\text{peak}} = \frac{m}{2}(c_b^2 - c_a^2) + b(c_b - c_a) \tag{A.13}$$

where N_{peak} is the background contribution to the peak, and c_a and c_b are the lower and upper bound

channel numbers on N_{peak}. With Eqs. A.8, A.9, and A.10, Eq. A.13 becomes:

$$N_{\text{peak}} = \frac{wB_1}{v} + B_2\left(\frac{c_b - c_a}{c_4 - c_3} - \frac{uw}{v}\right) \tag{A.14}$$

where

$$w = (c_b^2 - c_a^2) - \frac{c_4^2 - c_3^2}{c_4 - c_3}(c_b - c_a). \tag{A.15}$$

A partial differential equation is used to calculate the uncertainty associated with the background contribution to the peak:

$$\partial N_{\text{peak}}^2 = \left(\frac{\partial N_{\text{peak}}}{\partial B_1}\right)^2 \partial B_1^2 + \left(\frac{\partial N_{\text{peak}}}{\partial B_2}\right)^2 \partial B_2^2 \tag{A.16}$$

which reduces to:

$$\partial N_{\text{peak}}^2 = \partial B_1 \frac{w}{v} + \partial B_2\left(\frac{c_b - c_a}{c_4 - c_3} - \frac{uw}{v}\right). \tag{A.17}$$

For data, $\partial B_1 = \sqrt{B_1}$ and $\partial B_2 = \sqrt{B_2}$. For sorted GEANT4 histograms, $\partial B_1 = \sqrt{B_1 + \partial B_{1,sys}^2}$ and $\partial B_2 = \sqrt{B_2 + \partial B_{2,sys}^2}$ where, in this case, the subscript *sys* refers to the 1.3% systematic uncertainty associated with LENA GEANT4 simulations [101]. The gross area of the peak, from bins $c_b - c_a$, is calculated with ROOT, and then N_{peak} is subtracted from this gross area to yield a net area. The uncertainty of the gross area is added in quadrature with the uncertainty of the background contribution to the peak.

These net area calculations were tested by comparing JAM peak intensities to the intensities calculated with this routine. It was found that peak intensities from JAM and *fitter.c* agreed within 0.05%.

Even a reliable routine like *fitter.c* can be misused, so to arrive at the correct peak intensities from spectra sorted with *sort.cxx*, histogram bins were selected carefully to make sure the code did not accidentally miss the peaks of interest. The user inputs the required bins manually before a calculation, and the user can inspect histograms that show what bins were considered in a peak intensity calculation.

APPENDIX B: THERMONUCLEAR REACTION RATES

Appendix B.1: Rate Calculation Input

B.1.1: ^{17}O(p,γ)^{18}F

The ^{17}O(p,γ)^{18}F reaction rate calculation includes 16 resonances with energies $E_R^{cm} \leq 1270$ keV [143]. A majority of the resonance energies are calculated with the proton separation energy $Q_{p\gamma} = 5607.1 \pm 0.5$ keV [41] and the energies of excited states presented in Ref. [40]. Two sub-threshold resonances, $E_R^{cm} =$ -2.2 keV ($J^\pi = 1^-$) and $E_R^{cm} =$ -3.7 keV ($J^\pi = 1^+$), are also included in the rate calculation. The sub-threshold resonances and their associated level parameters are tabulated in Table B.1. The product of the spectroscopic factor and the reduced width, $C^2S\theta_{sp}^2$, is substituted for the proton partial width in this table and in the reaction rate calculations (see Ref. [143]). The remaining 14 resonances are tabulated alongside resonance level parameters in Table B.2. These parameters—including the (p,γ) resonance strength, proton partial width, α-particle partial width, and γ-ray partial width—were collected from the literature. The following set of equations are a generalization of equations presented in Ref. [129] and are used here to solve for unknown parameters not included in the literature:

$$\Gamma_p = \frac{(2J_{t_p}+1)(2J_p+1)}{(2J+1)}\left[\frac{(2J_{t_p}+1)(2J_p+1)}{(2J_{t_\alpha}+1)(2J_\alpha+1)}\frac{\omega\gamma_{p\gamma}\omega\gamma_{p\alpha}}{\omega\gamma_{\alpha\gamma}} + \omega\gamma_{p\alpha} + \omega\gamma_{p\gamma}\right] \tag{B.1}$$

$$\Gamma_\alpha = \frac{(2J_{t_\alpha}+1)(2J_\alpha+1)}{(2J+1)}\left[\frac{\omega\gamma_{\alpha\gamma}\omega\gamma_{p\alpha}}{\omega\gamma_{p\gamma}} + \omega\gamma_{\alpha\gamma} + \frac{(2J_{t_p}+1)(2J_p+1)}{(2J_{t_\alpha}+1)(2J_\alpha+1)}\omega\gamma_{p\alpha}\right] \tag{B.2}$$

$$\Gamma_\gamma = \frac{(2J_{t_\alpha}+1)(2J_\alpha+1)}{(2J+1)}\left[\frac{\omega\gamma_{\alpha\gamma}\omega\gamma_{p\gamma}}{\omega\gamma_{p\alpha}} + \omega\gamma_{\alpha\gamma} + \frac{(2J_{t_p}+1)(2J_p+1)}{(2J_{t_\alpha}+1)(2J_\alpha+1)}\omega\gamma_{p\gamma}\right] \tag{B.3}$$

In these equations, J_{t_p} is the spin of the (p,γ) and (p,α) target nucleus, J_{t_α} is the spin of the (α,γ) target nucleus, J_p is the proton spin, J_α is the α-particle spin, and J is the spin of the ^{18}F excited state. In Tables B.1 and B.2, discrepancies between parameters reported in different publications are reconciled generally with the weighted mean unless the reconfigured mean (see Section A.2) is applicable. Note that for the higher energy resonances, the strengths extracted from Ref. [77] are renormalized to the correct ^{27}Al(p,γ)^{28}Si resonance strength of the $E_R^{cm} = 609$ keV resonance [176]. The resonance strengths reported by Sens *et al.* [177] are excluded here because they disagree consistently with the results presented in Refs. [77], [75], and [81] by about a factor of 2. This inconsistency may be due to the use of unpublished stopping power values, according to Ref. [81]. Refer to Tables B.1 and B.2 for a detailed catalog of adopted resonance state values and what literature was either evaluated or reconciled to arrive at the adopted parameters.

Table B.1: Resonance parameters for sub-threshold $^{17}O(p,\gamma)^{18}F$ resonances were collected from the literature. The product of the spectroscopic factor and single-particle reduced width is substituted for Γ_p in this table. The resonance energies are calculated from the revised proton separation energy presented in Ref. [41] and the energy of the ^{18}F excited state reported in Ref. [40].

Source	E_R^{cm} (keV)	$C^2S\theta_{sp}^2$	Γ_γ (eV)	Γ_α (eV)
Ref. [129]	-3.12(57)	0.054(18)[1]	–	–
Ref. [178]	–	–	0.485(46)	42.8(16)
adopted	-3.7(6)	0.054(18)	0.485(46)	42.8(16)
Ref. [129]	-1.64(57)	≤0.0082[1]	–	–
Ref. [178]	–	–	0.891(74)	32.0(21)
adopted	-2.2(6)	≤0.0082	0.891(74)	32.0(21)

[1] Estimated from reduced widths in Ref. [87] and spectroscopic factors in Refs. [156, 85].

Table B.2: Resonance parameters for the $^{17}O(p,\gamma)^{18}F$ reaction were collected from the literature. The reconfigured mean was calculated when necessary to account for uncertainties associated with these parameters. Otherwise, the weighted mean is used. Unless noted, the resonance energies are calculated from the revised proton separation energy presented in Ref. [41] and the energy of the ^{18}F excited state reported in Ref. [40].

Source	E_R^{cm} (keV)	$\omega\gamma_{p\gamma}$ (eV)	Γ_p (eV)	Γ_γ (eV)	Γ_α (eV)
Ref. [119][1]	–	$1.6\times10^{-11}(3)$	$1.9\times10^{-8}(3)$	0.45(2)	–
Ref. [178]	–	–	–	–	130(5)
Ref. [179][1]	–	$1.7\times10^{-11}(4)$	$1.9\times10^{-8}(3)$	0.46(6)	–
Ref. [77][1]	60(2)	$1.7\times10^{-11}(5)$	$1.9\times10^{-8}(3)$	0.47(10)	–
Ref. [180][1]	–	$1.6\times10^{-11}(3)$	$1.9\times10^{-8}(3)$	0.45(5)	–
adopted	64.5(5)[2]	$1.65\times10^{-11}(18)$[3]	$1.89\times10^{-8}(16)$[3]	0.453(18)[3]	130(5)
present	–	$1.89\times10^{-6}(15)$	0.0040(4)	0.009(4)	8(3)
Ref. [80][4]	183	$1.67\times10^{-6}(12)$	0.0040(4)	0.009(4)	9(4)
Ref. [181]	$183.5^{+0.1}_{-0.4}$	–	–	–	–
Ref. [182]	183.2(6)[5]	–	–	–	–
Ref. [75][4]	182.4(8)[5]	$1.2\times10^{-6}(2)$	0.0040(4)	0.009(4)	13(6)
adopted	183.4(2)[3]	$1.76\times10^{-6}(9)$[7]	0.0040(3)[7]	0.009(3)[7]	9(3)[7]
present	–	0.0129(9)	–	–	–
Ref. [81]	490	0.0130(15)	–	–	–
Ref. [78]	490	0.0137(22)	–	–	–
Ref. [75]	489.9(9)	0.012(3)	–	–	–
Ref. [77]	488.3(18)	0.0130(17)[8]	–	–	–
adopted	489.3(12)	0.0130(7)[3]	–	–	–
Ref. [77]	529.2(16)	0.11(3)[8]	–	–	–
adopted	529.4(6)	0.11(3)	–	–	–
Ref. [81]	557	0.37(5)	$1.41\times10^{4}(3)$	0.594(6)[9]	8(1)
Ref. [183]	558(4)[10]	–	$1.40\times10^{4}(5)$	–	5.0(6)
Ref. [77]	554.9(16)	0.33(8)[8]	–	0.57(13)[11]	–
adopted	556.1(10)	0.36(4)[3]	$1.41\times10^{4}(3)$[3]	0.594(6)[3]	6.4(15)[6]
Ref. [77]	632.1(16)	0.16(3)[8]	–	–	–
adopted	633.3(9)	0.16(3)	–	–	–
Ref. [81]	677	0.58(7)	$1.13\times10^{4}(2)$	1.235(19)[9]	30(4)
Ref. [183]	677(4)[10]	–	$1.0\times10^{4}(5)$	–	27(3)
Ref. [77]	674.9(16)	0.45(10)[8]	–	1.1(2)[11]	–

Table B.2 – continued

Source	E_R^{cm} (keV)	$\omega\gamma_{p\gamma}$ (eV)	Γ_p (eV)	Γ_γ (eV)	Γ_α (eV)
adopted	676.1(10)	0.53(6)[6]	1.07×10^4(7)[6]	1.234(19)[3]	28(2)[3]
Ref. [77]	701.4(14)	0.032(7)[8]	–	–	–
adopted	703.4(9)	0.032(7)	–	–	–
Ref. [81]	780	0.0323(25)	–	0.281(69)[9]	–
Ref. [183]	782(4)[10]	–	109(11)[12]	–	286(87)
Ref. [77]	774(3)	0.030(8)[8]	–	0.26(9)[11]	–
adopted	778.4(18)	0.032(2)[3]	109(11)	0.27(6)[3]	286(87)
Ref. [81]	878	0.0194(18)	–	–	–
Ref. [77]	871(2)	0.018(7)[8]	–	–	–
adopted	877.8(16)	0.0193(17)[3]	–	–	–
Ref. [81]	1037	0.297(33)	–	1.16(17)[11]	–
Ref. [184]	1036.5	0.31(4)	–	1.21(19)[11]	–
Ref. [183]	1044(4)[10]	–	368(61)[12]	–	231(40)
Ref. [84]	1033.9(19)	0.32(6)[13]	–	1.2(3)[11]	–
Ref. [77]	1033.9(19)	0.21(5)[8]	–	0.8(2)[11]	–
adopted[14]	1036.6(9)	0.30(2)[3]	368(61)	1.20(11)[3]	231(40)
Ref. [77]	1168(2)	0.14(3)[8]	–	–	–
adopted	1169.9(15)	0.14(3)	–	–	–
Ref. [77]	1193.9(19)	0.027(9)[8]	–	–	–
adopted	1196.0(16)	0.027(9)	–	–	–
Ref. [77]	1269(2)	0.050(19)[8]	–	–	–
adopted	1270.3(18)	0.050(19)	–	–	–

[1] All parameters calculated with this $\omega\gamma_{\alpha\gamma}$, $\omega\gamma_{p\alpha}$ from Refs. [185, 75], Γ_α from [178], and Eqs. B.1, B.2, and B.3.
[2] Resonance energy calculated from correct excited state energy in Ref. [144] and proton separation energy in Ref. [41].
[3] Weighted mean.
[4] Partial widths calculated with this $\omega\gamma_{p\gamma}$, $\omega\gamma_{\alpha\gamma}$ from Ref. [77], $\omega\gamma_{p\alpha}$ from Ref. [186], and Eqs. B.1, B.2, and B.3.
[5] Calculated with atomic masses from Ref. [41] and mass of electron in amu (atomic mass converted to nuclear mass).
[6] Reconfigured mean.
[7] Weighted mean of present value and value from Ref. [80].
[8] Strength renormalized with incorrect ^{27}Al(p,γ)^{28}Si strength in Ref. [187] and correct E_R = 632 keV resonance strength in Ref. [188].
[9] Sum of primary γ-ray decay partial widths from Ref. [81].
[10] Ref. [183] used excited state energies and Q-value from Ref. [177].
[11] Calculated with partial widths from Ref. [183].
[12] Sum of partial widths reported in Ref. [183].
[13] Includes $(2J_t+1)(2J_p+1)$ because only $(2J+1)\Gamma_p\Gamma_\gamma/\Gamma_t$ reported in Ref. [84].
[14] Ref. [77] excluded as outlier.

Appendix B.2: RatesMC Input Files

Section B.2.1 contains the RatesMC input file used in the ^{18}O(p,γ)^{19}F reaction rate calculations in this work. This input file is similar to the input file from Ref. [91]. The E_R^{cm} = 20.4 keV proton width is from Refs. [189, 190] while total and radiative widths come from a private communication cited within Ref. [112]. The E_R^{cm} resonance strength expectation value and variance come from this work [1] as does the adopted direct capture S-factor. A new cutoff temperature is used because the S-factor was calculated through 2500

keV in this work. The remainder of the input comes from Refs. [120, 118, 133, 191, 119, 132, 192] and was not reconciled or updated for this study. Rates are extrapolated using the Hauser-Feshbach rate from Ref. [142] above $T = 5$ GK. Reaction rate output and comparisons between the new rates and the literature can be found in Sec. 5.4 of this thesis. This input file was made available on the STARLIB reaction rate library website and is include in Ref. [90].

In Sec. B.2.2, the RATESMC input file used for ^{17}O$(p,\gamma)^{18}$F reaction rate calculations in this work is presented. This input file was updated dramatically since reaction rates were calculated originally with RATESMC [88] and the results from Ref. [78] in Refs. [143, 135, 139]. Nuclear masses were calculated by subtracting the mass of electrons from the atomic mass presented in Ref. [41]. Resonance energies, partial widths, and strengths were reconciled from the literature using the methodology outline in Appendix A.2 and the results of reconciliation are tabulated in Tab. B.2. The new astrophysical S-factor and factor uncertainty come directly from the experiment presented in this thesis (see Eq. 6.30). The literature value for the cutoff energy was selected [88, 78]. Reaction rate output and comparisons between the new rates and the literature can be found in Sec. 6.4 of this thesis.

B.2.1: ^{18}O$(p,\gamma)^{19}$F

```
18O(p,g)19F
****************************************************************************************************
1               ! Zproj
8               ! Ztarget
2               ! Zexitparticle (=0 when only 2 channels open)
1.0078          ! Aproj
17.999          ! Atarget
4.0026          ! Aexitparticle (=0 when only 2 channels open)
0.5             ! Jproj
0.0             ! Jtarget
0.0             ! Jexitparticle (=0 when only 2 channels open)
7993.6          ! projectile separation energy (keV)
4013.8          ! exit particle separation energy (=0 when only 2 channels open)
1.25            ! Radius parameter R0 (fm)
2               ! Gamma-ray channel number (=2 if ejectile is a g-ray; =3 otherwise)
****************************************************************************************************
1.0             ! Minimum energy for numerical integration (keV)
10000            ! Number of random samples (>5000 for better statistics)
0               ! =0 for rate output at all temperatures; =NT for rate output at selected temperatures
****************************************************************************************************
Non-Resonant Contribution
S(keVb)         S'(b)           S''(b/keV)      fracErr         Cutoff Energy (keV)
7.06e0          2.98e-3         -5.20e-7        0.5             2500.0                ! BU12
0.0             0.0             0.0             0.0             0.0
****************************************************************************************************
Resonant Contribution
Note: G1 = entrance channel, G2 = exit channel, G3 = spectator channel !! Ecm, Exf in (keV); wg, Gx in (eV) !!
Note: if Er<0, theta^2=C2S*theta_sp^2 must be entered instead of entrance channel partial width
Ecm     DEcm  wg      Dwg     Jr    G1      DG1     L1  G2    DG2   L2  G3      DG3     L3  Exf   Int
  20.4  0.7   0       0       2.5   2.3e-19 0.5e-19 2   2.3   1.0   1   2.5e3   1.0e3   3   0.0   1
  90.4  3.0   5.3e-8  9.0e-6  0     0       0       0   0     0     0   0       0       0   0.0   0
 142.8  0.1   0       0       0.5   1.67e-1 0.12e-1 0   0.72  0.15  1   1.23e2  0.24e2  1   0.0   1
 205.4  1.0   5.0e-6  1.0e-6  0     0       0       0   0     0     0   0       0       0   0.0   0
```

```
 260.7  2.6   3.7e-5  0.5e-5  0      0       0       0   0     0     0   0       0       0   0.0   0
 316.4  1.3   0       0       2.5    1.9e-2  0.3e-2  2   0.78  0.34  1   47.0    19.0    3   0.0   1
 589.9  1.7   1.0e-2  0.2e-2  0      0       0       0   0     0     0   0       0       0   0.0   0
 598.3  1.2   0       0       1.5    1.4e2   0.7e2   1   0.71  0.39  1   2.0e3   0.1e3   2   0.0   1
 799.6  1.6   0       0       0.5    24.6e3  1.4e3   0   2.5   0.4   1   20.e3   1.0e3   1   0.0   1
 933.1  2.8   0       0       1.5    76.0    7.0     1   0.34  0.06  1   3.5e3   0.3e3   2   0.0   1
1106.1  4.0   0.29    0.03    0      0       0       0   0     0     0   0       0       0   0.0   0
1173.4  1.5   0       0       0.5    0.38e3  0.03e3  0   1.4   1.0   1   5.4e3   0.38e3  1   0.0   1
1324.4  2.1   0.08    0.01    0      0       0       0   0     0     0   0       0       0   0.0   0
1327.4  1.2   0       0       0.5    0.22e3  0.02e3  0   3.4   1.7   1   4.7e3   0.4e3   1   0.0   1
1542.8  2.1   0.025   0.005   0      0       0       0   0     0     0   0       0       0   0.0   0
1572.4  3.0   0.041   0.010   0      0       0       0   0     0     0   0       0       0   0.0   0
1581.4  4.0   0.06    0.01    0      0       0       0   0     0     0   0       0       0   0.0   0
1592.4  3.0   0.025   0.004   0      0       0       0   0     0     0   0       0       0   0.0   0
1673.9  1.6   0       0       1.5    2.0e3   0.6e3   2   1.0   0.4   1   1.4e3   0.4e3   1   0.0   1
1826.4  1.2   2.8     0.7     0      0       0       0   0     0     0   0       0       0   0.0   0
1880.4  1.9   0.13    0.04    0      0       0       0   0     0     0   0       0       0   0.0   0
1893.4  3.0   0       0       0.5    11.e3   3.0e3   0   0.36  0.20  1   18.0e3  5.4e3   1   0.0   1
**************************************************************************************************
Upper Limits of Resonances
Note: enter partial width upper limit by choosing non-zero value for PT, where PT=<theta^2> for particles and...
Note: ...PT=<B> for g-rays [enter: "upper_limit 0.0"]; for each resonance: # upper limits < # open channels!
Ecm     DEcm   Jr   G1        DG1    L1   PT       DPT     G2      DG2     L2  PT   DPT    G3     DG3    L3  PT   DPT  Exf  Int frac
!0.0    0.0    0    0.0       0.0    0    0.0      0.0     0.0     0.0     0   0.0  0.0    0.0    0.0    0   0.0  0.0  0.0  0   0.0
**************************************************************************************************
Interference between Resonances [numerical integration only]
Note: + for positive, - for negative interference; +- if interference sign is unknown
Ecm     DEcm   Jr   G1        DG1    L1   PT   DPT    G2      DG2     L2  PT  DPT  G3     DG3    L3  PT  DPT    Exf
!+-
0.0     0.0    0    0.0       0.0    0    0.0  0.0    0.0     0.0     0   0.0 0.0  0.0    0.0    0   0.0 0.0    0.0
0.0     0.0    0    0.0       0.0    0    0.0  0.0    0.0     0.0     0   0.0 0.0  0.0    0.0    0   0.0 0.0    0.0
**************************************************************************************************
Reaction Rate and PDF at NT selected temperatures only
Note: default values are used for reaction rate range if Min=Max=0.0
T9 Min Max
0.01 0.0 0.0
0.1 0.0 0.0
**************************************************************************************************
```

B.2.2: $^{17}\mathrm{O}(p,\gamma)^{18}\mathrm{F}$

```
17O(p,g)18F
**************************************************************************************************
1               ! Zproj
8               ! Ztarget
2               ! Zexitparticle (=0 when only 2 channels open)
1.00727645232054   ! Aproj [Wan12] - Zp*Me
16.9947431172243   ! Atarget [Wan12] - Zo*Me
4.00150609431108   ! Aexitparticle (=0 when only 2 channels open) [Wan12] - Zhe*Me
0.5             ! Jproj
2.5             ! Jtarget
0.0             ! Jexitparticle (=0 when only 2 channels open)
5607.1          ! projectile separation energy (keV) [Wan12]
4415.23         ! exit particle separation energy (=0 when only 2 channels open) [Wan12]
1.25            ! Radius parameter R0 (fm)
2               ! Gamma-ray channel number (=2 if ejectile is a g-ray; =3 otherwise)
**************************************************************************************************
1.0             ! Minimum energy for numerical integration (keV)
10000           ! Number of random samples (>5000 for better statistics)
0               ! =0 for rate output at all temperatures; =NT for rate output at selected temperatures
**************************************************************************************************
Non-Resonant Contribution
```

```
S(keVb)  S'(b)   S''(b/keV)     fracErr  Cutoff Energy (keV)
4.82     0.0     0.0            0.086    1200
*****************************************************************************************************
Resonant Contribution
Note: G1 = entrance channel, G2 = exit channel, G3 = spectator channel !! Ecm, Exf in (keV); wg, Gx in (eV) !!
Note: if Er<0, theta^2=C2S*theta_sp^2 must be entered instead of entrance channel partial width
Ecm      DEcm   wg       Dwg      Jr     G1      DG1     L1    G2      DG2     L2  G3      DG3     L3 Exf  Int
 -3.70   0.6    0        0        1      5.4e-2  1.8e-2  2     4.85e-1 0.46e-1 1   4.28e1  0.16e1  0  0.0  1
 183.4   0.2    1.76e-6  0.09e-6  0      0       0       0     0       0       0   0       0       0  0.0  0
 489.3   1.2    1.3e-2   0.07e-2  0      0       0       0     0       0       0   0       0       0  0.0  0
 529.4   0.6    1.1e-1   0.3e-1   0      0       0       0     0       0       0   0       0       0  0.0  0
 556.1   1.0    0        0        3      1.41e4  0.03e4  0     5.94e-1 0.06e-1 1   6.4     1.5     2  0.0  1
 633.3   0.9    1.6e-1   0.3e-1   0      0       0       0     0       0       0   0       0       0  0.0  0
 703.4   0.9    3.2e-2   0.7e-2   0      0       0       0     0       0       0   0       0       0  0.0  0
 877.8   1.6    1.93e-2  0.17e-2  0      0       0       0     0       0       0   0       0       0  0.0  0
1036.6   0.9    0        0        2      3.68e2  0.61e2  1     1.20    0.11    1   2.31e2  0.40e2  1  0.0  1
1169.9   1.5    1.40e-1  0.3e-1   0      0       0       0     0       0       0   0       0       0  0.0  0
1196.0   1.6    2.7e-2   0.9e-2   0      0       0       0     0       0       0   0       0       0  0.0  0
1270.3   1.8    5.0e-2   1.9e-2   0      0       0       0     0       0       0   0       0       0  0.0  0
*****************************************************************************************************
Upper Limits of Resonances
Note: enter partial width upper limit by choosing non-zero value for PT, where PT=<theta^2> for particles and...
Note: ...PT=<B> for g-rays [enter: "upper_limit 0.0"]; for each resonance: # upper limits < # open channels!
Ecm     DEcm   Jr   G1       DG1    L1   PT       DPT     G2      DG2     L2  PT   DPT    G3     DG3    L3  PT   DPT  Exf  Int frac
!0.0    0.0    0    0.0      0.0    0    0.0      0.0     0.0     0.0     0   0.0  0.0    0.0    0.0    0   0.0  0.0  0.0  0   0.0
*****************************************************************************************************
Interference between Resonances [numerical integration only]
Note: + for positive, - for negative interference; +- if interference sign is unknown
Ecm     DEcm   Jr   G1       DG1    L1   PT   DPT    G2      DG2     L2  PT  DPT  G3     DG3    L3  PT  DPT   Exf
+-
-2.2    0.6    1    8.2e-3   0.0    1    4.5e-3 0.0  8.91e-1 0.74e-1 1   0.0 0.0  3.20e1 0.21e1 1   0.0 0.0   0.0
64.5    0.5    1    1.89e-8  1.6e-9 1    0.0  0.0    4.53e-1 0.18e-1 1   0.0 0.0  1.30e2 0.05e2 1   0.0 0.0   0.0
+-
778.4   1.8    2    1.09e2   0.11e2 0    0.0  0.0    2.7e-1  0.6e-1  1   0.0 0.0  2.86e2 0.87e2 2   0.0 0.0   0.0
676.1   1.0    2    1.07e4   0.07e4 0    0.0  0.0    1.234   0.019   1   0.0 0.0  2.8e1  0.2e1  2   0.0 0.0   0.0
*****************************************************************************************************
Reaction Rate and PDF at NT selected temperatures only
Note: default values are used for reaction rate range if Min=Max=0.0
T9       Min      Max
0.01     0.0      0.0
0.1      0.0      0.0
*****************************************************************************************************
```

APPENDIX C: ANGULAR CORRELATIONS

Appendix C.1: Direct Capture and Broad Resonance Interference

As explained in Ref. [75], the tails of broad resonances have a significant impact on the total ^{17}O(p,γ)^{18}F cross section at low bombarding energies. Fox *et al.* [75] pointed out that the total astrophysical S-factor is, in actuality, the incoherent sum of the direct capture S-factor and the S-factor associated with these two broad resonances. From calculations prepared for this dissertation (see Appendix B), the adopted center-of-mass energies of these two resonances are E_R^{cm} = 556 keV and E_R^{cm} = 676 keV. Aside from complicating analysis and the extraction of the direct capture astrophysical S-factor at low bombarding energies, the broad resonances increase the complexity of angular correlation calculations. Interference between broad resonance and direct capture primaries require the calculation of angular correlation interference terms. The sensitivity of the total cross section to these interference terms is an integral component in the assessment of angular correlations and whether they are included in the final analysis.

Rolfs (1973) [84] and Ferguson (1965) [157] set forth a handful of key equations for the determination of angular correlation resonant/direct capture (R,D) interference terms. From Ref. [84]:

$$\sigma(\mathrm{E},\theta) = \sigma_{\mathrm{R}}(\mathrm{E})\mathrm{W}_{\mathrm{R}}(\theta) + \sigma_D(\mathrm{E})\mathrm{W}_D(\theta) \pm 2\sqrt{\sigma_{\mathrm{R}}(\mathrm{E})\sigma_D(\mathrm{E})}cos(\phi_{\mathrm{R}} - \phi_D)\mathrm{W}_{R,D}^{int}(\theta) \tag{C.1}$$

where σ(E,θ) is the total differential cross section for a transition [193]; σ_{R}(E) is the cross section of the broad resonance; $\mathrm{W}_{\mathrm{R}}(\theta)$ is the angular correlation associated with the resonance; σ_D(E) is the direct capture cross section; $\mathrm{W}_D(\theta)$ is the direct capture angular correlation; ϕ_{R} and ϕ_D are the resonant and direct capture phase shifts, respectively, and $\mathrm{W}_{R,D}^{int}(\theta)$ is the interference term. Note that according to Ref. [84], $\mathrm{W}_{\mathrm{R}}(\theta)$ = 1 (isotropic) for all ^{17}O(p,γ)^{18}F resonances with spin $J \leq$3 due to poor alignment during the reaction. The two broad resonances of interest, E_R^{cm} = 556 keV and E_R^{cm} = 676 keV, have spins and parities of $J^\pi = 3^+$ and 2^+, respectively [40]. From Ref. [157], the resonant phase shift is:

$$\phi_{\mathrm{R}} = \arctan\left(\frac{\Gamma}{2(\mathrm{E}_0 - \mathrm{E})}\right) - \arctan\left(\frac{F_\ell}{G_\ell}\right) + \sum_{n=1}^{\ell} \arctan\left(\frac{\eta}{n}\right) \tag{C.2}$$

where Γ is the total width, E_0 is the resonant energy, E is the bombarding energy, F_ℓ is the regular radial wave function, G_ℓ is the irregular radial wave function, and η is the Coulomb parameter. Also from Ferguson [157], the non-resonant phase shift is:

$$\phi_D = -\arctan\left(\frac{F_\ell}{G_\ell}\right) + \sum_{n=1}^{\ell} \arctan\left(\frac{\eta}{n}\right). \tag{C.3}$$

The interference term is calculated with the following equation from Rolfs [84]:

$$W_{R,D}^{int}(\theta) = (-)^{P}\hat{J}_2\hat{\ell_f}W(\ell_{\rm R}L_{\rm R}J_1J_3;\ell_f J_2)\sum_k(\ell_{\rm R}0\ell_D0|k0)\overline{Z}_1(L_{\rm R}\ell_{\rm R}L_D\ell_D;\ell_f k)P_k\big(cos(\theta)\big) \tag{C.4}$$

where J_1 and J_3 are the initial and final state spins, respectively, and J_2 is the spin of the resonance state. The formation of the resonance state occurs due to the partial $\ell_{\rm R}$ wave capture (J_2 + $\ell_{\rm R}$ + J_1); the quantum numbers ℓ_D and ℓ_f are the scattering and bound state direct capture orbital angular momenta, respectively. Additionally, $L_{\rm R}$ is the γ-ray multipolarity of the resonance primaries, L_D is the direct capture γ-ray multipolarity, and k is the order of Legendre polynomial. In this equation,

$$P = J_2 + J_3 + \ell_{\rm R} + \ell_D + L_D + \frac{1}{2}(\ell_D + \ell_{\rm R} + L_D + L_{\rm R}) + P_{L_DL_{\rm R}}, \tag{C.5}$$

the interfering multipole transitions are represented by $P_{L_DL_{\rm R}} = L_D$, L_D+$\frac{3}{2}$, $\frac{1}{2}$ and 0 for (EL_D, $EL_{\rm R}$), (EL_D, $ML_{\rm R}$), (ML_D, $EL_{\rm R}$), and (ML_D, $ML_{\rm R}$), respectively. Note that for ^{17}O(p,γ)^{18}F direct capture, it is only necessary to consider E1 γ-ray transitions because additional calculations indicate negligible contributions from higher order γ-ray multipoles [84, 78, 85]. Also, from Ref. [183], calculating the angular correlation interference terms is simplified dramatically by the fact that the broad resonances, $E_{\rm R}^{\rm cm}$ = 556 keV and $E_{\rm R}^{\rm cm}$ = 676 keV, only form by s-wave capture. Finally, it is important to note that in Eq. C.4, terms in the $\overline{Z}_1$ coefficient are rearranged to resolve differences in the definition of this function between Refs. [157] and [84]. The $\overline{Z}_1$ coefficient, Racah coefficient, and Clebsch-Gordan coefficient are defined below.

It is clear from Eq. C.4 that the input can undergo a staggering number of permutations; however, due to the selection rules associated with the Clebsch-Gordan coefficient, Racah coefficient, and $\overline{Z}_1$ coefficient, only a handful of these permutations satisfy Eq. C.4 producing a non-zero solution for an angular correlation interference term. A code was written to solve for the allowed Clebsch-Gordan coefficients, Racah coefficients, and $\overline{Z}_1$ coefficients. The non-zero results are tabulated below and combined finally in Table C.4. As expected, only a handful of direct capture decays actually interfere with resonant capture primaries producing a non-zero angular correlation R,D interference term.

From Ferguson [157], the Clebsch-Gordan coefficient is defined, in terms of the Wigner 3$-j$ symbol, as:

$$(a\alpha, b\beta|c\gamma) = \hat{c}(-)^{a-b+\gamma}\begin{pmatrix} a & b & c \\ \alpha & \beta & -\gamma \end{pmatrix} \tag{C.6}$$

where α + β = γ and the triangle condition (abc) is satisfied. For the angular correlation interference calculation, the Clebsch-Gordan coefficients can immediately be simplified to $(00\ell_D0|k0)$ because the two

broad resonances in question are only formed by s-wave capture and $\ell_{\rm R} = 0$ [84, 183]. See Tab. C.1 for the complete set of Clebsch-Gordan coefficients allowed to contribute to the angular correlation interference term.

Table C.1: Clebsch-Gordan coefficients allowed due to the interference between $E_R^{cm} = 556$ keV and direct capture or $E_R^{cm} = 676$ keV and direct capture. These resonances are only formed by s-wave capture [183], $\ell_{\rm R} = 0$.

E_x (keV)	ℓ_D	$(00\ell_D0\|10)$	$(00\ell_D0\|30)$
0	3	–	1
0	1	1	–
1042	3	–	1
1042	1	1	–
1121	3	–	1
1121	1	1	–

Ferguson [157] defines the Racah coefficient in terms of the Wigner $6-j$ symbol as:

$$W(abcd;ef) = (-)^{a+b+c+d} \begin{Bmatrix} a & b & e \\ d & c & f \end{Bmatrix} \tag{C.7}$$

where the (abe), (cde), (acf), and (bdf) triangles must be satisfied in order to obtain a Racah coefficient that does not vanish. Again, because of resonance state formation by s-wave capture, the Racah coefficients in Eq. C.4 simplify immediately to the form $\mathrm{W}(0L_{\rm R}J_1J_3;\ell_f 3)$ for the $E_R^{cm} = 556$ keV resonance and $\mathrm{W}(0L_{\rm R}J_1J_3;\ell_f 2)$ for the $E_R^{cm} = 676$ keV resonance. See Tab. C.2 for the Racah coefficients that are allowed to contribute to the angular correlation interference terms.

Table C.2: In the top portion, Racah coefficients allowed due to the interference between $E_R^{cm} = 556$ keV ($J_2 = 3$) and direct capture. In the bottom portion, Racah coefficients allowed due to the interference between $E_R^{cm} = 676$ keV ($J_2 = 2$) and direct capture. These resonances are only formed by s-wave capture [183], $\ell_{\rm R} = 0$.

E_x (keV)	$L_{\rm R}$	J_1	J_2	J_3	ℓ_f	$\mathrm{W}(0L_{\rm R}J_1J_3;\ell_f J_2)$
0	2	3	3	1	2	$\frac{1}{\sqrt{35}}$
1121	2	3	3	5	2	$\frac{1}{\sqrt{35}}$
1042	2	2	2	0	2	$\frac{1}{5}$

Finally, Ferguson [157] defines the $\overline{Z}_1$ coefficient as:

$$\overline{Z}_1(LbL'b';ck) = (-)^{k-L+L'-1}\hat{L}\hat{L}'\hat{b}\hat{b}'(L1,L'-1|k0)\mathrm{W}(LbL'b';ck). \tag{C.8}$$

The $\overline{Z}_1$ coefficients that survive selection rules are tabulated for each broad resonance in Table C.3.

Table C.3: In the top portion, $\overline{Z}_1$ coefficients allowed due to the interference between $E_R^{cm} = 556$ keV and direct capture. In the bottom portion, $\overline{Z}_1$ coefficients allowed due to the interference between $E_R^{cm} = 676$ keV and direct capture. These resonances are only formed by s-wave capture [183], $\ell_R = 0$.

E_x (keV)	L_R	L_D	ℓ_D	ℓ_f	$\overline{Z}_1(L_R 0 L_D \ell_D;\ell_f 1)$	$\overline{Z}_1(L_R 0 L_D \ell_D;\ell_f 3)$
0	2	1	3	2	–	$-\sqrt{\frac{3}{5}}$
0	2	1	1	2	$-\frac{3}{\sqrt{10}}$	–
1121	2	1	3	2	–	$-\sqrt{\frac{3}{5}}$
1121	2	1	1	2	$-\frac{3}{\sqrt{10}}$	–
1042	2	1	3	2	–	$-\sqrt{\frac{3}{5}}$
1042	2	1	1	2	$-\frac{3}{\sqrt{10}}$	–

The Clebsch-Gordan coefficients tabulated in Tab. C.1, the Racah coefficients in Tab. C.2, and the $\overline{Z}_1$ coefficients in Tab. C.3 were plugged into Eq. C.4 to calculate the angular correlation interference coefficients. The results of this calculation are tabulated in Tab. C.4 for the $E_R^{cm} = 556$ keV and $E_R^{cm} = 676$ keV broad resonances.

Table C.4: In the top portion, angular correlation terms allowed due to interference between $E_R^{cm} = 556$ keV ($J_2 = 3$) and direct capture. In the bottom portion, angular correlation terms allowed due to interference between $E_R^{cm} = 676$ keV ($J_2 = 2$) and direct capture. These resonances are only formed by s-wave capture [183], $\ell_R = 0$. The coefficients associated with Legendre polynomials of order $k = 1$ and $k = 3$, a_1 and a_3 respectively, are tabulated.

E_x (keV)	L_R	L_D	ℓ_D	ℓ_f	J_1	J_3	a_1	a_3
0	2	1	3	2	3	1	–	$-\sqrt{\frac{3}{5}}$
0	2	1	1	2	3	1	$\frac{3}{\sqrt{10}}$	–
1121	2	1	3	2	3	5	–	$-\sqrt{\frac{3}{5}}$
1121	2	1	1	2	3	5	$\frac{3}{\sqrt{10}}$	–
1042	2	1	3	2	2	0	–	$-\sqrt{\frac{3}{5}}$
1042	2	1	1	2	2	0	$\frac{3}{\sqrt{10}}$	–

Based on these results, it is clear that only ($p \to d$) and ($f \to d$) direct capture contributions interfere with a handful of resonant capture primaries. In order to compare the individual interference terms and gauge their affect on Eq. C.1, fragments of this equation were assessed, computed, and plotted. The interference

terms were removed and the following fragment of Eq. C.1 was plotted in Fig. C.3:

$$\sigma_{R,D}^{frag}(\mathrm{E},\theta) = \sigma_{\mathrm{R}}(\mathrm{E})\mathrm{W}_{\mathrm{R}}(\theta) + \sigma_{p\to d}(\mathrm{E})\mathrm{W}_{p\to d}(\theta) + \sigma_{f\to d}(\mathrm{E})\mathrm{W}_{f\to d}(\theta) \tag{C.9}$$

where p and f refer to p-wave ($\ell_D = 1$) and f-wave ($\ell_D = 3$) formation, respectively, and d refers to the d-shell ($\ell_f = 2$) orbital. Next, the two interference fragments were calculated and plotted alongside $\sigma_{R,D}^{frag}$(E,θ):

$$\sigma_{R,p\to d}^{frag}(\mathrm{E},\theta) = 2\sqrt{\sigma_{\mathrm{R}}(\mathrm{E})\sigma_{p\to d}(\mathrm{E})}cos(\phi_{\mathrm{R}} - \phi_{p\to d})\mathrm{W}_{R,p\to d}^{int}(\theta) \tag{C.10}$$

and

$$\sigma_{R,f\to d}^{frag}(\mathrm{E},\theta) = 2\sqrt{\sigma_{\mathrm{R}}(\mathrm{E})\sigma_{f\to d}(\mathrm{E})}cos(\phi_{\mathrm{R}} - \phi_{f\to d})\mathrm{W}_{R,f\to d}^{int}(\theta). \tag{C.11}$$

The phase shifts in these two equations become:

$$\phi_{\mathrm{R}} - \phi_{p\to d} = \arctan\left(\frac{\Gamma}{2(\mathrm{E}_0 - \mathrm{E})}\right) - \arctan\left(\frac{F_s}{G_s}\right) + \arctan\left(\frac{F_p}{G_p}\right) - \arctan\left(\frac{\eta}{1}\right) \tag{C.12}$$

and

$$\begin{aligned}\phi_{\mathrm{R}} - \phi_{f\to d} = \arctan\left(\frac{\Gamma}{2(\mathrm{E}_0 - \mathrm{E})}\right) - \arctan\left(\frac{F_s}{G_s}\right) + \arctan\left(\frac{F_f}{G_f}\right) \\ - \arctan\left(\frac{\eta}{1}\right) - \arctan\left(\frac{\eta}{2}\right) - \arctan\left(\frac{\eta}{3}\right).\end{aligned} \tag{C.13}$$

The cross sections used in this calculation are plotted in Fig. C.1. The direct capture cross sections were calculated with the computer code TEDCA [138]. The resonant capture cross sections were computed with a numerical code [154] and input reconciled from the literature and tabulated in Tabs. B.2 and 6.13. The calculated direct capture cross sections are multiplied by their associated spectroscopic factors—also reconciled from the literature and tabulated in Tab. 6.14 in order to arrive at experimental cross sections:

$$\sigma_{exp} = \sum_{\ell_i,\ell_f} C^2 S(\ell_f)\sigma_{calc}. \tag{C.14}$$

Also, note that from Ref. [84],

$$W_{p\to d}(\theta) = 1 - \frac{1}{10}P_2\big(cos(\theta)\big) \tag{C.15}$$

and

$$W_{f\to d}(\theta) = 1 - \frac{2}{5}P_2\big(cos(\theta)\big). \tag{C.16}$$

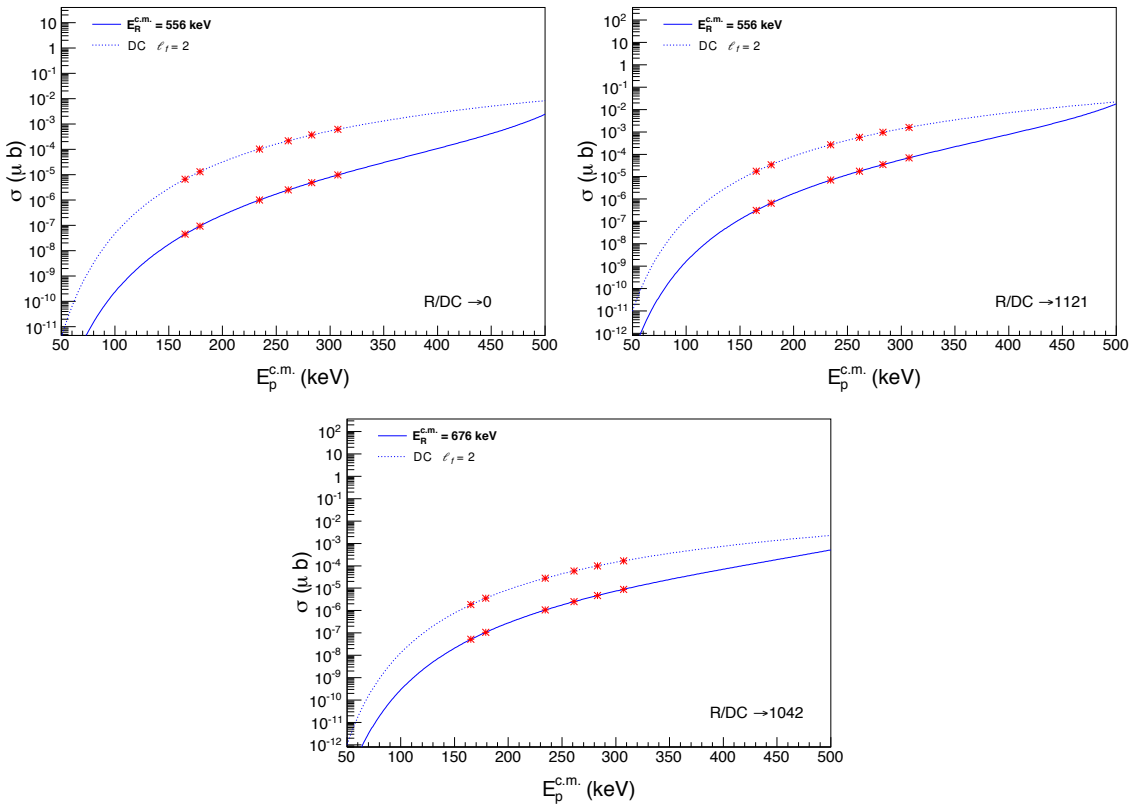

Figure C.1: Equation C.14 was solved to determine the experimental direct capture and resonant capture cross sections computed with TEDCA [138] and a numerical code [154], respectively. Spectroscopic factors, branching ratios, and resonance parameters are reconciled from the literature and tabulated in Tabs. 6.14, 6.13, and B.2. The dotted blue line represents the combined direct capture ($p \rightarrow d$) and ($f \rightarrow d$) cross sections ($\ell_f = 2$). The solid blue line is the cross section of the broad resonance for a particular transition. Red asterisks indicate the experimental proton bombarding energy in the center-of-mass frame.

Additionally, absorption coefficients for the LENA HPGe (135%) detector are taken from Longland *et al.* [99], and Q-coefficients Q_1, Q_2, and Q_3 are shown in Fig. C.2. These values are used to perform these calculations, because during the evaluation stage of selecting the appropriate angular correlation terms, the HPGe absorption coefficients at 0° are reasonable approximations.

With all of the input defined, the three fragment equations, Eqs. C.9, C.10, and C.11, are compared to probe the sensitivity of the differential cross section to $(p \rightarrow d)$ and $(f \rightarrow d)$ partial direct capture cross sections. If either Eq. C.10 or C.11 impact Eq. C.9 substantially, these terms must be analyzed further and perhaps included in the angular correlation analysis. From Fig. C.3, it is clear that Eq. C.10 contributes ±10% to the differential cross section, but Eq. C.11 does not contribute significantly enough to warrant additional scrutiny. Note that Eq. C.11 approaches zero at ≈40° due to its dependence on the P_3 Legendre polynomial. Pure transitions were assumed during these calculations because mixing ratios are not known; this is consistent with what Fox *et al.* [75] did when faced with angular correlation calculations for the E_R^{cm} = 183 keV resonance.

In order to verify whether the additional 10% introduced by Eq. C.10 is significant enough to deserve inclusion in the analysis, Eq. C.1 is modified so that

$$\sigma_{R,p\rightarrow d}(\mathrm{E},\theta) = \sigma_{\mathrm{R}}(\mathrm{E})\mathrm{W}_{\mathrm{R}}(\theta) + \sigma_{p\rightarrow d}(\mathrm{E})\mathrm{W}_{p\rightarrow d}(\theta) + 2\sqrt{\sigma_{\mathrm{R}}(\mathrm{E})\sigma_{p\rightarrow d}(\mathrm{E})}cos(\phi_{\mathrm{R}} - \phi_{p\rightarrow d})\mathrm{W}^{int}_{R,p\rightarrow d}(\theta). \quad \text{(C.17)}$$

The approximation

$$W_{R,p\rightarrow d}(\theta) \approx \frac{\sigma_{R,p\rightarrow d}(\mathrm{E},\theta)}{\sigma_{\mathrm{R}}(\mathrm{E}) + \sigma_{p\rightarrow d}(\mathrm{E})} \quad \text{(C.18)}$$

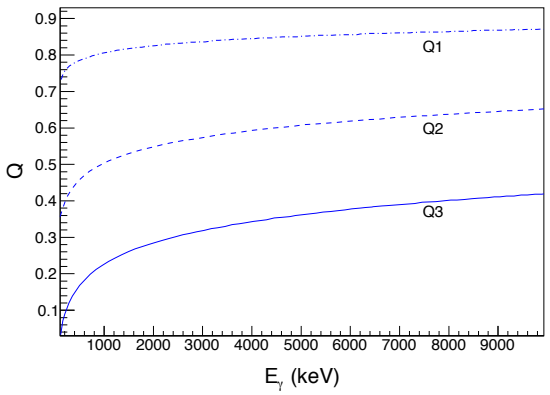

Figure C.2: The Q-coefficients used in the R,D interference angular correlation calculation. The Q_3 coefficient is a blue line, the Q_2 coefficient is a dashed blue line, and the Q_1 coefficient is a dash-dotted blue line. These values are extracted from Ref. [99] for the LENA high-purity germanium detector. While evaluating several angular correlation terms, it is assumed that the absorption coefficients at 0° are reasonable approximations while assessing which correlation terms to include in the analysis.

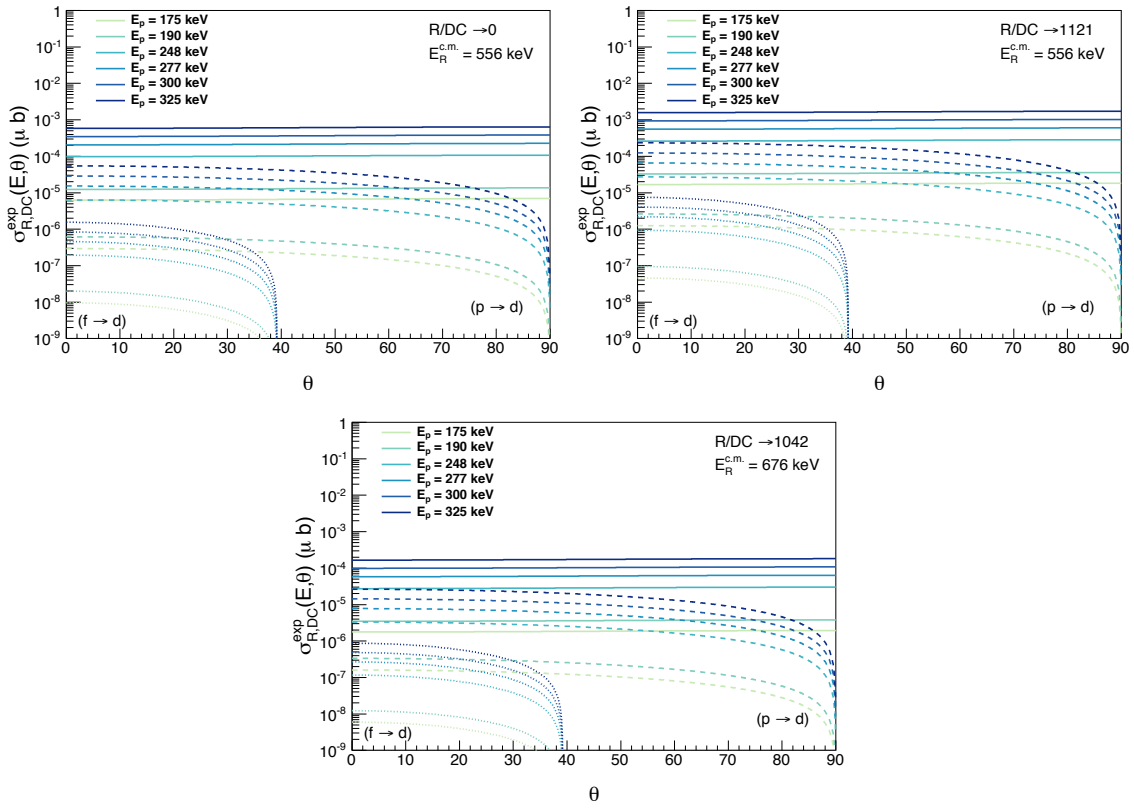

Figure C.3: Equations C.10 and C.11 are solved to determine if the differential cross section is affected by the angular correlation terms associated with direct capture and broad resonance interference. Eqs. C.9 (solid lines), C.10 (dashed lines), and C.11 (dotted lines) are plotted for all experimental bombarding energies over the angular range $\theta = 0{-}90°$. It is clear from these plots that the $(p \rightarrow d)$ interference terms contribute an additional $\approx \pm 10\%$ to the cross section, and the contributions due to $(f \rightarrow d)$ terms are negligible at $\theta = 0°$. These contributions diminish with increasing angle. The $(f \rightarrow d)$ contribution drops off at around 40° due to the dependence of Eq. C.11 on the P_3 Legendre polynomial.

can now be made. From this calculation, the total angular correlation term due to interference between direct capture transitions and broad resonance primaries is not distinguishable from unity; as a result, no anisotropies are included in the analysis due to R,D interference (see Fig. C.4).

Appendix C.2: Bound State Orbital Angular Momenta Terms

Bound state orbital angular momenta can also produce angular correlation terms. From Refs. [84, 78, 85], only E1 γ-ray transitions are considered for ^{17}O$(p,\gamma)^{18}$F direct capture. After performing coupling calculations for all of the known direct capture primaries [84]—keeping the dominance of the E1 multipolarity in mind—the only possible interfering bound state orbital angular momenta come from capture into s-shell and d-shell orbitals ($\ell_f = 0$ and $\ell_{f^*} = 2$, respectively). The coupling calculations reveal that several of these transitions only capture into d-shell orbitals. From Rolfs [84], the s-shell and d-shell angular correlation

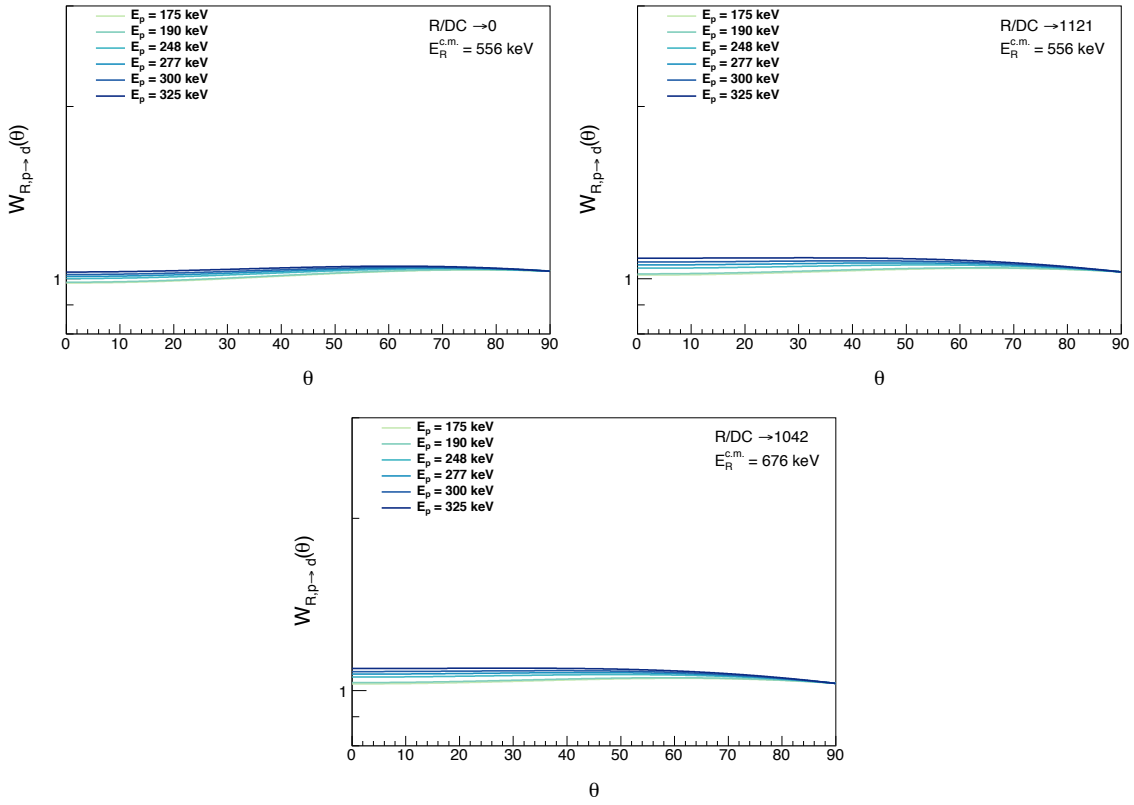

Figure C.4: Equation C.18 was solved to assess whether angular correlation terms calculated for interference between the two broad resonances, $E_R^{cm} = 556$ keV and $E_R^{cm} = 676$ keV, and $(p \rightarrow d)$ direct capture are anisotropic. In each figure, Eq. C.18 (solid lines), is plotted on a log-scale for all experimental bombarding energies over the angular range $\theta = 0{-}90°$. It is clear from the figures that the $(p \rightarrow d)$ interference terms produce an isotropic angular correlation, and R,D interference can be neglected from the analysis.

terms are:

$$W_{\ell_f}(\theta) = W_{p\to s}(\theta) = 1 - P_2\big(cos(\theta)\big) \tag{C.19}$$

and

$$W_{\ell_{f^*}}(\theta) = W_{p\to d}(\theta) = 1 - \frac{1}{10}P_2\big(cos(\theta)\big), \tag{C.20}$$

respectively. These two terms are incorporated into the calculation as an incoherent sum, defined by Ref. [84] as:

$$W(\theta) = \frac{1}{1+z}\Big(W_{\ell_f}(\theta) + zW_{\ell_{f^*}}(\theta)\Big) \tag{C.21}$$

where

$$z = \frac{\sigma_{p\to d}}{\sigma_{p\to s}}. \tag{C.22}$$

This z-factor is the ratio between the $(p \to d)$ and $(p \to s)$ cross sections for a particular direct capture transition.

The direct capture cross section code TEDCA [138] was used to calculate each direct capture primary's contribution to the total cross section (see Fig. C.5). In this figure, the $(p \to d)$ contributions are shown as dotted blue lines and the $(p \to s)$ contributions are depicted as dashed blue lines. Spectroscopic factors, reconciled from the literature and tabulated in Tab. 6.14, are not included in the cross sections presented in Fig. C.5; however, spectroscopic factors were introduced in the angular correlation calculations and are folded into the results displayed in Fig. C.6 (the solid red lines incorporate experimental values including the spectroscopic factors). The inclusion of the spectroscopic factors satisfies the definition of the experimental cross section from Eq. C.14. It is clear from Fig. C.5 that the DC→0, 1042, 1121, 4360, and 4652 keV transitions do not have $(p \to s)$ components. This can easily be demonstrated with the coupling calculations. It is evident from Fig. C.6 that these five transitions do not introduce anisotropies and can be disregarded from the final analysis; the angular correlations do not deviate from unity over the angular range $0°-90°$.

The remaining seven transitions do have $(p \to s)$ components and anisotropies are present. In Fig. C.6, the dashed lines represent $(p \to d)$ contributions (Eq. C.20), dotted lines represent $(p \to s)$ contributions (Eq. C.19), and solid lines represent the incoherent sum (Eq. C.21). Blue lines are strictly theoretical calculations while red lines include absorption coefficients from Longland *et al.* [99] (shown in Fig. C.2) and the spectroscopic factors tabulated in Tab. 6.14. The same assumptions made in Section C.1 with respect to the adoption of the absorption coefficients from Ref. [99] apply here.

Very minor deviations between angular correlation terms were observed between different beam energies for the seven transitions with anisotropic angular correlations. These deviations are represented in the figure by overlapping the final experimental incoherent sum at each beam energy for each DC primary. The

thickness associated with the solid red line in each plot shows that there is only a slight deviation between correlation terms over the beam energy range for each DC primary. Uncertainty was handled independently and is not incorporated into these plots. Uncertainty was sampled carefully at 0° and the method employed is described in more detail in Appendix A.1. The uncertainties calculated have little bearing on the final analysis because the GEANT4 simulations do not incorporate the Longland *et al.* absorption coefficients and instead solve Eq. C.21 each time an event is generated.

Appendix C.3: Scattering State Orbital Angular Momenta Interference

Finally, scattering state orbital angular momenta will produce interfering angular correlation terms if multiple partial waves form a particular bound state. From the coupling calculations, it is clear that only p-wave and f-wave captures are relevant for ^{17}O$(p,\gamma)^{18}$F direct capture. These two partial waves correspond to orbital angular momenta $\ell_i = 1$ and $\ell_{i^*} = 3$, respectively. From Rolfs [84], the angular correlations are:

$$W_{\ell_i}(\theta) = W_{p\to d}(\theta) = 1 - \frac{1}{10}P_2\big(cos(\theta)\big) \tag{C.23}$$

and

$$W_{\ell_{i^*}}(\theta) = W_{f\to d}(\theta) = 1 - \frac{2}{5}P_2\big(cos(\theta)\big), \tag{C.24}$$

respectively. Interference between these angular correlations can be resolved with a coherent sum, defined by Rolfs as:

$$W(\theta) = \frac{1}{1+y}\left(W_{\ell_i}(\theta) + yW_{\ell_{i^*}}(\theta) \pm 2\sqrt{y}cos(\epsilon)\mathrm{W}^{int}_{\ell_i\ell_{i^*}}(\theta)\right) \tag{C.25}$$

where

$$y = \frac{\sigma_{f\to d}}{\sigma_{p\to d}} \tag{C.26}$$

This y-factor is the ratio between the $(f \to d)$ and $(p \to d)$ cross sections for a particular transition. In the coherent sum,

$$\epsilon = \phi_{\ell_{i^*}} - \phi_{\ell_i} + \delta_{\ell_{i^*}} - \delta_{\ell_i} = \xi_{\ell_{i^*}} - \xi_{\ell_i}. \tag{C.27}$$

Eq. C.27 refers to both the Coulomb phase shift (ϕ) and the nuclear phase shift (δ), and they can be rewritten in terms of the Sommerfeld parameter and the Coulomb wave functions, respectively. From Ref. [157], the combination of nuclear and Coulomb phase shifts becomes:

$$\xi_\ell = -\arctan\frac{F_\ell}{G_\ell} + \sum_{n=1}^{\ell}\arctan\frac{\eta}{n}. \tag{C.28}$$

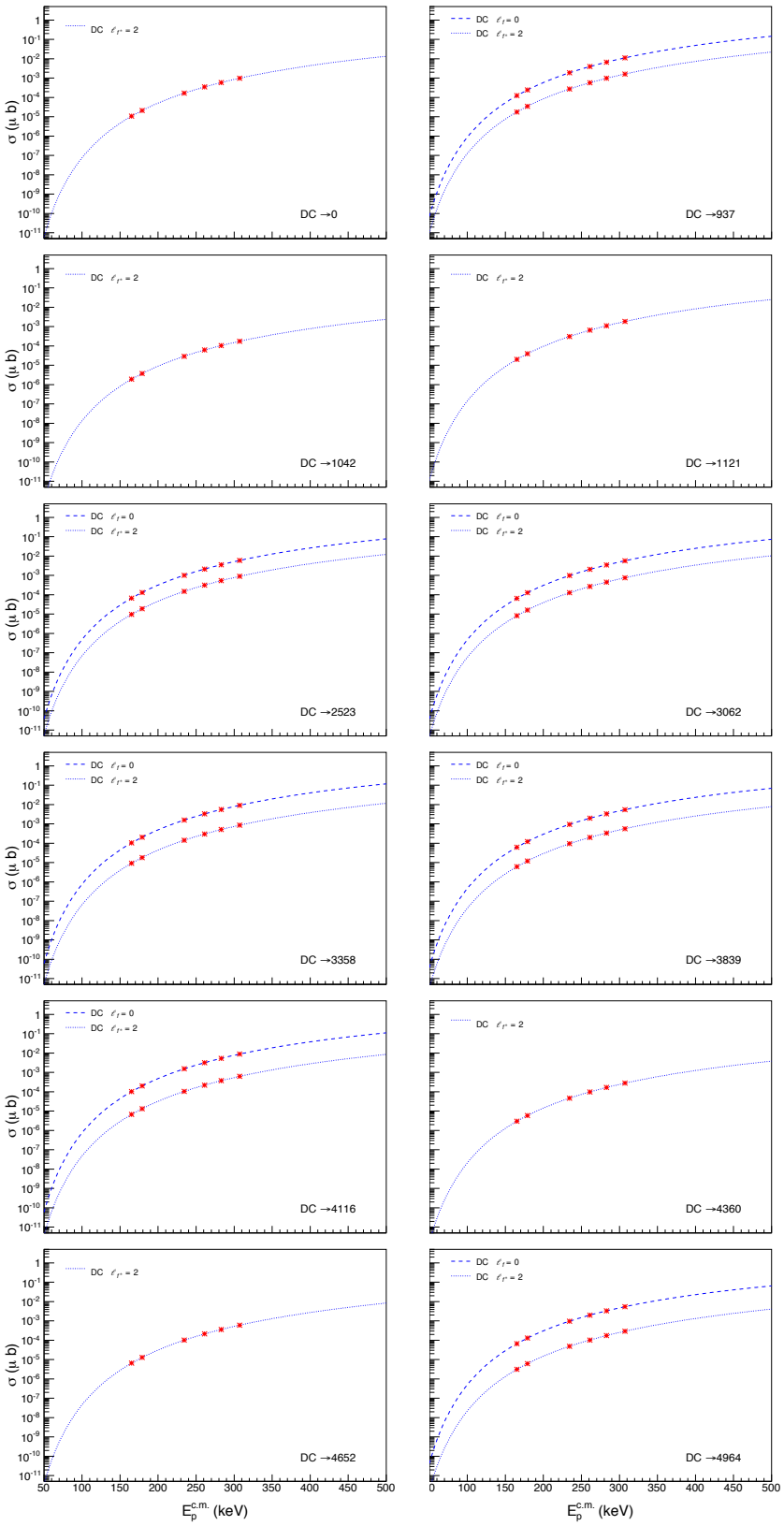

Figure C.5: Cross sections (in μb) calculated for each ^{17}O(p,γ)^{18}F DC primary with TEDCA [138] for $\ell_f = 0$ ($p \rightarrow s$) and $\ell_{f^*} = 2$ ($p \rightarrow d$) over the energy range $E_p^{cm} = 50{-}500$ keV. Beam energies $E_p = 175$, 190, 250, 275, 300, and 325 keV are shown as red asterisks.

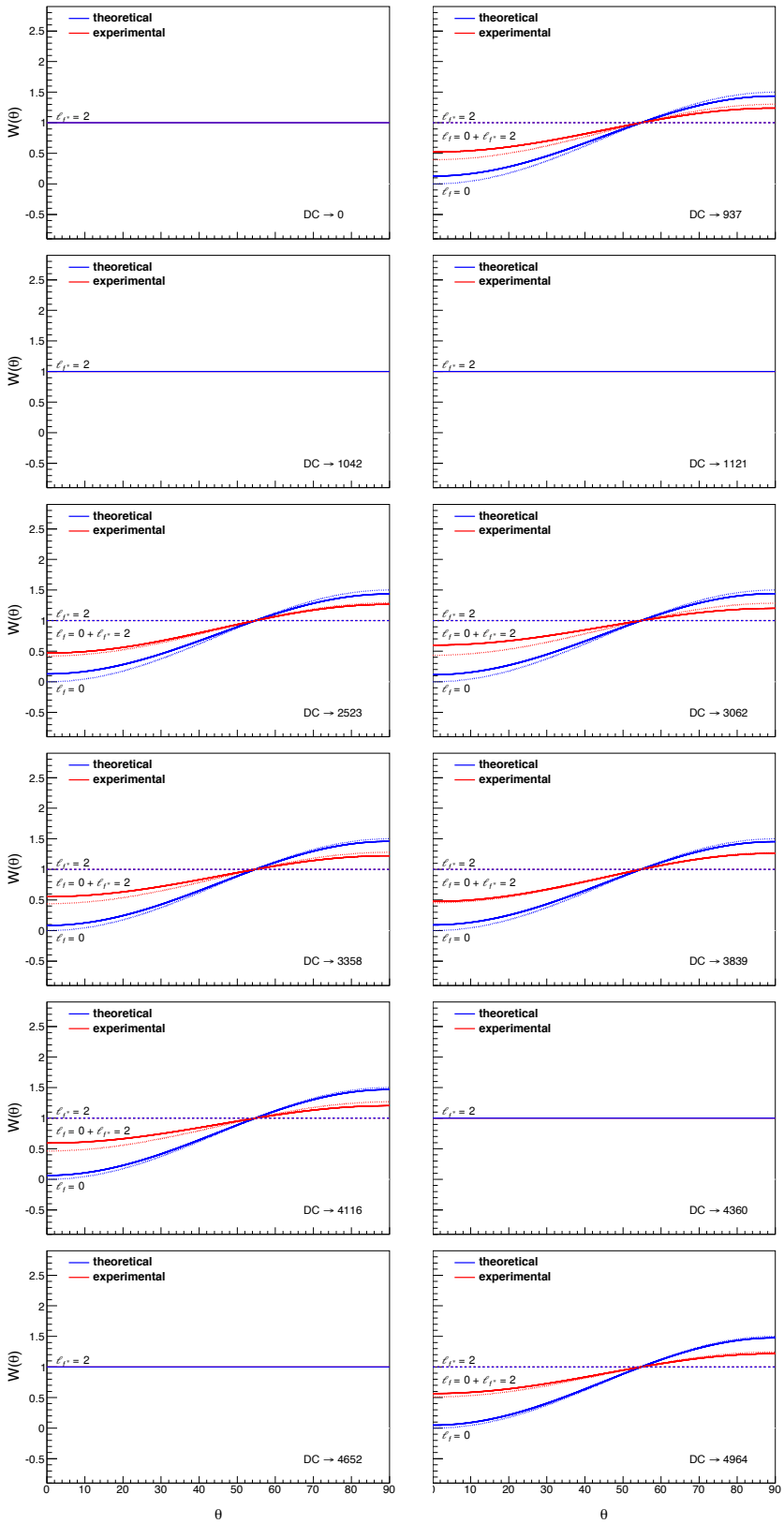

Figure C.6: For the known ^{17}O(p,γ)^{18}F DC primaries, $\ell_{f^*} = 2$ (dashed lines), $\ell_f = 0$ (dotted lines), and summed (solid lines) angular correlations were calculated from 0°−90°. Blue lines are theoretical calculations and red lines include spectroscopic factors and absorption coefficients.

For interference between p-wave and f-wave scattering,

$$\xi_{\ell_{i^*}=3} - \xi_{\ell_i=1} = \arctan\frac{F_1}{G_1} - \arctan\frac{F_3}{G_3} + \arctan\frac{\eta}{2} + \arctan\frac{\eta}{3}. \tag{C.29}$$

From Rolfs [84], the interference portion of the coherent sum becomes:

$$W^{int}_{\ell_i=1,\ell_{i^*}=3}(\theta) = \frac{3}{5}\sqrt{\frac{3}{2}}P_2\big(cos(\theta)\big). \tag{C.30}$$

To solve these equations and assess whether these orbital angular momenta cause anisotropic angular correlations, $(p \rightarrow d)$ and $(f \rightarrow d)$ cross sections were calculated with the direct capture code TEDCA [138] for the known direct capture primaries [84]. In Fig. C.7, the $(p \rightarrow d)$ cross sections are shown as dashed blue lines and the $(f \rightarrow d)$ cross sections are shown as dotted blue lines. Red asterisks represent the six experimental bombarding energies, E_R = 175, 190, 250, 275, 300, and 325 keV. Eq. C.25 was then solved over the angular range, $0°-90°$ for each transition at each experimental bombarding energy (see Fig. C.8). In the figure, the solutions to Eqs. C.23 and C.24 are plotted as dashed and dotted lines, respectively. The coherent sums are plotted as solid lines. Blue lines indicate theoretical input (excluding spectroscopic factors and absorption coefficients) and red lines represent experimental correlations terms (with absorption coefficients from Longland *et al.* [99], see Fig. C.2, included). Once again, the absorption coefficients from Ref. [99] were adopted as reasonable approximations for the purposes of assessing the possible angular correlation terms. From the results presented in Fig. C.8, it is evident that scattering state orbital angular momenta are not responsible for angular correlation anisotropies, and the correlation terms do not deviate from unity. Uncertainties in the angular correlations were calculated and assessed using the methodology explained in Appendix A.1. The isotropic angular correlations that result from the coherent sum of p-wave and f-wave contributions are not included in the final analysis.

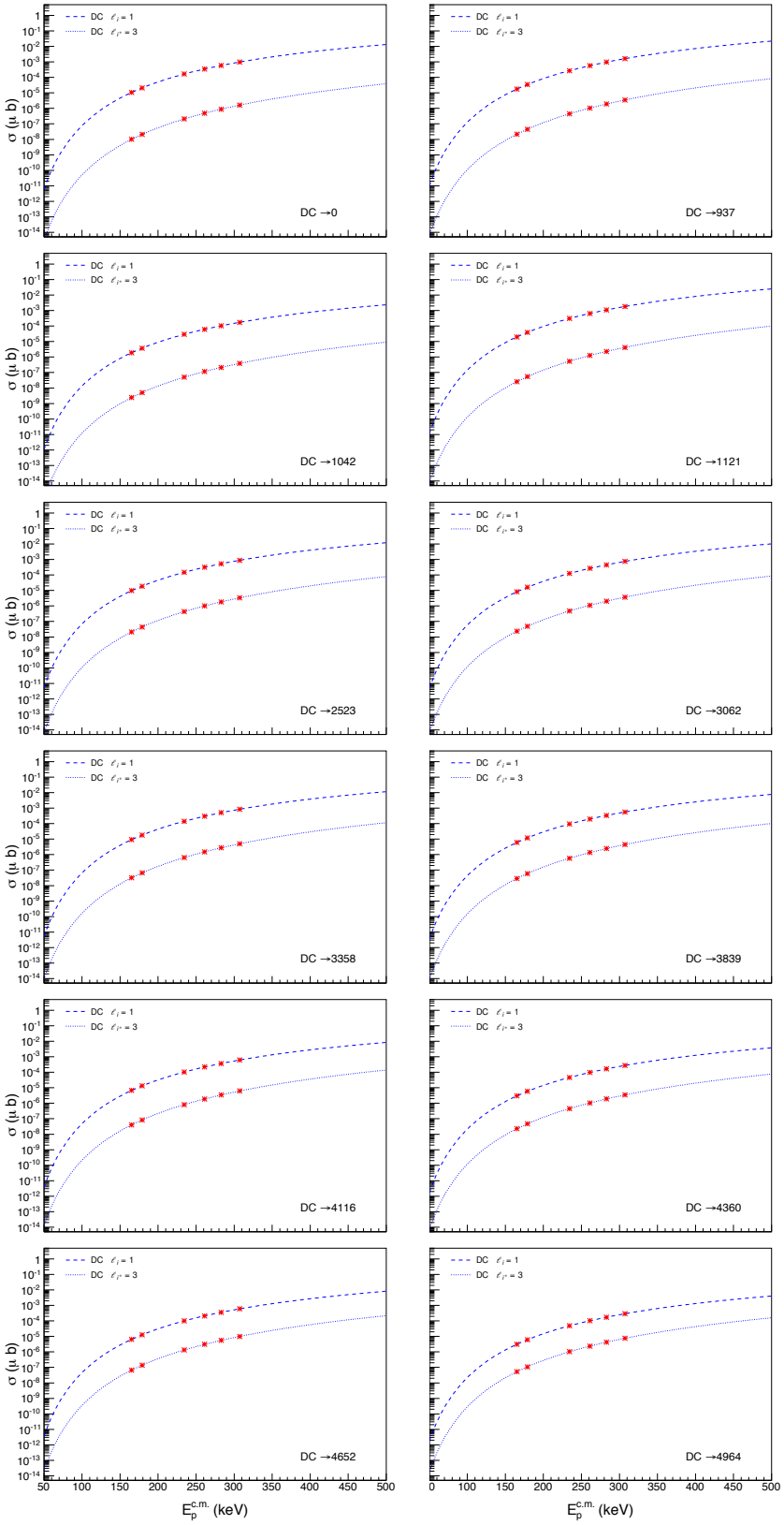

Figure C.7: Cross sections (in μb) calculated for each observed ^{17}O$(p,\gamma)^{18}$F DC primary with TEDCA [138] for $\ell_i = 1$ and $\ell_{i^*} = 3$ over the energy range $E_p^{cm} = 50-500$ keV. Beam energies $E_p = 175$, 190, 250, 275, 300, and 325 keV are shown as red asterisks.

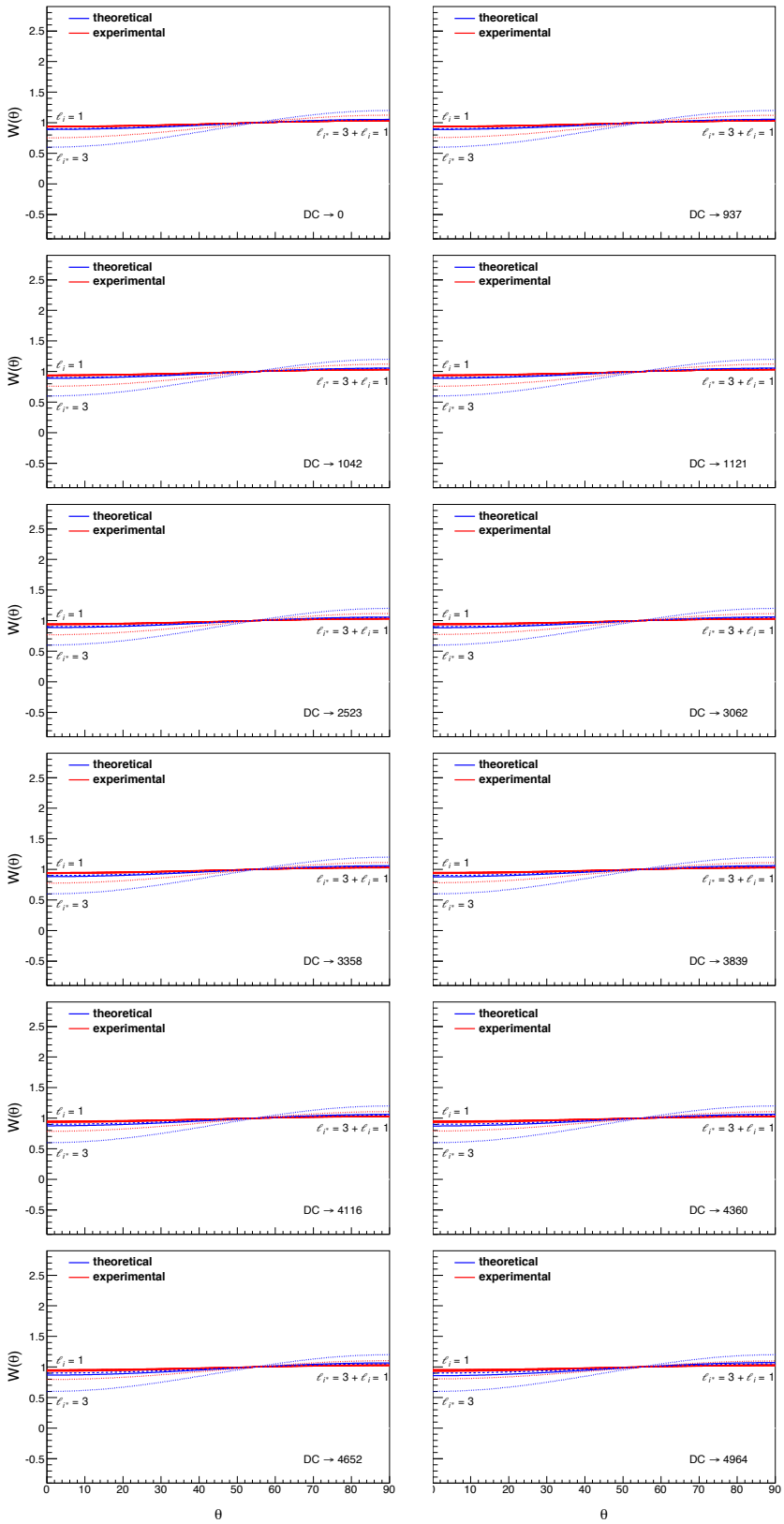

Figure C.8: For the known ^{17}O$(p,\gamma)^{18}$F DC primaries, $\ell_{i^*} = 3$ (dotted lines), $\ell_1 = 1$ (dashed lines), and interference (solid lines) angular correlations were calculated from $0°-90°$. Blue lines are theoretical calculations and red lines include absorption coefficients.

APPENDIX D: MONTE CARLO DETECTOR EFFICIENCIES

Appendix D.1: Monte Carlo HPGe Peak Efficiencies

A new analysis method from Ref. [194] was tested to sum-correct experimental peak intensities. This new sum-correction method is accomplished by complicated book-keeping of the energy deposition during a GEANT4 [102, 103] simulation. When an event occurs in the simulated LENA GEANT4 detector system, a *ParentID* is assigned to that event. A *ProcessID* describes the event: if it is Compton scattering, the photoelectric effect, pair production, etc. Additionally, GEANT4 keeps track of the creation direction of the original event (in three dimensions). These attributes, unique ParentIDs and a record of creation directions, allow the user to track events through the detector and group related events—here related events will be referred to as *groups*. For example, ^{60}Co decays preferentially via a two step γ-cascade, 2→1→0, where E_γ^{21} = 1173 keV and E_γ^{10} = 1332 keV. The two γ-rays will not be considered a part of the same group—they will have different ParentIDs, different creation directions, and are considered "unrelated." Only the chronological energy depositions within the detector, associated with a single γ-ray, are considered the constituents of each γ-ray's group. In a group, the related events are each depositing a portion of the total event energy (so either 1173 keV or 1332 keV in this example). At this point, the progenitor event (the first instance that a portion of E_γ is deposited in the detector) can not be identified, but GEANT4 keeps track of *when* during a simulation an event occurs—thus deposition can be tracked chronologically. GEANT4 stores a *time stamp* for each deposition event that can be queried for each member of a group, and in a given group, the event with the lowest time stamp is the progenitor (the first instance of energy deposition in the crystal). Starting with the progenitor event, energy deposited in the detector by subsequent (related) events can be summed to calculate the total energy deposited in the detector by the incident γ-ray. With a post-processing sort routine, a new spectrum is populated with γ-ray energies calculated by tracking deposition events instead of the traditional way—populating a HPGe singles spectrum during a simulation with a "snapshot" of detected energies. Because each γ-ray's energy deposition is individually being followed from start to finish, there will not be any summing in the new spectrum—these counts are decoupled from simultaneous detections.

To summarize, for the ^{60}Co decay, every instance of a 1173 keV γ-ray detected by the HPGe detector deposits some initial portion of its energy in the crystal. This instance is identified as the progenitor event and all subsequent deposition events are summed that share a ParentID, creation direction, and occur chronologically after the progenitor. The 1332 keV secondaries are also individually distinguished in this manner as energy is deposited in the detector. GEANT4 stores events chronologically so the post-processing code that sorts Monte Carlo events into spectra—*sort.cxx* discussed in more detail in Sec. 6.3.1—can discriminate between the 1173 keV and 1332 keV γ-rays and will not misinterpret them as a single 2505

keV γ-ray. Figure D.1 is a simplified illustration of how GEANT4 interprets the detection of 1173 and 1332 keV γ-rays from the ^{60}Co decay. A pink source puck was drawn in the DAWN [104] schematic of the LENA $\gamma\gamma$-coincidence spectrometer in Fig. 3.10. Thick arrows labeled "1173" and "1332" represent the two ^{60}Co γ-rays. In this example, the 1173 keV progenitor event deposits 500 keV in the HPGe detector while the 1332 keV progenitor event deposits 1000 keV. The 1173 keV group contains two more depositions, 500 keV and 173 keV. The 1332 keV group terminates after a final 332 keV deposition in the crystal. The regular HPGe singles histogram would be populated with a 2505 keV γ-ray while the new sum-corrected spectrum records separate 1173 and 1332 keV γ-rays.

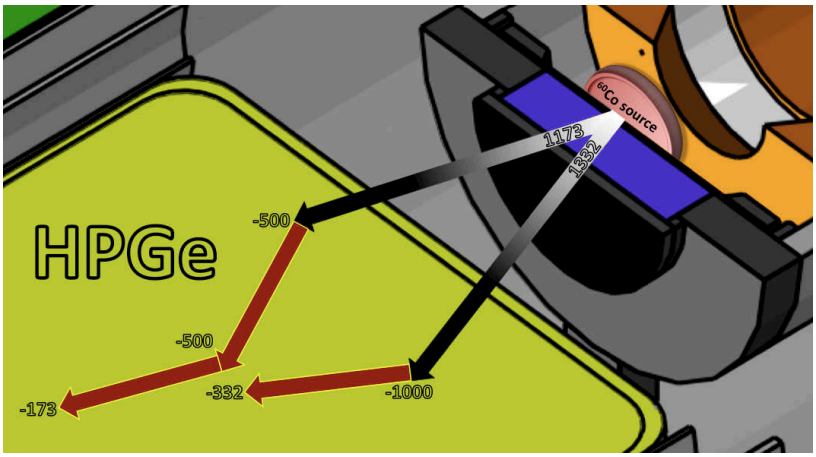

Figure D.1: From the DAWN [104] schematic of the LENA $\gamma\gamma$-coincidence spectrometer in Fig. 3.10, a simplified illustration of how GEANT4 handles a ^{60}Co decay. A pink source puck was added against the target surface. Thick arrows labeled "1173" and "1332" represent the primary and secondary, respectively. The red arrows are subsequent energy depositions by dislodged electrons. The negative values labeled within the crystal indicate energy deposition sites and what portion of the total γ-ray energy has been deposited. When filling a regular HPGe singles spectrum, GEANT4 interprets this example of a simultaneous detection as a single, 2505 keV γ-ray. With the GEANT4 sum-correction method, these separate γ-rays initiate two distinct energy deposition chains. The sum of the energy deposited by each chain individually populate a sum-corrected singles spectrum.

By comparing a peak intensity in the regular HPGe singles spectrum and the same intensity in the new spectrum, a sum-correction factor (the ratio between the two intensities) can be determined for a particular γ-ray. This correction factor can then be multiplied by the experimental peak intensity to sum-correct the data. The equation for the number of disintegrations from Ref. [4] becomes:

$$N_{\mathrm{R}} = \frac{N_{\gamma} r}{B_{\gamma} \eta^{Ge,P} \mathrm{W}(\theta)} \tag{D.1}$$

where N_{R} is the number of disintegrations, N_{γ} is the experimental HPGe singles peak intensity (subject

to summing), B_γ is the branching ratio, $\eta^{Ge,P}$ is the germanium peak efficiency, and W(θ) is the angular correlation. The new term, r, is the sum-correction factor where:

$$r = \frac{N_{n.s.}^{MC}}{N_{\gamma}^{MC}} \tag{D.2}$$

when $N_{n.s.}^{MC}$ is the Monte Carlo peak intensity with summing removed and N_{γ}^{MC} is the Monte Carlo peak intensity with summing handled naturally by GEANT4.

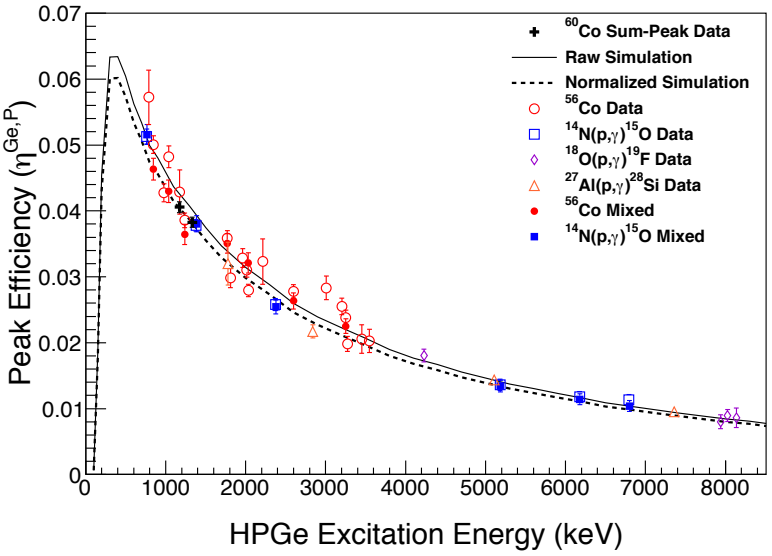

Figure D.2: The absolute ^{60}Co peak efficiency from the sum-peak method [105] (black crosses) is plotted alongside the experimental efficiencies from Fig. 3.11, raw simulated efficiencies (solid line), normalized Monte Carlo efficiencies (dashed line), and GEANT4 sum-corrected efficiencies [194]. The GEANT4 sum-correction method [194] was used to calculate source and reaction peak efficiencies for ^{56}Co and the ^{14}N(p,γ)^{15}O resonance E$_R$ = 278 keV, respectively. They are labeled "Mixed" in this figure because they contain experimental and simulated components. Note that these experimental components are independent from the data that were sum-corrected with the matrix method (see Sec. 3.5.1). Mixed efficiencies are not included in either the ^{18}O(p,γ)^{19}F or ^{17}O(p,γ)^{18}F analyses.

To calculate experimental efficiencies with this sum-correction technique, the only additional information needed is the number of disintegrations. A routine was written that relies upon ROOT's *TFractionFitter* class to compare GEANT4 and experimental spectra. The *TFractionFitter* class calculates what fractions of background and Monte Carlo spectra make up the total experimental singles (or coincidence) spectrum. Figure D.2 includes the HPGe ^{56}Co and ^{14}N(p,γ)^{15}O peak efficiencies calculated with the new methods outlined in this section and are labeled "Mixed" because they contain both simulated and experimental components. They are plotted alongside the ^{60}Co absolute peak efficiency, determined with the sum-peak method, GEANT4 mono-energetic γ-ray raw and normalized efficiencies, and the experimental efficiencies

that were sum-corrected with the matrix method from Fig. 3.11. They were shifted to match the absolute peak efficiency at E_γ^{10} = 1332 keV. Before this shift was applied, the "Mixed" ^{14}N(p,γ)^{15}O peak efficiency and the absolute efficiency differed only by 1.3% at E_γ^{10} = 1332 keV. The ^{56}Co "Mixed" peak efficiency agreed with the absolute efficiency within 2.2%. The "Mixed" efficiencies, the "Data" efficiencies, and the absolute efficiency agree well; this is the first indication that ROOT's *TFractionFitter* class can be used to calculate total reaction numbers. Determining total reaction numbers with *TFractionFitter* is tested and discussed in detail in Sec. 6.3.

Appendix D.2: Monte Carlo NaI(Tl) Gated Total Efficiencies

As discussed in the previous section, GEANT4 simulations are used to calculate coincidence correction factors—complex quantities that depend on the NaI(Tl) total efficiency—because the Monte Carlo method can easily account for events summing into the software gate. The analytical method described in Refs. [108, 117] is an alternative that has some difficulty accounting for this summing. In Fig. D.2, mono-energetic γ-rays were simulated with GEANT4 to produce the Monte Carlo HPGe peak efficiency curve. The goal here was to produce an analogous plot of NaI(Tl) total efficiencies using GEANT4. For a two step decay scheme, like the deexctiation of the ^{15}O nucleus from the ^{14}N(p,γ)^{15}O E_R = 278 keV resonance, Eq. 3.13 can be rewritten for a primary detected in a coincidence spectrum:

$$N_{21}^c = N_R \eta_{21}^{Ge,P} B_{21} B_{10} \eta_{10}^{NaI(Tl),T}. \tag{D.3}$$

In this equation, $B_{10}\eta_{10}^{NaI(Tl),T}$ is f_γ. In a HPGe singles spectrum, the intensity of the 2→1 primary transition, N_{21}^s, is simply:

$$N_{21}^s = N_R \eta_{21}^{Ge,P} B_{21}. \tag{D.4}$$

The procedure discussed in Appendix D.1 provides a Monte Carlo-based method of sum-correcting peak intensities in simulated GEANT4 spectra. If the peak intensities in Eqs. D.3 and D.4 are sum-corrected, the ratio of the two equations should yield:

$$\frac{N_{21}^c r^c}{N_{21}^s r^s} = B_{10}\eta_{10}^{NaI(Tl),T} = f_\gamma \tag{D.5}$$

where r^c and r^s are the sum-correction factors calculated for the 2→1 peak in the coincidence and singles spectra, respectively:

$$r^c = \frac{N_{n.s.}^{MC,c}}{N_\gamma^{MC,c}} \tag{D.6}$$

and

$$r^s = \frac{N_{n.s.}^{MC,s}}{N_{\gamma}^{MC,s}}. \tag{D.7}$$

Now, a GEANT4 simulation can be performed analogous to the mono-energetic γ-ray simulations that are run for peak efficiencies. In order to solve for $\eta_{10}^{NaI(Tl),T}$ in Eq. D.5, an arbitrary two-step decay scheme can be assembled. In this decay scheme, B_{10} can be set to "1.0" to simplify the calculation—all secondaries in this artificial decay scheme will have a 100% probability of emission. The primaries can also be set to any value. Five artificial two-step decay schemes were run; each had eight primaries, with $B_{21} = 0.125$, and eight secondaries, with $B_{10} = 1.0$, for a total of forty two-step decays (these were run separately to reduce the likelihood of overlapping peaks in the artificial spectra). A high value for N_{R} was selected by the user to improve the statistics of the Monte Carlo output. The coincidence gate 3.5 MeV $\leq \mathrm{E}_{\gamma}^{Ge} + \mathrm{E}_{\gamma}^{NaI(Tl)} \leq$ 9.0 MeV was selected. The artificial excited state in all five decay schemes was set to E_x = 8900 keV so that all transition pairs would satisfy this coincidence condition. The five simulations were run and the GEANT4 output was sorted into HPGe singles sum-corrected histograms and coincidence sum-corrected histograms (because experimental data are not being sum-corrected here, multiplying by r becomes an unnecessary step). The ratio for each primary intensity, N_{21}^c/N_{21}^s with sum-corrections applied, can then be plotted with respect to the energy of the secondary, $\mathrm{E}_{10} = \mathrm{E}_{\gamma}^{NaI(Tl)}$, because this is the energy detected by the NaI(Tl) annulus—satisfying the coincidence condition. In this case, where a two step decay is used and branching ratios of all secondaries are 100%, the plot of N_{21}^c/N_{21}^s versus E_{10} is the total efficiency of the NaI(Tl) annulus and the f_{γ} correction factor. The result is plotted as a dashed black line in Fig. D.3 and labeled "Arbitrary GEANT4." There is a noticeable *turn-off point* in the slope that is discussed below.

This procedure was then tested with the $^{14}\mathrm{N}(p,\gamma)^{15}\mathrm{O}$ $\mathrm{E_R}$ = 278 keV resonance. The same steps were followed—five artificial decay schemes—however the excited state was set to E_x = 7567.14 keV for the $\mathrm{E_R}$ = 278 keV resonance [121, 41]. The result is plotted in Fig. D.3 as a dashed blue line. Here the turn-off point has shifted to a lower energy (discussed below). Experimental $\mathrm{E_R}$ = 278 keV resonance primary peak intensities were sum-corrected with the technique described in Appendix D.1 and plugged into Eq. D.5 and secondaries were plugged into the analogous equation:

$$\frac{N_{10}^c r^c}{N_{10}^s r^s} = B_{21}\eta_{21}^{NaI(Tl),T} \tag{D.8}$$

where now B_{21} can not be neglected (primary emission probabilities are not 100% for the $\mathrm{E_R}$ = 278 keV resonance). The blue squares in Fig. D.3 are the calculated NaI(Tl) gated total efficiencies of the $\mathrm{E_R}$ = 278 keV primaries and secondaries from the experimental data. The ground state transition is excluded from the

figure because it is not coincident with any other γ-ray and will not appear in a gated coincidence spectrum. A total efficiency uncertainty of 5% is adopted based on the analysis of these efficiencies.

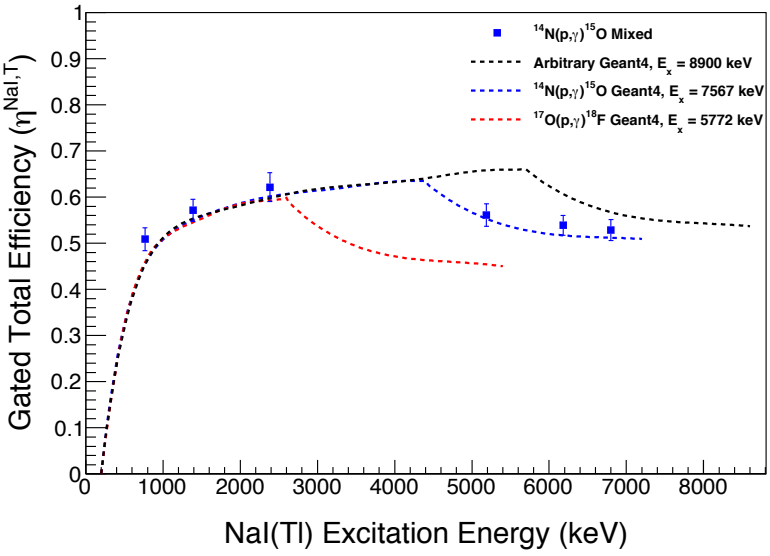

Figure D.3: The new GEANT4 sum-correction method was used to calculate gated NaI(Tl) total efficiencies for the ^{14}N(p,γ)^{15}O E$_R$ = 278 keV resonance. The ^{14}N(p,γ)^{15}O gated efficiencies are labeled "Mixed" because they contain experimental and simulated components. Forty artificial two-step decays from E$_x$ = 7567.14 keV were simulated in five 8-decay sets. Then Eq. D.8 was solved to calculate the gated total efficiency for each transition. The gated total efficiency was also calculated from experimental E$_R$ = 278 keV resonance data and is plotted as blue squares in this figure. An arbitrary decay scheme from E$_x$ = 8900 keV (dashed black line) and a decay scheme from ^{17}O(p,γ)^{18}F direct capture reaction where E$_x$ = 5772 keV (dashed red line) are also plotted. The coincidence conditions here are E$_{low}$ = 3500 keV and E$_{high}$ = 9000 keV.

Next, a NaI(Tl) gated total efficiency versus detected NaI(Tl) energy plot was generated for the ^{17}O(p,γ)^{18}F direct capture reaction where E$_x$ = 5772 keV (E$_p$ = 175 keV) [121, 41]. This curve is plotted as a dashed red line in Fig. D.3.

All three curves in Fig. D.3 feature a turn-off point at progressively higher energies. Recall that these curves are plotted with respect to $E_\gamma^{NaI(Tl)}$ so high energies in this figure correspond to low energies in the HPGe detector, E_γ^{Ge}. The dip in each plot comes from the coincidence gate. The γ-rays detected by the annulus at high energies are coincident with γ-rays in the HPGe where $E_\gamma^{Ge} < E_{low}$, but the condition $E_{low} \leq E_\gamma^{Ge} + E_\gamma^{NaI(Tl)} \leq E_{high}$ is still satisfied. This was tested with the artificial decay from E$_x$ = 8900 keV sorted through three different coincidence gates: E$_{low}$ = 3500, 5500, and 7500 keV. The E$_{high}$ = 9000 keV threshold was held constant. The dip in the three curves shifted due to the change in the E$_{low}$ coincidence condition.

The gated total efficiency, like the peak efficiency, was calculated to illustrate the agreement between simulations and experimental results. It was important to demonstrate that Monte Carlo simulations of the

LENA $\gamma\gamma$-coincidence spectrometer agree well with experimental results.

APPENDIX E: SPECTRA

Spectra collected with the high purity germanium detector and gated coincidence spectra from the $^{17}O(p,\gamma)^{18}F$ study are shown in this section (all spectra include the muon veto anticoincidence condition). Peaks associated with the deexcitation of the ^{18}F nucleus are labeled on each figure by transition. Transition intensities can be found in Tab. 6.3. First and second escape peaks are labeled "FE" and "SE," respectively, and only correspond to the ^{18}F deexcitations. Environmental backgrounds are not labeled, save for the 1460 keV ^{40}K, the 2614 keV ^{208}Tl peak, and the 511 keV e^+e^--annihilation peak; however, the observed environmental backgrounds are itemized in Tab. E.1 [195]. Beam-induced backgrounds are also labeled by reaction, but there is no differentiation between the first and second escape peaks from the beam-induced background resonance transitions. The beam-induced reactions are tabulated in Tab. 4.1.

Table E.1: The environmental backgrounds observed during these experiments. The dominant decay chains include ^{226}Ra and ^{232}Th daughter nuclei, and the γ-ray energies from Ref. [195] are tabulated.

Decay	E_γ (keV)	Decay	E_γ (keV)
$^{226}Ra(\alpha)^{222}Rn$	186.211±0.013	$^{214}Bi(\beta^-\overline{\nu}_e)^{214}Po$	1280.96±0.02
$^{212}Pb(\beta^-\overline{\nu}_e)^{212}Bi$	238.632±0.002	$^{24}Na(\beta^-\overline{\nu}_e)^{24}Mg$	1368.626±0.005
$^{214}Pb(\beta^-\overline{\nu}_e)^{214}Bi$	295.224±0.002	$^{214}Bi(\beta^-\overline{\nu}_e)^{214}Po$	1377.669±0.012
$^{214}Pb(\beta^-\overline{\nu}_e)^{214}Bi$	351.932±0.002	$^{214}Bi(\beta^-\overline{\nu}_e)^{214}Po$	1407.98±0.04
$^{208}Tl(\beta^-\overline{\nu}_e)^{208}Pb$	510.77±0.10	$^{40}K(\beta^+\nu_e)^{40}Ar$	1460.830±0.005
$^{208}Tl(\beta^-\overline{\nu}_e)^{208}Pb$	583.191±0.002	$^{228}Ac(\beta^-\overline{\nu}_e)^{228}Th$	1495.91±0.02
$^{214}Bi(\beta^-\overline{\nu}_e)^{214}Po$	609.312±0.007	$^{214}Bi(\beta^-\overline{\nu}_e)^{214}Po$	1509.228±0.015
$^{228}Ac(\beta^-\overline{\nu}_e)^{228}Th$	726.863±0.015	$^{228}Ac(\beta^-\overline{\nu}_e)^{228}Th$	1588.20±0.03
$^{212}Bi(\beta^-\overline{\nu}_e)^{212}Po$	727.330±0.009	$^{212}Bi(\beta^-\overline{\nu}_e)^{212}Po$	1620.50±0.10
$^{214}Bi(\beta^-\overline{\nu}_e)^{214}Po$	768.356±0.010	$^{228}Ac(\beta^-\overline{\nu}_e)^{228}Th$	1630.627±0.010
$^{228}Ac(\beta^-\overline{\nu}_e)^{228}Th$	794.947±0.005	$^{214}Bi(\beta^-\overline{\nu}_e)^{214}Po$	1661.28±0.06
$^{208}Tl(\beta^-\overline{\nu}_e)^{208}Pb$	860.564±0.005	$^{214}Bi(\beta^-\overline{\nu}_e)^{214}Po$	1729.595±0.015
$^{228}Ac(\beta^-\overline{\nu}_e)^{228}Th$	911.204±0.004	$^{214}Bi(\beta^-\overline{\nu}_e)^{214}Po$	1764.494±0.014
$^{214}Bi(\beta^-\overline{\nu}_e)^{214}Po$	934.061±0.012	$^{214}Bi(\beta^-\overline{\nu}_e)^{214}Po$	1847.42±0.025
$^{228}Ac(\beta^-\overline{\nu}_e)^{228}Th$	964.766±0.010	$^{214}Bi(\beta^-\overline{\nu}_e)^{214}Po$	2118.55±0.03
$^{228}Ac(\beta^-\overline{\nu}_e)^{228}Th$	968.971±0.017	$^{214}Bi(\beta^-\overline{\nu}_e)^{214}Po$	2204.21±0.04
$^{228}Ac(\beta^-\overline{\nu}_e)^{228}Th$	1000.69±0.15	$^{214}Bi(\beta^-\overline{\nu}_e)^{214}Po$	2293.40±0.12
$^{214}Bi(\beta^-\overline{\nu}_e)^{214}Po$	1120.287±0.010	$^{214}Bi(\beta^-\overline{\nu}_e)^{214}Po$	2447.86±0.10
$^{214}Bi(\beta^-\overline{\nu}_e)^{214}Po$	1238.11±0.012	$^{208}Tl(\beta^-\overline{\nu}_e)^{208}Pb$	2614.533±0.013

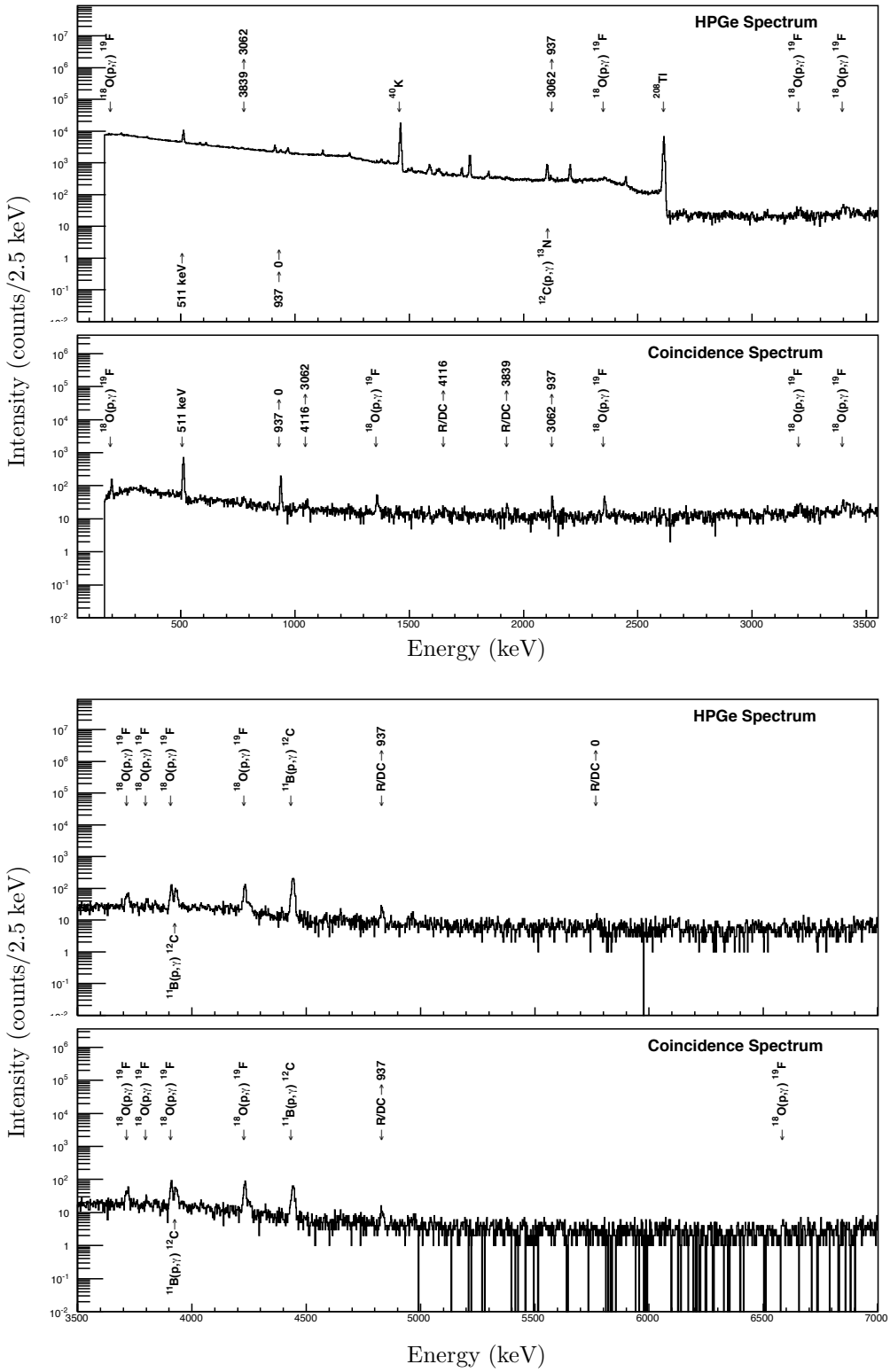

Figure E.1: Muon vetoed HPGe spectrum compared with muon vetoed $\gamma\gamma$-coincidence spectrum at $E_p = 175$ keV. A 3.5 MeV $\leq E_\gamma^{Ge} + E_\gamma^{NaI(Tl)} \leq$ 9.0 MeV coincidence gate was used. Deexcitations of ^{18}F are indicated by transition. First and second escape peaks are labeled "FE" and "SE," respectively. Beam-induced contaminants are labeled, and the remaining peaks are environmental backgrounds (see Tab. E.1).

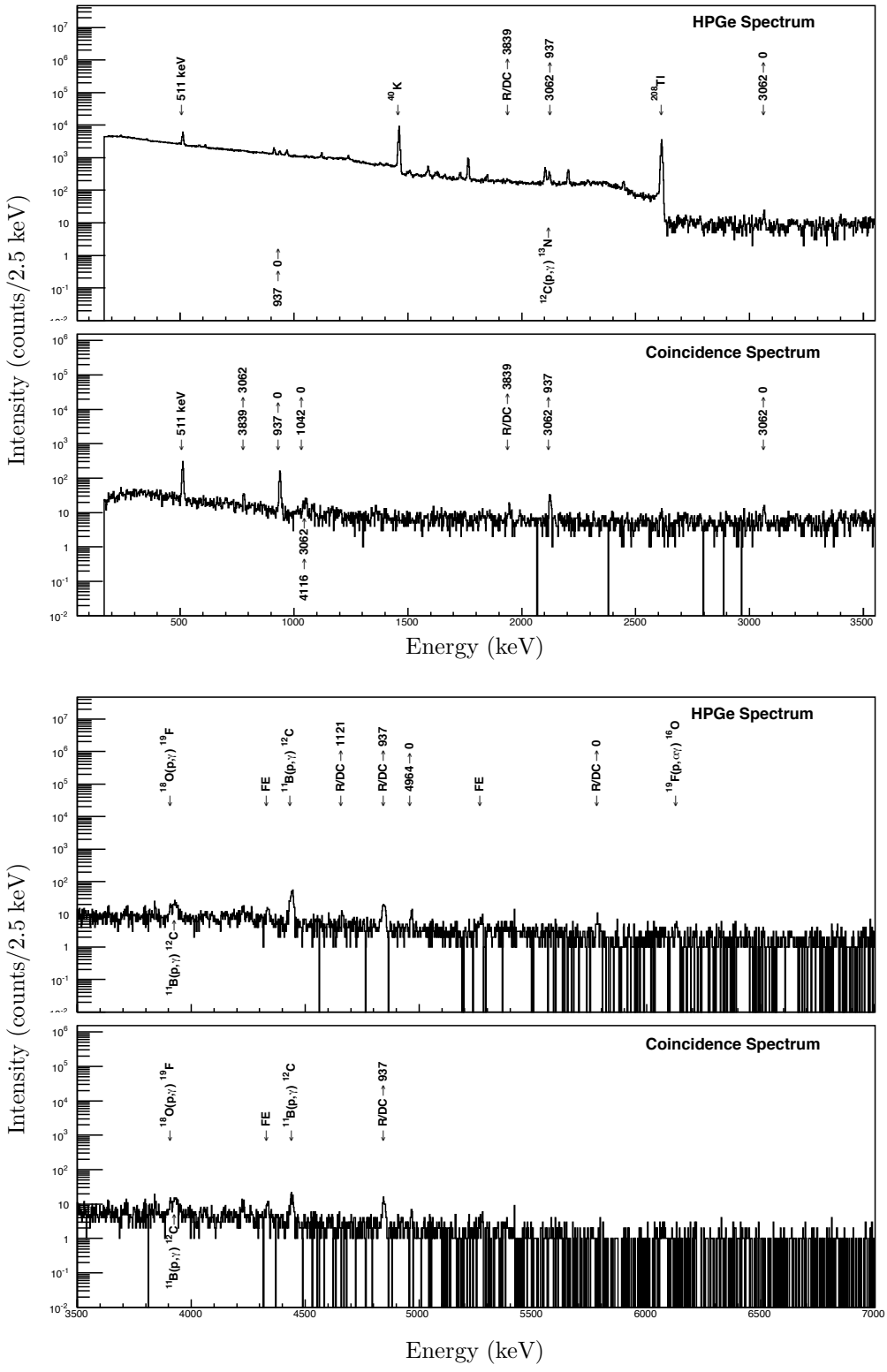

Figure E.2: Muon vetoed HPGe spectrum compared with muon vetoed $\gamma\gamma$-coincidence spectrum at $E_p = 190$ keV. A 3.5 MeV $\leq E_\gamma^{Ge} + E_\gamma^{NaI(Tl)} \leq$ 9.0 MeV coincidence gate was used. Deexcitations of ^{18}F are indicated by transition. First and second escape peaks are labeled "FE" and "SE," respectively. Beam-induced contaminants are labeled, and the remaining peaks are environmental backgrounds (see Tab. E.1).

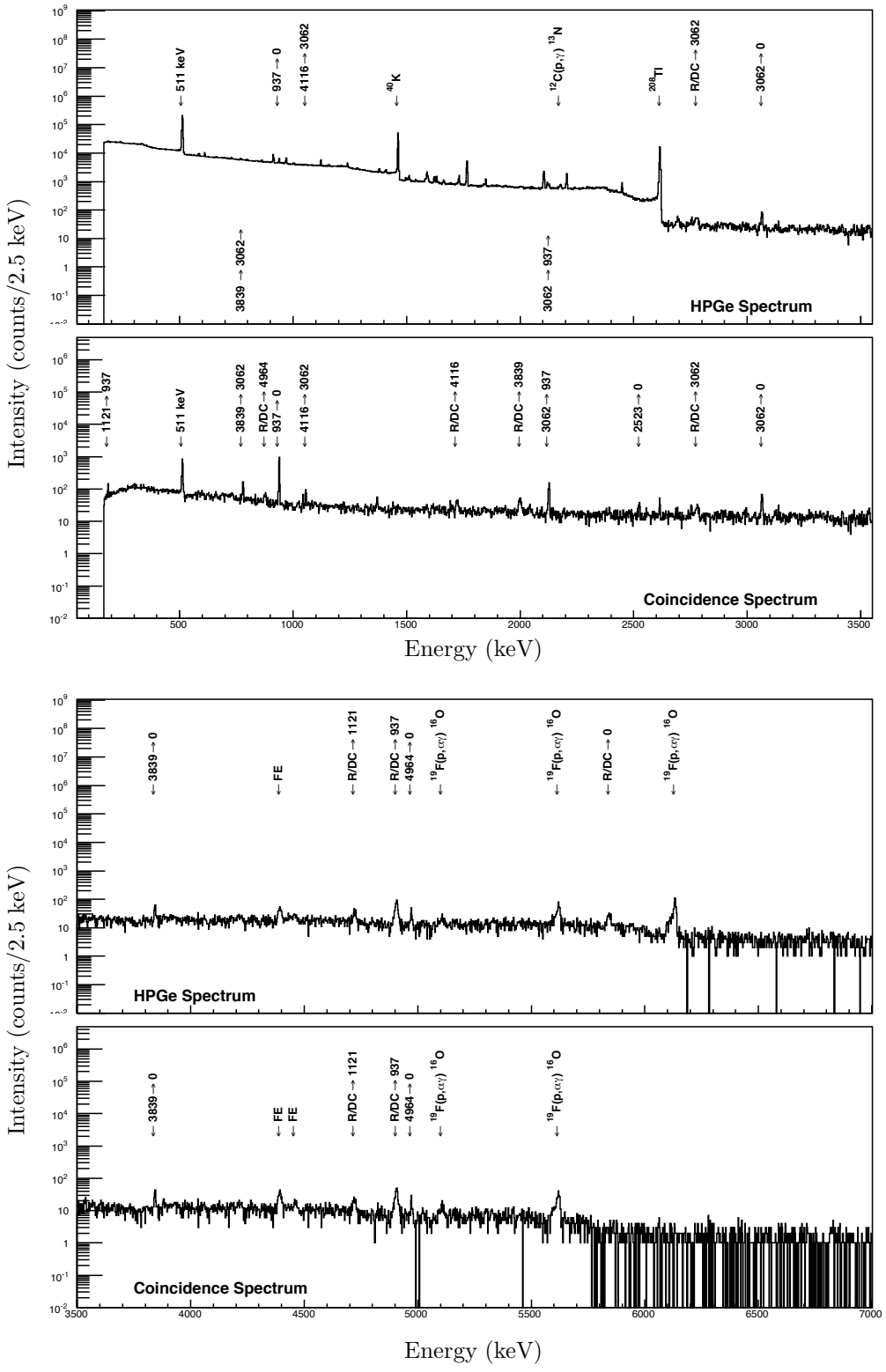

Figure E.3: Muon vetoed HPGe spectrum compared with muon vetoed $\gamma\gamma$-coincidence spectrum at $E_p = 250$ keV. A 3.5 MeV $\leq E_\gamma^{Ge} + E_\gamma^{NaI(Tl)} \leq$ 9.0 MeV coincidence gate was used. Deexcitations of ^{18}F are indicated by transition. First and second escape peaks are labeled "FE" and "SE," respectively. Beam-induced contaminants are labeled, and the remaining peaks are environmental backgrounds (see Tab. E.1).

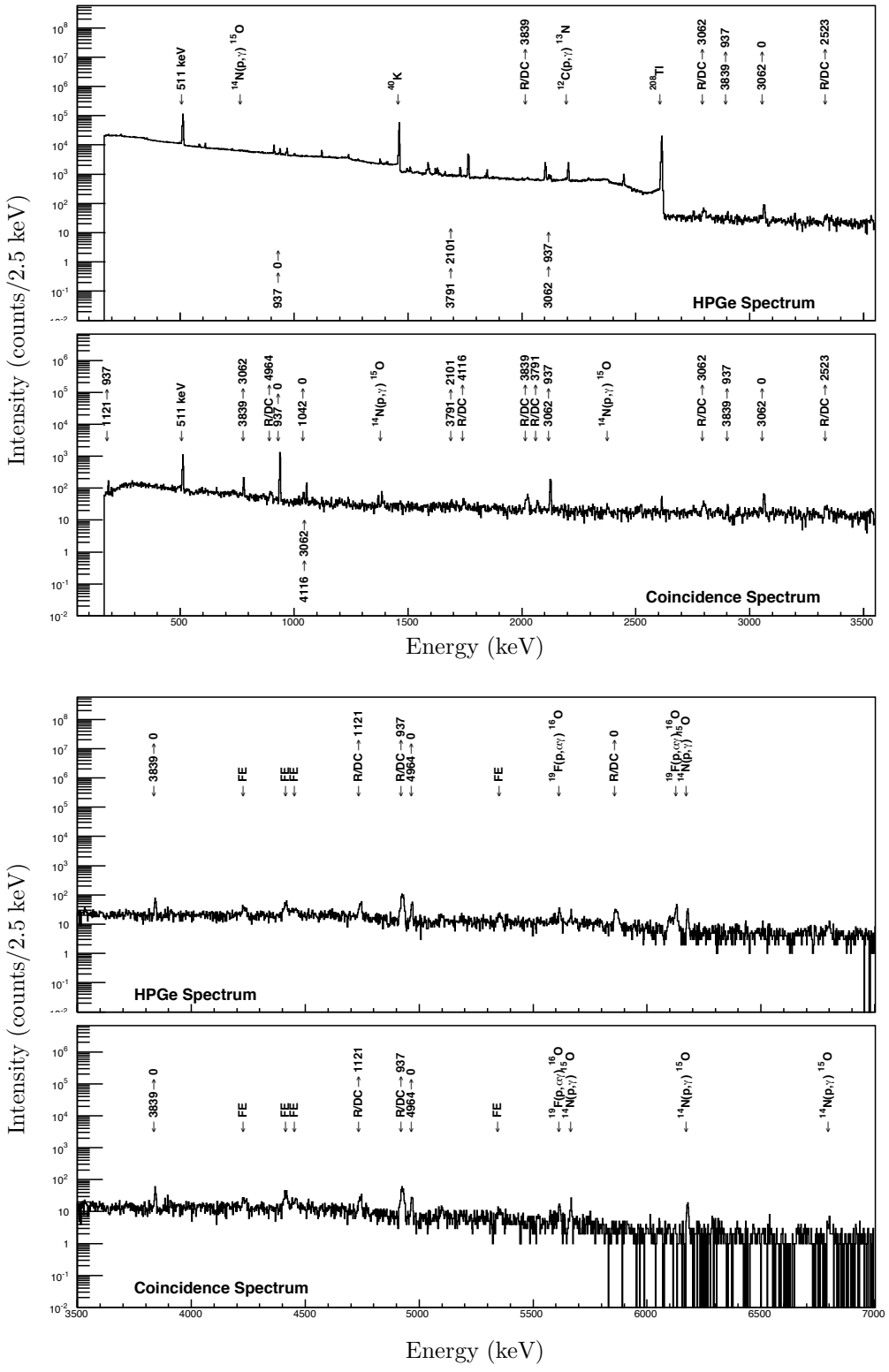

Figure E.4: Muon vetoed HPGe spectrum compared with muon vetoed $\gamma\gamma$-coincidence spectrum at $E_p = 275$ keV. A 3.5 MeV $\leq E_\gamma^{Ge} + E_\gamma^{NaI(Tl)} \leq$ 9.0 MeV coincidence gate was used. Deexcitations of ^{18}F are indicated by transition. First and second escape peaks are labeled "FE" and "SE," respectively. Beam-induced contaminants are labeled, and the remaining peaks are environmental backgrounds (see Tab. E.1).

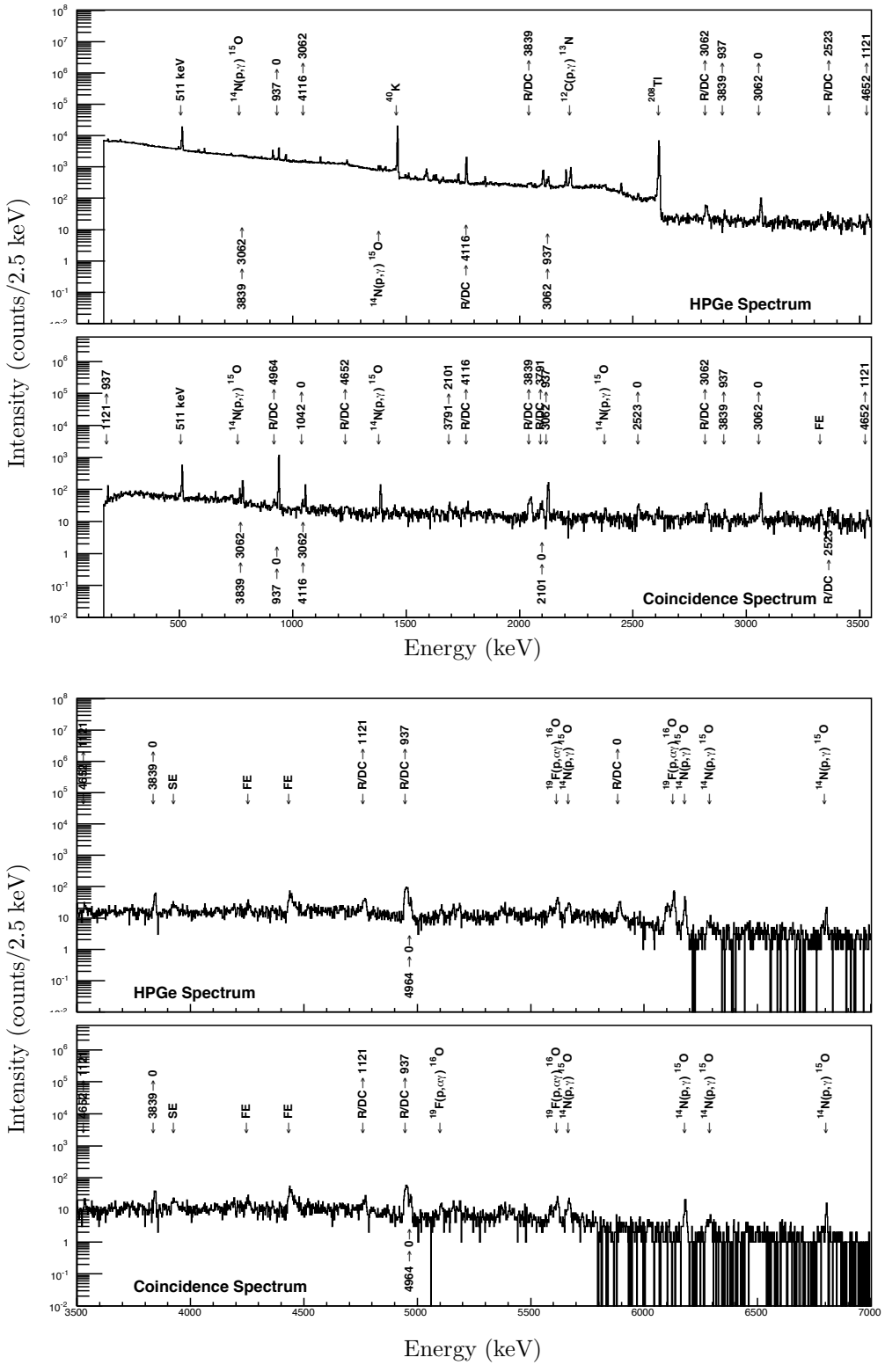

Figure E.5: Muon vetoed HPGe spectrum compared with muon vetoed $\gamma\gamma$-coincidence spectrum at $E_p = 300$ keV. A 3.5 MeV $\leq E_\gamma^{Ge} + E_\gamma^{NaI(Tl)} \leq$ 9.0 MeV coincidence gate was used. Deexcitations of ^{18}F are indicated by transition. First and second escape peaks are labeled "FE" and "SE," respectively. Beam-induced contaminants are labeled, and the remaining peaks are environmental backgrounds (see Tab. E.1).

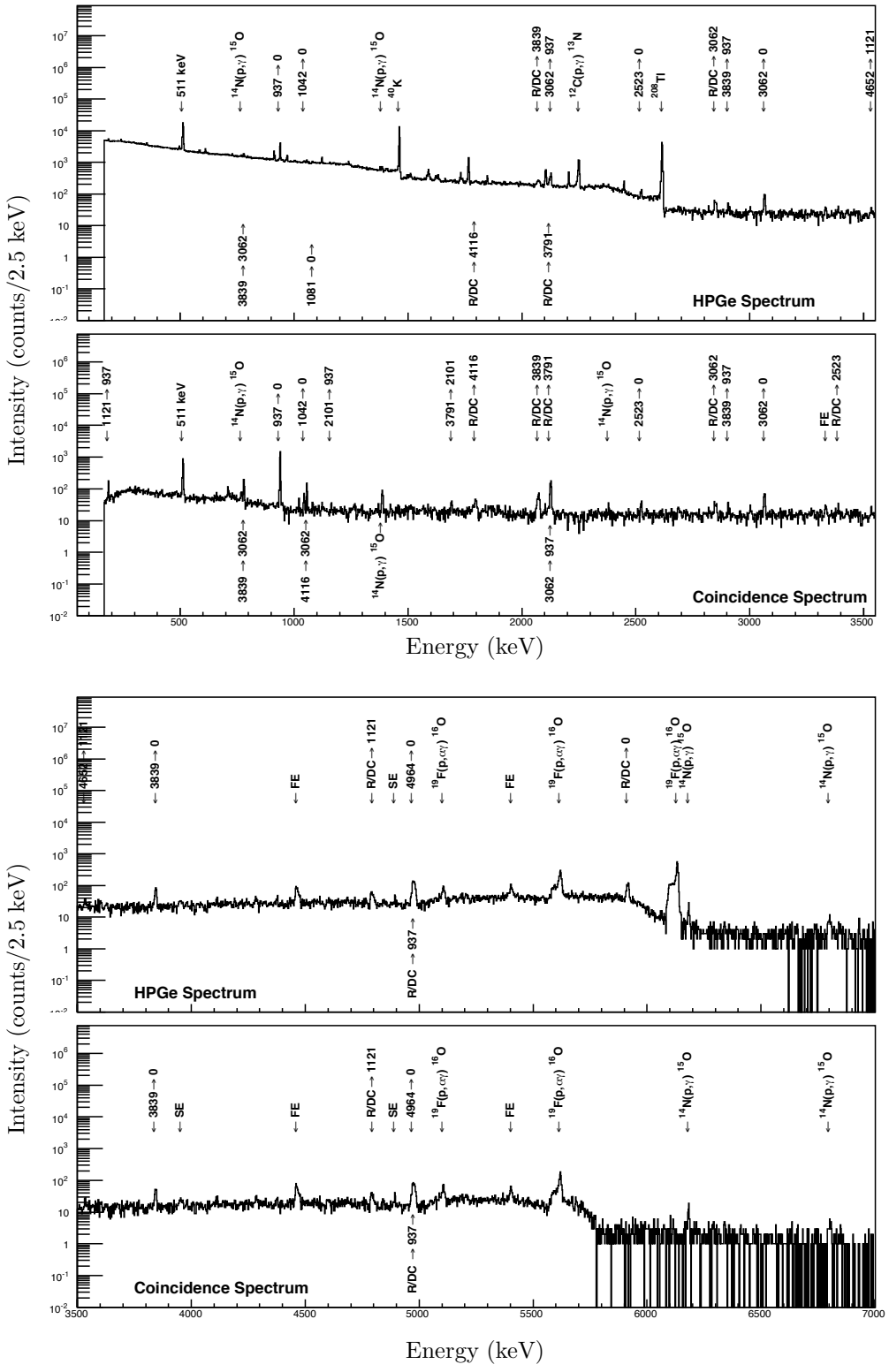

Figure E.6: Muon vetoed HPGe spectrum compared with muon vetoed $\gamma\gamma$-coincidence spectrum at $E_p = 325$ keV. A 3.5 MeV $\leq E_\gamma^{Ge} + E_\gamma^{NaI(Tl)} \leq$ 9.0 MeV coincidence gate was used. Deexcitations of ^{18}F are indicated by transition. First and second escape peaks are labeled "FE" and "SE," respectively. Beam-induced contaminants are labeled, and the remaining peaks are environmental backgrounds (see Tab. E.1).

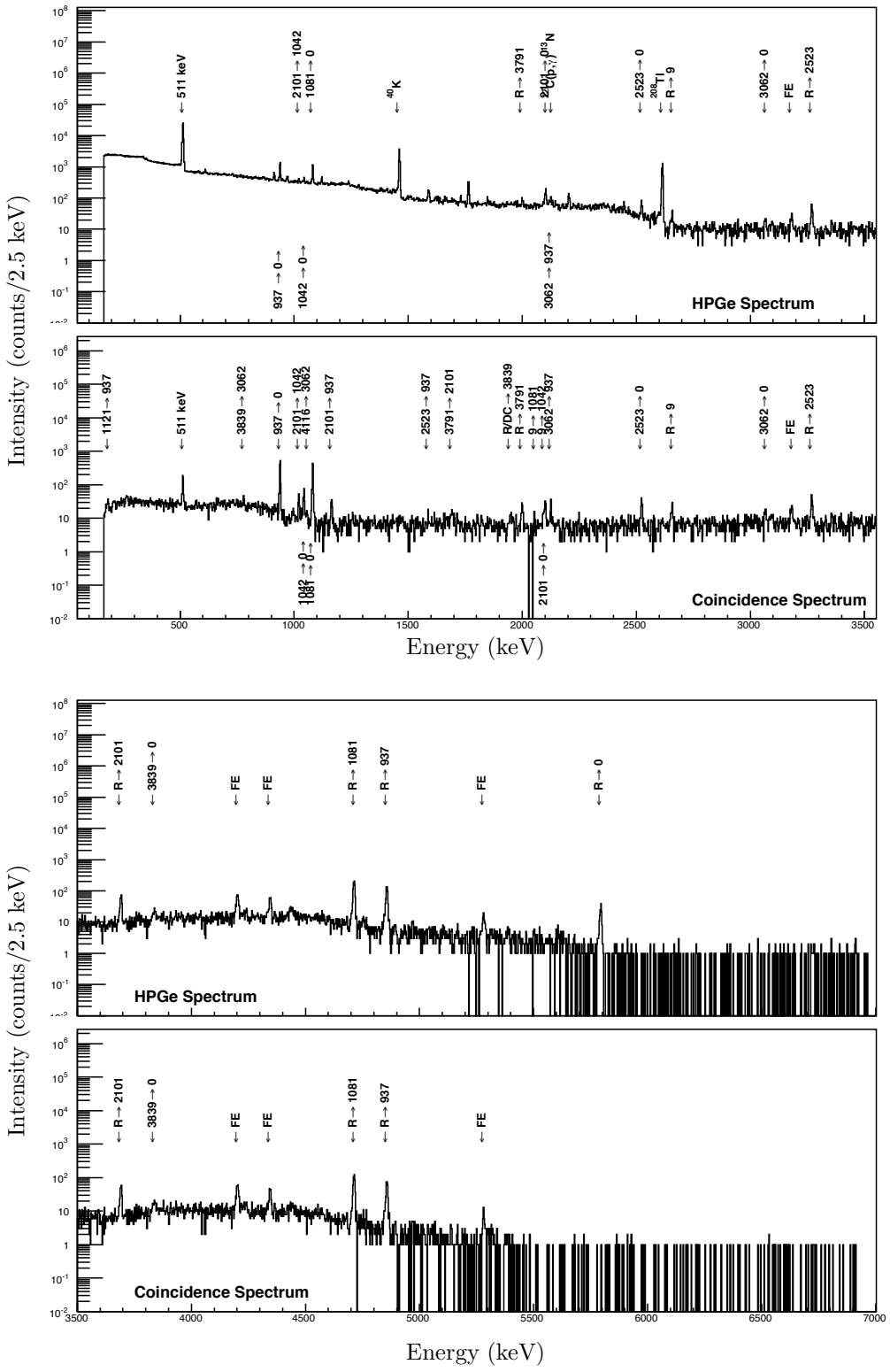

Figure E.7: Muon vetoed HPGe spectrum compared with muon vetoed $\gamma\gamma$-coincidence spectrum at E_R = 193 keV. A 3.5 MeV $\leq E_\gamma^{Ge} + E_\gamma^{NaI(Tl)} \leq$ 9.0 MeV coincidence gate was used. Deexcitations of ^{18}F are indicated by transition. First and second escape peaks are labeled "FE" and "SE," respectively. Beam-induced contaminants are labeled, and the remaining peaks are environmental backgrounds (see Tab. E.1).

REFERENCES

[1] M. Q. Buckner, C. Iliadis, J. M. Cesaratto, C. Howard, T. B. Clegg, A. E. Champagne, and S. Daigle. Thermonuclear reaction rate of $^{18}O(p,\gamma)^{19}F$. *Phys. Rev. C*, 86(6):065804, 2012.

[2] Homer and R. Fagles. *Homer: The Odyssey*. Softback Preview, 1997.

[3] R. Buonanno, C. E. Corsi, A. Buzzoni, C. Cacciari, F. R. Ferraro, and F. Fusi Pecci. The stellar population of the globular cluster m3. i. photographic photometry of 10000 stars. *A&A*, 290:69, 1994.

[4] C. Iliadis. *Nuclear Physics of Stars*. Wiley - VCH, Weinheim, 2007.

[5] P. C. Scott, M. Asplund, N. Grevesse, and A. J. Sauval. Line formation in solar granulation. VII. CO lines and the solar C and O isotopic abundances. *A&A*, 456:675, 2006.

[6] L. R. Nittler, C. M. O. Alexander, R. Gallino, P. Hoppe, A. N. Nguyen, F. J. Stadermann, and E. K. Zinner. Aluminum-, Calcium- and Titanium-rich Oxide Stardust in Ordinary Chondrite Meteorites. *ApJ*, 682:1450, 2008.

[7] P. Hoppe. Stardust in primitive solar system materials. In *Fifth European Summer School on Experimental Nuclear Astrophysics*, volume 1213, page 84, 2010.

[8] M. Lugaro. *Stardust from meteorites: an introduction to presolar grains*, volume 9. World Scientific, 2005.

[9] D. D. Clayton and L. R. Nittler. Astrophysics with presolar stardust. *A&A*, 42, 2004.

[10] S. Palmerini, M. La Cognata, S. Cristallo, and M. Busso. Deep Mixing in Evolved Stars. I. The Effect of Reaction Rate Revisions from C to Al. *ApJ*, 729:3, 2011.

[11] F. Gyngard, E. Zinner, L. R. Nittler, A. Morgand, F. J. Stadermann, and K. M. Hynes. Automated NanoSIMS measurements of spinel stardust from the Murray meteorite. *ApJ*, 717(1):107, 2010.

[12] G. J. Wasserburg, A. I. Boothroyd, and I.-J. Sackmann. Deep Circulation in Red Giant Stars: A Solution to the Carbon and Oxygen Isotope Puzzles? *ApJ*, 447:L37, 1995.

[13] K. M. Nollett, M. Busso, and G. J. Wasserburg. Cool Bottom Processes on the Thermally Pulsing Asymptotic Giant Branch and the Isotopic Composition of Circumstellar Dust Grains. *ApJ*, 582:1036, 2003.

[14] N. Prantzos, C. Charbonnel, and C. Iliadis. Light nuclei in galactic globular clusters: constraints on the self-enrichment scenario from nucleosynthesis. *A&A*, 470:179, 2007.

[15] C. Kobayashi, A. I. Karakas, and H. Umeda. The evolution of isotope ratios in the Milky Way Galaxy. *MNRAS*, 414(4):3231, 2011.

[16] M. Busso, G. J. Wasserburg, K. M. Nollett, and A. Calandra. Can extra mixing in RGB and AGB stars be attributed to magnetic mechanisms? *ApJ*, 671(1):802, 2007.

[17] P. A. Denissenkov, M. Pinsonneault, and K. B. MacGregor. Magneto-thermohaline mixing in red giants. *ApJ*, 696(2):1823, 2009.

[18] P. A. Denissenkov and C. A. Tout. Partial mixing and formation of the ^{13}C pocket by internal gravity waves in asymptotic giant branch stars. *MNRAS*, 340:722, 2003.

[19] J.-P. Zahn. Circulation and turbulence in rotating stars. *A&A*, 265:115, 1992.

[20] A. Maeder and J.-P. Zahn. Stellar evolution with rotation. III. Meridional circulation with MU - gradients and non-stationarity. *A&A*, 334:1000, 1998.

[21] A. Weiss, P. A. Denissenkov, and C. Charbonnel. Evolution and surface abundances of red giants experiencing deep mixing. *A&A*, 356:181, 2000.

[22] C. Charbonnel. The impact of rotation on chemical abundances in red giant branch stars. *Carnegie Observatories Astrophysics Series, Origin and Evolution of the Elements*, 4:60, 2004.

[23] A. V. Sweigart and J. G. Mengel. Meridional circulation and CNO anomalies in red giant stars. *ApJ*, 229:624, 1979.

[24] S. Talon. Numerical simulations of radiative zones and possible effects on evolutionary models. *EAS Publications Series*, 17:187, 2005.

[25] P. P. Eggleton, D. S. P. Dearborn, and J. C. Lattanzio. Deep mixing of ^{3}He: reconciling Big Bang and stellar nucleosynthesis. *Science*, 314(5805):1580, 2006.

[26] R. K Ulrich. Evolution of Stars Containing ^{3}He. *ApJ*, 168:57, 1971.

[27] C. Charbonnel and J.-P. Zahn. Thermohaline mixing: a physical mechanism governing the photospheric composition of low-mass giants. *A&A*, 467(1):L15, 2007.

[28] P. A. Denissenkov and W. J. Merryfield. Thermohaline Mixing: Does it Really Govern the Atmospheric Chemical Composition of Low-mass Red Giants? *ApJ*, 727(1):L8, 2011.

[29] C. Abia, S. Palmerini, M. Busso, and S. Cristallo. Carbon and oxygen isotopic ratios in arcturus and aldebaran. *A&A*, 548:A55, 2012.

[30] J. Nordhaus, M. Busso, G. J. Wasserburg, E. G. Blackman, and S. Palmerini. Magnetic mixing in red giant and asymptotic giant branch stars. *ApJ*, 684(1):L29, 2008.

[31] C. Charbonnel and N. Lagarde. Thermohaline instability and rotation-induced mixing. I. Low-and intermediate-mass solar metallicity stars up to the end of the AGB. *A&A*, 522:10, 2010.

[32] S. Palmerini, S. Cristallo, M. Busso, C. Abia, S. Uttenthaler, L. Gialanella, and E. Maiorca. Deep Mixing in Evolved Stars. II. Interpreting Li Abundances in Red Giant Branch and Asymptotic Giant Branch Stars. *ApJ*, 741(1):26, 2011.

[33] L. R. Nittler. Presolar oxide grains in meteorites. In *AIP Conf. Proc.*, page 59, 1997.

[34] M. Busso, S. Palmerini, E. Maiorca, S. Cristallo, O. Straniero, C. Abia, R. Gallino, and M. La Cognata. On the Need for Deep-mixing in Asymptotic Giant Branch Stars of Low Mass. *ApJ*, 717:L47, 2010.

[35] J. Lattanzio and M. Forestini. Nucleosynthesis in AGB Stars. In T. Le Bertre, A. Lebre, & C. Waelkens, editor, *Asymptotic Giant Branch Stars*, volume 191 of *IAU Symposium*, page 31, 1999.

[36] W. Nowotny, F. Kerschbaum, H. E. Schwarz, and H. Olofsson. A census of AGB stars in Local Group galaxies I. Photometry of a field in M 31. *A&A*, 367:557, 2001.

[37] NASA, ESA, and Hubble. M57: The ring nebula. http://apod.nasa.gov/apod/ap130605.html, 2013. Accessed: 2014-08-05.

[38] C. R. ODell, F. Sabbadin, and W. J. Henney. The three-dimensional ionization structure and evolution of ngc 6720, the ring nebula. *Astron. J.*, 134(4):1679, 2007.

[39] M. La Cognata, C. Spitaleri, A. Mukhamedzhanov, A. Banu, S. Cherubini, A. Coc, V. Crucillà,

V. Goldberg, M. Gulino, B. Irgaziev, et al. A Novel Approach to Measure the Cross Section of the $^{18}O(p, \alpha)^{15}N$ Resonant Reaction in the 0-200 keV Energy Range. *ApJ*, 708:796, 2010.

[40] D. R. Tilley, H. R. Weller, C. M. Cheves, and R. M. Chasteler. Energy levels of light nuclei a = 18-19. *Nucl. Phys. A*, 595(1):1, 1995.

[41] M. Wang, G. Audi, A. H. Wapstra, F. G. Kondev, M. MacCormick, X. Xu, and B. Pfeiffer. The Ame2012 atomic mass evaluation. *Chin. Phys. C*, 36:3, 2012.

[42] J. José, M. Hernanz, and C. Iliadis. Nucleosynthesis in classical novae. *Nucl. Phys. A*, 777:550, 2006.

[43] D. A. Hardy. Explosions from white dwarf star rs oph. http://antwrp.gsfc.nasa.gov/apod/ap060726.html, 2006. Accessed: 2009-11-09.

[44] S. Starrfield, J. W. Truran, W. M. Sparks, and G. S. Kutter. CNO abundances and hydrodynamic models of the nova outburst. *ApJ*, 176:169, 1972.

[45] B. Warner. Cataclysmic variable stars. *Cambridge Astrophysics Series*, 28, 1995.

[46] B. Warner. Properties of novae: an overview. *Cambridge Astrophysics Series*, 43:16, 2008.

[47] J. Richelson. *Spying on the bomb: American nuclear intelligence from Nazi Germany to Iran and North Korea*. WW Norton & Company, 2007.

[48] C. Wrede. Introduction to classical novae. In *Classical Novae in the Cosmos Workshop, XIII International Symposium on Nuclei in the Cosmos, Debrecen, Hungary*, 2014.

[49] S. Starrfield, C. Iliadis, and W. R. Hix. Thermonuclear processes. *Classical Novae*, 43:77, 2008.

[50] G. Masi. Nova delphini 2013 – v339 delphini: a new image (9 may 2014) and movie. http://www.virtualtelescope.eu/tag/nova-delphini-2013/, 2014. Accessed: 2014-08-05.

[51] C. Fox, C. Iliadis, A. E. Champagne, A. Coc, J. José, R. Longland, J. R. Newton, J. Pollanen, and R. Runkle. Explosive Hydrogen Burning of ^{17}O in Classical Novae. *Phys. Rev. Lett.*, 93(8):081102, 2004.

[52] J. José and M. Hernanz. Nucleosynthesis in classical novae: CO versus ONe white dwarfs. *ApJ*, 494(2):680, 1998.

[53] D. Prialnik and A. Kovetz. An extended grid of multicycle nova evolution models. *ApJ*, 445:789, 1995.

[54] S. Starrfield, J. W. Truran, M. C. Wiescher, and W. M. Sparks. Evolutionary sequences for Nova V1974 Cygni using new nuclear reaction rates and opacities. *MNRAS*, 296(3):502, 1998.

[55] A. Kovetz and D. Prialnik. The composition of nova ejecta from multicycle evolution models. *ApJ*, 477(1):356, 1997.

[56] J. Gómez-Gomar, M. Hernanz, J. José, and J. Isern. Gamma-ray emission from individual classical novae. *MNRAS*, 296(4):913, 1998.

[57] M. D. Leising and D. D. Clayton. Positron annihilation gamma rays from novae. *ApJ*, 323:159, 1987.

[58] M. Hernanz, J. José, A. Coc, J. Gómez-Gomar, and J. Isern. Gamma-ray emission from novae related to positron annihilation: constraints on its observability posed by new experimental nuclear data. *ApJ*, 526(2):L97, 1999.

[59] A. Evans, C. M. Callus, P. A. Whitlock, and D. Laney. Infrared Photometry and Spectroscopy of Nova

Pw-Vulpecuale. *MNRAS*, 246:527, 1990.

[60] R. D. Gehrz, J. W. Truran, R. E. Williams, and S. Starrfield. Nucleosynthesis in classical novae and its contribution to the interstellar medium. *PASP*, 110(743):3, 1998.

[61] S. N. Shore, S. Starrffield, R. Gonzalez-Riestrat, P. H. Hauschildt, and G. Sonneborn. Dust formation in Nova Cassiopeiae 1993 seen by ultraviolet absorption. *Nature*, 369(6481):539, 1994.

[62] R. D. Gehrz. Infrared and radio observations of classical novae: physical parameters and abundances in the ejecta. In *Classical Nova Explosions: International Conference on Classical Nova Explosions*, volume 637, page 198, 2002.

[63] J. M. C. Rawlings and A. Evans. Formation and evolution of dust in novae. In *Classical Nova Explosions: International Conference on Classical Nova Explosions*, volume 637, page 270, 2002.

[64] S. Amari, L. R. Nittler, E. Zinner, K. Lodders, and R. S. Lewis. Presolar SiC grains of type A and B: Their isotopic compositions and stellar origins. *ApJ*, 559(1):463, 2001.

[65] M. Politano, S. Starrfield, J. W. Truran, A. Weiss, and W. M. Sparks. Hydrodynamic studies of accretion onto massive white dwarfs: ONeMg-enriched nova outbursts. I. Dependence on white dwarf mass. *ApJ*, 448:807, 1995.

[66] G. S. Kutter and W. M. Sparks. Stellar accretion of matter possessing angular momentum. *ApJ*, 321:386, 1987.

[67] W. M. Sparks and G. S. Kutter. Nuclear runaways in a C/O white dwarf accreting H-rich material possessing angular momentum. *ApJ*, 321:394, 1987.

[68] R. Rosner, A. Alexakis, Y.-N. Young, J. W. Truran, and W. Hillebrandt. On the C/O enrichment of nova ejecta. *ApJ*, 562(2):L177, 2001.

[69] A. Alexakis, A. C. Calder, A. Heger, E. F. Brown, L. J. Dursi, J. W. Truran, R. Rosner, D. Q. Lamb, F. X. Timmes, B. Fryxell, et al. On heavy element enrichment in classical novae. *ApJ*, 602(2):931, 2004.

[70] D. Prialnik and A. Kovetz. The effect of diffusion on prenova evolution-CNO-enriched envelopes. *ApJ*, 281:367, 1984.

[71] A. Kovetz and D. Prialnik. CNO abundances resulting from diffusion in accreting nova progenitors. *ApJ*, 291:812, 1985.

[72] J. Casanova, J. José, E. García-Berro, S. N. Shore, and A. C. Calder. Kelvin-Helmholtz instabilities as the source of inhomogeneous mixing in nova explosions. *Nature*, 478(7370):490, 2011.

[73] L. R. Nittler and P. Hoppe. Are presolar silicon carbide grains from novae actually from supernovae? *ApJ*, 631(1):L89, 2005.

[74] A. Evans and J. M. C. Rawlings. Dust and molecules in nova environments. *Cambridge Astrophysics Series*, 43:308, 2008.

[75] C. Fox, C. Iliadis, A. E. Champagne, R. P. Fitzgerald, R. Longland, J. Newton, J. Pollanen, and R. Runkle. Thermonuclear reaction rate of ^{17}O(p,γ)^{18}F. *Phys. Rev. C*, 71(5):055801, 2005.

[76] A. Chafa, V. Tatischeff, P. Aguer, S. Barhoumi, A. Coc, F. Garrido, M. Hernanz, J. José, J. Kiener, A. Lefebvre-Schuhl, et al. Hydrogen Burning of ^{17}O in Classical Novae. *Phys. Rev. Lett.*, 95(3):031101, 2005.

[77] C. Rolfs, A. M. Charlesworth, and R. E. Azuma. Nuclear structure of ^{18}F (I). Radiative capture experiments. *Nuclear Physics A*, 199:257, 1973.

[78] J. R. Newton, C. Iliadis, A. E. Champagne, J. M. Cesaratto, S. Daigle, and R. Longland. Measurement of ^{17}O(p,γ)^{18}F between the narrow resonances at $E_r{}^{lab}$=193 and 519 keV. *Phys. Rev. C*, 81(4):045801, 2010.

[79] U. Hager, L. Buchmann, B. Davids, J. Fallis, B. R. Fulton, N. Galinski, U. Greife, D. A. Hutcheon, D. Ottewell, A. Rojas, et al. Measurement of the ^{17}O(p,γ)^{18}F reaction rate at astrophysically relevant energies. *Phys. Rev. C*, 85(3):035803, 2012.

[80] D. A. Scott, A. Caciolli, A. Di Leva, A. Formicola, M. Aliotta, M. Anders, D. Bemmerer, C. Broggini, M. Campeggio, P. Corvisiero, Z. Elekes, Z. Fülöp, G. Gervino, A. Guglielmetti, C. Gustavino, G. Gyürky, G. Imbriani, M. Junker, M. Laubenstein, R. Menegazzo, M. Marta, E. Napolitani, P. Prati, V. Rigato, V. Roca, E. Somorjai, C. Salvo, O. Straniero, F. Strieder, T. Szücs, F. Terrasi, and D. Trezzi. First Direct Measurement of the ^{17}O(p,γ)^{18}F Reaction Cross Section at Gamow Energies for Classical Novae. *Phys. Rev. Lett.*, 109(20):202501, 2012.

[81] A. Kontos, J. Görres, A. Best, M. Couder, R. deBoer, G. Imbriani, Q. Li, D. Robertson, D. Schürmann, E. Stech, E. Uberseder, and M. Wiescher. Proton capture on ^{17}O and its astrophysical implications. *Phys. Rev. C*, 86(5):055801, 2012.

[82] A. Di Leva, D. A. Scott, A. Caciolli, A. Formicola, F. Strieder, M. Aliotta, M. Anders, D. Bemmerer, C. Broggini, P. Corvisiero, et al. Underground study of the ^{17}O(p,γ)^{18}F reaction relevant for explosive hydrogen burning. *Phys. Rev. C*, 89(1):015803, 2014.

[83] C. E. Rolfs and W. S. Rodney. *Cauldrons in the cosmos: Nuclear astrophysics*. University of Chicago Press, 1988.

[84] C. Rolfs. Spectroscopic factors from radiative capture reactions. *Nucl. Phys. A*, 217:29, 1973.

[85] C. Iliadis and M. Wiescher. Spectroscopic factors from direct proton capture. *Phys. Rev. C*, 69:064305, 2004.

[86] W. A. Fowler, G. R. Caughlan, and B. A. Zimmerman. Thermonuclear reaction rates. *ARA&A*, 5:525, 1967.

[87] C. Iliadis. Proton single-particle reduced widths for unbound states. *Nucl. Phys. A*, 618:166, 1997.

[88] R. Longland, C. Iliadis, A.E. Champagne, J.R. Newton, C. Ugalde, A. Coc, and R. Fitzgerald. Charged-particle thermonuclear reaction rates: I. monte carlo method and statistical distributions. *Nucl. Phys. A*, 841:1, 2010.

[89] G. Cowan. *Statistical data analysis*. Oxford University Press on Demand, 1998.

[90] A. L. Sallaska, C. Iliadis, A. E. Champange, S. Goriely, S. Starrfield, and F. X. Timmes. STARLIB: A Next-generation Reaction-rate Library for Nuclear Astrophysics. *ApJS*, 207:18, 2013.

[91] C. Angulo, M. Arnould, M. Rayet, P. Descouvemont, D. Baye, C. Leclercq-Willain, A. Coc, S. Barhoumi, P. Aguer, C. Rolfs, R. Kunz, J.W. Hammer, A. Mayer, T. Paradellis, S. Kossionides, C. Chronidou, K. Spyrou, S. Degl'Innocenti, G. Fiorentini, B. Ricci, S. Zavatarelli, C. Providencia, H. Wolters, J. Soares, C. Grama, J. Rahighi, A. Shotter, and M. Lamehi Rachti. A compilation of charged-particle induced thermonuclear reaction rates. *Nucl. Phys. A*, 656:3, 1999.

[92] J. M. Cesaratto, A. E. Champagne, T. B. Clegg, M. Q. Buckner, R. Runkle, and A. Stephan. Nuclear astrophysics studies at lena: The accelerators. *Nucl. Instrum. Methods A*, 623:888, 2010.

[93] G. Ryding. *private communication*, 2013.

[94] M. Q. Buckner, A. E. Champagne, G. Rich, B. P. Carlin, T. B. Clegg, and A. Cooper. The LENA electron cyclotron resonance ion source: an upgraded I_p = 2 mA accelerator for low-energy nuclear astrophysics. *TUNL Progress Report*, 52, 2013.

[95] J. Surbrook, M. Q. Buckner, B. P. Carlin, K. Kelly, T. B. Clegg, and A. E. Champagne. A beam rastering system to reduce target wear. *TUNL Progress Report*, 52, 2013.

[96] J. M. Cesaratto, A. E. Champagne, and T. B. Clegg. ECR Ion Source for the LENA Laboratory. *TUNL Progress Report*, 46:134, 2007.

[97] V. P. Derenchuk, R. R. Kupper, H. R. Petri, G. P. A. Berg, R. J. Brown, W. R. Fox, D. L. Friesel, W. Hunt, W. P. Jones, and W.R. Lozowski. A pulsed ion source for the iucf cooler injector synchrotron. In *Proceedings of the 1997 Particle Accelerator Conference*, volume 3, page 2737, 1997.

[98] M. Q. Buckner, B. P. Carlin, J. M. Cesaratto, and T. B. Clegg. Pulsed Proton Beam from an ECR Ion Source. *TUNL Progress Report*, 48:131, 2008.

[99] R. Longland, C. Iliadis, A. E. Champagne, C. Fox, and J. R. Newton. Nuclear astrophysics studies at the lena facility: The γ-ray detection system. *Nucl. Instrum. Methods A*, 566:452, 2006.

[100] S. Carson, Iliadis C, J. M. Cesaratto, A. E. Champagne, L. N. Downen, M. Ivanovic, J. Kelley, R. Longland, J. R. Newton, G. Rusev, and A. P. Tonchev. Ratio of germanium detector peak efficiencies at photon energies of 4.4 and 11.7 mev: Experiment versus simulation. *Nucl. Instrum. Methods A*, 618:190, 2010.

[101] C. Howard, C. Iliadis, and A. E. Champagne. Monte carlo simulation of the lena detector system. *Nucl. Instrum. Methods A*, 729:254, 2013.

[102] S. Agostinelli, J. Allison, K. al Amako, J. Apostolakis, H. Araujo, P. Arce, M. Asai, D. Axen, S. Banerjee, G. Barrand, et al. GEANT4-a simulation toolkit. *Nucl. Instrum. Methods A*, 506:250, 2003.

[103] J. Allison, K. Amako, J. Apostolakis, H. A. A. H. Araujo, P. Arce Dubois, M. A. A. M. Asai, G. A. B. G. Barrand, R. A. C. R. Capra, S. A. C. S. Chauvie, R. A. C. R. Chytracek, et al. GEANT4 developments and applications. *IEEE Trans. Nucl. Sci.*, 53:270, 2006.

[104] S. Tanaka and M. Kawaguti. Dawn for gEANT4 visualization. In *Proceedings of the CHEP*, volume 97, 1997.

[105] I. J. Kim, C. S. Park, and H. D. Choi. Absolute calibration of ^{60}co by using sum-peak method and an hpge detector. *Appl. Radiat. Isotopes*, 58:227, 2003.

[106] R. G. Helmer and C. Van der Leun. Recommended standards for γ-ray energy calibration (1999). *Nucl. Instrum. Methods A*, 450(1):35, 2000.

[107] H. H. Bolotin. Experimental determinations of directional-correlation solid-angle attenuation factors for Ge (Li) γ-ray detectors: comparison of experimental and calculated values. *Nucl. Instrum. Methods*, 178(1):237, 1980.

[108] J. M. Cesaratto. *Resonant proton capture on ^{23}Na and elemental variations in globular cluster stars*. PhD thesis, The University of North Carolina at Chapel Hill, 2011.

[109] T. M. Semkow, G. Mehmood, P. P. Parekh, and M. Virgil. Coincidence summing in gamma-ray spectroscopy. *Nucl. Instrum. Methods A*, 290:437, 1990.

[110] P. M. Endt. Energy levels of a = 21-44 nuclei (vii). *Nucl. Phys. A*, 521:1, 1990.

[111] M. Marta, A. Formicola, D. Bemmerer, C. Broggini, A. Caciolli, P. Corvisiero, H. Costantini, Z. Elekes, Z. Fülöp, G. Gervino, et al. The ^{14}N(p,γ)^{15}O reaction studied with a composite germanium detector. *Phys. Rev. C*, 83(4):045804, 2011.

[112] M. Wiescher, H. W. Becker, J. Görres, K.-U. Kettner, H. P. Trautvetter, W. E. Kieser, C. Rolfs, R. E. Azuma, K. P. Jackson, and J. W. Hammer. Nuclear and astrophysical aspects of ^{18}O(p, γ)^{19}F. *Nucl. Phys. A*, 349:165, 1980.

[113] D. C. Powell, C. Iliadis, A. E. Champagne, S. E. Hale, V. Y. Hansper, R. A. Surman, and K. D. Veal. Low-energy resonance strengths for proton capture on Mg and Al nuclei. *Nucl. Phys. A*, 644:263, 1998.

[114] K. Debertin and R. G. Helmer. *Gamma- and X-ray Spectrometry with Semiconductor Detectors*. Elsevier Science Publisher B. V., 1988.

[115] C. Rowland, C. Iliadis, A. E. Champagne, A. K. Dummer, R. Fitzgerald, E. C. T. Harley, J. Mosher, and R. Runkle. Studies of weak capture-γ-ray resonances via coincidence techniques. *Nucl. Instrum. Methods A*, 480:610, 2002.

[116] K. B. Swartz, D. W. Visser, and J. M. Baris. A java-based data acquisition system for nuclear physics. *Nucl. Instrum. Methods A*, 463(1):354, 2001.

[117] J. M. Cesaratto, A. E. Champagne, M. Q Buckner, T. B. Clegg, S. Daigle, C. Howard, C. Iliadis, R. Longland, J. R. Newton, and B. M. Oginni. Measurement of the $E_r^{c.m.} = 138$ keV resonance in the ^{23}Na(p,γ)^{24}Mg reaction and the abundance of sodium in AGB stars. *Phys. Rev. C*, 88(6):065806, 2013.

[118] H. W. Becker, M. Bahr, M. Berheide, M. Buschmann, C. Rolfs, G. Roters, S. Schmidt, W. H. Schulte, G. E. Mitchell, and J. S. Schweitzer. Hydrogen depth profiling using ^{18}O ions. *Z. Phys. A*, 351:453, 1995.

[119] H. W. Becker, W. E. Kieser, C. Rolfs, H. P. Trautvetter, and M. Wiescher. Resonance strengths of some light nuclei. *Z. Phys. A*, 305:319, 1982.

[120] R. B. Vogelaar, T. R. Wang, S. E. Kellogg, and R. W. Kavanagh. Low-energy reaction yields for ^{18}o(p,γ) and ^{18}o(α,γ). *Phys. Rev. C*, 42:753, 1990.

[121] D. Tilley, C. Cheves, J. Godwin, G. Hale, H. Hofmann, J. Kelley, G. Sheu, and H. Weller. Energy Levels of Light Nuclei, A= 3-20. *URL http://www.tunl.duke.edu/nucldata*, 2007.

[122] H. C. Chow, G. M. Griffiths, and T. H. Hall. The ^{16}O(p,γ)^{17}F direct capture cross section with an extrapolation to astrophysical energies. *Canadian J. Phys.*, 53(17):1672, 1975.

[123] K. Spyrou, C. Chronidou, S. Harissopulos, S. Kossionides, and T. Paradellis. Cross section and resonance strengths of the ^{19}F(p,$\alpha\gamma$)^{16}O reaction in the energy range $E_p = 0.8$–3.6 MeV. *Z. Phys. A*, 357(3):283, 2007.

[124] G Amsel. Semiconductor Detector Spectroscopy of the Nuclear Reactions ^{16}O+d, ^{18}O+p. *Ann. Phys. (Paris)*, 13, 1964.

[125] D. Phillips and J. P. S. Pringle. Preparation of isotopic oxygen targets via the anodic oxidation of tantalum. *Nucl. Instrum. Methods A*, 135(2):389, 1976.

[126] D. A. Vermilyea. The kinetics of formation and structure of anodic oxide films on tantalum. *Acta Metallurgica*, 1(3):282, 1953.

[127] S. N. Wosu. Anodic oxidation of tantalum in water and biological solutions using current limiting constant voltage method. *J. Mater. Sci.*, 42(11):4087, 2007.

[128] G. Amsel, J. P. Nadai, C. Ortega, and J. Siejka. Precision absolute thin film standard reference targets for nuclear reaction microanalysis of oxygen isotopes: Part II: ^{18}O and ^{17}O standards. *Nucl. Instrum. Methods*, 149(1):713, 1978.

[129] J. R. Newton. *Hydrogen burning of oxygen-17*. PhD thesis, The University of North Carolina at Chapel Hill, 2010.

[130] J. F. Ziegler. Srim-2003. *Nucl. Instrum. Methods B*, 219:1027, 2004.

[131] J. Hoefs. *Stable isotope geochemistry*. Springer, 2008.

[132] T. J. M. Symons, L. K. Fifield, M. J. Hurst, F. Watt, C. H. Zimmerman, and K. W. Allen. A study of the ^{15}N(α,γ)^{19}F reaction for bombarding energies between 5.2 and 8.4 MeV. I. Yield curves and γ decay schemes. *J. Phys. G Nucl. Phys.*, 4:411, 1978.

[133] H. Lorenz-Wirzba, P. Schmalbrock, H. P. Trautvetter, M. Wiescher, C. Rolfs, and W. S. Rodney. The ^{18}O(p, α)^{15}N reaction at stellar energies. *Nucl. Phys. A*, 313:346, 1979.

[134] C. Schmidt and H. H. Duhm. The ^{18}O(^{3}He, d) ^{19}F reaction at E_{3He} = 16 MeV. *Nucl. Phys. A*, 155:644, 1970.

[135] C. Iliadis, R. Longland, A. E. Champagne, and A. Coc. Charged-particle thermonuclear reaction rates: Iii. nuclear physics input. *Nucl. Phys. A*, 841:251, 2010.

[136] H. E. Gove. *Resonance Reactions, Experimental*. North-Holland, Amsterdam, 1959.

[137] Y. Zhu. Upper limit for poisson variable incorporating systematic uncertainties by bayesian approach. *Nucl. Instrum. Methods A*, 578:322, 2007.

[138] H. Krauss, K. Grün, T. Rauscher, and H. Oberhummer. *computer code* `TEDCA`. TU Wien, Vienna, Austria, 1992.

[139] C. Iliadis, R. Longland, A. E. Champagne, and A. Coc. Charged-particle thermonuclear reaction rates: IV. Comparison to previous work. *Nucl. Phys. A*, 841:323, 2010.

[140] M. Wiescher. PhD thesis, Universität Münster, 1980.

[141] J. R. Newton, R. Longland, and C. Iliadis. Matching of experimental and statistical-model thermonuclear reaction rates at high temperatures. *Phys. Rev. C*, 78(2):025805, 2008.

[142] S. Goriely, S. Hilaire, and A. J. Koning. Improved predictions of nuclear reaction rates with the TALYS reaction code for astrophysical applications. *A&A*, 487:767, 2008.

[143] C. Iliadis, R. Longland, A. E. Champagne, A. Coc, and R. Fitzgerald. Charged-particle thermonuclear reaction rates: Ii. tables and graphs of reaction rates and probability density functions. *Nucl. Phys. A*, 841:31, 2010.

[144] A. Chafa, V. Tatischeff, P. Aguer, S. Barhoumi, A. Coc, F. Garrido, M. Hernanz, J. José, J. Kiener, A. Lefebvre-Schuhl, S. Ouichaoui, N. de Séréville, and J.-P. Thibaud. Experimental determination of the ^{17}O(p,α)^{14}N and ^{17}O(p,γ)^{18}F reaction rates. *Phys. Rev. C*, 75(3):035810, 2007.

[145] A. Chafa, V. Tatischeff, P. Aguer, S. Barhoumi, A. Coc, F. Garrido, M. Hernanz, J. José, J. Kiener, A. Lefebvre-Schuhl, et al. Erratum: Hydrogen Burning of ^{17}O in Classical Novae [Phys. Rev. Lett. 95, 031101 (2005)]. *Phys. Rev. Lett.*, 96(1):019902, 2006.

[146] E. W. Weisstein. Full width at half maximum. from mathworld—a wolfram web resource. http://mathworld.wolfram.com/FullWidthatHalfMaximum.html, 2014. Accessed: 2014-09-25.

[147] D. Poenaru and W. Greiner. *Handbook of nuclear properties*. Oxford: Clarendon Press, 1996.

[148] H. Junde. Nuclear data sheets for A= 56. *Nucl. Data Sheets*, 86(2):315, 1999.

[149] R. Barlow and C. Beeston. Fitting using finite Monte Carlo samples. *Comput. Phys. Commun.*, 77(2):219, 1993.

[150] F. James and MINUIT M. Roos. Minuit-a system for function minimization and analysis of the parameter errors and correlations. *Comput. Phys. Commun.*, 10(6):343, 1975.

[151] A. Nappi. A pitfall in the use of extended likelihood for fitting fractions of pure samples in a mixed sample. *Comput. Phys. Commun.*, 180(2):269, 2009.

[152] S. Daigle. *Low energy proton capture study of the $^{14}N(p,\gamma)^{15}O$ reaction*. PhD thesis, The University of North Carolina at Chapel Hill, 2013.

[153] J. F. Ziegler. Particle interactions with matter. *SRIM—The Stopping and Range of Ions in Matter*, 2012.

[154] C. Iliadis. computer code `reacnumeric.f`. *private communication*, 2013.

[155] L. M. Polsky, C. H. Holbrow, and R. Middleton. Nuclear structure of ^{18}f. *Phys. Rev.*, 186(4):966, 1969.

[156] V. Landre, P. Aguer, G. Bogaert, A. Lefebvre, J. P. Thibaud, S. Fortier, J. M. Maison, and J. Vernotte. ^{17}O(^{3}He,d)^{18}F reaction and its implication in the ^{17}O destruction in the CNO cycle in stars. *Phys. Rev. C*, 40:1972, 1989.

[157] A. J. Ferguson. *Angular correlation methods in gamma-ray spectroscopy*. North-Holland Amsterdam, 1965.

[158] C. R. Brune and D. B. Sayre. Energy deconvolution of cross-section measurements with an application to the ^{12}C(α,γ)^{16}O reaction. *Nucl. Instrum. Methods A*, 698:49, 2013.

[159] P. Dyer and C. A. Barnes. The ^{12}C(α,γ)^{16}O reaction and stellar helium burning. *Nucl. Phys. A*, 233(2):495, 1974.

[160] J. C. Helton, F. J. Davis, and J. D. Johnson. A comparison of uncertainty and sensitivity analysis results obtained with random and latin hypercube sampling. *Reliab. Eng. Syst. Safe*, 89(3):305, 2005.

[161] M. D. McKay, R. J. Beckman, and W. J. Conover. Comparison of three methods for selecting values of input variables in the analysis of output from a computer code. *Technometrics*, 21(2):239, 1979.

[162] R. L. Iman and W. J. Conover. Small sample sensitivity analysis techniques for computer models. with an application to risk assessment. *Commun. Stat. A−Theor.*, 9(17):1749, 1980.

[163] R. L. Iman, J. E. Campbell, and J. C. Helton. An approach to sensitivity analysis of computer models. i- introduction, input, variable selection and preliminary variable assessment. *J. Qual. Technol.*, 13:174, 1981.

[164] R. L. Inman, J. C. Helson, and J. E. Campbell. An approach to sensitivity analysis of computer models: Part ii-ranking of input variables, response surface validation, distribution effect and technique synopsis. *J. Qual. Technol.*, 13(4), 1981.

[165] A. Saltelli and J. Marivoet. Non-parametric statistics in sensitivity analysis for model output: a comparison of selected techniques. *Reliab. Eng. Syst. Safe*, 28(2):229, 1990.

[166] R. L. Iman. Uncertainty and sensitivity analysis for computer modeling applications. In T. A. Cruse,

editor, *Reliability technology—1992*, volume 28 of *the winter meeting of the American Society of Mechanical Engineers, Anaheim, CA*, page 153, 1992.

[167] J. C. Helton. Uncertainty and sensitivity analysis techniques for use in performance assessment for radioactive waste disposal. *Reliab. Eng. Syst. Safe*, 42(2):327, 1993.

[168] J. P. C. Kleijnen and J. C. Helton. Statistical analyses of scatterplots to identify important factors in large-scale simulations, 1: Review and comparison of techniques. *Reliab. Eng. Syst. Safe*, 65(2):147, 1999.

[169] A. Saltelli, K. Chan, E. M. Scott, et al. *Sensitivity analysis*, volume 134. Wiley New York, 2000.

[170] J. C. Helton and F. J. Davis. Illustration of sampling-based methods for uncertainty and sensitivity analysis. ncsu. In *USDA Workshop on Sensitivity Analysis Methods, Dept. of Civil Engineering, NC State University*, 2001.

[171] J. C. Helton and F. J. Davis. Latin hypercube sampling and the propagation of uncertainty in analyses of complex systems. *Reliab. Eng. Syst. Safe*, 81(1):23, 2003.

[172] I. Pogrebnyak, C. Howard, C. Iliadis, R. Longland, and G. E. Mitchell. Mean proton and α-particle reduced widths of the Porter-Thomas distribution and astrophysical applications. *Phys. Rev. C*, 88(1):015808, 2013.

[173] F. E. Wietfeldt and G. L. Greene. Colloquium: The neutron lifetime. *Rev. Mod. Phys.*, 83:1173, 2011.

[174] R. Longland, C. Iliadis, and A. I. Karakas. Reaction rates for the s-process neutron source ^{22}Ne+ α. *Phys. Rev. C*, 85(6):065809, 2012.

[175] A. Sallaska. computer code `fitter.cxx`. *private communication*, 2012.

[176] C. Iliadis, J. M. D'Auria, S. Starrfield, W. J. Thompson, and M. Wiescher. Proton-induced Thermonuclear Reaction Rates for A=20-40 Nuclei. *ApJS*, 134:151, 2001.

[177] J. C. Sens, A. Pape, and R. Armbruster. A spectroscopic study of ^{18}F . (II). The ^{17}O(p,γ)^{18}F reaction. *Nucl. Phys. A*, 199:241, 1973.

[178] H.-B. Mak, G. T. Ewan, H. C. Evans, J. D. MacArthur, W. McLatchie, and R. E. Azuma. The alpha widths of the 5603, 5605 and 5668 keV states in ^{18}F. *Nucl. Phys. A*, 343:79, 1980.

[179] I. Berka, K. P. Jackson, C. Rolfs, A. M. Charlesworth, and R. E. Azuma. Isospin mixing of the 5605 and 5668 keV states in ^{18}F in the light of a new state at 5603 keV. *Nucl. Phys. A*, 288:317, 1977.

[180] P. D. Parker. ^{14}N(α,γ)^{18}F Reaction. *Phys. Rev.*, 173:1021, 1968.

[181] B. H. Moazen, D. W. Bardayan, J. C. Blackmon, K. Y. Chae, K. Chipps, C. P. Domizioli, R. Fitzgerald, U. Greife, W. R. Hix, K. L. Jones, R. L. Kozub, E. J. Lingerfelt, R. J. Livesay, C. D. Nesaraja, S. D. Pain, L. F. Roberts, J. F. Shriner, Jr., M. S. Smith, and J. S. Thomas. Measurement of the 183 keV resonance in ^{17}O(p,α)^{14}N using a novel technique. *Phys. Rev. C*, 75(6):065801, 2007.

[182] A. Chafa, V. Tatischeff, P. Aguer, S. Barhoumi, A. Coc, F. Garrido, M. Hernanz, J. José, J. Kiener, A. Lefebvre-Schuhl, S. Ouichaoui, N. de Séréville, and J.-P. Thibaud. Experimental Study of ^{17}O(p,α)^{14}N and ^{17}O(p,γ)^{18}F for Classical Nova Nucleosynthesis. In S. V. Harissopulos, P. Demetriou, and R. Julin, editors, *Frontiers in Nuclear Structure, Astrophysics, and Reactions*, volume 831 of *American Institute of Physics Conference Series*, page 304, 2006.

[183] W. E. Kieser, R. E. Azuma, and K. P. Jackson. The ^{17}O(p, α)^{14}N reaction: Physics and astrophysics. *Nucl. Phys. A*, 331:155, 1979.

[184] K. A. Chipps, D. W. Bardayan, J. C. Blackmon, K. Y. Chae, U. Greife, R. Hatarik, R. L. Kozub, C. Matei, B. H. Moazen, C. D. Nesaraja, S. D. Pain, W. A. Peters, S. T. Pittman, J. F. Shriner, Jr., and M. S. Smith. First Direct Measurement of the ^{17}F(p,γ)^{18}Ne Cross Section. *Phys. Rev. Lett.*, 102(15):152502, 2009.

[185] J. C. Blackmon, A. E. Champagne, M. A. Hofstee, M. S. Smith, R. G. Downing, and G. P. Lamaze. Measurement of the ^{17}O(p,α)^{14}N Cross Section at Stellar Energies. *Phys. Rev. Lett.*, 74:2642, 1995.

[186] J. R. Newton, C. Iliadis, A. E. Champagne, R. Longland, and C. Ugalde. Remeasurement of the 193 keV resonance in ^{17}O(p,α)^{14}N. *Phys. Rev. C*, 75(5):055808, 2007.

[187] G. A. P. Engelbertink and P. M. Endt. Measurements of (p, γ) resonance strengths in the sd shell. *Nucl. Phys.*, 88(1):12, 1966.

[188] B. M. Paine and D. G. Sargood. (p, γ) Resonance strengths in the s-d shell. *Nucl. Phys. A*, 331:389, 1979.

[189] A. E. Champagne and M. L. Pitt. The destruction of ^{18}O in red giants: A search for a sub-threshold resonance in the ^{18}O+p system. *Nucl. Phys. A*, 457(2):367, 1986.

[190] M. La Cognata, C. Spitaleri, A. M. Mukhamedzhanov, B. Irgaziev, R. E. Tribble, A. Banu, S. Cherubini, A. Coc, V. Crucillà, V. Z. Goldberg, et al. Measurement of the 20 and 90 keV Resonances in the ^{18}O(p,α)^{15}N Reaction via the Trojan Horse Method. *Phys. Rev. Lett.*, 101(15):152501, 2008.

[191] K. Yagi. Analysis of Elastic Scattering of Protons by ^{18}O and the Energy Levels of ^{19}F. *J. Phys. Soc. Jpn.*, 17(4):604, 1962.

[192] D. L. Sellin, H. W. Newson, and E. G. Bilpuch. High resolution investigation of resonances in ^{19}F. *Ann. Phys.*, 51(3):461, 1969.

[193] C. Iliadis, U. Giesen, J. Görres, M. Wiescher, S. M. Graff, R. E. Azuma, and C. A. Barnes. Direct proton capture on ^{32}S. *Nucl. Phys. A*, 539:97, 1992.

[194] K. J. Kelly, M. Q. Buckner, and A. E. Champagne. Full Spectrum Coincidence Summing Corrections with GEANT4 During Simulation Runtime. *In preparation*, 2014.

[195] Idaho National Engineering and Environmental Laboratory. Gamma-ray spectrum catalog of isotopes. 2003.